Vortex Ring Evolution and Wall Interaction in Polymer Solutions

A Thesis

Submitted for the Degree of

M.S.(Engineering)

by

Swastik Hegde

Engineering Mechanics Unit
Jawaharlal Nehru Centre for Advanced Scientific Research
(A Deemed University)
Bangalore – 560 064

June 2019

DECLARATION

I hereby declare that the matter embodied in the thesis entitled "**Vortex Ring Evolution and Wall Interaction in Polymer Solutions**" is the result of investigations carried out by me at the Engineering Mechanics Unit, Jawaharlal Nehru Centre for Advanced Scientific Research, Bangalore, India under the supervision of **Prof. K R Sreenivas**, and that it has not been submitted elsewhere for the award of any degree or diploma.

In keeping with the general practice in reporting scientific observations, due acknowledgment has been made whenever the work described is based on the findings of other investigators.

Swastik Hegde

CERTIFICATE

I hereby certify that the matter embodied in this thesis entitled "**Vortex Ring Evolution and Wall Interaction in Polymer Solutions**" has been carried out by **Mr. Swastik Hegde** at the Engineering Mechanics Unit, Jawaharlal Nehru Centre for Advanced Scientific Research, Bangalore, India under my supervision and that it has not been submitted elsewhere for the award of any degree or diploma.

Prof. K R Sreenivas
(Research Supervisor)

Acknowledgements

I would like to express my sincere gratitude to Prof. K. R. Sreenivas, for his guidance and encouragement throughout my masters. I am very grateful to him for providing me the freedom to take up the project of my choice. His physical intuition was very helpful at key moments during the project. He has patiently listened to my doubts and has helped me to solve them. All the discussions with him have been very insightful and thought-provoking. Also, I am very indebted to him for his suggestions and support for my post-MS career.

I would like to thank Prof. Ganesh Subramanian, Prof. Santosh Ansumali, Prof. S V Diwakar, Prof. Meheboob Alam and Prof. Jaywant Arakeri for their courses, and various suggestions at times. Also, they were very approachable and kind to me throughout these years. Rigorous course-work has been of great help while carrying out this project.

I immensely thank Shashank without whom I couldn't have done much progress in this project. He has sacrificed a lot of his precious time teaching me how to carry out experiments. Many ideas tried out in this project have come out of discussions with him.

All my labmates Vybhav, Rafi, Dhiraj, Pushpit and Mayank have been very co-operative and helped me at different times. I have learnt a lot from them during both Heat Transfer project and masters thesis work.

I am grateful to Piyush and Sarath for very thoughtful discussions. I am thankful to all my classmates Prashant, Pulkit, Nishant, Albin, Shaurya and Prateek Anand for a great time throughout the masters, and for cheerful conversations. I would like to thank all EMU for their help during this journey.

This work wouldn't have been possible without the continuous and strong support of my parents and family. I am very grateful to them for the motivation and confidence they provided during the course of this work.

Abstract

Addition of small quantity of polymer to a turbulent flow is shown to reduce the drag drastically. This phenomena (also known as Tom's effect) is studied very rigorously, because of industrial applications and also as a tool to understand the physics behind fluid turbulence. In recent years it is discovered that addition of polymers can change the flow behavior in many spectacular ways: It can either stabilize a flow or can cause instability on its own, either reduce the drag or cause turbulence thereby increasing drag etc. Since polymers interact with the flow in a very complex way, it is very necessary to study the phenomena in a systematic way, by first considering only the simple flows. One main reason for not clearly understanding the polymer drag reduction is that, most studies done so far are in turbulent flows, which by itself is not clearly understood yet. Another important reason being the difficulty in characterizing the dilute polymer solution properties. Hence, we have chosen a simplistic version of this complex problem, i.e vortex ring in polymer solutions. Turbulent flow consists of eddies, which interact with polymers in different ways depending upon the time and length scales involved. A simplest model for such eddies is the vortex ring, which is easy to generate experimentally and is well understood. Hence, studying vortex rings in polymer solution should bring us one step closer to understand the physics behind polymer drag reduction.

In our experiments, vortex ring generated by piston cylinder mechanism, travels freely for around $4D$ distance, after which it is made to interact with the wall which is kept at $5D$. The reason to place the wall is to account for the wall effects. We break the flow into four parts, (1) Vortex ring formation phase (2) Vortex ring free shear phase (3) Vortex Ring interacting with wall (4) After vortex ring impacting the wall. We try to demonstrate the effect of polymer in each of these phases. Particle Image Velocimetry and Planar Laser Induced Fluorescence are the two methods used in our experiments. Along with these experiments, we also present the efforts done in characterizing the polymer solution. From classical viscometer methods to latest oscillatory rheometry, we present different ways of characterizing polymer solution, and the difficulties involved in it. Addition of polymer to a fluid changes its viscosity and elasticity. Its highly debated

in early works on which property contributes largely. We try to relate the possible contribution of each of these properties with the observed changes.

Table of contents

List of figures

List of tables

Nomenclature

Greek Symbols

δ	Boundary layer thickness
Γ	Circulation
Γ^*	Non-dimensional Circulation
η^*	Complex viscosity
ρ	Density
η_∞	Infinite shear viscosity
μ_{inh}	Inherent viscosity
$[\mu]$	Intrinsic viscosity
ν	Kinematic Viscosity
G''	Loss modulus
M_u	Molar mass constant
μ_{red}	Reduced viscosity
$\mu_{relative}$	Relative viscosity
τ_r	Rozhokov relaxation time
τ_z	Zimm relaxation time
λ	Relaxation time
σ	Standard deviation

$\mu_{specific}$ Specific viscosity

G' Storage modulus

$\dot{\gamma}$ Shear rate

γ Strain

M_μ Viscosity averaged molecular weight

η Dynamic Viscosity

ω Vorticity

η_0 Zero shear viscosity

Acronyms / Abbreviations

a Vortex ring core radius

C Concentration

D Diameter of vortex ring

De Deborah Number

DLS Dynamic Light Scattering

DNS Direct Numerical Simulation

DR Drag Reduction

I Impulse

K.E Kinetic Energy

LDV Laser Doppler Velocimetry

L Piston stroke-length

MDR Maximum Drag Reduction

m Consistency co-efficient

n Power Law index

PAMH Polyacrylamide-hydrolyzed

PEO Polyethylene oxide

PIV Particle Image Velocimetry

PLIF Planar Laser Induced Florescence

Re Reynolds Number

R_{nozzle} Radius of nozzle exit

R Vortex ring radius

t^* Non-dimensional time

t Time

t_{wall} Time when vortex ring reaches wall

U Translational velocity of vortex ring

V Piston velocity

Chapter 1

Introduction

1.1 Polymer Drag Reduction

Addition of small quantity of polymer to turbulent flow is shown to reduce the drag dramatically compared to the solvent alone (Graham, 2004; Virk, 1975; Virk et al., 1967; Yang, 2009). This phenomena is studied extensively mainly because of its applications in oil pipelines, fire engine pipes and in marine vehicles. Most notable application being Trans-Alaskan pipeline, where this principle is used to reduce the total throughput needed to pump oil and to reduce the number of pumping stations required. Also, it is a tool to understand the complex physics behind fluid turbulence. Addition of polymers also effect the stability of laminar flow (Garg et al., 2018), causes elasto-inertial instability (Samanta et al., 2013), and can drive turbulence with elastic stresses (Groisman and Steinberg, 2000). It is also shown to be causing a change in turbulent transport of heat and mass (Benzi and Ching, 2018). First discovered by Toms in 1948, this effect is also called "Tom's Effect". Development of this field over the last 70 years is nicely documented in multiple review articles (Berman, 1978; Lumley, 1969; Procaccia et al., 2008; White and Mungal, 2008). Recent interests in this field are driven by biological applications. It is shown that Polymer Drag Reduction principles can be used to improve blood flow in certain blood vessels (Marhefka and Kameneva, 2016; Marhefka et al., 2009). But even after much efforts the phenomena of drag reduction still remains an enigma. The main reason being it is overlap of two complex fields, polymer physics and fluid turbulence. However, certain things are clear about this phenomena. Basic mechanism for drag reduction involves, dynamic interaction between polymers and turbulence. This is clear because of two reasons. (1) No drag reduction is observed in laminar flow of polymer solution (2) The Re, at which DR is first observed depends on the number of monomers

in the macromolecule.

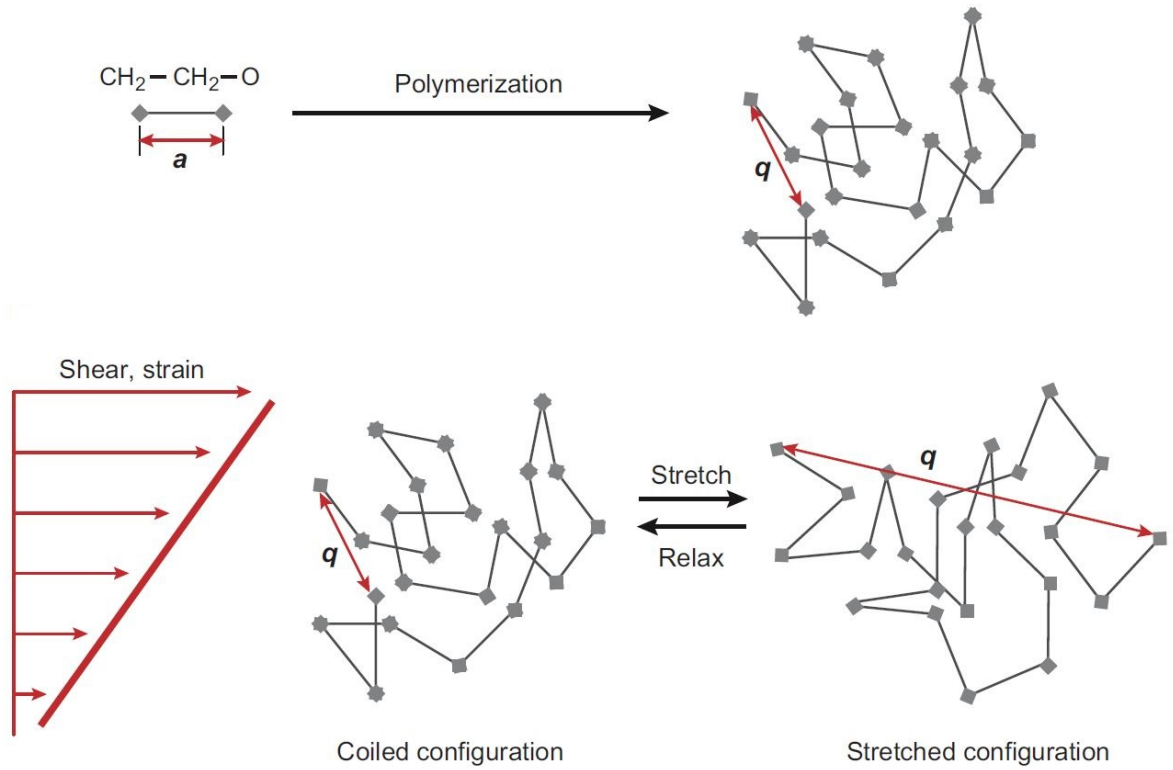

Fig. 1.1 Schematic of polymer stretch (and relaxation) in shear flow (White and Mungal, 2008)

Detailed explanation for this phenomena can be broadly classified into two classes. (1) Viscous Theory, in which increment in viscosity because of addition of polymers is thought to play the major role (De Angelis et al., 2004; Lumley, 1969; L'vov et al., 2004; L'Vov et al., 2004; Ryskin, 1987). (2) Elastic Theory, wherein elasticity of polymer molecules is assumed to play the key role (De Gennes, 1990; Joseph, 1990; Sreenivasan and White, 2000; Tabor and De Gennes, 1986). Both the theories have their own advantages and drawbacks, which will be explained in section 1.1.2 and 1.1.3.

1.1.1 Experimental Evidence

After demonstration of this effect by Toms in 1948, lot of experimental works have been carried out in this field. Most of the works are on turbulent pipe flow, driven by very strong commercial application (Choueiri et al., 2018; Den Toonder et al., 1997; Samanta et al., 2013; Virk et al., 1967). However, considerable amount of work is done on turbulent

channel flow (Min et al., 2003; Ptasinski et al., 2003), homogeneous isotropic turbulence i.e grid turbulence (van Doorn et al., 1999; Vonlanthen and Monkewitz, 2013) and flat plate boundary layer (White et al., 2004). In this subsection pipe flow experimental results are considered.

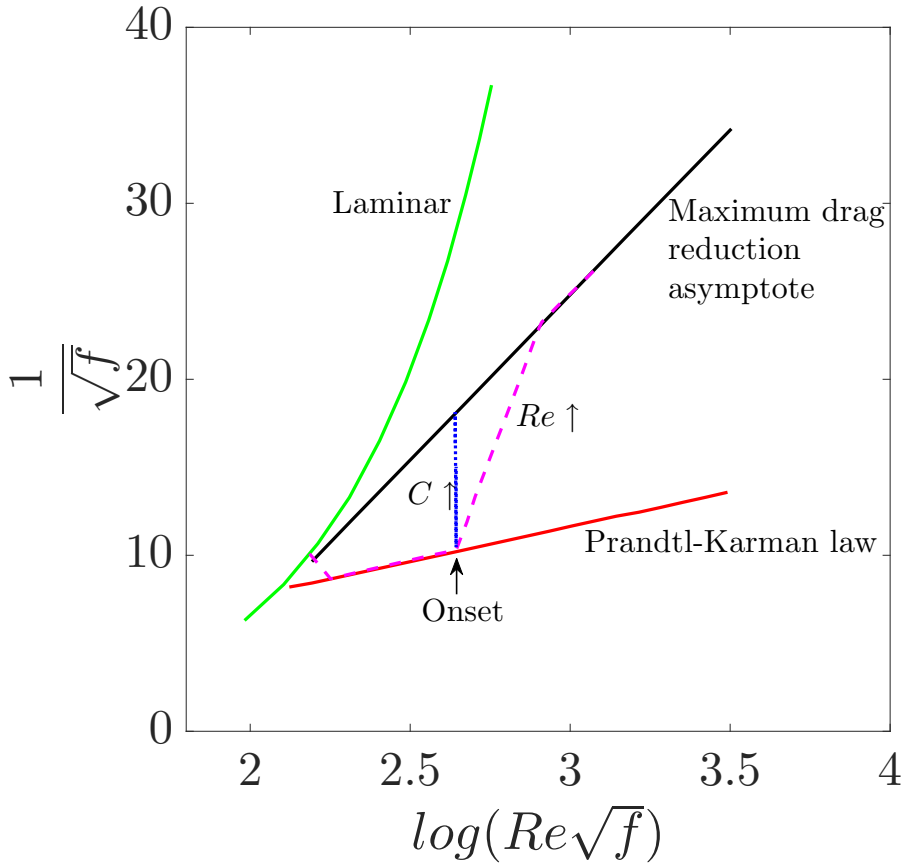

Fig. 1.2 Schematic illustrating the onset and different trajectories of polymer drag reduction. The blue dotted line represents the case in which Re is fixed and polymer concentration C is increased. The pink dashed line represents the case in which C is fixed and Re is increased. (Adopted from White and Mungal (2008))

Figure 1.2 shows onset of drag reduction and a unique state i.e. Maximum Drag Reduction state (MDR) and the different paths in which this asymptotic state can be reached. In the works of Virk et al. (1967), it is observed that, the onset of drag reduction depends on polymer properties. Once the flow is in drag reduced state, addition of polymer will reduce the drag further. This state corresponds to the space between MDR and the Prandtl-Karmann line. In this region, the amount of drag reduction depends on the properties and the quantity of the polymer added. As the quantity of polymer added increases, the drag reduction increases until the flow reaches MDR state. This is a unique state which will be attained by all the drag reduced flows when sufficiently

large quantity of polymers are added, irrespective of polymer and solvent properties. A drag reduction value of 80% was observed by Virk et al. (1967) at this MDR state, and further increase was not observed even when more and more polymers were added. Hence it was concluded as the maximum possible drag reduction by polymer addition. Similar MDR state was observed for channel flows also. MDR was reported in multiple other experiments (Den Toonder et al., 1997; Min et al., 2003; Ptasinski et al., 2003; Samanta et al., 2013; Warholic et al., 1999). It was widely thought that, MDR is the final state of polymer drag reduced flows. However, recently by using polymers of different concentration and different Re, Choueiri et al. (2018), showed that for some parameters, polymers relaminarize the flow completely, thus by exceeding MDR with 100% drag reduction (Refer figure 1.3).

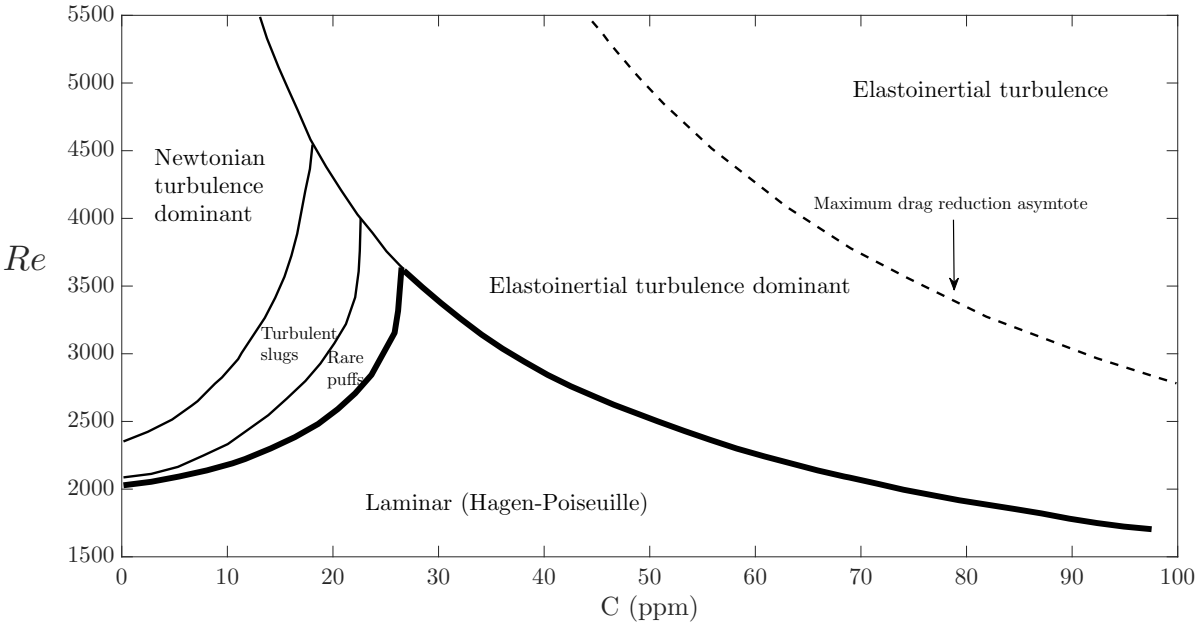

Fig. 1.3 State map for Reynolds number versus polymer concentration (Adopted from Choueiri et al. (2018)).

Above the Re of 3500, the drag reduced flow will reach the MDR state without relaminarising at all the concentrations (Refer figure 1.4a). However, below that Re the flow becomes laminar, and on continuous addition of polymers will reach MDR state from below (Refer figure 1.4b). Also in the same paper, Choueiri et al. (2018) showed that the same dynamical pathway holds for other polymers too, though at different concentrations depending on the polymer properties.

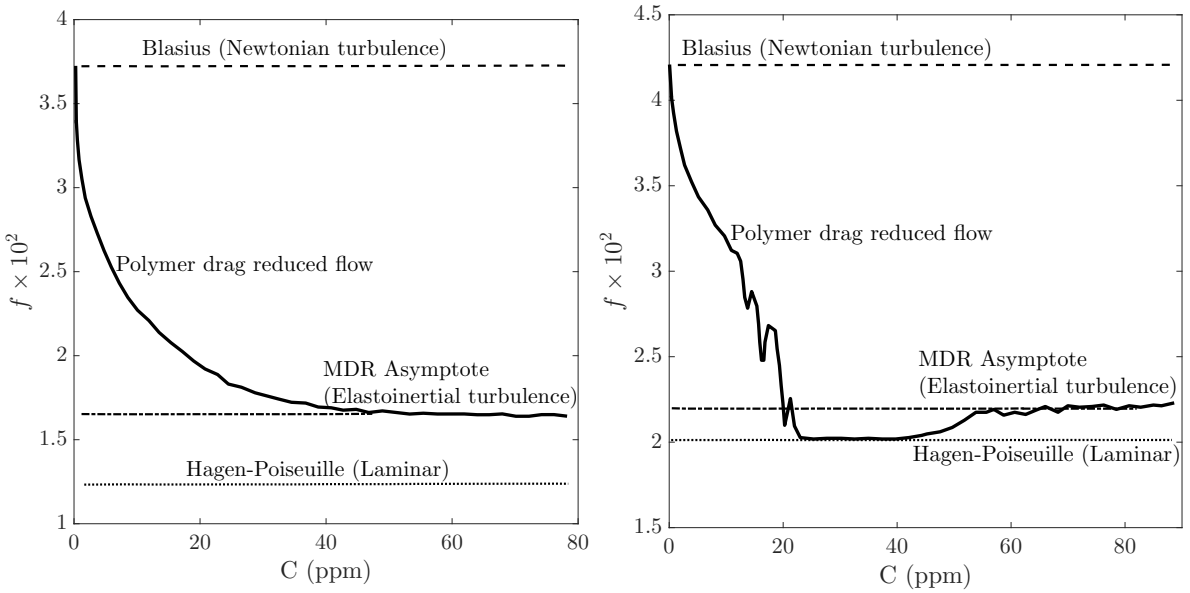

(a) $Re = 5200$ (b) $Re = 3150$

Fig. 1.4 The Darcy-Weisbach friction factor f, as a function of continuously increasing polyacrylamide (PAM) concentration (Adopted from Choueiri et al. (2018)).

This experiment also showed that the MDR state is a different turbulent state altogether. The addition of polymers to laminar flows can create instability, known as elasto-inertial instability, which will take the flow to a state of elasto-inertial turbulence. And this experiment proved that the MDR is a state of elasto-inertial turbulence, where elastic stresses drive the turbulence more than the Reynolds stresses (Refer figure 1.5). Although absence of Reynolds stress was observed in few experiments (Virk et al., 1967; Warholic et al., 1999), and possibility of elastic stresses driving the turbulence was proposed earlier (Samanta et al., 2013; White and Mungal, 2008), this experiment established the state of MDR clearly. The structure of MDR differs from that of Newtonian Turbulence (Refer figure 2 in Choueiri et al. (2018)). In elasto-inertial turbulence short wavelength high intensity puffs are replaced by long low intensity streaks and this is accompanied by reduction in Reynolds stresses (Refer figure 1.5). A similar stabilized streaks compared to pure solvent's meandering span-wise puffs were observed by (White et al., 2004) using Particle Image Velocimetry (PIV) measurements (Refer figure 1 in White and Mungal (2008)).

Analysis of mean velocity profile of the drag reduced flow show two different properties compared to solvent alone (Virk, 1975). Addition of polymers will not cause changes in viscous sublayer, and the linear relation between non-dimensional coordinates of U^+ and

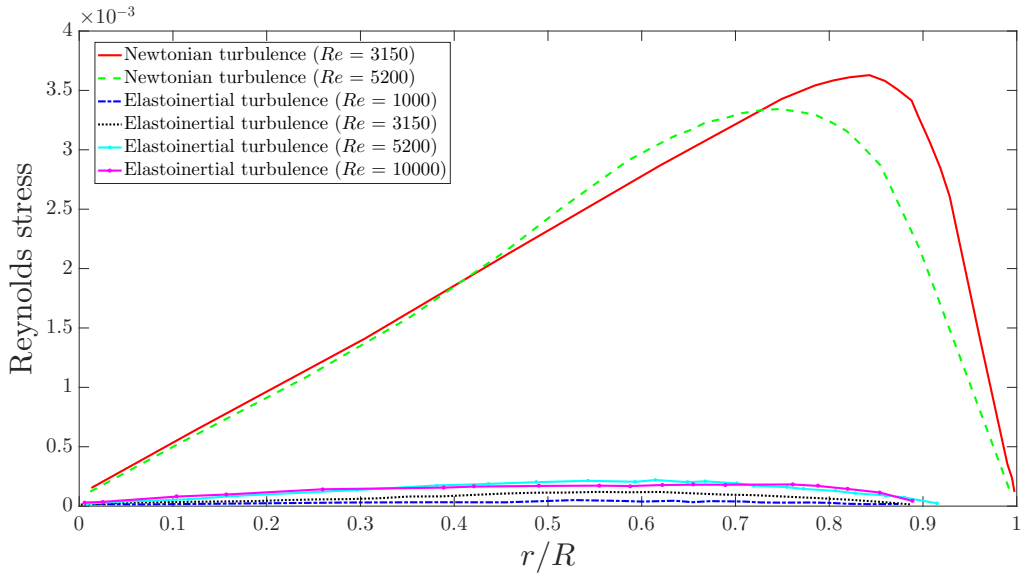

Fig. 1.5 Reynolds stresses for Newtonian and Elasto-inertial turbulence (Adopted from Choueiri et al. (2018)).

y^+ still holds good. After this linear relation, there exists a log law region for pure solvent. This log law for solvent is also known as Newtonian law of the wall, which is recovered when the amount of polymer added is so small that the DR is not onset. As the DR is onset, there appears another log law which is parallel to the original Newtonian law of the wall, but just shifted upwards. This parallel upward shift is called "effective slip", which increases with DR. This has been observed in multiple experiments with different amount of DR as shown in figure 1.7(Virk, 1975). Another mean velocity profile with logarithmic relation corresponds to MDR asymptote, which is also termed as "ultimate profile". As the DR increases, the line corresponding to polymer solution log-law will start to change the slope and aligns itself with the MDR profile. The slope of MDR being about five times that of solvent's Newtonian log-law, shows the increment in mass flow rate for the same pressure drop. Figure 1.6 and 1.7 shows the polymer DR from the mean velocity perspective as studied in the earlier experiments.

There are few articles reporting increased axial velocity fluctuations and reduced velocity fluctuations in other directions. Based on this, a possible explanation is given that the polymers decouple the axial velocity from radial and azimuthal velocities. Based on all above observations, few theories are proposed. The main goal of these theories is to predict the onset of drag reduction and give an explanation for it.

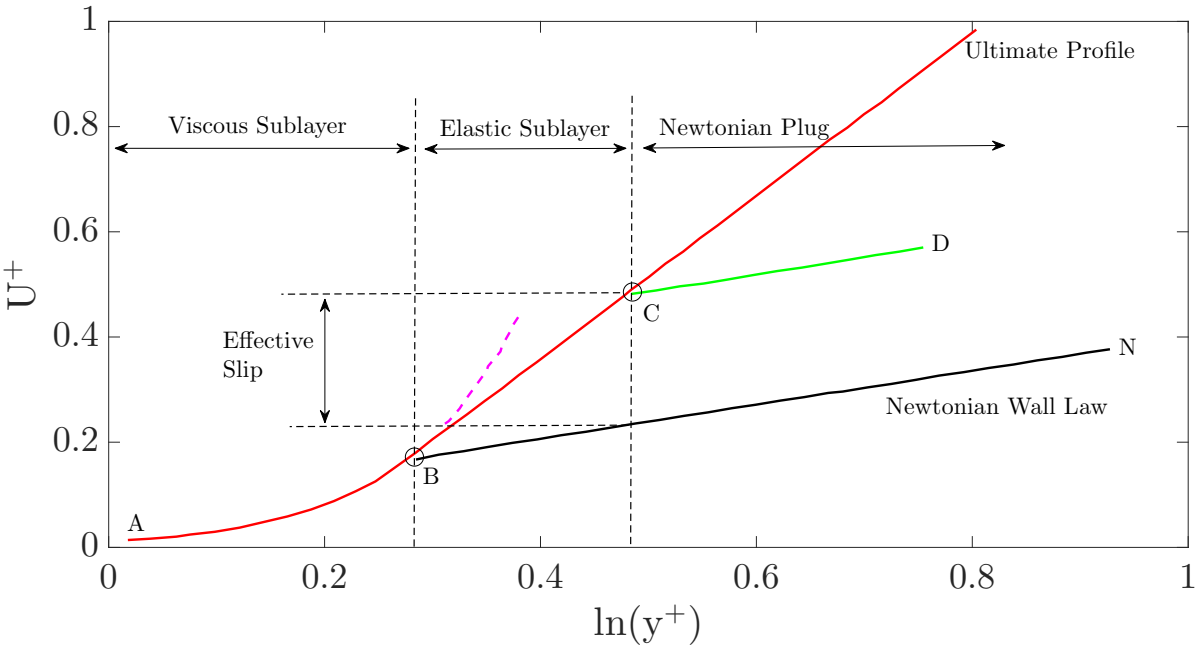

Fig. 1.6 Schematic of mean velocity profile during drag reduction (Adopted from Virk (1975)).

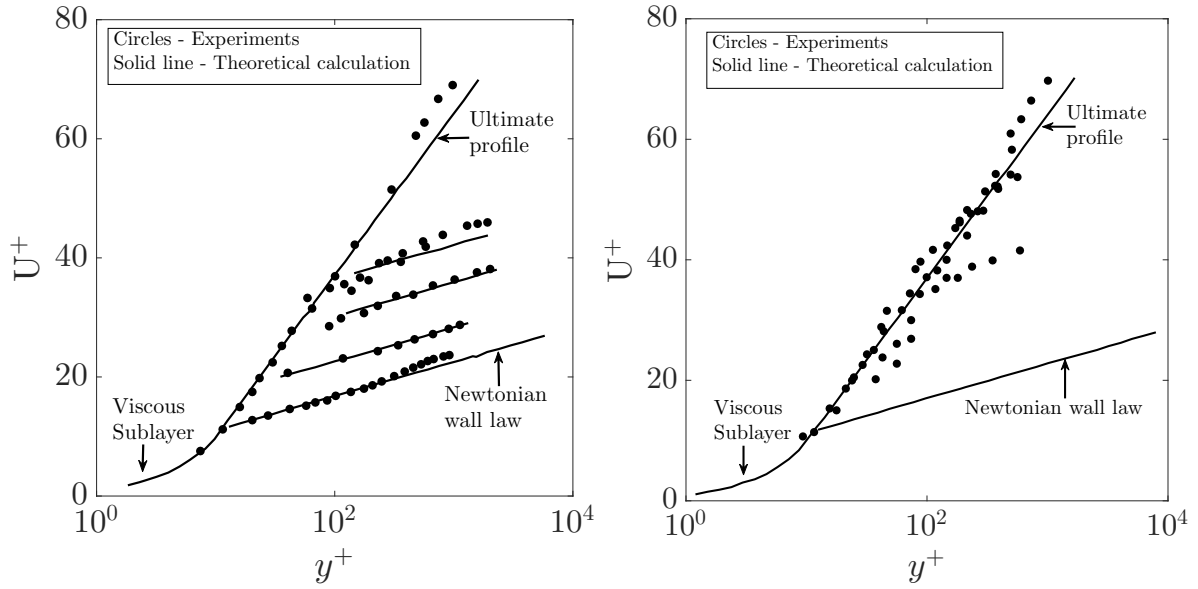

(a) During DR (b) During MDR

Fig. 1.7 Mean velocity profile in non-dimensional coordinates. (Adopted from Virk (1975))

1.1.2 Viscous Theory

According to viscous theory, increase in viscosity caused by addition of polymers plays a key role in drag reduction (Lumley, 1969; L'Vov et al., 2004; Ryskin, 1987). Shear viscosity of polymer solutions show shear thinning behavior. Shear thinning behavior originates from polymers getting stretched and aligned along the flow direction. However, stretching of polymers increases elongational (and effective) viscosity (De Angelis et al., 2004; Ryskin, 1987). It is assumed that the strain rates and the vorticity fields in the buffer layer are suitable for the extension of the polymer molecules, which in turn increases the effective viscosity just outside the viscous sublayer, and prevents the turbulent momentum transport. Ryskin (1987) calculated the effective viscosity increase in turbulence due to unraveling macromolecules, and arrived at a relation between this viscosity increase and a drag reduction parameter. It has been shown that space dependent viscosity alone can give rise to drag reduction (L'vov et al., 2004), without even considering the energy stored in the polymer molecules, which is the basic mechanism in elastic theory. In the follow-up work (De Angelis et al., 2004), considered a linearly varying space dependent effective viscosity profile, and demonstrated drag reduction using computational simulation (Refer figure 1.8). The space dependent effective viscosity simulation was compared with full fledged FENE-P (Finitely Extensible Nonlinear Elastic-Peterlin) simulation which included elastic effects. The comparison showed that the mean velocity, Reynolds stress and velocity fluctuations match very nicely in the elastic sublayer (buffer layer) for both the cases, suggesting that the mechanism of drag reduction is same for both the simulations. This will imply that, in FENE-P simulations though it includes elastic effects, it is the viscosity which causes drag reduction. Also this simulation suggests that the main mechanism of drag reduction takes place in the buffer layer than in the core of the pipe, since both FENE-P and linear viscosity simulations gave the same DR even after having huge difference in the viscosity in the core of the pipe. Overall idea is that the increase in viscosity causes a reduction in reynolds stress, thereby reducing the momentum flux towards wall. As the slope of the viscosity profile increased, more and more drag reduction is observed, which implies that the reduction in Reynolds stress always overwhelms the increased viscous drag.

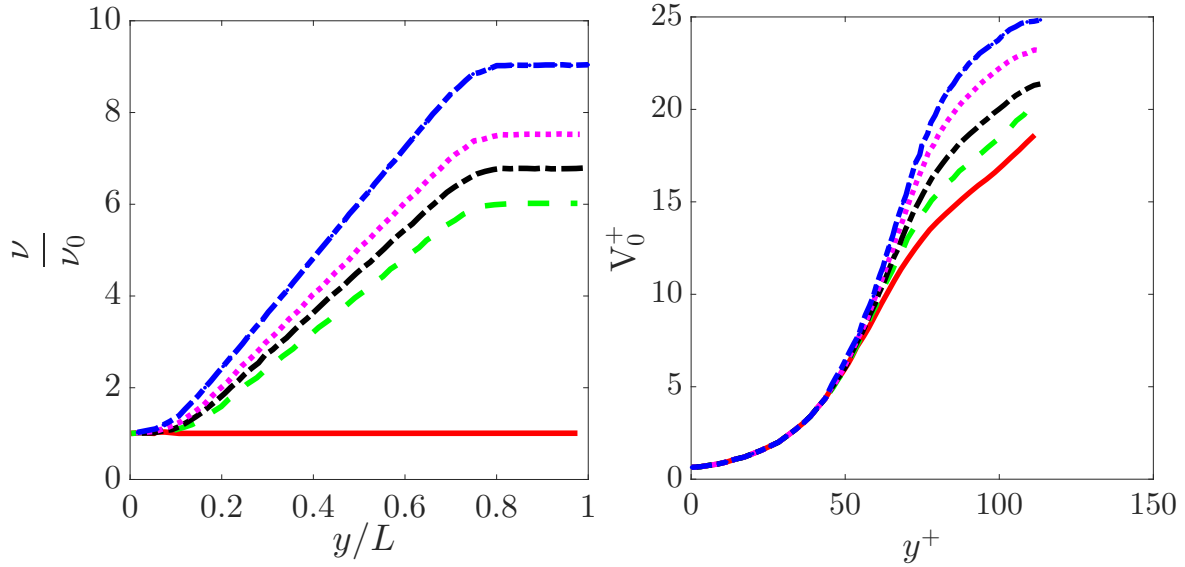

(a) Linear effective viscosity profiles

(b) Mean velocity profiles

Fig. 1.8 Linear viscosity profile demonstrating the DR (Adopted from De Angelis et al. (2004)).

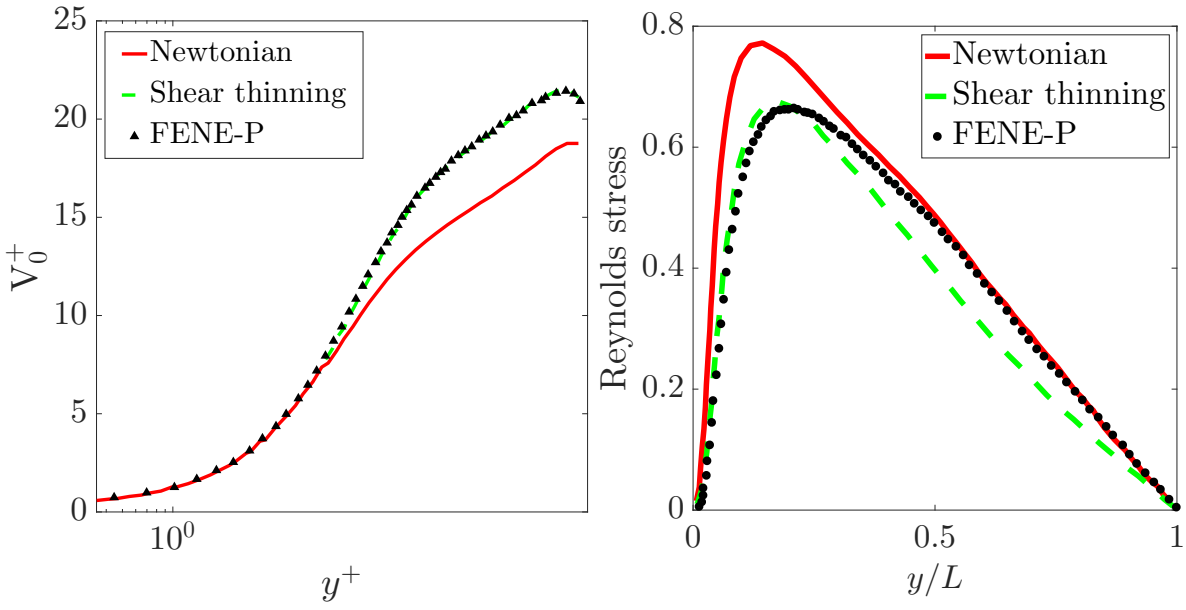

(a) Mean velocity profile

(b) Reynolds stress

Fig. 1.9 Mean velocity profile and Reynolds stresses. Continuous line: Newtonian. Dashed line: linear viscosity profile. Symbols: FENE-P. (Adopted from De Angelis et al. (2004))

1.1.3 Elastic Theory

Elastic theory was first proposed by P.G. de Gennes (De Gennes, 1990; Joseph, 1990; Sreenivasan and White, 2000; Tabor and De Gennes, 1986). According to this theory, though the shear rate near the wall is high, it fluctuates both in space and time, hence polymers are only partially stretched (Smith and Chu, 1998). Increase in effective viscosity because of this partial stretching of polymers is negligible and inconsequential. According to this theory onset of DR occurs when the cumulative elastic energy stored by polymer molecules becomes comparable to kinetic energy in the buffer layer at some length scale larger than the Kolmogorov length scale. There after the usual Kolmogorov turbulence cascade breaks down prematurely and all the scales below this breakdown scale are assumed to behave elastically. Equipped with this Joseph (1990) hypothesized that drag reduction must be an elastic phenomena, because polymers always attenuate turbulence at small scales. Essential idea of this theory is that, the actions that generate small scales of turbulence will be terminated at some scale larger than the Kolmogorov scale, thus by reducing the turbulence intensity.

Other advantage of elastic theory is that it does not require the wall. Hence the best evidence for this theory comes from experiments, wherein polymers were injected at the centerline of the pipe, and the drag reduction begins even before the polymers reached the wall (Bewersdorff et al., 1993; McComb and Rabie, 1979). However follow-up works to McComb and Rabie (1979) and Bewersdorff et al. (1993), have failed to clearly establish this fact (Cadot et al., 1998). The amount of elastic energy stored depends on number of polymer molecules and hence on concentration of the solution. Hence the merit of this theory is in explaining the dependence of drag reduction onset on polymer concentration (Sreenivasan and White, 2000).

1.1.4 Effect on Near-Wall Structures of Turbulence

Recent progress in DNS has enabled the researchers to have a close look at the near wall vortex structures and their interaction with the polymers, to understand the drag reduction in a better way (Dubief et al., 2005). The self sustaining mechanism of drag reduction involves near wall vortex structures and streaks. Vortex structures extract energy from main flow and generates streamwise streaks. Instability in the streamwise streaks gives rise to vortex structures. However upon addition of polymers this self sustaining mechanism of wall turbulence is disrupted (Refer figure 1.10). Addition of polymer reduces meandering and stabilizes the streamwise streaks. As far as the

mechanism is concerned, there are again multiple theories including viscous and elastic theory. One of the explanation given is that the polymers dampen the near wall vortex structures through their body force. Another explanation is that polymers stretch along the near wall vortex thus by taking out the energy from the vortex and weakening it. Experimentally visualizing near wall vortex structures is still out of the reach given the experimental limitations. Hence, we have chosen to study the simplest version of this flow phenomena i.e vortex rings in polymer solutions.

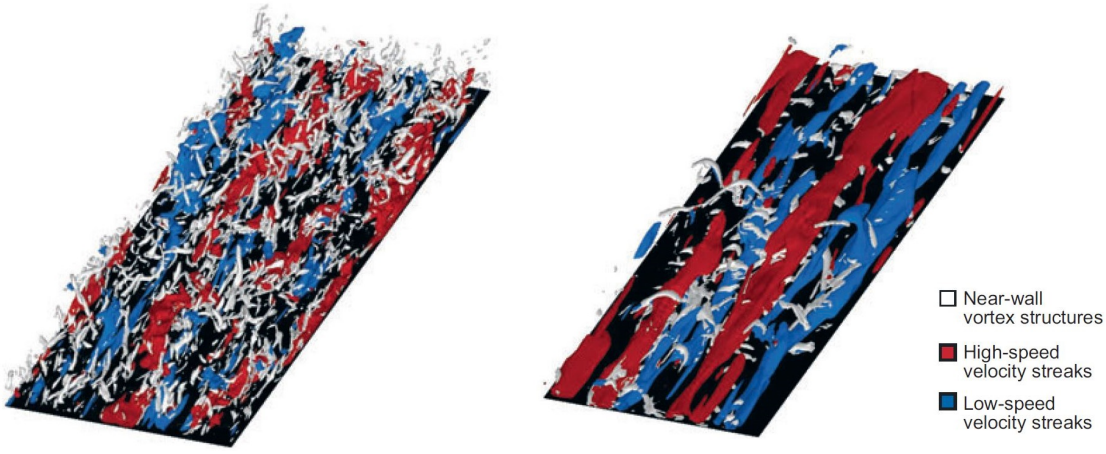

(a) Pure solvent flow (b) Drag reduced flow

Fig. 1.10 Near wall vortex structures (White and Mungal, 2008).

1.2 Vortex Ring

Vortex ring is a fundamental and fascinating flow structure. Systematic study of vortex rings dates back to 1876 (Reynolds, 1876). In his famous book on vortex dynamics (Saffman, 1981), Saffman describes vortex rings as follows. "One particular motion exemplifies the whole range of problems of vortex motion and is also a commonly known phenomenon, namely, the vortex ring .... Their formation is a problem of vortex sheet dynamics, the steady state is a problem of existence, their duration is a problem of stability, and if there are several we have a problem of vortex interactions."

Vortex rings are ubiquitous in almost all the real flow phenomenas. From aircraft design to understanding propulsive mechanism of squids and jellyfish, knowledge of vortex rings has proven to be useful. Early works in this field was by Maxworthy (1972, 1977), wherein he studied the vortex rings using dye and hydrogen-bubble technique (Later it will be explained how dye visualization might misinterpret vortex ring behavior).

He observed that the translational velocity of stable vortex rings varies as t^{-1}, which is contradicted in few other works. This reduction in velocity is thought to be coming from entrainment and the dumping of vorticity into the wake. In this work it was observed that the ring is stable till Re of 500. It is further noted that under some circumstances, the turbulent rings generated or the rings that transitioned to turbulence can relaminarize after they loose sufficient vorticity to the wake, which is confirmed by Weigand and Gharib (1994).

In a review paper on vortex rings Shariff and Leonard (1992), nicely put all the theoretical works till that time in a coherent manner. Slug-flow as a model for vortex ring formation with its advantages and disadvantages is explained in this work. Model of self-similar roll-up, effect of wake formation and entrainment on the ring slow down, leapfrogging of vortex rings are discussed. Glezer and Coles (1990) studied turbulent vortex rings using Laser-Doppler Velocimetry (LDV). Through ensemble averaging, mean vorticity, mean velocity, Reynolds stresses and turbulence production are plotted in similarity coordinates. Mean vorticity and mean velocity plots are similar to laminar vortex ring plots, however, Reynolds stress plots demonstrate the turbulence in the flow.

Vortex rings can be generated in multiple ways in a laboratory experimental setup. One such way is to use the constant head setup and solenoidal valve. When the solenoidal valve opens, the fluid from constant head setup moves out of the nozzle/orifice generating a ring (Tinaikar et al., 2018). The most used one is the piston cylinder mechanism. In this mechanism a slug of fluid is pushed out of the pipe by impulsive motion of the piston.

Major drawback of using piston-cylinder mechanism for vortex ring generation is that they give rise to stopping vortex (Didden, 1979; Maxworthy, 1977) and piston vortex (Allen and Auvity, 2002; Cater et al., 2004) at the end of the stroke. Both the stopping and piston vortex will affect the dynamics of vortex ring. In their recent paper Das et al. (2017) discussed the reason behind stopping vortex and piston vortex in detail. Through careful observation the reason behind the stopping vortex was found out to be the sudden stoppage of the piston. Das et al. (2017) showed a novel way of vortex generation, where piston stoppage was gradual, to produce a vortex ring without stopping vortex. Then by decoupling piston from the nozzle, Das et al. (2017) could produce clean vortex ring without both the stopping vortex and piston vortex.

Gharib et al. (1998) showed that there exists a critical number called formation number which is a ratio of piston stroke length L to nozzle diameter D (Also known as L/D ratio). L/D ratio signifies that there exists a saturation level for circulation, above which a ring can't hold any excess circulation. For formation number below four, only a vortex ring is generated but with circulation lesser than the saturation level. For formation number above four, vortex ring and a trailing jet is generated. Vortex ring's circulation increases with increase in stroke length, till it reaches formation number, and thereafter circulation ejected out of the pipe will follow the ring as a trailing jet (Refer figure 3 in Gharib et al. (1998)).

This phenomena of saturation of circulation in a vortex ring is found to be used by jellyfish to increase the efficiency of propulsion (Dabiri, 2009). Motivated by this a huge amount of work is being done in making the underwater propulsion more efficient using this principle. Mohseni et al. (2001) showed through their simulations that by modifying the kinematics of the ring, it is possible to delay the pinch-off process. Mohseni et al. (2001) and Mohseni and Gharib (1998) tried to understand the phenomena with numerical simulations and analytical calculations. Krueger et al. (2006) showed that the formation number could be changed by adding a background co-flow or counter-flow. Dabiri and Gharib (2005) did experiments on vortex rings using temporally variable nozzle exit diameter and found that the formation time remains the same.

Recently Gharib et al. (2006) demonstrated that the cardiac health is related to its efficiency in generating optimal vortex rings. The fluid involved, i.e. blood, is shear thinning and viscoelastic. However no work is done so far to understand the dependence of formation number on the properties of the fluid involved, especially elasticity and shear thinning. Hence, we in the later part of the work will examine the formation number for our polymer solutions which are also shear thinning and viscoelastic.

Saffman (1981) in his book analytically derived the formation of vortex ring by considering rolling up of cylindrical vortex sheet. By assuming conservation of hydrodynamic impulse he derived an expression for ring radius as,

$$R = \sqrt{\frac{2}{3}} R_{nozzle}$$

Also he derived ratio of ring velocity to piston velocity as

$$\frac{U}{V} = 0.44$$

where U is ring velocity and V is piston velocity. The ratio of core radius to ring radius is

$$\frac{a}{R} = 0.19$$

where a is ring core radius.

Sullivan et al. (2008) in their work on thin vortex rings tried to develop expressions for the radius, core size, circulation and vortex bubble dimension. Some relevant expressions are as follows.

Translational velocity of the ring:

$$U = \frac{\Gamma}{4\pi R}\left[\ln\frac{8R}{a} - \beta\right] \tag{1.1}$$

Kinetic Energy of the ring:

$$K.E = \frac{1}{2}\rho\Gamma^2 R\left[\ln\frac{8R}{a} - \alpha\right] \tag{1.2}$$

Momentum or Impulse:

$$I = \rho\Gamma\pi R^2 \tag{1.3}$$

where Γ is circulation, a is ring core diameter, R is ring diameter and $a << R$. α and β depends on different models. For hollow core model

$$\alpha = 2, \qquad \beta = \frac{1}{2}$$

.

Equation 1.1 gives the relation between U, R, Γ and a for inviscid fluid. Saffman (1981) derived the vortex propagation velocity for the viscous case by assuming Gaussian vorticity distribution (Lamb-Oseen vorticity distribution) inside the ring core. His

equation is identical to 1.1, where,

$$a = \sqrt{4\nu T}, \qquad \beta = 0.558$$

Vorticity distribution inside the core of the ring:

$$\omega(r,t) = \frac{\Gamma}{4\pi\nu t} e^{-(r^2/4\nu t)} \tag{1.4}$$

According to this calculation, the core spreading is same as the heat diffusion. Sullivan et al. (2008) found the core spreading of thin vortex ring using dye visualization and then by doing intensity of dye calculation. His calculations of core spreading almost matches with saffman's calculations. However, care has to be taken in this way of calculating the core spreading, given that the dye diffuses around 5000 times slower than the vorticity.

Analytical works on vortex rings can be classified into two models. First model is for thin core vortex rings ($a << R$) and the second is for thick core vortex rings ($a \sim O(R)$). Hence, both models corresponds to asymptotic behavior of an experimentally generated vortex ring. Thin core theory which is developed based on Lamb-Oseen's Gaussian vorticity distribution is valid for small time $t << T$, where T corresponds to piston stroke time. Translational velocity of the ring from this model is given by Equation 1.1. For the viscous ring, this expression is modified by Saffman (1981) to get the below expression.

$$U = \frac{\Gamma}{4\pi R}\left[\ln\frac{8R}{\sqrt{4\nu T}} - 0.558\right] \tag{1.5}$$

Equation 1.5 is derived with the assumption of equation 1.4, for which, circulation turns out to be

$$\Gamma = \int_0^\infty \omega dA = constant \tag{1.6}$$

This constant circulation along with constant hydrodynamic impulse, will result in constant vortex ring diameter. But experimentally it is observed that the circulation of the ring decreases and the diameter of the ring increases. Hence the Saffman's thin core theory fails for $t > T$. Fukumoto and Moffatt (2000) accounted for the viscous effects on the vortex ring movement and derived a correction for Saffman's equation. Their corrected equation is,

$$U = \frac{\Gamma}{4\pi R}\left[\ln\frac{8R}{\sqrt{4\nu T}} - 0.558 - 3.6716\frac{\nu T}{R^2}\right] \tag{1.7}$$

Fraenkel (1972) related translational velocity to energy and impulse of the vortex ring using Hamilton's equation as,

$$U = \frac{\partial E}{\partial I} \tag{1.8}$$

where E and I for thin but finite ($\epsilon = a/R$) core rings are given by,

$$E = \frac{1}{2}\rho R\Gamma^2 \left[\ln \frac{8}{\epsilon} - \frac{7}{4} + \frac{3}{16}\epsilon^2 \ln \frac{8}{\epsilon} \right] \tag{1.9}$$

$$I = \rho\Gamma\pi R^2 \left[1 + \frac{3}{4}\epsilon^2 \right] \tag{1.10}$$

Das et al. (2017) matched their experiments with theoretical results and found that the translational velocity expression by Fraenkel (1972) to be the most accurate.

Using dimensional arguments, Saffman derived thick core vortex model, which is given below. These equations are derived from the assumption of conservation of hydrodynamic impulse, and vortex ring is nearly a blob.

$$R^2 \approx R_0^2 + k'\nu t \tag{1.11}$$

$$U \approx \frac{I}{k}(R_0^2 + k'\nu t)^{-3/2} \tag{1.12}$$

Maxworthy (1972) showed that the increase in diameter of the ring as given by thick core model is over-predicted. Using entrainment model and scaling arguments Maxworthy (1972) predicted vortex behavior at longer times to be,

$$U \propto t^{-1} \qquad a \propto t^{1/3} \qquad \Gamma \propto t^{-2/3}$$

In another notable work, Shusser and Gharib (2000) derived the expression for thick core vortex ring translational velocity as,

$$U = 0.5352\sqrt{\frac{\rho\Gamma^3}{\pi I}} \tag{1.13}$$

However all these models are applicable only at asymptotic limits and intermediate evolution of the ring can't be explained. Recently Tinaikar et al. (2018), derived the expression for intermediate evolution of viscous vortex ring and verified it with their low Re vortex ring experiments. Instead of starting with Dirac delta distribution of vorticity

inside the core for $t = 0$ (as it is done in thin core model), they started with finite width Gaussian distribution at $t = 0$. The expressions derived by Tinaikar et al. (2018) are presented below:

Peak Vorticity:

$$\omega_{max,t} = \frac{\omega_{max,0}}{\left[1 + \frac{2\phi\nu t}{\sigma_0^2}\right]^2} \tag{1.14}$$

Vorticity Profile:

$$\omega(r,t) = \frac{\Gamma_0}{(\sigma_0^2 + 2\phi\nu t)} e^{-(r/\sqrt{\sigma_0^2 + 2\phi\nu t})^2} \tag{1.15}$$

Circulation:

$$\Gamma(t) = \frac{\Gamma_0}{\left(1 + \frac{2\phi\nu t}{\sigma_0^2}\right)} \tag{1.16}$$

Vortex Ring Diameter:

$$R(t) = R_0 \sqrt{1 + \frac{2\phi\nu t}{\sigma_0^2}} \tag{1.17}$$

Translational velocity of the ring (With correction to Saffman's formula):

$$U = \frac{\Gamma_0}{4\pi R_0 \left(1 + \frac{2\phi\nu t}{\sigma_0^2}\right)^{3/2}} \left[\ln\left(\frac{8R_0}{\sigma_0}\right) - 0.558\right] \tag{1.18}$$

Where $\omega_{max,0}, R_0, \Gamma_0, \sigma_0$ are peak vorticity, diameter of the ring, circulation and the standard deviation of the Gaussian vorticity profile at time $t = 0$. ϕ is a constant. Circulation as calculated by Tinaikar et al. (2018) is not constant but decreases with time, and is validated with experimental results. Translational velocity as a function of time is also matched with experimental results. Hence, these expressions predict spatiotemporal variation of vortex ring properties.

1.3 Vortex Rings in Non-Newtonian Solution

As explained in section 1.2, there is considerable amount of work available for Newtonian vortex rings. However, very limited work is available for vortex rings in non-Newtonian solutions. Palacios-Morales and Zenit (2013) did experiments on vortex rings in shear-thinning liquids. Aqueous solution of Xanthan gum in three different concentration along with Newtonian water-glycerol solution were used for experiments. Rheological measurements showed clear shear-thinning behavior with negligible elasticity. Instead of impulse, Reynolds number based on power law model was used to compare the rings of two different solution. It was showed that the formation number for shear thinning liquids remains unchanged (i.e L/D $\approx$ 4). Palacios-Morales et al. (2015) didn't observe any trailing jet at L/D = 4, in viscoelastic fluids. We in later part will show that the formation number remains unchanged even in viscoelastic shear-thinning liquids.

Palacios-Morales and Zenit (2013) observed a peculiar behavior in shear-thinning vortex rings. Traveling vortex rings slowed down drastically along with sudden expansion of the ring (Refer figure 1.11 and 1.12). This behavior increases with increase in shear-thinning property of the liquid and is absent in their Re matched Newtonian rings. However, Bentata (2013) has observed this sudden expansion in ring even in water, at a very low Re ($Re = 15$). Bentata (2013) has also observed this behavior in shear-thinning liquids. Similar behavior of slowing down and drastic increase in diameter of rings is observed in experiments of our group by Shashank (2019) for certain concentration polymer solution. Shashank (2019) in his experiments observed that, even when rings are generated at higher Re, as they travel, velocity keeps falling. When the rings reach lower Re (because of reduction in velocity), they show the dramatic increase in diameter along with complete stoppage of the ring.

Palacios-Morales and Zenit (2013) observed that the shear-thinning rings are slower when compared with Re matched Newtonian ring, which is corroborated by Bentata (2013). Palacios-Morales and Zenit (2013) also observed that the circulation of shear-thinning rings is always smaller than the Newtonian counterpart. He analytically proved this, by assuming Poiseuille flow inside the pipe which feeds to vortex ring. Bentata (2013) through his experiments showed that the peak vorticity reduces at a faster rate for shear-thinning ring compared to the Re matched Newtonian ring.

Palacios-Morales et al. (2015) did experiments on vortex rings in viscoelastic (also shear-thinning) aqueous polymer solution. The polymer solution used in their exper-

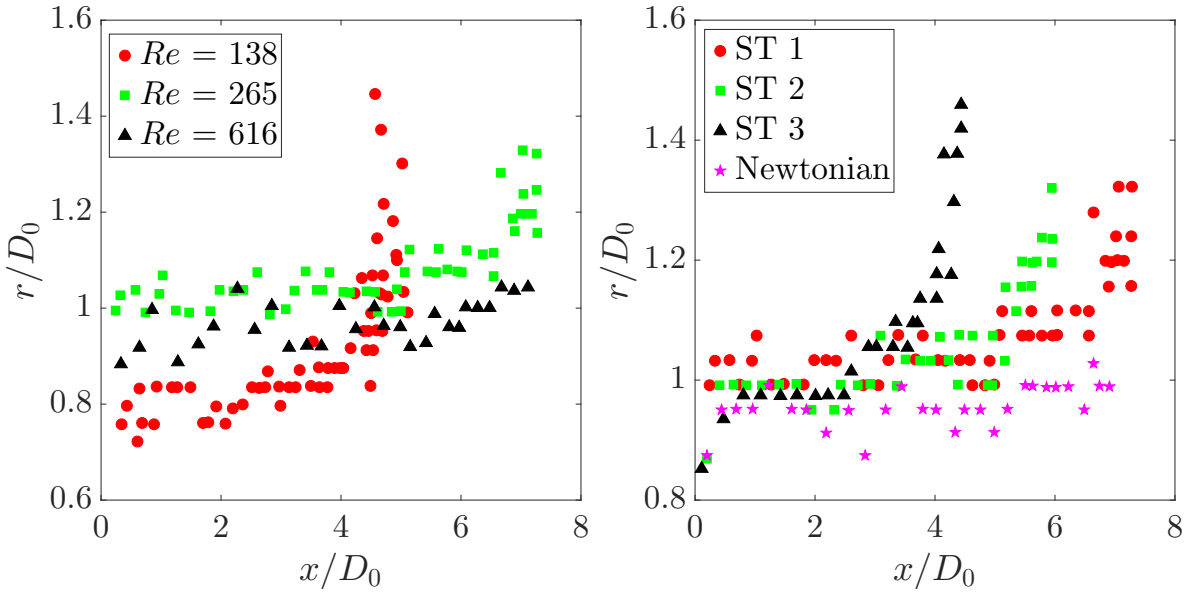

(a) Different Reynolds Number (b) Different shear thinning liquids

Fig. 1.11 Increase in diameter of vortex rings in shear thinning liquid. (a) ST 1 liquid, L/D = 4. (b) $Re = 260$, L/D = 4. ST 1, ST 2 and ST 3 stands for three different shear thinning liquids in increasing order of shear-thinning (Adopted from Palacios-Morales and Zenit (2013)).

iments had relaxation time of 0.63 s (Deborah Number ≈ 5). Also, it had a power index $n = 0.63$, consistency co-efficient, $m = 0.409 PaS^n$, according to power law model. These viscoelastic vortex rings were compared with Re(Based on power law) matched Newtonian vortex rings. Experiments were conducted at low inertia regime, so that elastic effects are prominent ($Re = 20$ to 30). It was observed that, the viscoelastic rings were considerably small in size, and had considerably low circulation, even after accounting for shear-thinning effects. Hence this additional reduction in size and circulation is attributed to elastic properties.

Palacios-Morales et al. (2015) observed that in viscoelastic liquids, a secondary ring which is opposite in vorticity appears in-front of the primary ring, and causes the primary ring to die down soon. Once the primary ring disappears, the secondary ring start to travel in the opposite direction towards the nozzle, and finally gets dissipated out by viscosity. Palacios-Morales et al. (2015) showed that the region with highest extension (i.e. the front portion of the primary ring) is where the secondary ring first appears. Hence, concluded that the polymers stretched in this extensional region relax back, generating a vortex ring of opposite sign. This phenomena is similar to negative wake

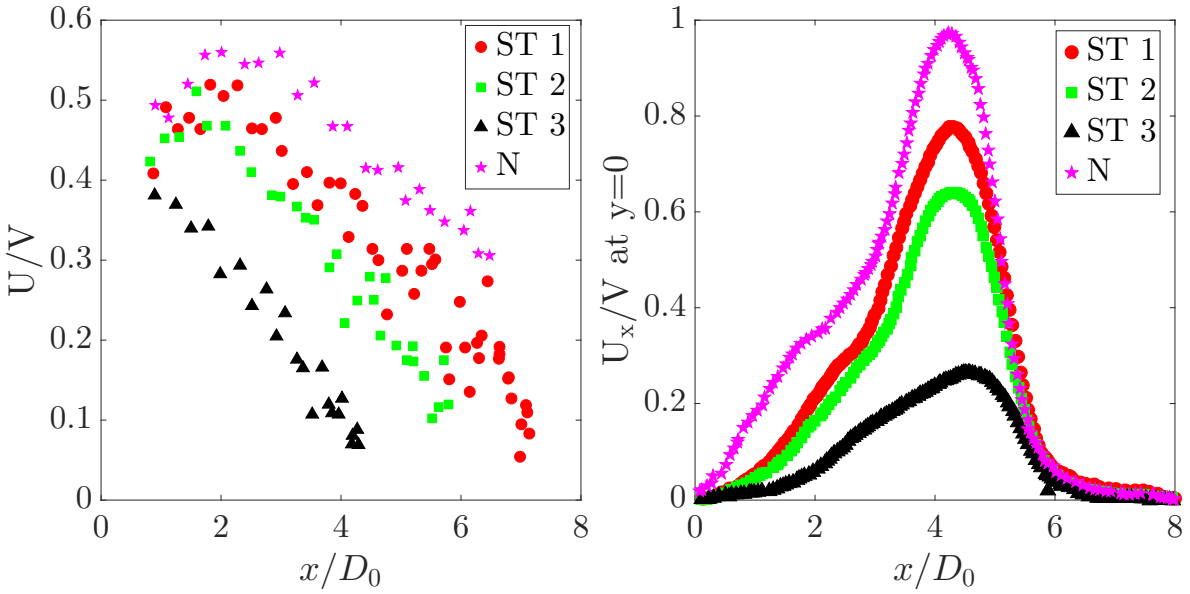

(a) Propagation velocity of rings

(b) Axial velocity at centerline

Fig. 1.12 Translational velocity and Axial velocity profile for vortex rings in shear thinning liquid. $Re = 260, \mathrm{L/D} = 4$. ST 1, ST 2 and ST 3 stands for three shear thinning liquids in increasing order of shear-thinning. N stands for Newtonian solution. (Adopted from Palacios-Morales and Zenit (2013))

observed by Mendoza-Fuentes et al. (2009); Soto et al. (2006). However, surprisingly throughout this process the ring diameter doesn't change (Note: Ring expansion took place in shear-thinning fluids).

Bentata (2013), in his experiments qualitatively observed the same. However, he even observed the tertiary ring, which got generated in-front of secondary ring. This tertiary ring causes the secondary ring to die down, and starts to move in the direction of the primary ring. Shashank (2019) has observed a reversal in vorticity once the primary ring stops. Observation of his experiments are given below:

1. Vortex ring is generated with high Re. ($Re \sim \mathcal{O}(1000)$)
2. As the ring travels, it looses circulation. Hence the velocity drops.
3. Once the Re of the ring becomes small, the diameter starts to increase drastically, along with quick drop in velocity.
4. Finally the ring stops. Vorticity of the ring disappears. Circulation of the ring becomes zero.

5. Reverse vorticity is observed, but with much less magnitude. Reverse circulation is observed, with very small magnitude.

6. Movement in opposite direction observed, but with negligible velocity.

7. Reverse movement stops.

We have repeated this work of Shashank (2019) with few additional analysis, and will present in the later part of the thesis. We speculate that the dynamics of the primary ring is driven by shear-thinning effects, whereas the formation and dynamics of the secondary ring is driven by elastic effects.

Olsthoorn et al. (2014) computationally simulated a vortex dipole in Newtonian and shear-thinning solution. In his simulations, Newtonian viscosity is equal to the zero shear viscosity of shear thinning fluid (not the infinite shear viscosity). The decrease in kinetic energy and the enstrophy by this psuedospectral simulation is given in figure 1.13.

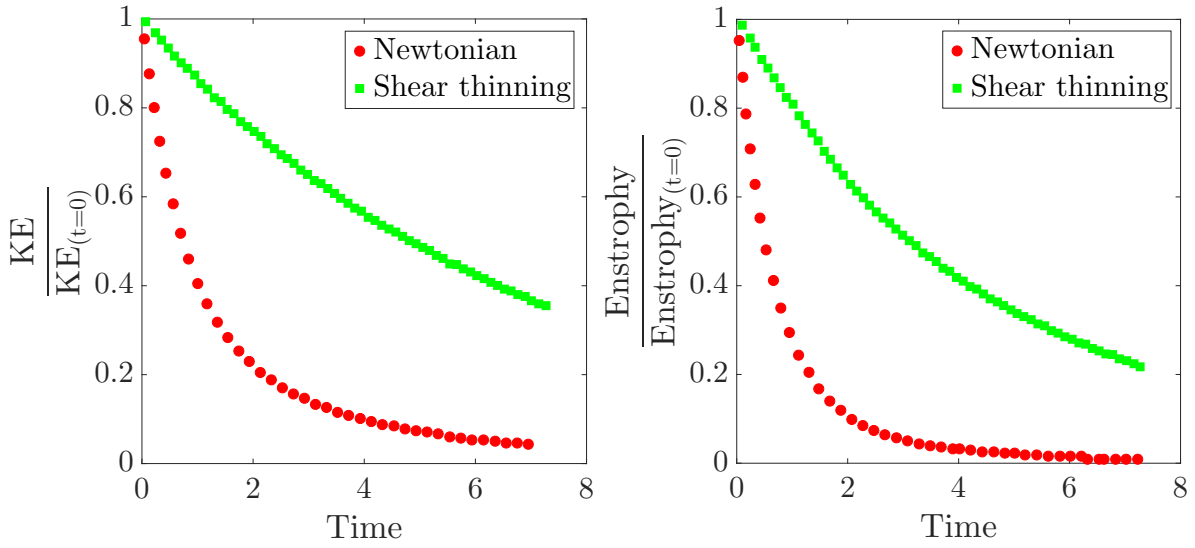

Fig. 1.13 Decrease in kinetic energy and enstrophy for vortex dipole over time. Note: Viscosity of Newtonian solution is equal to zero shear viscosity of shear thinning solution. (Adopted from Olsthoorn et al. (2014))

Gyr et al. (1992) in their experiments, did not observe any difference between vortex rings in water and in the dilute polymer solution. The whole behavior of vortex rings in non-Newtonian fluids depends strongly on the concentration of the polymers used. Hence we conduct experiments on three different concentrations. We study the rings with moderate to high Re ($Re \sim \mathcal{O}(10,000)$), which has not been studied extensively.

We also calculate few additional quantities along with velocity, diameter and circulation to see the effect of polymers on them.

1.4 Vortex Ring Wall Interaction

Vortex ring impinging on a plane solid wall is a fundamental flow and is considered to mimic the mechanism of turbulence generation. It involves both viscous and inviscid interactions. For inviscid case, it is analytically solved using the method of images. However, in reality the flow gets complicated, because of appearance of boundary layer due to viscosity and subsequent detachment into secondary vortex ring. Doligalski et al. (1994); Walker et al. (1987) did initial experiments, and observed the secondary and tertiary rings along with rebounding of primary vortex ring. They showed that the trajectory of primary and secondary rings depend on Re, and once secondary ring is formed, it affects the motion of primary ring through inviscid interaction.

Chu et al. (1993) studied this phenomena using laser-induced photochemical anemometry (LIPA). The flow was divided into three stages. (1) Free traveling (2) Vortex Stretching and (3) Vortex Rebounding. It was showed that the enstrophy rather than circulation, clearly signifies the three stages of vortex wall interaction. Enstrophy is related to kinetic energy as,

$$\frac{dK}{dt} = -\nu E \tag{1.19}$$

Hence, production of enstrophy signifies the dissipation of energy. It was shown that, during free shear motion, circulation remains the same but enstrophy decreases due to viscous diffusion. During vortex stretching stage, enstrophy increases drastically which suggests that the vortex stretching is associated with fast rate of energy dissipation. Vortex rebounding stage is associated with viscous diffusion of enstrophy. Circulation, however, decreases during both vortex stretching and vortex rebounding stage. Chu et al. (1993) also studied vortex ring free surface interaction. Vortex ring free surface interaction is qualitatively similar to vortex ring solid wall interaction, but has lesser magnitude of circulation and enstrophy, which could be attributed to weaker boundary layer involved in the case of free surface-vortex interaction.

Chu et al. (1995) using numerical simulation showed the evolution of circulation and enstrophy for vortex ring wall interaction, which is in good agreement with Chu et al. (1993); Fabris et al. (1996); Orlandi and Verzicco (1993). Also the trajectory of primary

vortex ring and the evolution of secondary ring are in good agreement with Chu et al. (1993).

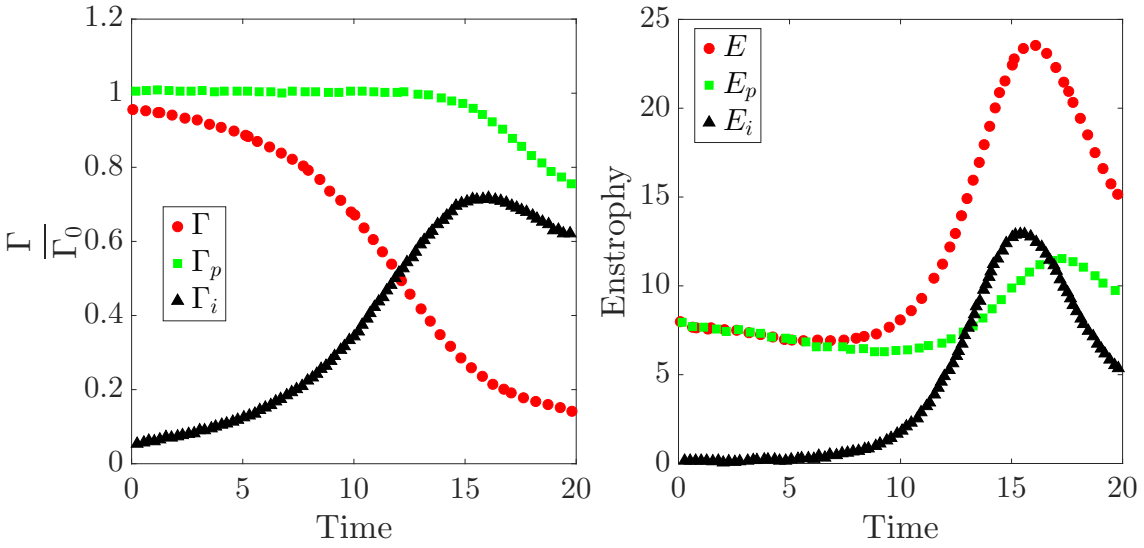

(a) Circulation (b) Enstrophy

Fig. 1.14 Evolution of circulation and enstrophy for vortex ring wall interaction for Re 1500. Γ_p is circulation of primary vortex ring, Γ_i is circulation of induced flow, Γ is total circulation, E_p is enstrophy of primary vortex ring, E_i is enstrophy of the induced flow, E is total enstrophy. (Adopted from Chu et al. (1995))

Further evidence for the observations of Chu et al. (1993) was provided by PIV experiments of Fabris et al. (1996). In their experiments, it was observed that the peak vorticity of the ring is increased by 50% as it reaches the wall. The reason being vortex stretching, which occurs because of increase in vortex ring diameter and the associated core shrinkage. Vortex stretching stage is again associated with generation of enstrophy, which implies dissipation of the energy. Circulation is observed to remain constant during free shear motion, and decreases during vortex stretching and rebound stage, which is in agreement with previous studies.

Fabris et al. (1996) also plotted the trajectory of the ring and observed monotonous increase in diameter during vortex rebounding stage. This is attributed to weaker secondary ring, which couldn't stall and reverse the direction of motion of the primary ring. However it is observed that, at larger Re, the induced boundary layer will be stronger, hence the stronger secondary ring, which stalls the primary ring expansion, causing the contraction of the primary ring (Doligalski et al., 1994; Walker et al., 1987). In the experiment of Fabris et al. (1996), the primary ring undergoes two rebounds. First rebound is associated with secondary ring and the second rebound is associated with

tertiary ring. Many such rebounds are possible for a strong primary ring.

Experimental limitations on resolution has restricted the complete understanding of boundary layer and the secondary ring generation in vortex wall interaction. Fabris et al. (1996) carried out numerical simulation with two initial vorticity distribution of primary ring. (1) Gaussian distribution (2) Matching with experimental observation. It was observed that the simulation with experimentally observed vorticity distribution reproduced the flow better than the Gaussian distribution simulation. Initial Gaussian vorticity distribution simulation over-predicts the boundary layer and hence the secondary vortex ring.

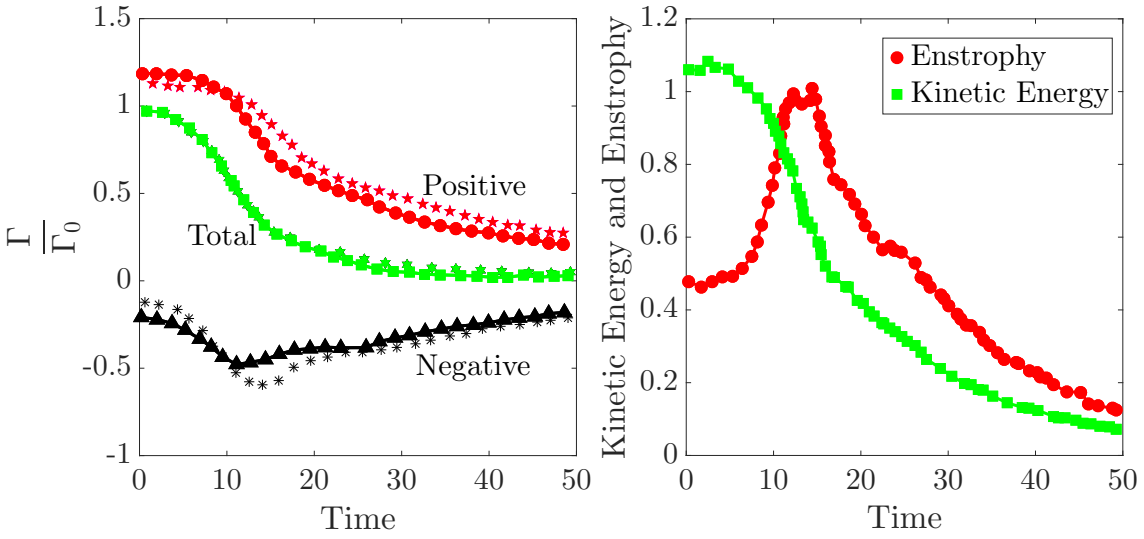

(a) Circulation (b) Enstrophy

Fig. 1.15 Circulation and enstrophy for vortex ring wall interaction. Experiment is shown in solid lines and the simulation is shown in symbols. (Adopted from Fabris et al. (1996))

Naguib and Koochesfahani (2004) tried to capture the wall pressure signatures that are responsible for boundary layer separation using Molecular tagging velocimetry. Olsthoorn et al. (2014) carried out pseudo-spectral simulation of vortex dipole impinging wall in shear-thinning solutions. Carreau fluid rheology was assumed for shear thinning solution with zero shear viscosity matching with Newtonian case. Through simulations they showed that the non-Newtonian rheology can generate vorticity on their own. However, it is assumed in their simulation that the $\nu_\infty = 0$. Hence their simulation results are far from reality.

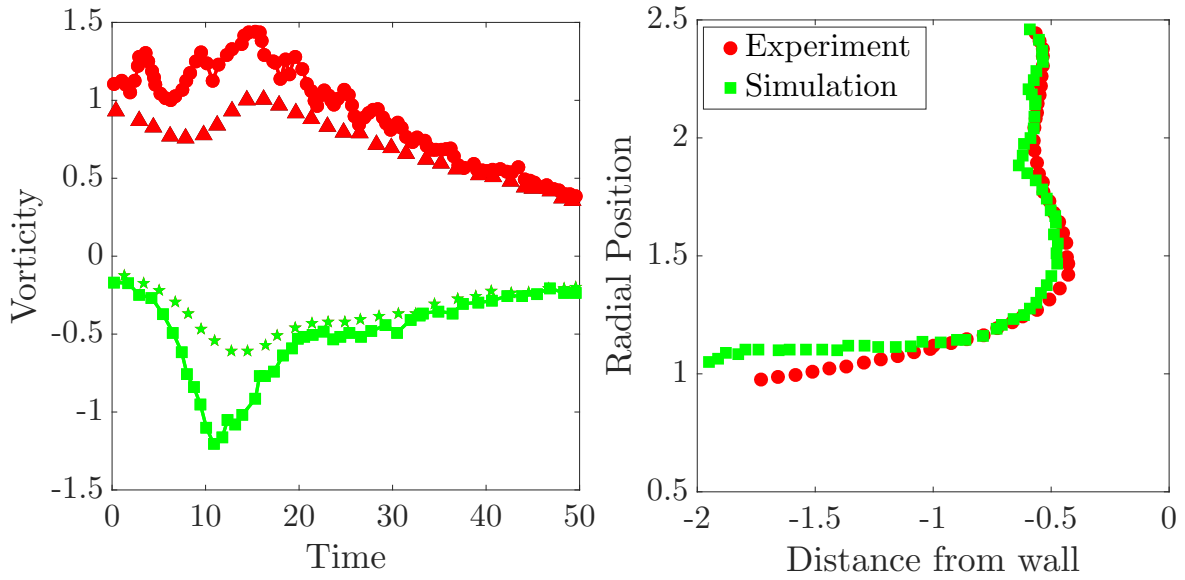

(a) Peak vorticity (b) Trajectory

Fig. 1.16 Peak vorticity and trajectory of primary vortex ring for vortex ring wall interaction. In figure (a), Experiment is shown in solid lines and the simulation is shown in symbols. (Adopted from Fabris et al. (1996))

Gyr et al. (1992) carried out experiments on vortex ring wall collision in dilute and semi-dilute polymer solutions. No deviation from Newtonian rings is observed during free shear motion. However, they report enhanced reflection of the polymer ring compared to water ring. This enhanced reflection will imply that the interaction with the high near-wall velocity gradient is reduced, which implies enstrophy production is reduced, hence, reduced energy dissipation. However, this result is obtained by dye visualization and the deviation observed being too small, falls in the error-range. We, in our work, will address this question of vortex ring wall interaction in polymeric solution using sophisticated PIV technique. Using PIV vector field we obtain enstrophy, kinetic energy and other properties of the flow-field in pure solvent and in polymer solutions. The effect of polymers on the flow field and the possible connection to turbulent drag reduction will be demonstrated.

1.4.1 Vortex Ring Interaction with Other Solid Structures

Vortex ring impacting on multiple other solid structures (like cylinder, bump, sphere) are reported in literature so far. But all these interactions are driven by the same mechanism. As the ring approaches the solid body, a boundary layer will appear on the body, because of no slip condition, which eventually interacts with the vortex ring through viscous and

inviscid mechanisms. Naitoh et al. (1995) studied the vortex ring traveling across a thin circular cylinder. It was observed that when cylinder diameter is much smaller than that of the vortex ring, ring will move over the cylinder, but gets distorted in this process. Further Verzicco et al. (1995) studied similar vortex interaction with cylinder, but with cylinder diameter of the order of diameter of the ring. Secondary ring formation, and the expansion of the primary ring was observed.

Das et al. (2016) carried out experiments on axial interaction of vortex ring with a thin cylinder. Allen et al. (2007) did experiments on vortex ring interacting with a sphere. New and Zang (2017) carried out experimental studies on vortex ring colliding with cylinders of larger diameter. Ren and Xu (2014) numerically studied vortex ring impacting a bump. Lim (1989) studied vortex ring impacting an inclined wall. Similarly, there are plenty of research articles available for vortex interactions. However, all these interactions are guided by the same mechanism, wherein a boundary layer appears on the solid body, and this boundary layer interacts with the primary ring. Hence, vortex ring wall interaction, in a very simple way incorporates this mechanism. Hence, we have chosen vortex wall interaction for our study.

1.5 Non-Newtonian Rheology

Addition of polymer changes the rheological properties of water. Viscosity (Shear viscosity) will become shear rate dependent. It also brings elastic properties to the solution (Water shows elasticity at a frequency of $\mathcal{O}(10^{12})$ Hz).

Primary effect of the polymer addition is the shear-thinning viscosity. Polymers are in coiled state. When shear is applied, polymers align and get stretched in the direction of the shear. As the polymers align and stretch, they offer less resistance to the flow, compared to their coiled configuration. Hence, as the shear rate increases viscosity of the polymer solution decreases. Power law model is the simplest model, used to explain the shear-thinning behavior. But this model has problem at low shear rates, as viscosity shoots up to infinity. Carreau model is an improved model, in which power law is bounded by zero shear and infinite shear viscosities. Since, the polymer also show similar plateau of viscosities at low and high shear rates, this model is best suited for polymer solutions.

Inverse of the shear rate at which the transition from zero-shear plateau to power law region of shear-thinning occurs, gives the relaxation time for the polymer solution

(Srinivas and Kumaran, 2017). Polymers have an intrinsic time-scale. If time scale of the applied force is larger than that of the polymer time scale, then the polymers will relax back to their original coiled state. When the time scale of the flow (i.e. inverse shear rate) is smaller than this polymer time scale, then the polymers will start to get stretched, instead of relaxing back to their original state.

However, the polymer solution properties depends on many parameters. The structure of monomer (branched, unbranched etc) plays a key role. Molecular weight, Molecular weight distribution also determine the properties of polymer solution. Nature of the polymer (anionic, cationic, nonionic) and the reactivity towards salt are the other important parameters. The rheological properties of the polymer solution also depend on the way of preparation (High shear rates involved during preparation can break the polymers), and the aging of the solution. Hence, it is frequently observed that the results of one group of researchers doesn't match with another group's results. Even in the same research group, with the same polymer, the observed results in two research articles deviate quite a lot (Example: Choueiri et al. (2018) and Samanta et al. (2013)), which they attribute to change in the batch of polymer and a slight modification in preparation methodology.

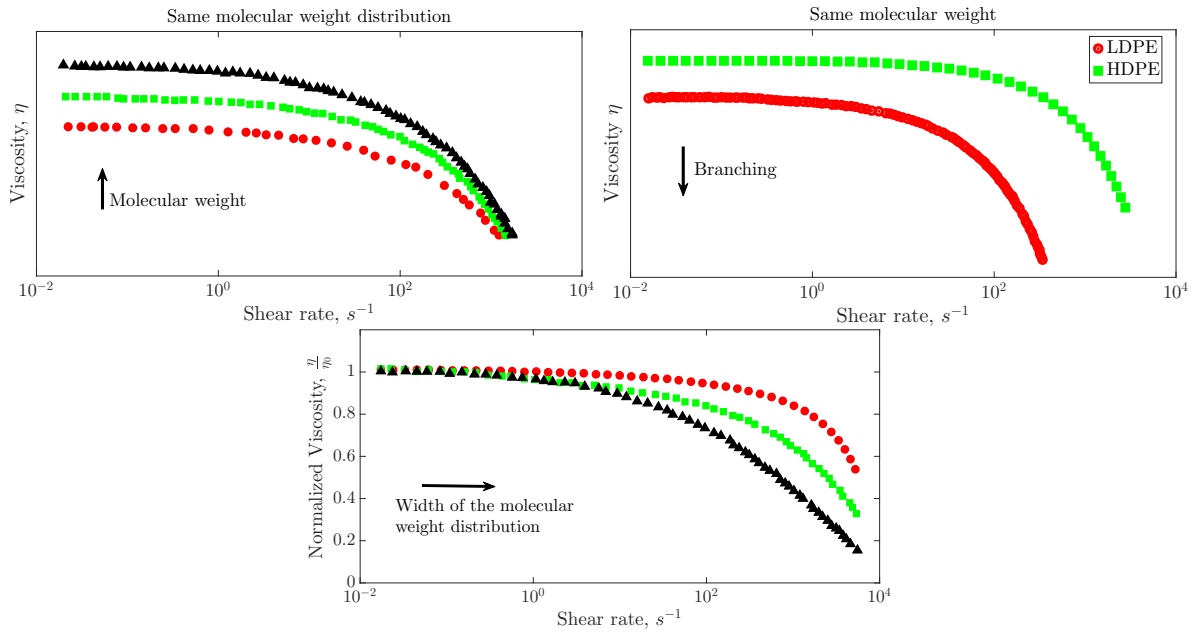

Fig. 1.17 Influence of molecular weight, molecular weight distribution and branching on shear thinning rheology of polymer solution. (Adopted from Osswald (2014))

Elastic properties of polymer solution are characterized by Storage Modulus (G') and Loss Modulus (G''). Relaxation time can be calculated by these two quantities too. Oscillatory rheometry is used to measure the storage and loss modulus. Normal stress difference is another quantity used to characterize the elasticity of the solution. Elastic properties are more pronounced at higher shear rates than in lower shear rates.

We, in our work, carried out multiple ways of characterizing the polymer solution from classical viscometer method to oscillatory rheometry. The challenges involved and the limitations in each method of measurement will be explained in detail.

Chapter 2

Experiments

In this chapter, the experimental setup, flow visualization methods and characterization of the polymer solution used are briefly explained.

2.1 Experimental Setup

Experiments are conducted in glass tank which is three meter in length and one meter in width. It has a capacity of 1200 litre. Tank is filled with the solution in which vortex rings are to be studied (Refer figure 2.1).

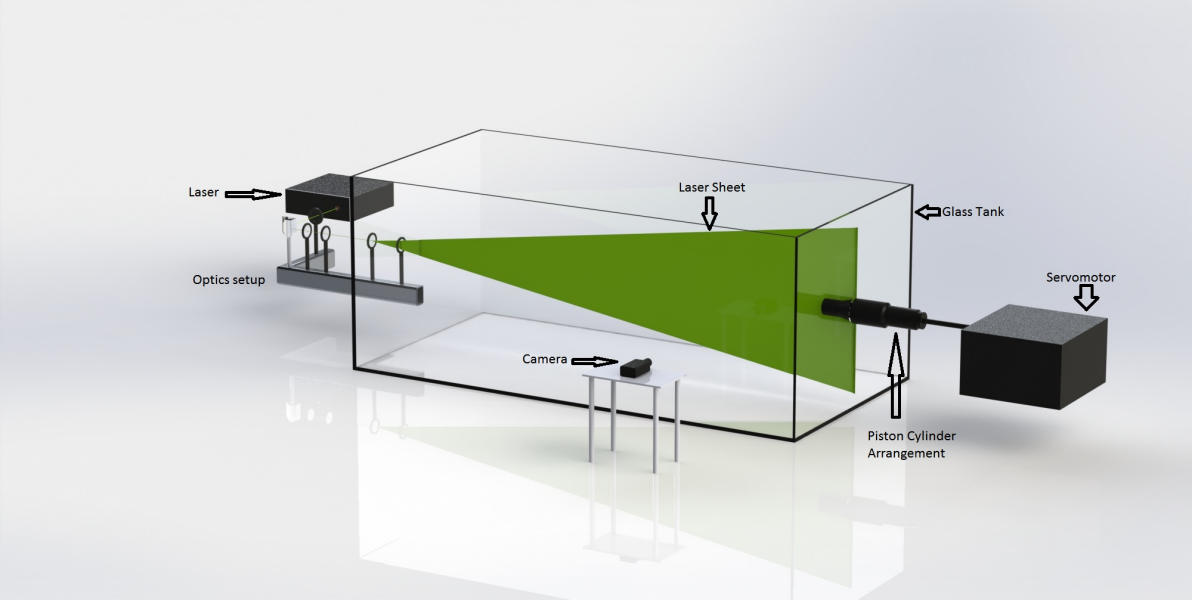

Fig. 2.1 Schematics of Experimental setup

Vortex rings are generated using piston cylinder mechanism. Piston mechanism is driven by a servomotor. A computer program controls the speed and stroke-length of the piston through servomotor. Accuracy of piston velocity and stroke length are measured and verified by Shashank (2019). Diameter of the piston and the pipe holding it is 60 mm. A nozzle with exit diameter (D) of 50 mm is connected at the end of the pipe. Nozzle end is located at a distance of 300 mm (6D) from both bottom and backside wall, and at the same distance from free surface of the liquid. This nozzle, piston mechanism is in open arrangement, i.e. there is no barrier in-front of nozzle which separates the fluid inside the piston cylinder mechanism from the fluid outside of it. Hence, when vortex rings are created, there is no rheological difference between the ring fluid and the ambient fluid. Nozzle has tiny holes, through which dye is injected into the fluid, which will form the vortex ring when pushed out of the piston. During PIV experiments, particles are injected, so as to have better particle number density, which is necessary to get good vectors.

One end of the tank houses the vortex ring generating mechanism, and the laser sheet enters from the opposite end, passing through the central plane of the nozzle vertically. 100 mJ Nd:YAG pulsed laser (Litron Nano-series) operating at 532 nm with 25 Hz frequency is used in PIV experiments. The laser beam coming out of the laser is converted to a laser sheet of width 2-3 mm using a combination of five lenses. The spread of the laser sheet is such that, nearly parallel rays enter the area of interest. Laser is synchronized with camera using Stanford delay generator.

To study vortex wall interaction, a solid glass wall is placed vertically, perpendicular to the direction of travel of the ring, at a distance of 250 mm (5D) from the nozzle exit. Distance of 5D is chosen, such that the vortex formation transients have died down. In other similar works too the wall was placed at a distance of 4D - 6D so that the ring is fully grown up before interacting with the wall (Fabris et al., 1996; Naguib and Koochesfahani, 2004; New and Zang, 2017; Walker et al., 1987). The perpendicularity of the wall is ensured, and the wall is fixed firmly, so that upon impinging of the ring, there is no movement of wall.

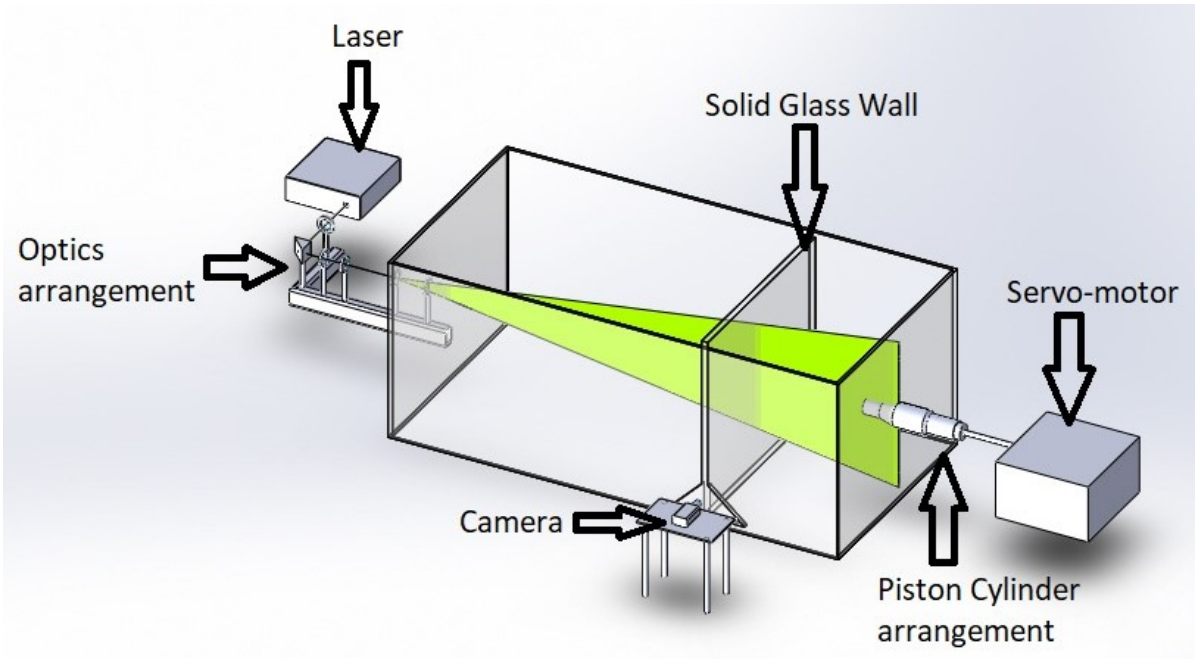

Fig. 2.2 Schematics of Experimental setup

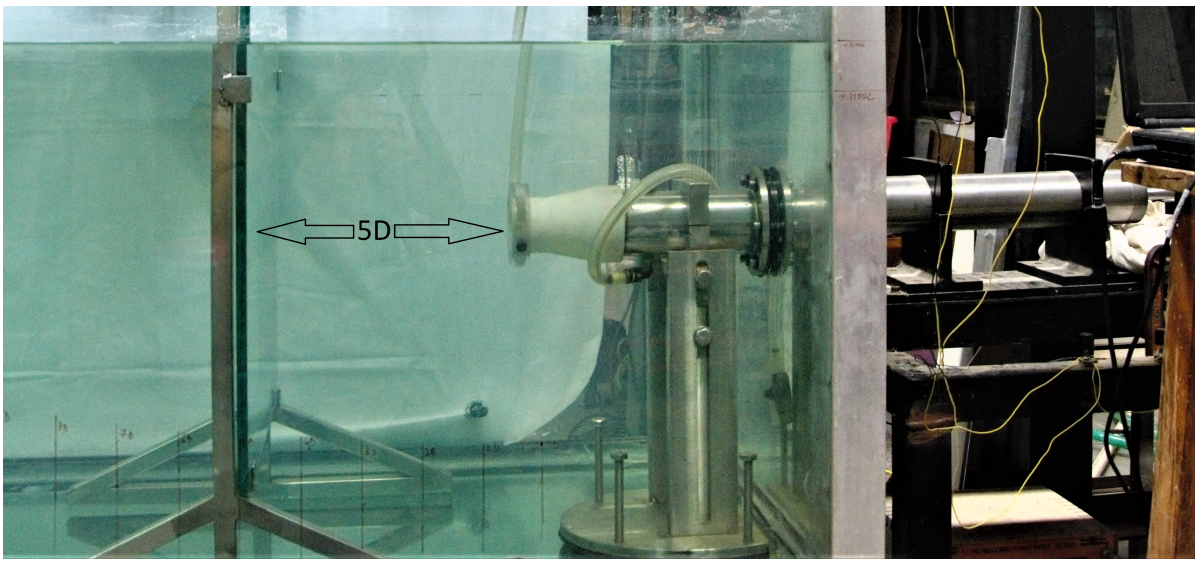

Fig. 2.3 Experimental setup

2.2 Particle Image Velocimetry

Particle image velocimetry (PIV) is a technique to get instantaneous velocity field over a domain (Adrian, 2005; Adrian and Westerweel, 2011; Prasad, 2000; Raffel et al., 2018; Westerweel, 1997; Willert and Gharib, 1991). This method involves, measuring the displacement of small tracer particles introduced into the flow, then obtaining velocity from this displacement data. The basic requirement for carrying out PIV are illuminating light source (Laser), camera to record the images, tracer particles, and the image processing tools.

Litron nano-series dual pulse laser operating at 532 nm, 25 Hz is used for all PIV experiments. Optical arrangement of convex and concave lenses is used to get the laser sheet of required width and 3 mm thickness. 50 micron polyamide particles with density of 1.2 g/cm^3 are used as tracers. 2 g of particles are added in the whole tank. Additional 1 g of particles is added to vortex rings over the trials. Addition of extra particles help to get better correlation inside the ring, which is necessary since the vortex ring is a highly vortical region. Because of difference in density, the particles settle down with time, and had to be brought up by stirring the liquid. However, the particle settling time is much larger than all the time scales involved in the flow, hence, doesn't effect the velocity measurement. Also, particle inertial effects are small, and it is safe to assume that the particles follow the flow faithfully.

Phantom v9.1 high speed camera with 1632 $\times$ 1200 pixels (2 MP) is used for image acquiring. Images are acquired at 25 Hz, and the camera is synchronized with the Laser using Stanford delay generator. Images are captured with 8-bit depth. Exposure time of the camera is kept at 900 μs so that, two Laser shots which are separated by a dt of 1 ms won't overlap. Timing diagram explaining the gap between two laser shots, and the camera shutter time is shown in figure 2.4. 17 -35 mm lens is used for the camera magnification. Viewing area of the camera is such that, the whole area of interest, i.e. from the Nozzle exit to wall is covered (Few experiments are conducted, wherein area of interest is restricted to near wall region, to get better resolution).

Basics of PIV is explained in figure 2.5. A dual pulse Laser illuminates the flow field twice in a short time interval known as 'dt'. The image captured by the camera, during these two illuminations, is broke down into small regions called interrogation window. Interrogation window size is chosen such that, each interrogation window has sufficient number of particles. Each interrogation window corresponding to time t is correlated

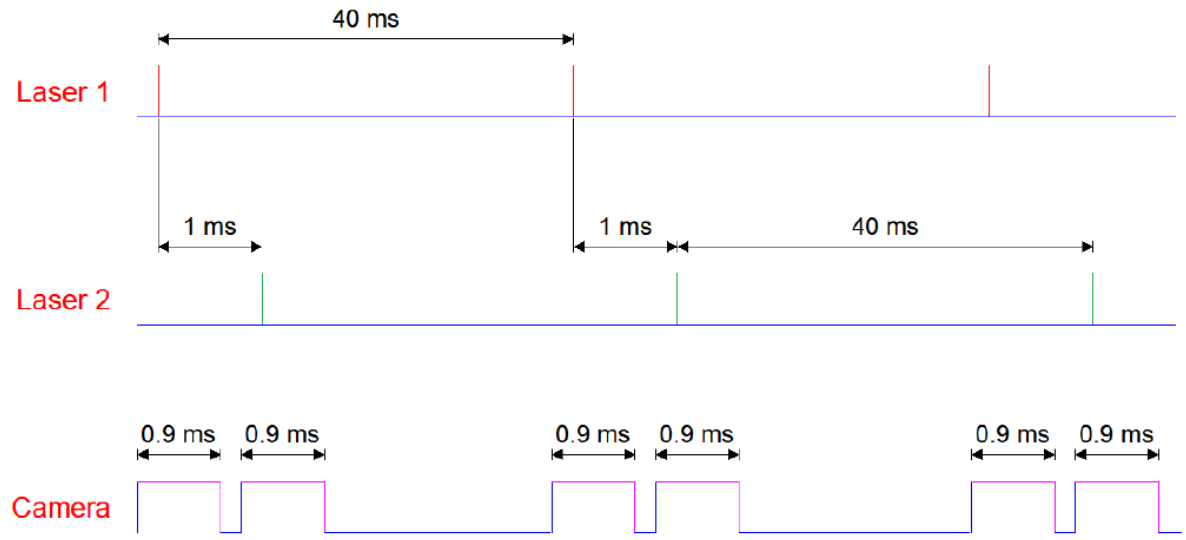

Fig. 2.4 Timing Diagram

with its counterpart corresponding to time $t + dt$. The location where the correlation is maximum between t and $t + dt$ for an interrogation window, is considered as the displacement for that particular interrogation window. This displacement when divided by the time interval dt gives velocity for that interrogation window. Similarly velocity for all the interrogation windows is obtained, which further can be interpolated to get the full velocity field.

However for certain interrogation windows velocity vectors obtained will be corrupted because of bad correlation. Median and standard deviation filters can be applied to remove the bad vectors. There could be several reasons for bad correlation. One of them is less particle density. Another, is incorrect dt. If dt is too large, then the particles move out of the interrogation window, causing the loss in correlation. If dt is too small, then the particle displacement will be of the order of error, causing the bad correlation. Movement of particles in the perpendicular direction, also causes the loss of correlation. Very small interrogation size having very few particles, is one more reason for loss of correlation. Hence, in our work, we have chosen particle density, interrogation window size and dt carefully, after few trial experiments.

As mentioned earlier, 2 g of particles are added to the whole tank along with a little additional quantity added to the rings. For this particle density, and the magnification of camera used, using multiple trials, we found that the dt of 1 ms suits for all the velocities

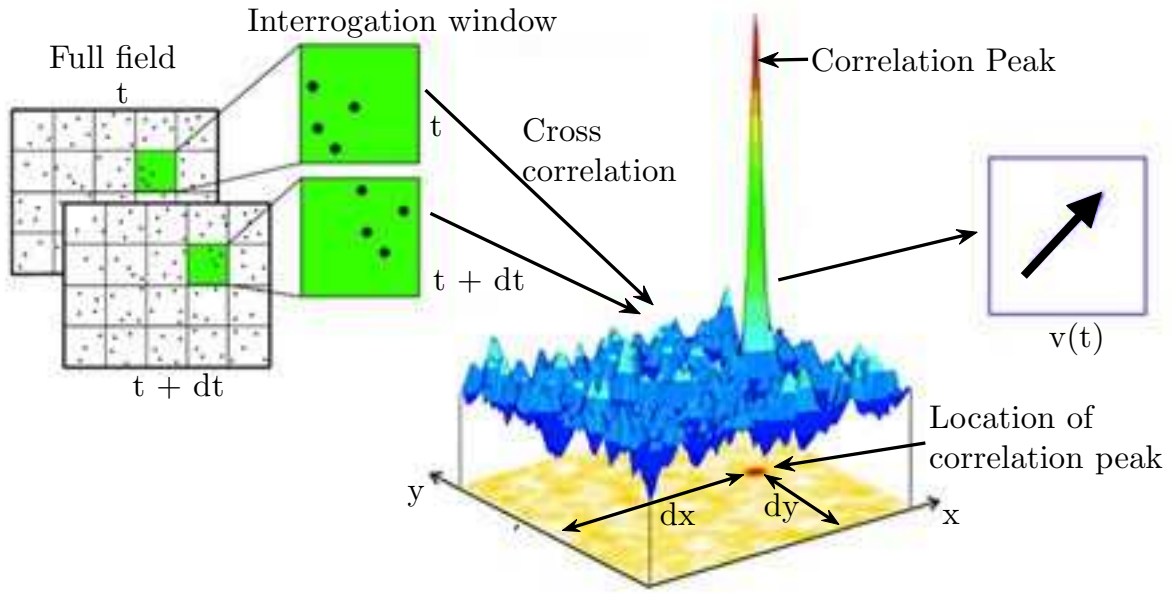

Fig. 2.5 Particle Image Velocimetry (Adopted from Deng et al. (2004))

used. For dt of 4 ms a few wrong vectors start to appear, and for dt of 8 ms almost all the vectors inside the ring are erroneous vectors (Refer figure 2.6). As the ring hits the wall, high shear, high vortical region is generated. To get good vectors in this region, it is necessary to use the dt of 1 ms.

Interrogation window used in all the PIV experiments is 32 × 32 with 50% overlap, which is suitable for our particle density, and the magnification of camera used (Refer figure 2.7). To remove the erroneous vectors, median and standard deviation filters are used. Universal Outlier Detection is also used to reject the erroneous vectors. While using filters, it is ensured that the number of vectors replaced is lesser than 2%. All the PIV analysis are done using automated PIVLab based MATLAB program. PIVLab is an open-source software developed by Thielicke and Stamhuis (2014), and its multi-purpose use is demonstrated by Thielicke (2014).

PIV resolution changes slightly for different experiments. Full 1632 × 1200 pixels of the camera can't be used, the reason being edges of the camera will give rise to distortions in the image, because of non-uniform magnification at the edges. Hence, the area of interest is made to occupy the pixels in the center, and made not to go till the edges. PIV resolution for different solutions is listed in the table 2.1. The smallest length scale resolved for velocity vector is the size of interrogation window, which is in the range

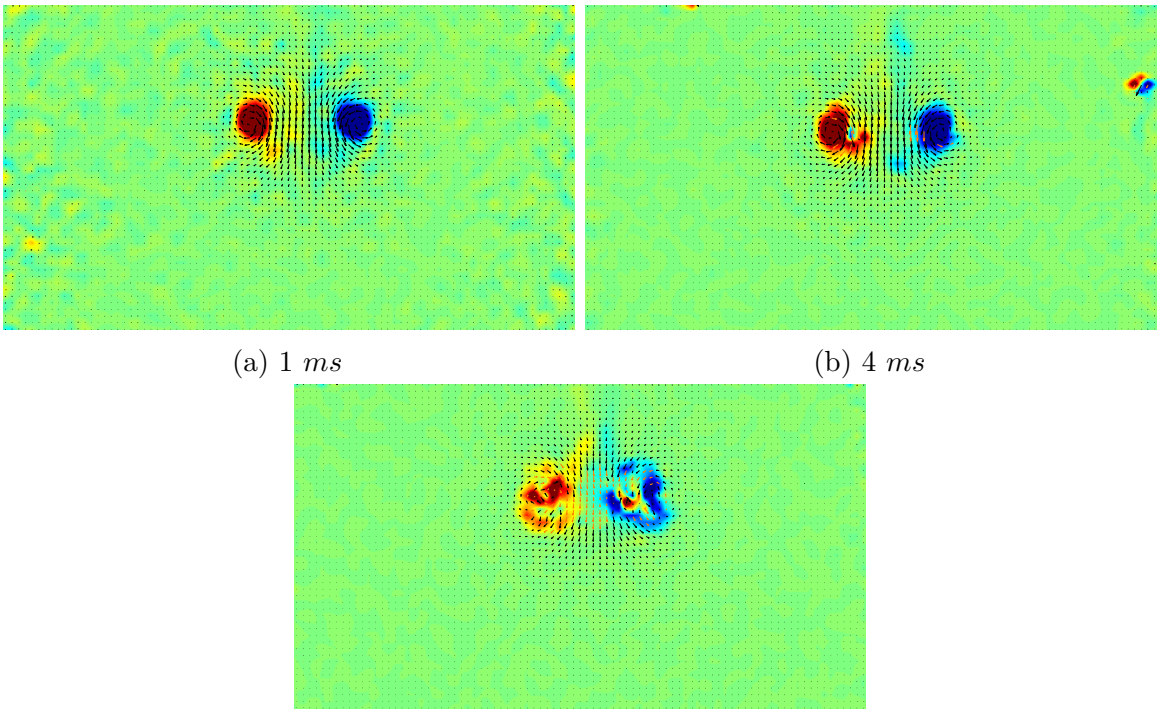

(a) 1 ms (b) 4 ms

(c) 8 ms

Fig. 2.6 PIV analysis for different dt, PAMH 5ppm, L100 V500 case

of 3.7 mm to 4.8 mm. Since we have used 50% overlap, there will be two vectors in one interrogation window length. Hence, resolution of PIV is half the length of interrogation window, and the smallest length scale resolved will be double that of the resolution.

Table 2.1 PIV Resolution

Solution	**Physical Domain** ($mm \times mm$)	**No of pixels in the domain**	$mm/pixel$	**Resolution** (mm)
Water	250 × 211	1090 × 920	0.23	3.68
PAMH 5 ppm	250 × 284	880 × 1000	0.2841	4.5456
PAMH 10 ppm	250 × 301	830 × 1000	0.301	4.816
PAMH 25 ppm	250 × 301	830 × 1000	0.301	4.816

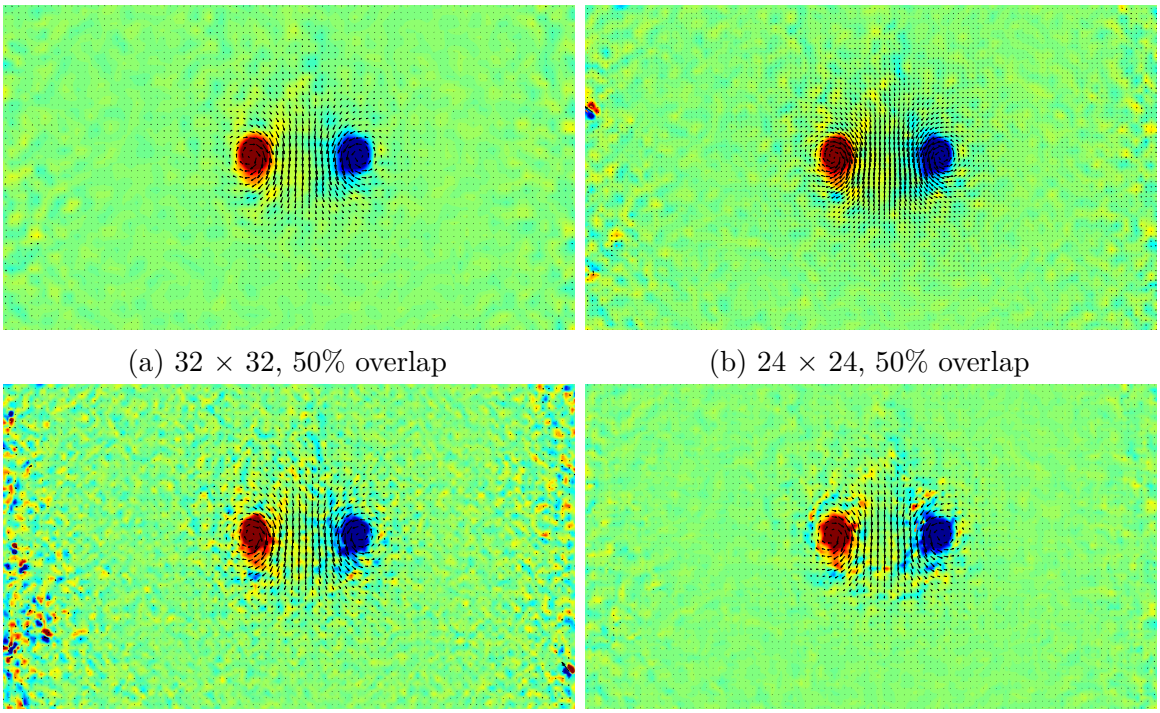

(a) 32 × 32, 50% overlap

(b) 24 × 24, 50% overlap

(c) 16 × 16, 50% overlap

(d) 32 × 32, 75% overlap

Fig. 2.7 PIV analysis for different interrogation windows, PAMH 5ppm, L100 V500 case

2.3 Dye Visualization

Dye visualization is a classical method used in fluid mechanics for understanding the flow structures. Though the method is very simple, the disadvantage is that the dye in the front planes block the visualization of the ones in the backward planes, which makes inner structures invisible. In our experiments blue color Aludine dye is added to the fluid inside the piston-cylinder mechanism. Images are captured using 21 MP DSLR camera Nikon D500 with 17-35 mm lens.

2.4 Planar Laser Induced Florescence

Planar Laser Induced Florescence (PLIF) is another popular flow visualization technique. This technique is fairly simple, and gives an idea about the dominant flow structures. This method uses florescent dye, which gets exited at a particular frequency and emits in another frequency band. The advantage of the technique lies in, illuminating a particular plane and visualizing, all the other planes act transparent without any blockage, because

of absence of excitation source. Hence, any plane can be visualized easily, which wasn't the case in dye visualization, where all the dye in front planes block the visual of backward planes.

Rhodamine 6G is the florescent dye used in our experiments, which gets excited at a frequency of 532 nm and emits in window of 600 - 625 nm with peak at 605 nm. For PLIF experiments continuous Laser of 1 W (by Wicked Lasers Inc.) was used. The laser has an in built sheet making optics, which was used to get the laser sheet of thickness 2 mm. Dye was added to the fluid inside the piston cylinder arrangement, and the vortex rings formed were visualized using 21 MP DSLR camera Nikon D500. 17-35 mm lens was used for magnification and focusing purpose. A 600 nm high pass filter was used for blocking the green light of the laser, so that only the light emitted by the dye will pass through, making the ring more clearly visible. Images were captured at 60 Hz.

Formation of the ring, rolls inside the ring, and the formation of secondary vortex ring are observed using PLIF experiments, which will be explained in the next chapter.

2.5 Polymer Solution Characterization

In our experiments, we have used three different polymer solutions. Characterizing these solutions was necessary to reason the difference in their behavior. As explained in section 1.5, addition of polymers to water, gives rise to non-Newtonian properties, such as shear-thinning and elasticity. Shear-thinning property is characterized using power law index (n), zero shear viscosity (η_0) and infinite shear viscosity (η_∞), whereas elasticity is characterized using relaxation time (λ). Different behaviors observed in polymer solutions, strongly depend on this non-Newtonian rheology. Though it is essential, polymer characterization is often neglected in drag reduction literatures, because of its complexity and the limitations of tools used for characterization. It is often seen that, the same polymer from the same company behaves in two different ways depending on the method of preparation, batch of production and aging etc (Example: Choueiri et al. (2018) and Samanta et al. (2013)). Often the irregularities in polymer drag reduction literature is suspected to be because of lack of polymer characterization. Hence, we present all the methods of polymer characterization (including the failed ones) used in our study in this section.

Rheological measurements in our study is mainly carried out using Anton Paar 302 rheometer (Refer figure 2.8). Both oscillatory and rotational rheometry are carried out. All the rheometry measurements are carried out on the third day after preparation at 25^o C temperature, so as to match the properties of the experimental solution. There are number of geometries that can be used for rheometrical studies. We have used the following four geometries.

- **Parallel Plate Geometry.** This geometry involves two parallel plates separated by a gap. The solution whose rheological properties has to be measured is placed between these two plates. Bottom plate is held fixed, whereas the top plate rotates, generating a shear in the gap. The shear rate at the center of the tool is zero. Shear rate increases as the radial distance from the center increases. In parallel plate geometry the gap between the plates can be varied from 10's of microns to 1 mm. Hence, shear rate depends on the gap between the plates also. We have used PP-50 (Parallel plate 50 mm outer diameter) tool of Anton Paar in our studies involving parallel plate.

- **Cone and Plate Geometry.** The disadvantage of the parallel plate geometry is the radially varying shear rates. This is overcome in cone and plate geometry by replacing the top plate by a cone. The bottom plate remains the same. Replacing the plate with cone makes the shear rate uniform throughout the radial direction. However, the gap between the cone and plate is fixed. We have used CP-50 (Cone plate 50 mm outer diameter with 1° cone angle) tool in our experiments.

- **Concentric Cylinder Geometry (Couette Geometry).** Less contact area between the fluid and the tool is the disadvantage of Cone and Plate and Parallel plate tools. This is overcome by concentric cylinder geometry. The fluid is filled in the gap between the concentric cylinders, and the inner cylinder is rotated, with outer cylinder being stationery. However, the end effects gives rise to errors. At higher shear rate, some flow patterns are setup (Taylor vortices) which increases the stress dramatically, which is an error. We have used CC-27 (Concentric cylinder, inner diameter of 26.6665 mm, outer diameter of 28.921 mm and length of 39.981 mm) tool in our experiments.

- **Double Gap Geometry.** Double gap geometry increases the contact area between the fluid and the tool even more, thus suitable for measuring low viscosities and at low shear rates. We have used DG-26.7 tool of Anton Paar in our studies.

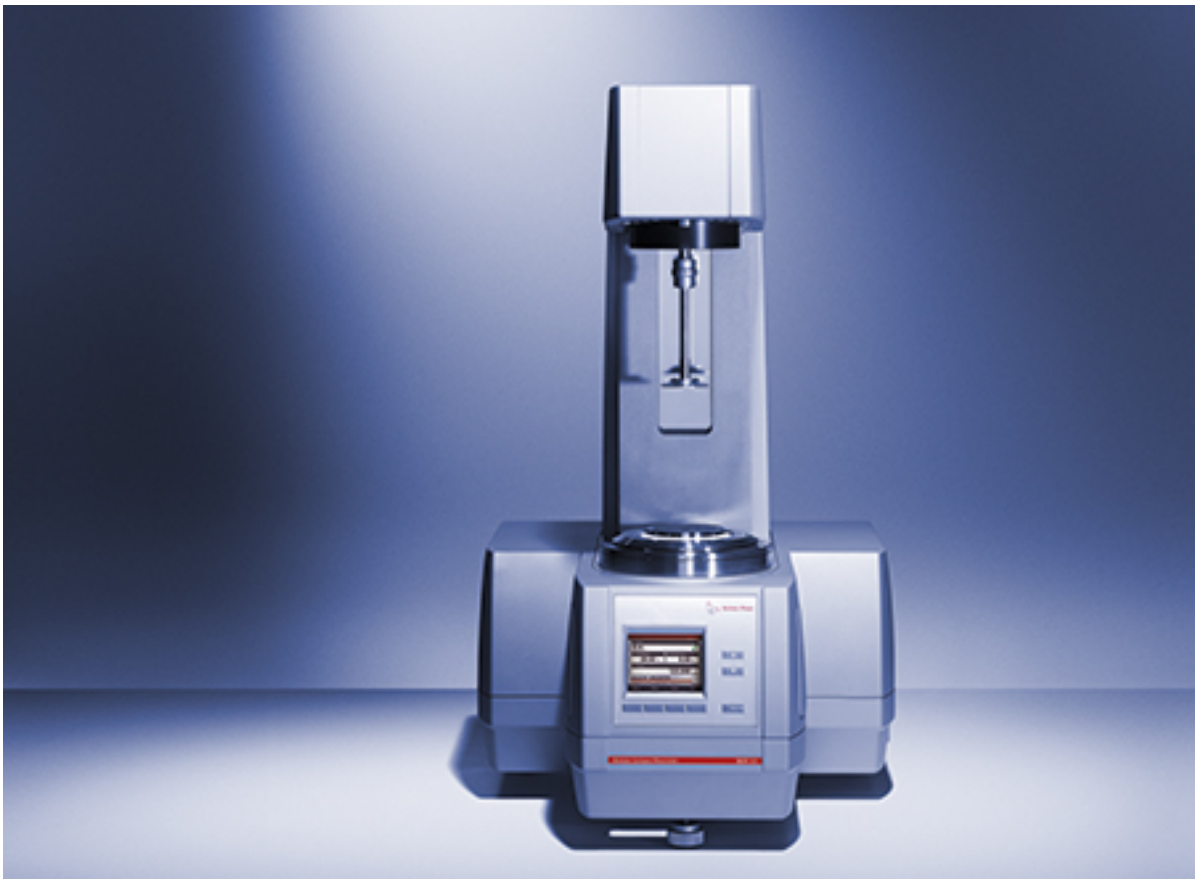

Fig. 2.8 Anton Paar MCR 302 Rheometer

2.5.1 Oscillatory Rheometry - Amplitude Sweep

Oscillatory rheometry is used to measure the viscoelastic properties, mainly the relaxation time λ. In this method, oscillatory shear is applied by rotating the top plate (or the cone) in sinusoidal manner. Stress is measured during this oscillatory shear. If the sample used is Newtonian liquid, then stress is proportional to strain rate. Hence, there is a 90° phase difference between the strain applied and the stress measured. However, for Hookian solid, stress is proportional to strain. Hence, there is no phase difference between the strain applied and stress measured. Since, the viscoelastic fluids fall in between these two extremes, there will be a phase difference (but not 90°) between strain applied and stress measured. By measuring this phase difference, and amplitude of the stress, other properties of viscoelasticity such as storage modulus (G'), loss modulus (G''), complex viscosity $\eta^\star$ and relaxation time λ are measured. Applied shear which is sinusoidal in nature has two independent parameters, amplitude and frequency. Hence, oscillatory rheometry involves two steps, (1) Amplitude Sweep (with constant frequency of 10 rad/s)

and (2) Frequency Sweep (with amplitude inside linear viscoelastic regime, as measured from amplitude sweep).

During amplitude sweep, the amplitude of strain applied is varied over a range, with constant frequency of 10 rad/s. The range of amplitudes of strain applied by the top rotating plate, in our experiments is from $10^{-2}\%$ to $10^{3}\%$ of the gap between top plate and bottom plate at the outermost radial location.

To begin with amplitude sweep of PAMH 25 ppm was carried out using standard cone and plate tool. For cone and plate tool the gap is fixed at 100 μm. The result obtained is shown in figure 2.9. Huge deviation was observed among different measurements. The reason being, polymer solution doesn't offer enough resistance to be measurable without errors. This is a common problem faced by whole of the rheology community, while measuring relaxation time of dilute solutions. Since PAMH 25ppm is the highest concentration we are using, everything else is more dilute than PAMH 25ppm. Hence, in all our oscillatory rheometry experiments, we stick with PAMH 25ppm, which has the best hope of giving a sensible result.

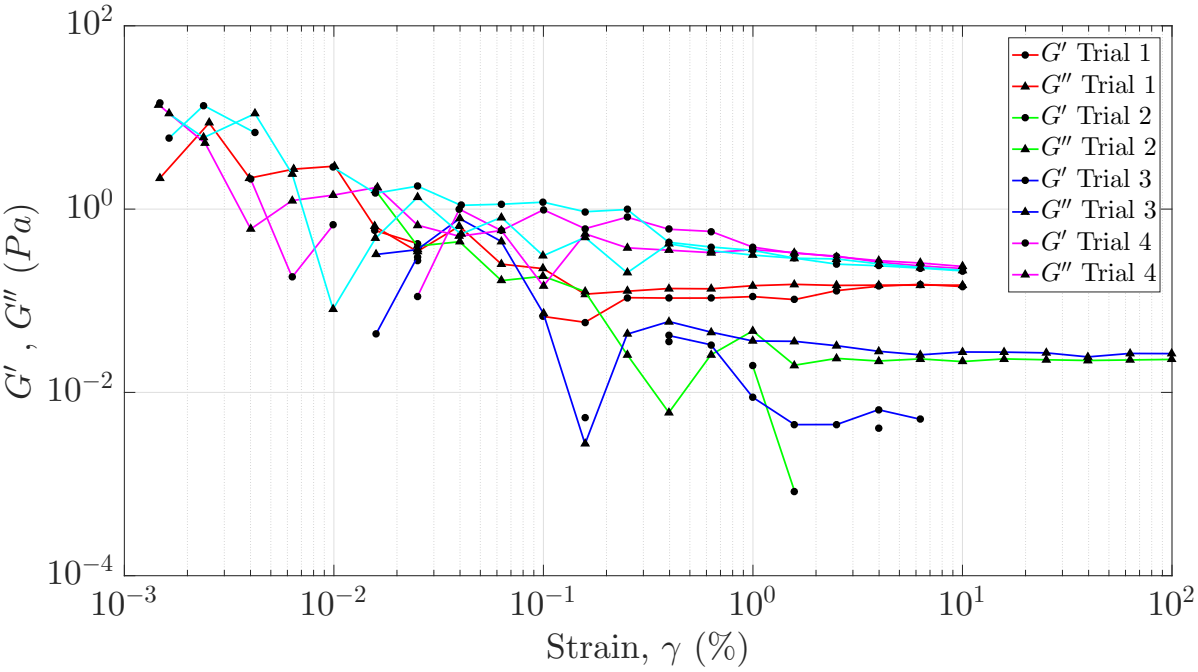

Fig. 2.9 Amplitude Sweep of PAMH 25ppm polymer solution using Cone and Plate tool. Gap between cone and plate is 100 μm.

Another way to increase the resistance offered by the polymer solution, so that the forces are measurable in the rheometer, is by decreasing the gap between the plates. Cone and plate has a fixed gap width of 100 μm, which can't be changed. Hence, we use parallel plate geometry, and reduce the gap between the plates to 20 μm. Since, the volume of polymer solution required to carry out these rheometry measurements are very small, a micro-pipette is used to measure the volume of liquid. The results obtained by this method are presented in figure 2.10.

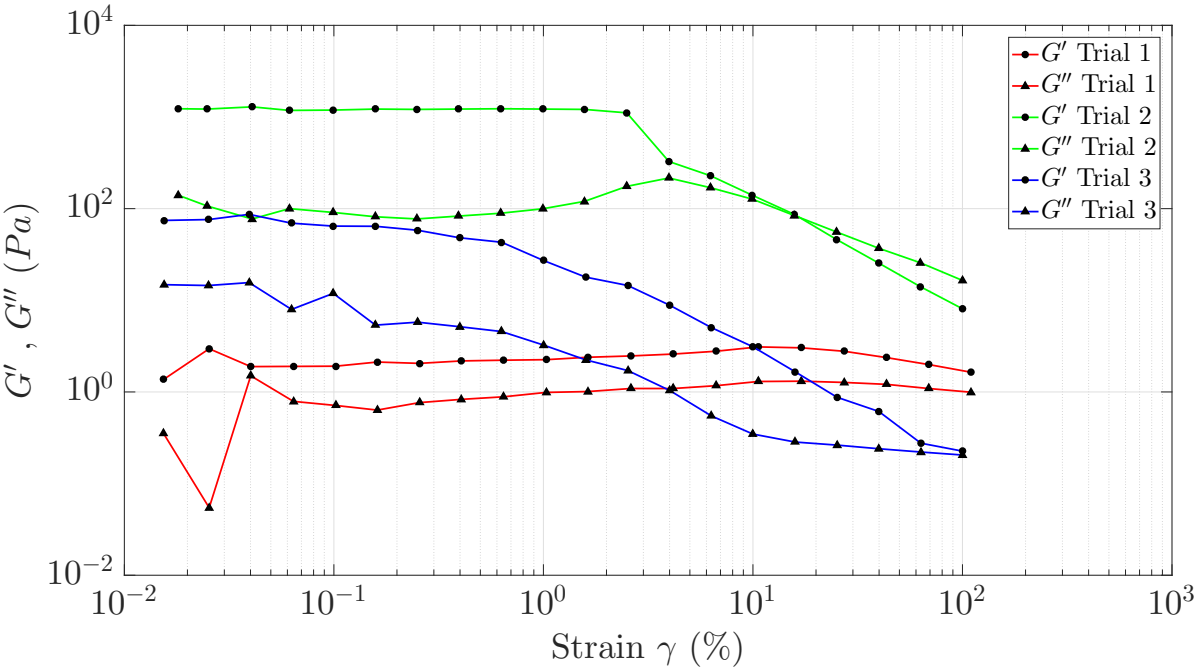

Fig. 2.10 Amplitude Sweep of PAMH 25ppm polymer solution using Parallel Plate tool. Gap between the plates is 20 μm.

As shown in the figure 2.10, for very small gaps like 20 μm, G' is larger than G'' with a very clear yield point for individual runs. However, measurements are not repeatable and there is an order of magnitude difference among the runs. Similar problem was faced for a gap of 30 μm also (Refer figure 2.11). Hence, carrying out rheological measurements at very small gap width is not recommended.

We carried out a set of experiments on concentrated, highly viscous polymer solution, PAMH 2500 ppm, to examine the importance of viscosity of the solution in the above said rheometrical measurements. Results of amplitude sweep for PAMH 2500 ppm, for gap widths varying from 20 μm to 100 μm is shown in figure 2.12. The measurement between different runs match very nicely, above shear rate of 10^{-1}%. G' is greater than

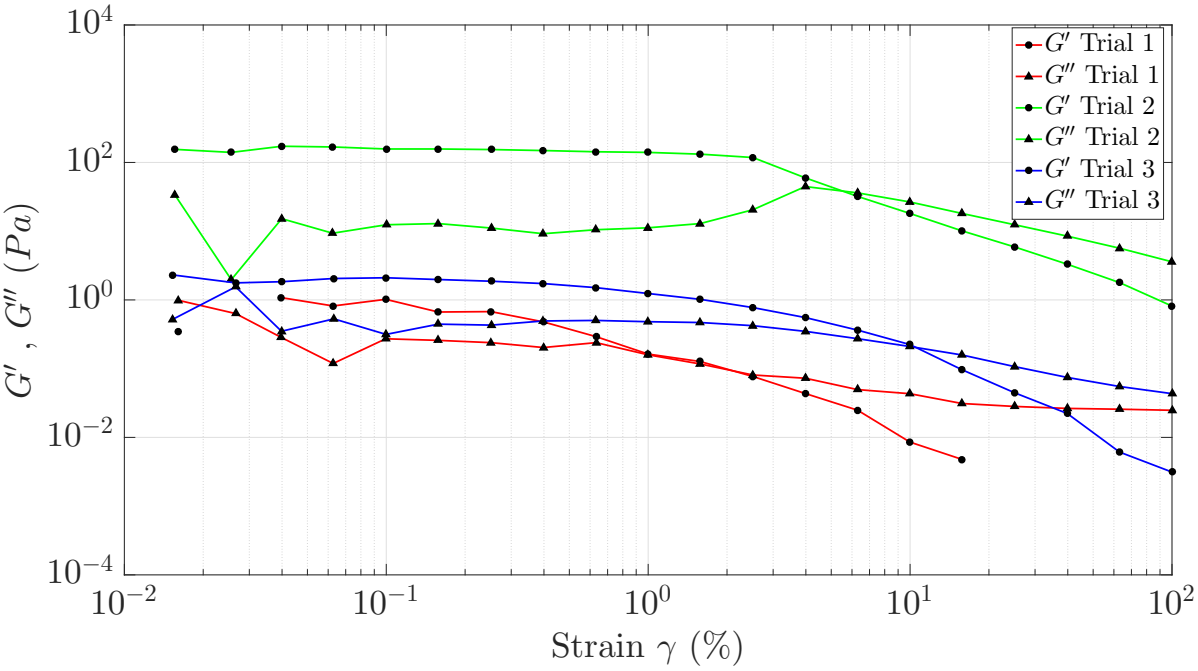

Fig. 2.11 Amplitude Sweep of PAMH 25ppm polymer solution using Parallel Plate tool. Gap between the plates is 30 μm.

G'', throughout the amplitude range, with yield point somewhere near 100 % strain amplitude. Since, the concentration used is way above the critical overlap concentration, G' is greater than G'' is expected. Even for visual inspection and physical feel, PAMH 2500 ppm resembles more like solid than liquid.

Successful measurements on PAMH 2500 ppm (even at different gap widths), and failed measurements on PAMH 25ppm (for all gap widths used) shows that the viscosity of the solution has to be large enough for oscillatory rheometry measurements to give satisfactory results. For a truly dilute polymer solution, according to Zimm (or Rouse) model, relaxation time is directly proportional to solvent viscosity. Hence, for a dilute polymer solution, it is allowed to carry out measurements at increased solvent viscosities, and then scale it down appropriately, provided that the polymer dynamics is unaltered (Chandra et al., 2018).

To characterize the polymer using the method mentioned above, a set of experiments were carried out by adding glycerol to PAMH 25 ppm. The idea is to make the measurements using glycerol mixed polymer solution (which has enhanced viscosity), then scale down storage and loss modulus by viscosity ratio of glycerol mixed PAMH 25 ppm and pure PAMH 25 ppm. We have tried this method of measurement with three different

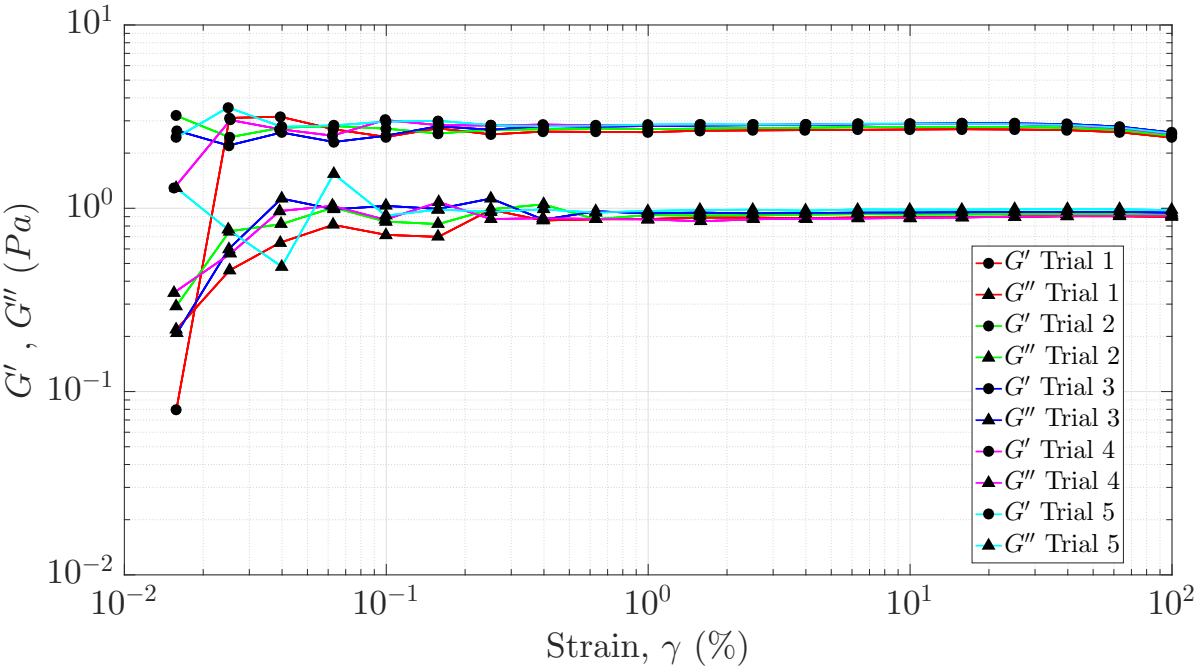

Fig. 2.12 Amplitude Sweep of PAMH 2500 ppm polymer solution using Parallel Plate tool. Gap between the plates varies from 20 μm to 100 μm over the trials.

glycerol concentration. The results are shown in figure 2.13.

As shown in figure 2.13, measurement of loss modulus is consistent with different runs. Also, loss modulus scales with viscosity ratio. However, even after addition of glycerol, storage modulus still remains unmeasurable. Hence, the relaxation time, can't be measured even with this method. Chandra et al. (2018) also couldn't measure the relaxation time, even after using increased solvent viscosity method for some of the concentrations used in their experiments.

Aim of carrying out amplitude sweep is to find out the linear viscoelastic regime, where, G' and G'' doesn't depend on amplitude of the strain. Then frequency sweep will be carried out, using an amplitude inside linear viscoelastic regime, to get G', G'', $\eta^\star$ and λ. However, all the methods we employed to measure the amplitude sweep has failed to find out the linear viscoelastic regime. However, for dilute solutions, linear viscoelastic regime ends at lower amplitudes. Hence, by assuming different strain amplitudes, from 0.01 % to 100 %, we have carried out frequency sweep for PAMH 25ppm, which will be presented in the next subsection.

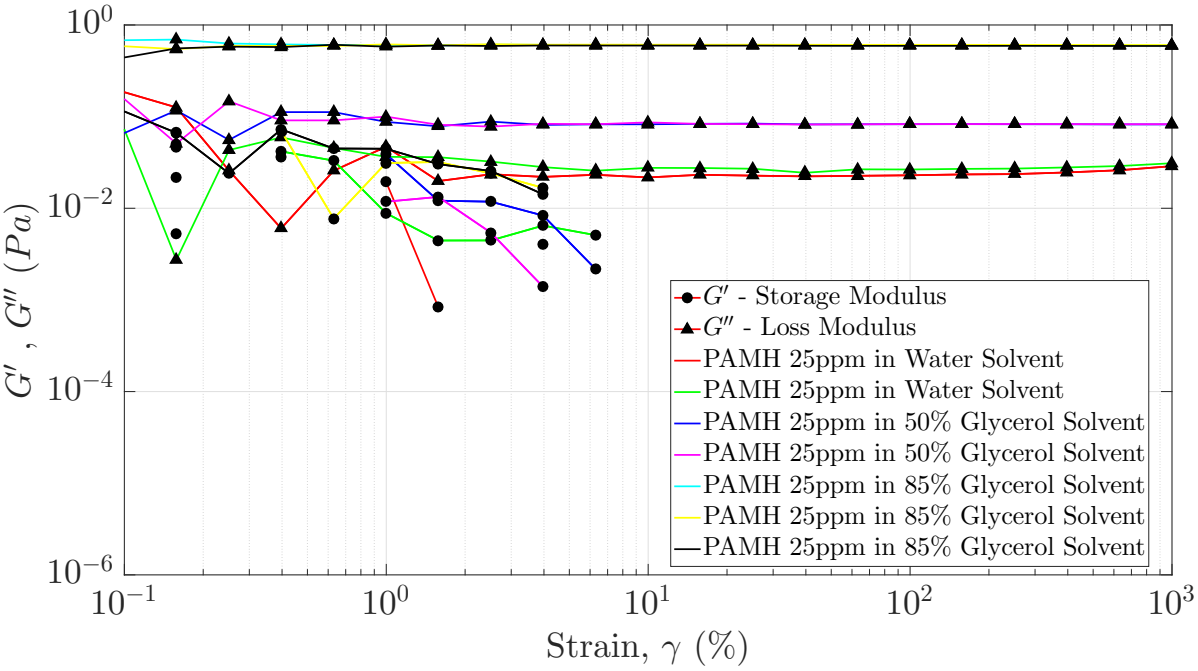

Fig. 2.13 Amplitude Sweep of PAMH 25ppm polymer solution added with Glycerol using Cone and Plate tool. Gap between cone and plate is 100 μm.

2.5.2 Oscillatory Rheometry - Frequency Sweep

Frequency sweep was carried out for PAMH 25 ppm solution using parallel plate tool with gap width of 100 μm, at a strain amplitude of 1 %. The results are shown in figure 2.14. Inconsistency among different runs is clear from the figure. G' is greater than G'' for trial 1, whereas G'' is greater than G' for trial 2 and 3. The reason for this inconsistency is the low viscosity of polymer solution.

As done in amplitude sweep, in frequency sweep also, reducing the gap between the plates was used to make the measurements. Gap between the plates in parallel plate tool was reduced to 20 μm. The same inconsistency which was observed for plate gap of 100 μm was observed here too, along with orders of magnitude difference among the runs. Measurements were carried out at other gap widths too. However, the results are not satisfactory at any gap width (Refer figure 2.16 for gap width of 30 μm).

Frequency sweep measurements were done using concentrated, viscous PAMH 2500ppm solution, to check whether satisfactory results are obtained at higher viscosities. For PAMH 2500 ppm, amplitude sweep had given a satisfactory, reproducible result at different gap widths. From amplitude sweep, it was found that linear viscoelastic regime

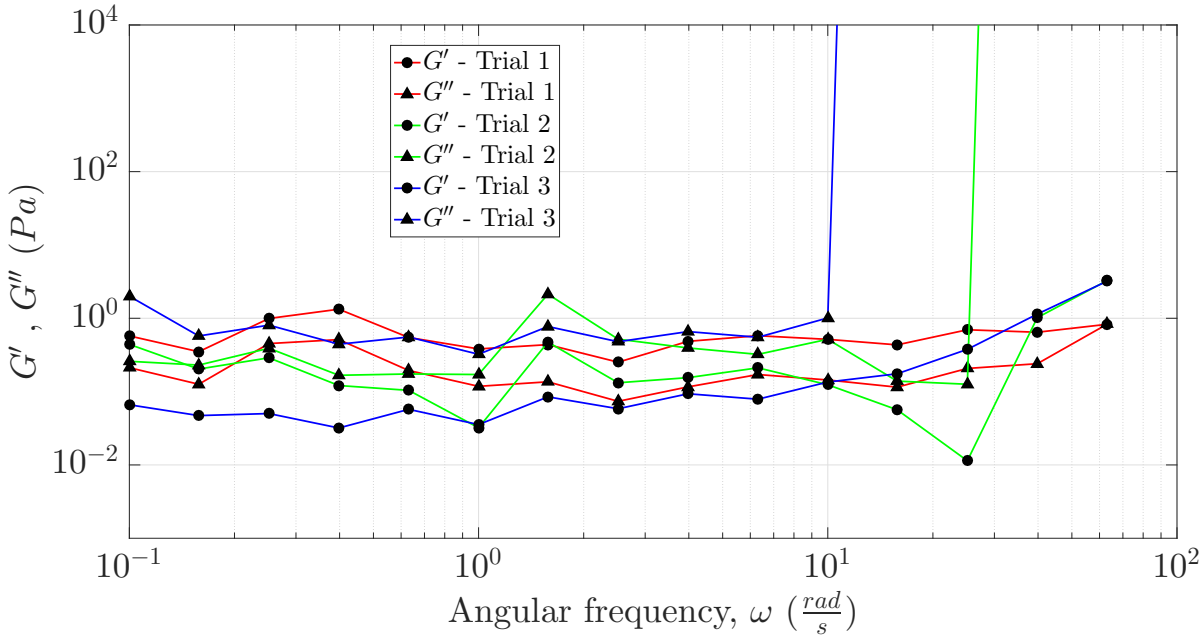

Fig. 2.14 Frequency Sweep of PAMH 25ppm polymer solution using Parallel Plate tool. Gap between the plates is 100 μm.

for PAMH 2500 ppm is till the strain amplitude of 100 %. Hence, strain amplitude of 10% was used for frequency sweep measurements. The results are shown in figure 2.17.

It is clear from figure 2.17 that at higher viscosities, the measurements are satisfactory and reproducible. Hence, similar to amplitude sweep, efforts were done to increase the solvent viscosity by glycerol addition and then carry out the measurements. Results are presented in figure 2.18. However, addition of glycerol to increase the solvent viscosity didn't improve the measurements. Along with the results presented in this section, multiple other runs were also done for PAMH 25ppm solution with strain amplitudes going from 0.01 % to 100 %. However, none of the measurements were satisfactory. With this all the possibilities of doing oscillatory rheometry measurements were exhausted.

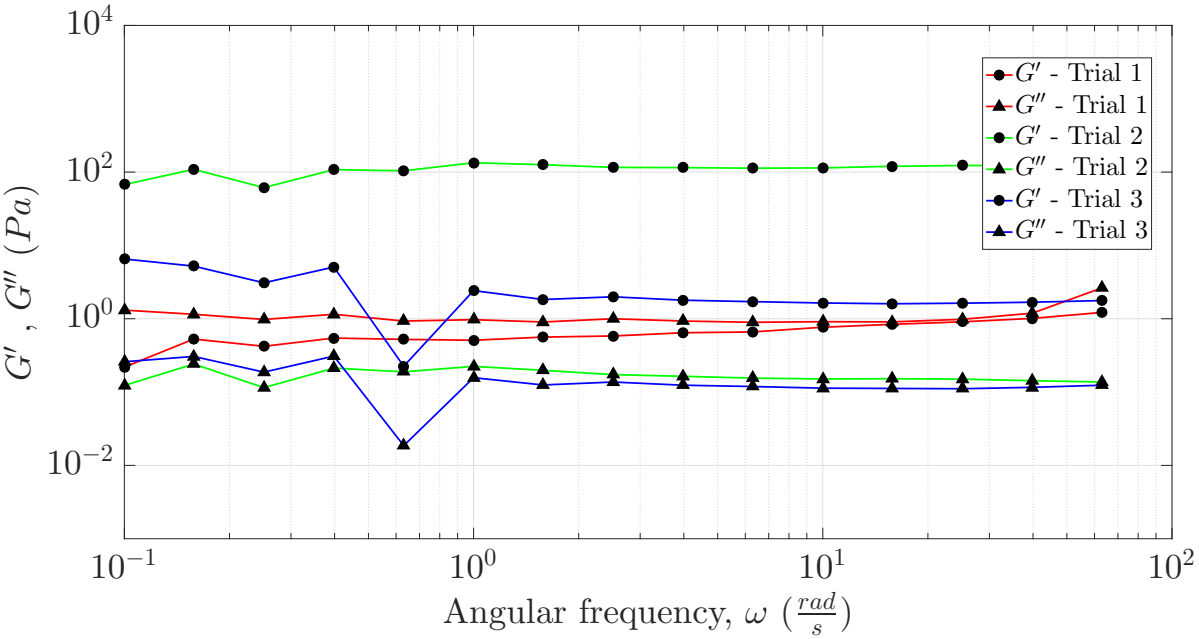

Fig. 2.15 Frequency Sweep of PAMH 25ppm polymer solution using Parallel Plate tool. Gap between the plates is 20 μm.

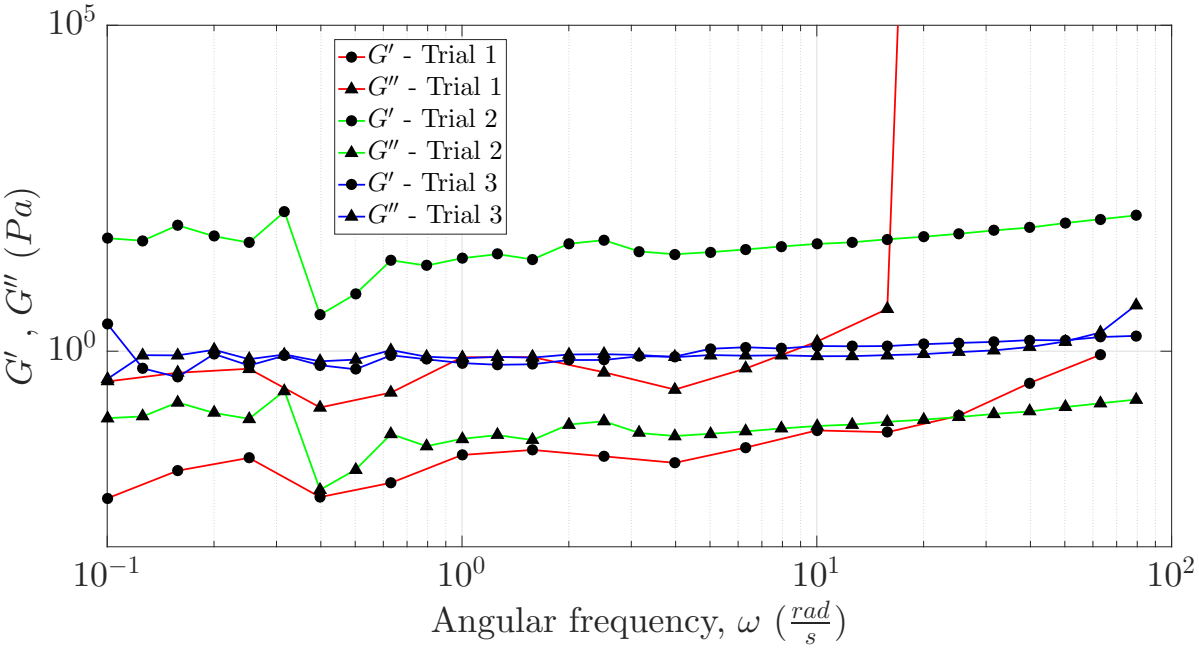

Fig. 2.16 Frequency Sweep of PAMH 25ppm polymer solution using Parallel Plate tool. Gap between the plates is 30 μm.

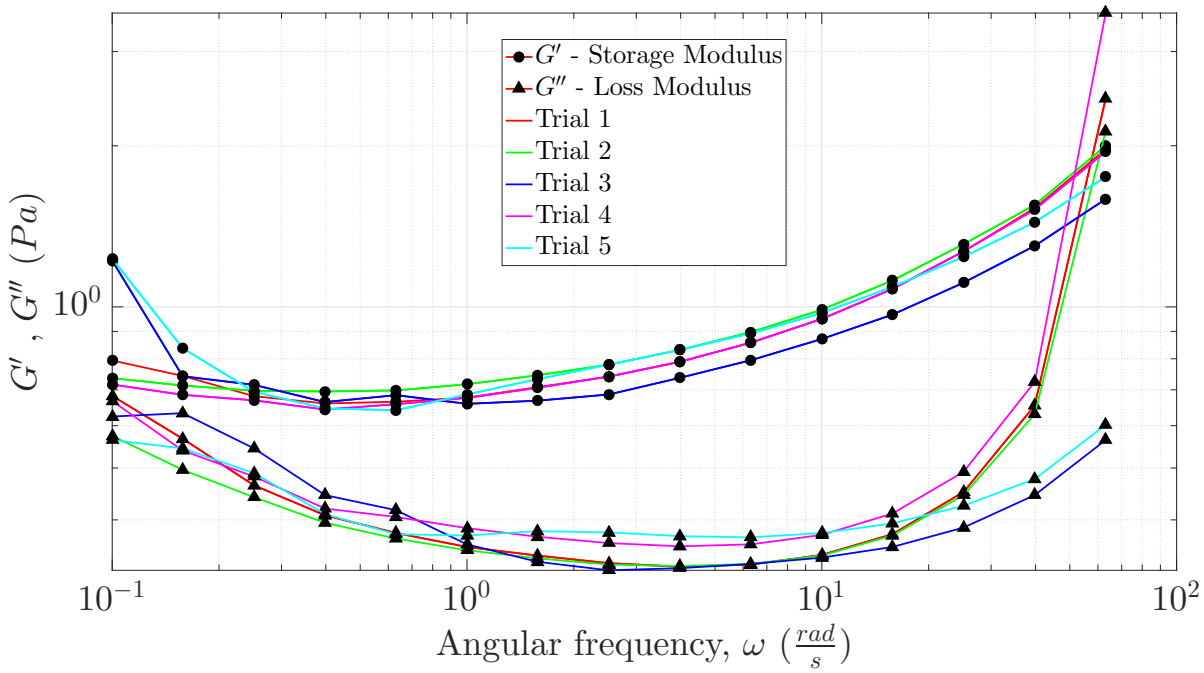

Fig. 2.17 Frequency Sweep of PAMH 2500 ppm polymer solution using Parallel Plate tool. Gap between the plates is varied from 20 μm to 100 μm. Circles represent storage modulus (G'), and triangles represent loss modulus (G'')

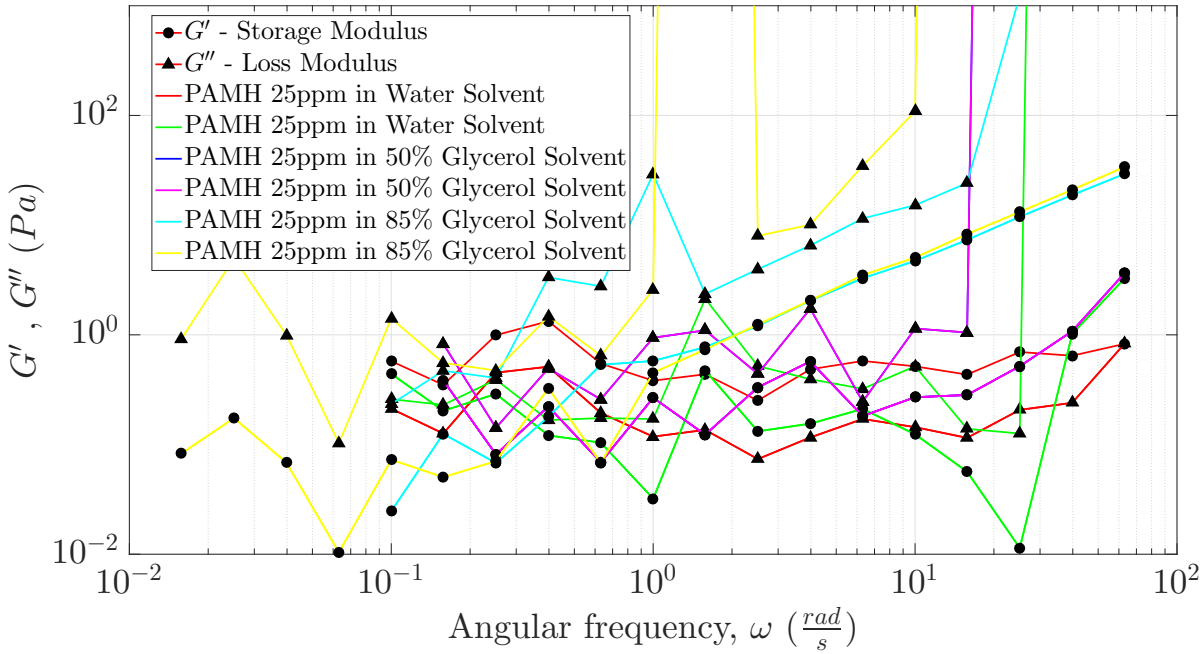

Fig. 2.18 Frequency Sweep of PAMH 25 ppm polymer solution added with Glycerol using Parallel Plate tool. Gap between the plates is 100 μm. Circles represent storage modulus (G'), and triangles represent loss modulus (G'')

2.5.3 Rotational Rheometry

In rotational rheometry the top plate is in steady rotation in only one direction, as opposed to sinusoidal oscillations in oscillatory rheometry. The rotational speed is changed to get different shear rates. The force necessary to maintain the shear rate is measured, which gives shear stress. Using the measured shear stress and the shear rate applied, viscosity will be calculated. All the different geometries mentioned in the earlier subsection, can be employed for rotational rheometry too. All the measurements are done at temperature of 25° C.

Water has constant viscosity of 0.9 $mPa-s$ at temperature of 25° C. Rotational rheometry measurements were carried out on 5ppm, 10ppm and 25ppm solutions. All the measurements were carried out using Double Gap tool of Anton Paar. Double gap tool gives accurate results at low shear rates, because of larger contact area. The results obtained after Carreau-Yasuda fit are shown in figure 2.19, 2.20, 2.21 and 2.22. Rotational rheometry measurements on 5 and 10ppm solutions were carried out by Shashank (2019).

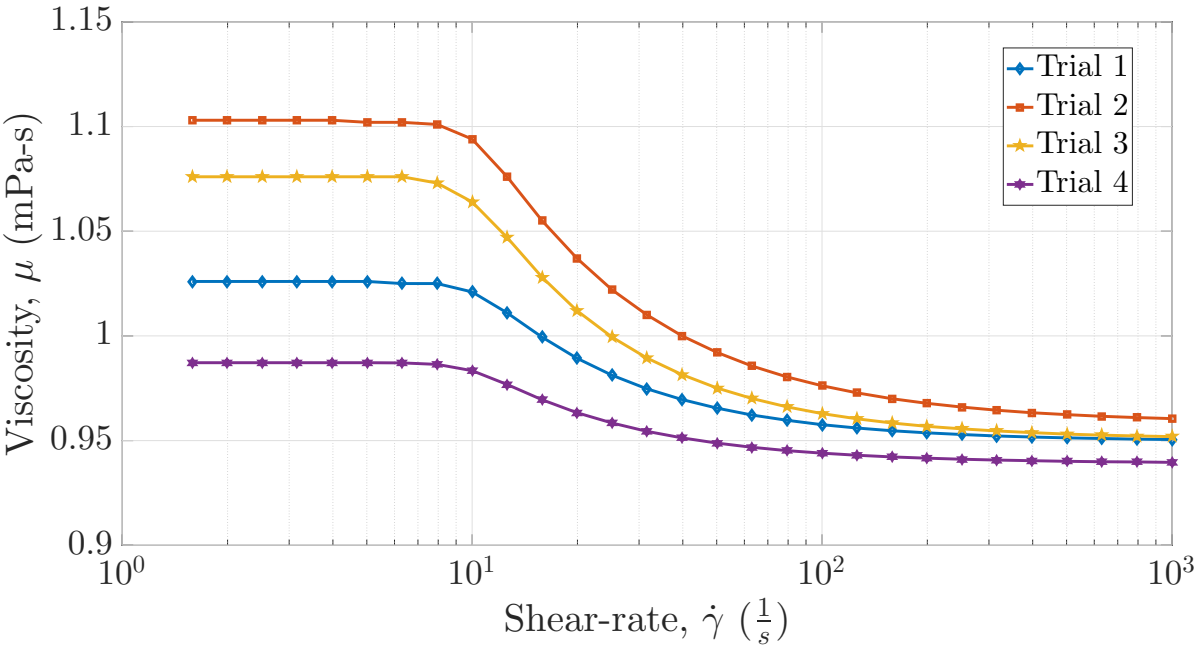

Fig. 2.19 Viscosity vs Shear rate plots for PAMH 5 ppm

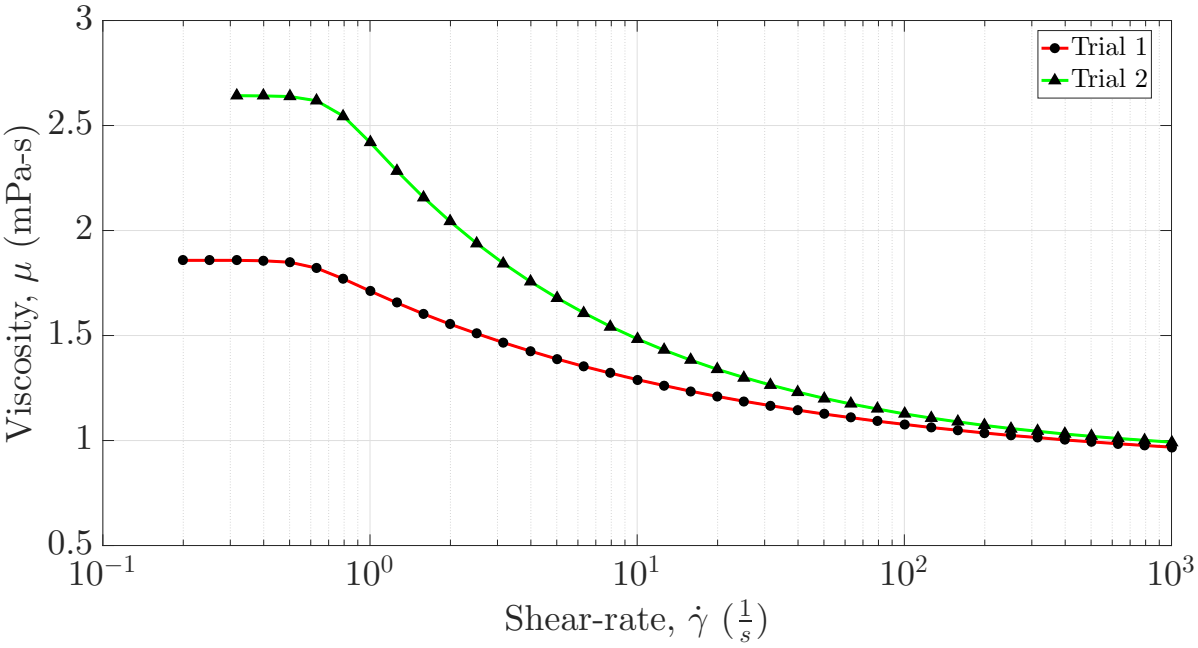

Fig. 2.20 Viscosity vs Shear rate plots for PAMH 10 ppm

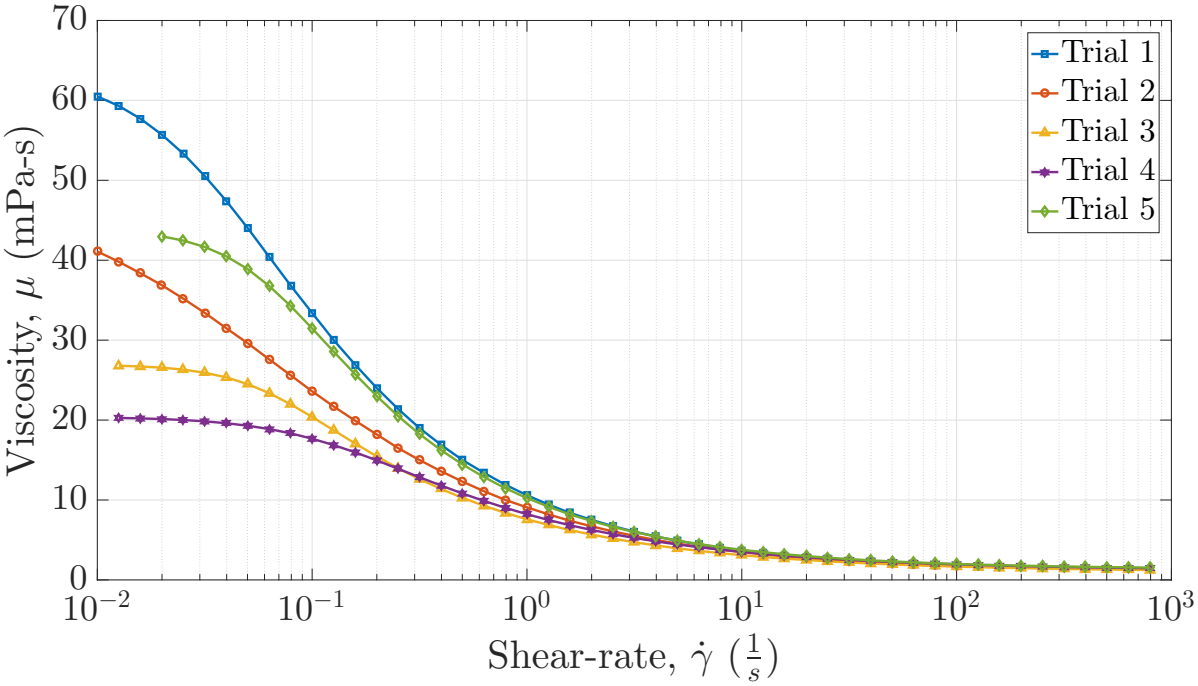

Fig. 2.21 Viscosity vs Shear rate plots for PAMH 25 ppm

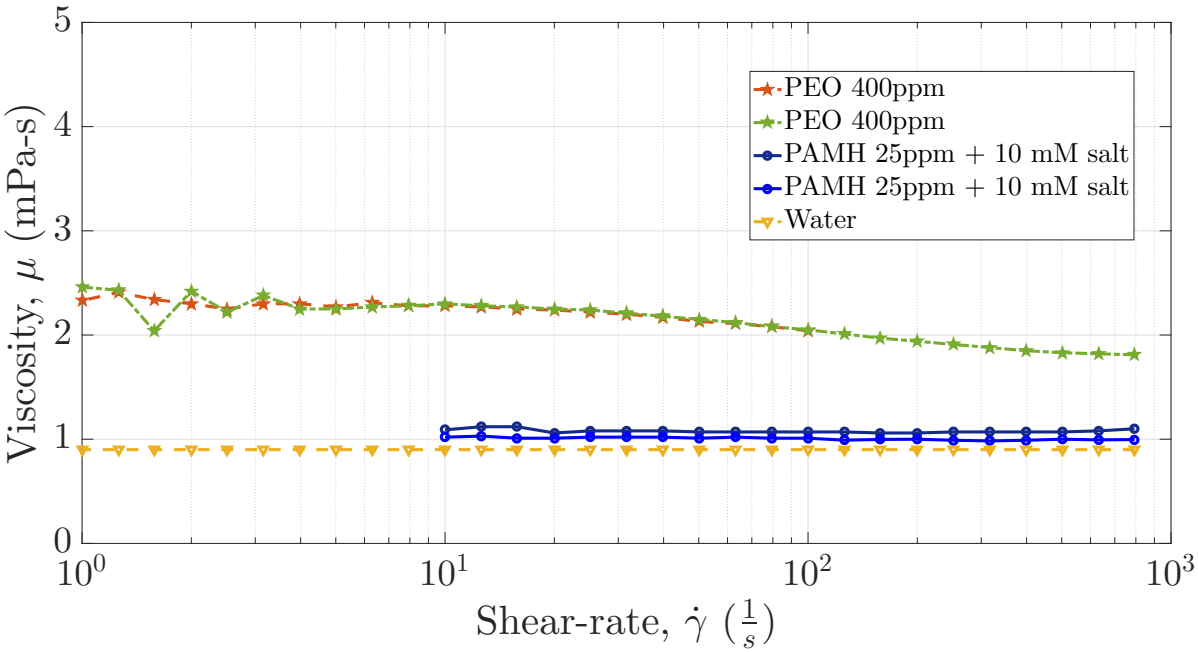

Fig. 2.22 Viscosity vs Shear rate plots for PAMH 25 ppm with 10 mM salt added

Viscosity vs Shear rate plots for all the polymer solutions used in our experiments show shear thinning effect. The reason for the shear thinning effect in polymer solutions is explained in section 1.5. However, shear thinning is negligible for PAMH 5 ppm and 10 ppm solutions when compared with PAMH 25 ppm. Power law index is obtained from these plots.

Inverse of the shear rate at which the transition from zero-shear plateau to power law region occurs, gives the relaxation time (Srinivas and Kumaran, 2017; Zhang and Muller, 2018). The reason for it is explained in section 1.5. Since, oscillatory rheometry doesn't work for dilute solutions, and normal stresses are too small to be measurable, relaxation time is measured using shear thinning viscosity profile. All the important properties of polymer solutions as measured using rotational rheometry are summarized in the table 2.2.

Table 2.2 Properties of polymer solutions

Solution	λ (s)	n	η_0 $(mPa-s)$
PAMH 5 ppm	0.1		0.9 - 1.1
PAMH 10 ppm	1 - 2	0.58 - 0.68	2 - 3
PAMH 25 ppm	12 - 25	0.46 - 0.56	20 - 60
PAMH 25 ppm + 10 mM Salt	0.025 - 0.05		0.9 - 1.1

η_∞ for all the polymer solutions is same as solvent viscosity i.e. 0.9 $mPa-s$. However, there is a drastic increase in η_0 for PAMH 25 ppm compared to all the other solutions. While vortex ring is traversing, shear rate falls onto zero-shear plateau within a distance of 2-3 ring diameters from the center of the ring. Hence, the ring is surrounded by ambient liquid of near to zero shear rate. Hence, some of the dramatic changes observed in the case of vortex rings in PAMH 25 ppm solution, can be explained by this increased zero shear viscosity.

From the table 2.2 it is clear that, relaxation time increases with concentration of the polymer. For a truly dilute polymer solution, relaxation time has to be independent of the concentration, which implies PAMH 25 ppm and PAMH 10 ppm are not in truly dilute regime. And nothing can be commented about diluteness of PAMH 5 ppm with the existing data. However, in literature too, concentration dependence of relaxation time is reported for solutions thought to be dilute (Chandra et al., 2018; Samanta et al., 2013). Another way of determining the diluteness is by classical viscometric methods, wherein specific viscosity is plotted against concentration to obtain the critical overlap

concentration. We have carried out classical viscometer method of characterization of polymers, which will be presented in the next section.

2.5.4 Viscometry

This method involves measuring the time polymer solution takes to fall down through a capillary viscometer and comparing it with that of the solvent. Ratio of the time solution takes to drain to the time solvent takes is known as relative viscosity (η_{rel}). Specific viscosity, reduced viscosity, inherent viscosity and intrinsic viscosity are calculated from the relative viscosity. Using these quantities and empirical relations, relaxation time for polymer solution is obtained. Also, there are ways to determine the diluteness of the solution using this classical viscometer method.

Ubbelohde viscometer is very commonly used for this purpose (Vonlanthen and Monkewitz, 2013). We have carried out experiments using both ubbelohde and ostwald viscometers. Images of ubbelohde and ostwald viscometers are shown in figure 2.23. Temperature was kept constant at $25°C$, throughout the measurement duration.

(a) Ubbelohde viscometer

(b) Ostwald viscometer

Fig. 2.23 Ubbelohde and Ostwald viscometer used for viscometry

Once the time ratio is obtained from experiment, other quantities are derived using below mentioned equations.

$$\frac{t}{t_s} = \frac{\mu}{\mu_s} = \mu_{relative} \tag{2.1}$$

where t is time required for polymer solution to flow down through the capillary of the viscometer, t_s is time required for solvent (water) to flow down through the capillary of the viscometer. μ is viscosity of the polymer solution and μ_s is viscosity of solvent (water). $\mu_{relative}$ is relative viscosity.

$$\mu_{red} = \frac{\mu - \mu_s}{c\mu_s} \tag{2.2}$$

$$\mu_{inh} = \frac{\ln(\mu/\mu_s)}{c} \tag{2.3}$$

$$\mu_{specific} = \mu_{relative} - 1 \tag{2.4}$$

where μ_{red} is reduced viscosity, μ_{inh} is inherent viscosity, $\mu_{specific}$ is specific viscosity and c is concentration.

$$[\mu] = \lim_{c\to 0} \mu_{red} = \lim_{c\to 0} \mu_{inh} \tag{2.5}$$

$[\mu]$ is intrinsic viscosity. It gives polymer contribution to solution viscosity as the polymer concentration c approaches zero. Experimentally, μ_{red} and μ_{inh} are calculated for different concentration of polymer solutions, then extrapolated to zero concentration to get the intrinsic viscosity. Once $[\mu]$ is found out, viscosity averaged molecular weight is calculated using Mark-Houwink relation.

$$[\mu] = K(M_\mu/M_u)^{3\beta-1} \tag{2.6}$$

where M_u is molar mass constant, M_μ is viscosity averaged molecular weight, K and β are constants which depends on specific polymers. $K = 0.00631 g/cm^3$ and $3\beta - 1 = 0.8$ for PAMH polymer. M_μ can be used to calculate relaxation time using Rouse-Zimm model.

$$\tau_z = A_1 \frac{\mu_s[\mu]M_\mu}{RT} \tag{2.7}$$

$$\tau_r = A_2(c[\mu])^{A_3} \tag{2.8}$$

τ_z is zimm relaxation time, τ_r is rozhokov relaxation time, R is universal gas constant, T is temperature and A_1, A_2, A_3 are polymer specific constants.

In our experiment, we measured time ratio for five polymer concentrations i.e 5, 10, 15, 20 and 25 ppm of PAMH. Using equation 2.1, 2.2 and 2.3, reduced and inherent viscosity are calculated. Reduced and inherent viscosity are plotted against concentration in figure 2.24.

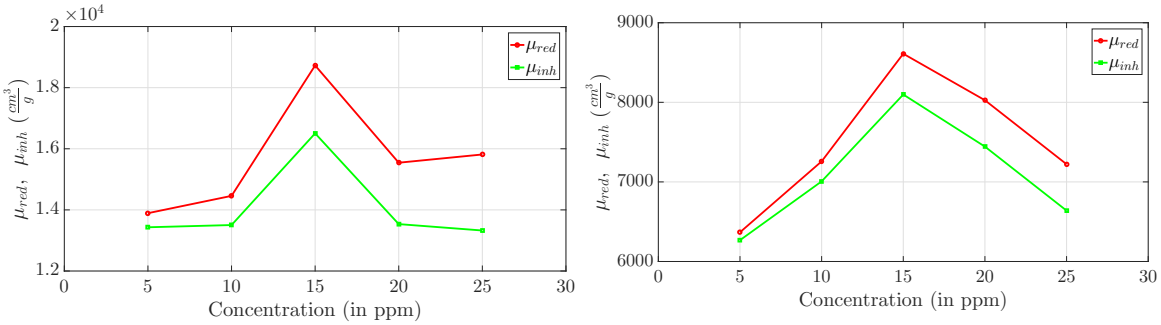

(a) Using Ubbelohde viscometer

(b) Using Ostwald viscometer

Fig. 2.24 Variation of reduced and inherent viscosity as a function of concentration

Monotonous behavior of μ_{red} and μ_{inh} is necessary to extrapolate to get the zero concentration $[\mu]$. However, it is evident from the figure that, there is no monotonous behavior of both μ_{red} and μ_{inh}. Also, measurements from ubbelohde viscometer is completely different from that of ostwald viscometer. Hence, extrapolating it to zero concentration is not possible. However, there are three empirical formulas, to get $[\mu]$ from single concentration measurements. (1) Billmeyer (2) Solomon-Ciuta and (3) Deb-Chatterjee are the three empirical formulas to get $[\mu]$. We have calculated $[\mu]$ from all the three empirical formulas, and from all five concentrations. $[\mu]$ matches quite well. However, difference in $[\mu]$ for ubbelohde and ostwald viscometers still remains. Since, ubbelohde viscometer is usually used for viscometric measurements, ostwald viscometer calculations are stopped at this point.

Using, $[\mu]$ obtained from Billmeyer emirical formula and Mark-Houwink relations, zimm relxation time was finally calculated for PAMH solutions. Zimm relaxation time for PAMH is approximately 2100 s. However, Rozhokov relaxation time is approximately 0.004 s. Also, a huge difference is observed between the relaxation time calculated from ostwald viscometer and ubbelohde viscometer.

There can be multiple reasons for this huge variation in relaxation time calculated from classical viscometric measurements. It is calculated based on multiple empirical formulas, which involves polymer specific constants. These constants are available only for standard

polymers. Any difference, be it molecular weight, molecular weight distribution or ionic structure can cause a large deviation in polymer specific constants. Some of the empirical formulas, inherently assume diluteness. Deviation from diluteness can give wrong answers.

Srinivas and Kumaran (2017) notes down the disadvantages of using viscometers for polymer measurements. Polymers get stretched considerably at the entry and exit of the capillary. Hence, the dynamics of the solution in viscometer could be different from that in the real flow. Also polymer molecules selectively migrate towards the center of the capillary tube. Thus the composition of the solution also could be different from that in the real flow. Also, Srinivas and Kumaran (2017) reports the differences of the order of 10^5 in relaxation time calculated from different methods. Hence, the viscometric measurements were concluded without clear results.

A set of measurements were done on PAMH polymer solution, using Anton Paar Lovis tool. Lovis is a rolling ball viscometer, which measures time required for a spherical ball to roll down the liquid column. This time required for solution is then compared with that of the solvent. By measuring the time ratio, Lovis directly gives the intrinsic viscosity. The liquid column is made from the solution whose viscosity is to be measured. The tube holding the liquid column can be tilted at different angles to change the speed of the rolling ball. Speed of the rolling ball is directly proportional to shear rate. However the results were not satisfactory, and found to deviate a lot from measurement to measurement, hence, not presented here.

2.5.5 Dynamic Light Scattering

Dynamic light scattering (DLS) measurements were carried out to measure the size of polymer molecules inside the solution. DLS gives radius of effective sphere. The size distribution of polymer solutions is shown in figure 2.25a. From DLS measurements it is clear that the polymer is not mono-disperse. Also as given by the supplier, molecular weight of PAMH polymer used in our experiments is 12 - 16 $\times$ 10^6, which also implies that the polymer is not mono-disperse. Figure 2.25b shows the size distribution for aged PAMH 25ppm solution (2 week old). Reduction in overall size of the polymer with aging, shows that the polymers breakdown with aging.

Polymer characterization was concluded with these efforts. The results obtained by rotational rheometry will be used for further analysis (Refer Table 2.2). Though it is

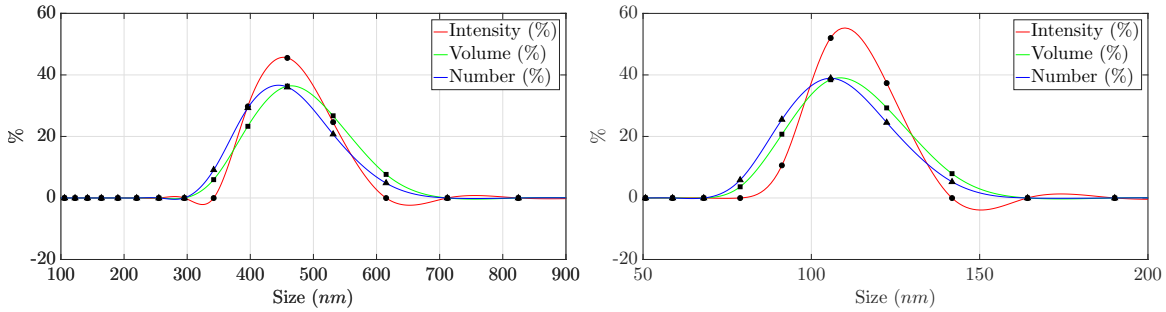

(a) PAMH 25 ppm Freshly prepared (b) PAMH 25 ppm aged

Fig. 2.25 Size distribution of polymer molecules in PAMH 25 ppm

difficult to comment about diluteness of PAMH 5 ppm and PAMH 10 ppm, we, for time being assume that they are dilute. PAMH 25 ppm falls in semi-dilute to overlap transition, and hence, won't be considered dilute. There is poly-dispersity in the polymer used, as it is evident from Dynamic light scattering measurements and also from the molecular weight given by the supplier. We, in further sections, discuss the effect of these polymers on the vortex rings, and the contribution of two competing effects i.e. shear thinning and elasticity for the changes observed.

Chapter 3

Observation

This chapter explains the experimental observations of vortex rings in water and in polymer solutions. First section presents visual differences between water and polymeric rings. Second section has the derived quantities like circulation, enstrophy and kinetic energy from PIV experiments.

3.1 Visualization

Visualization of vortex rings is carried out using two methods, (1) Dye visualization, and (2) Planar Laser Induced Florescence. The experimental setup and the methodology used are explained in sections 2.3 and 2.4.

3.1.1 Dye Visualization Experiments

Preliminary dye visualization experiments were conducted in water. Gross behavior of vortex ring wall interaction was captured using these experiments. As shown in figure 3.1a, during free-shear motion, in water, the ring structure doesn't change considerably. As vortex ring approaches the wall, it's diameter increases, and the core shrinks, which is clearly shown in figure 3.1b. There will be a growth of boundary layer on the wall, because of induced flow by the vortex ring. This boundary layer separates into secondary ring because of adverse pressure gradient (Refer figure 3.1c). Interaction between primary and secondary rings, makes primary ring to bounce back (Refer figure 3.1d). Further, there will be tertiary and many other separations. The whole flow turns turbulent because of multiple vortex interactions as shown in figure 3.1f.

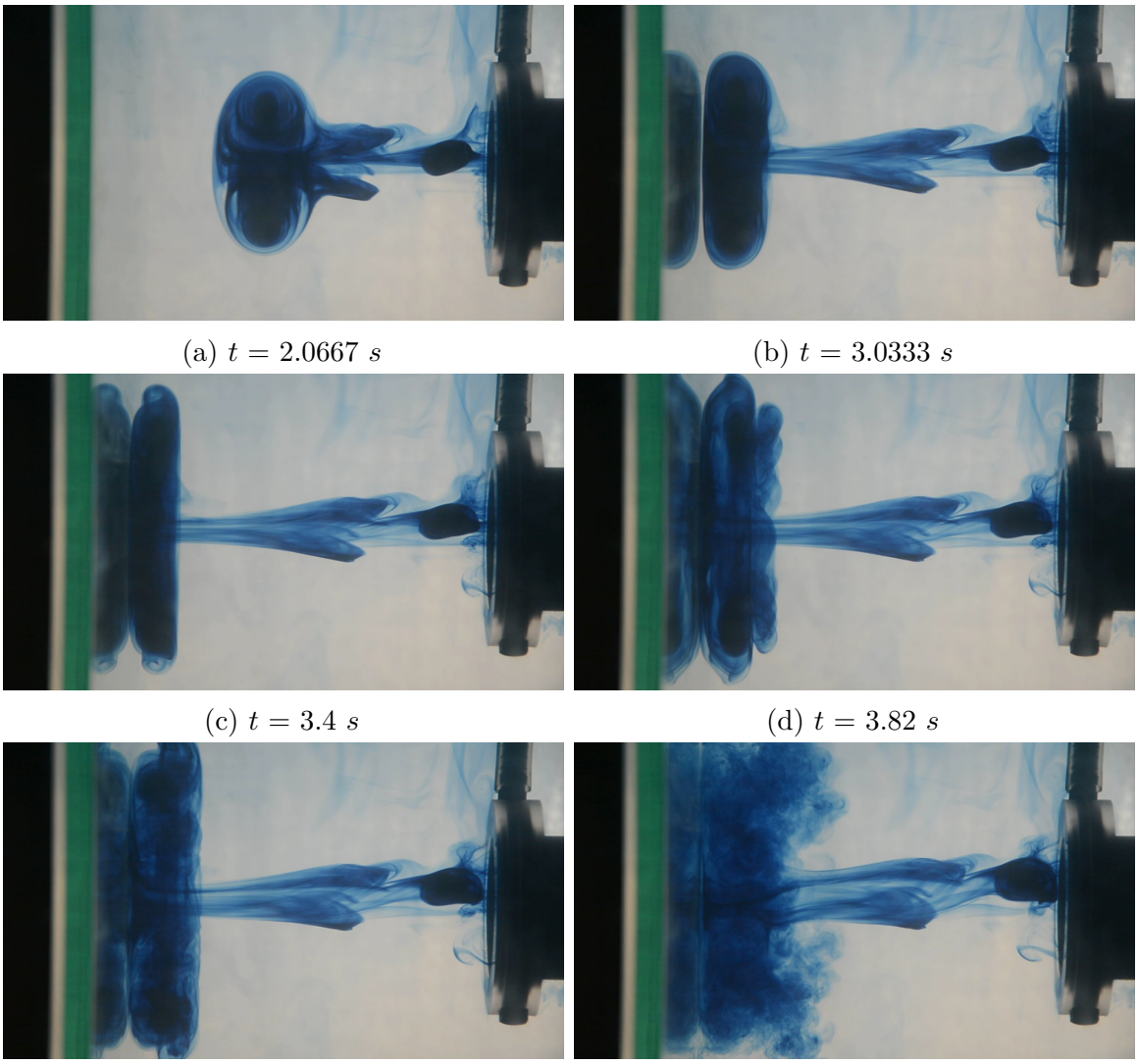

(a) $t = 2.0667\ s$ (b) $t = 3.0333\ s$

(c) $t = 3.4\ s$ (d) $t = 3.82\ s$

(e) $t = 4.4\ s$ (f) $t = 5.9\ s$

Fig. 3.1 Dye visualization showing different flow structures in vortex ring wall interaction for water L50 V100 case. Refer table 3.1 for nomenclature of experiments. Wall was placed at a distance of 150 mm (3D) from the nozzle exit. (a) Vortex ring in free shear motion (b) Vortex ring experiencing the wall, increased ring diameter, reduction in ring core size (c) Vortex ring impinging on wall. Secondary ring formation from the separated boundary layer (d) Interaction of primary and secondary ring causing the primary ring to bounce back (e) Tertiary separation (f) Turbulent flow

As it will be described in section 3.3.7, core size of vortex rings changes from thin to thick, as piston velocity increases. However, even in the case of smallest piston velocity (i.e L100 V100), in dye visualization vortex ring appears like hill's spherical vortex (Hill's spherical vortex is a limiting case of Fraenkel-Norbury vortex ring family, wherein both the cores are so thick that they are in contact with each other at the center-line). Hence, all the area occupied by dye doesn't have vorticity, and vorticity is confined to rolled-up thin sheet within the region. The whole blob of dye which moves with the ring is called vortex bubble (Sullivan et al., 2008). Hence, the method of addition of dye used in our experiments, visualizes vortex bubble rather than the vortex ring.

From the figure 3.1, it is clear that, visualization of core of the ring is harder in dye visualization. The dye added over the runs, makes the tank fluid to turn blue. Hence, in dye visualization only few runs can be carried out, once the tank is filled. Because of these disadvantages, dye visualization runs were carried out only for preliminary water experiments. However, in addition PLIF experiments were carried out for both water and polymer solutions, which are explained in the next section.

3.1.2 PLIF Experiments

PLIF experiments were conducted on different polymer solutions. Experimental methodology used here is explained in section 2.4. Figure 3.3 shows the PLIF visualization of vortex ring impinging on wall in PAMH 5ppm solution. Figure 3.2 shows the PLIF visualization of the free shear vortex ring for Water and PAMH 25ppm. Rolling up of free shear layer and the inner structure of the ring is clearly visible. As observed earlier by Shashank (2019), the gross flow differences between two solutions is clearly captured in PLIF experiments. Slowing down of PAMH 25ppm ring along with expansion in diameter is evident in figure 3.2.

PLIF experiment is used to get preliminary visualization of the flow. PLIF experiments also helped to visualize gross flow changes by addition of polymers. Distance traversed as a function of time is also obtained from the PLIF experiments using image processing techniques. PLIF experiments give qualitative idea about the flow. However, to get quantitative measurement of the flow, PIV experiments have been carried out, which are presented in the next section.

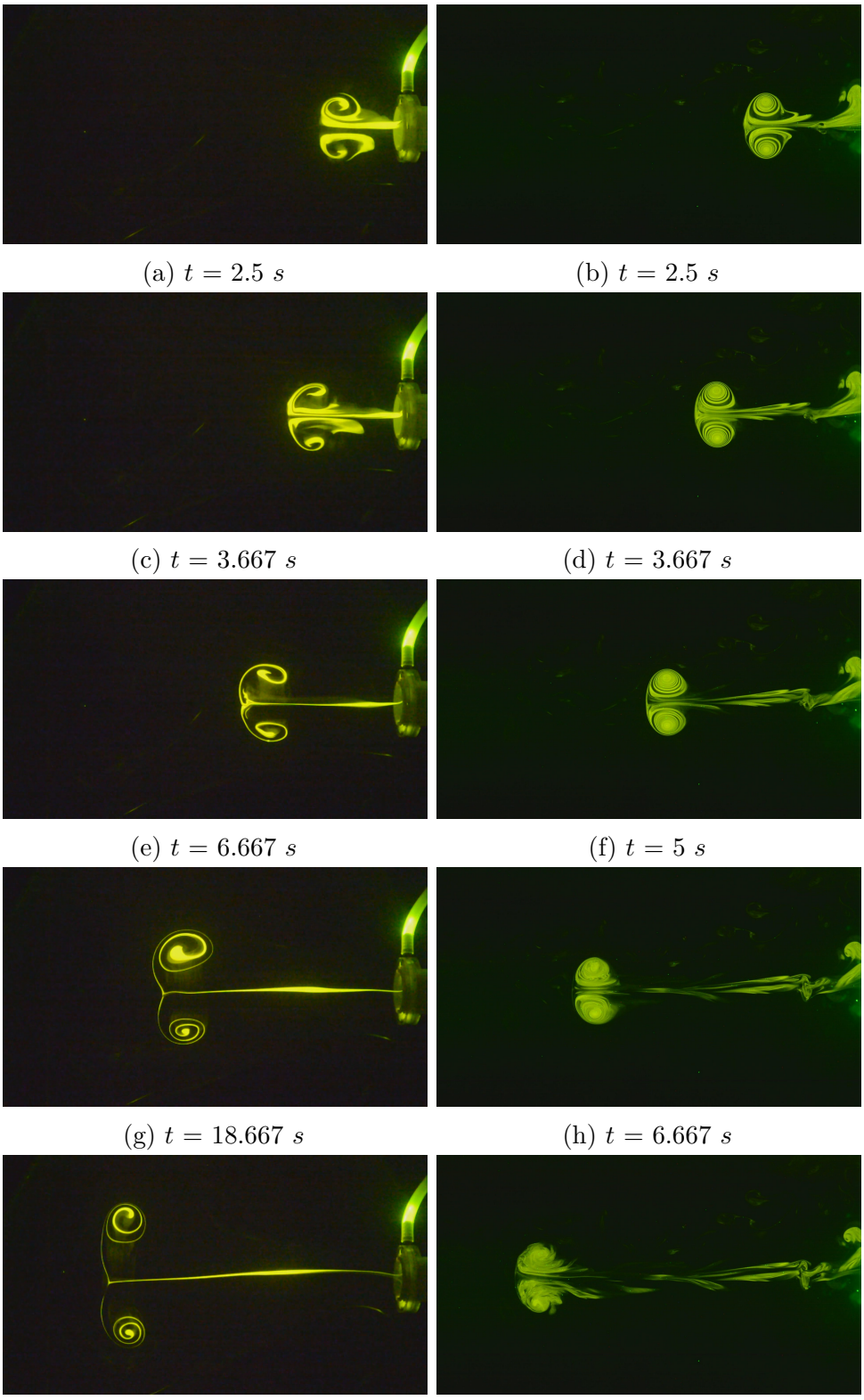

(a) $t = 2.5\ s$ (b) $t = 2.5\ s$

(c) $t = 3.667\ s$ (d) $t = 3.667\ s$

(e) $t = 6.667\ s$ (f) $t = 5\ s$

(g) $t = 18.667\ s$ (h) $t = 6.667\ s$

(i) $t = 58\ s$
PAMH 25 ppm

(j) $t = 8.333\ s$
Water

Fig. 3.2 PLIF experiments on free shear vortex ring in PAMH 25ppm and water, L100 V100 case. Images in left column corresponds to PAMH 25ppm. Images in right column corresponds to Water. Images show the inner structure of the ring. Considerable increase in diameter and reduction in velocity of vortex ring is observed in PAMH 25ppm solution as compared to water case.

(a) $t = 2\ s$ (b) $t = 5.333\ s$ (c) $t = 6.833\ s$

Fig. 3.3 PLIF experiments on vortex ring wall interaction in PAMH 5ppm, L100 V100 case. (a) Vortex ring in free shear motion (b) Vortex ring experiencing the wall, increase in diameter and reduction in core size (c) Formation of secondary ring

(a) $t = 4\ s$ (b) $t = 4.5\ s$ (c) $t = 4.72\ s$

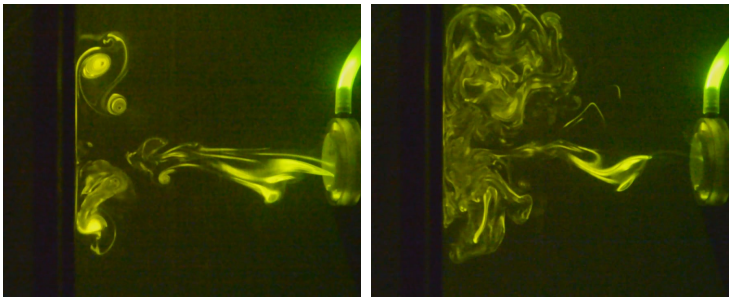

(d) $t = 5.2\ s$ (e) $t = 6\ s$

Fig. 3.4 Salient features of vortex ring wall interaction as captured using PLIF experiments. PAMH 25ppm with 10mM Salt added, L100 V100 case. (a) Vortex ring in free shear motion (b) Boundary layer separating into secondary vortex ring (c) Combined movement of primary and secondary vortex rings. Primary ring rebounds from the wall. (d) Boundary layer separating for the second time into tertiary ring (e) Chaotic flow

3.2 PIV Measurements

PIV measurements are done on vortex ring impinging on wall in water and in 5, 10 and 25 ppm of PAMH solutions. Experimental setup and the PIV methodology used are explained in section 2.1 and 2.2. A sample PIV vorticity field is shown in figure 3.5.

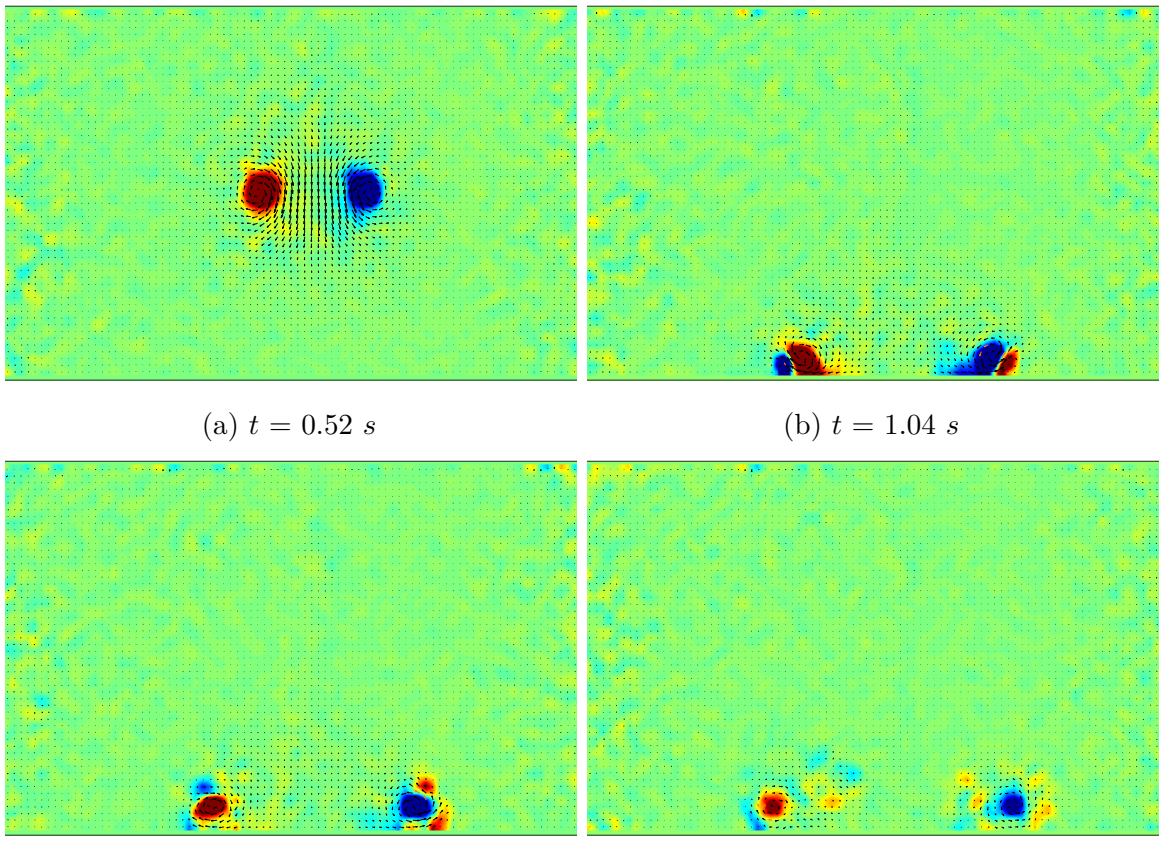

(a) $t = 0.52\ s$ (b) $t = 1.04\ s$

(c) $t = 1.12\ s$ (d) $t = 1.6\ s$

Fig. 3.5 Salient features of vortex ring wall interaction as captured using PIV experiments. PAMH 5ppm solution, L100 V500 case. (a) Vortex ring in free shear motion (b) Boundary layer separating into secondary vortex ring of opposite sign (c) Boundary layer separating for the second time into tertiary ring (d) Chaotic flow

Velocity field obtained from PIV measurements is used to calculate vorticity. Further it is used to obtain multiple other derived quantities. In-house MATLAB code was developed for processing PIV data. The quantities measured from PIV can be classified into three.

- **Field Properties.** The properties in which, they are averaged or summed over an area.

1. Circulation
2. Kinetic Energy
3. Enstrophy

- **Point Properties.** Center of core of the ring is a point having maximum vorticity. Tracking this point is used for tracking the ring. Multiple properties are obtained by monitoring core of the ring.

  1. Peak vorticity
  2. Trajectory
  3. Diameter of the ring
  4. Distance traveled

- **Ensemble averaged properties.**

  1. Reynolds stress

PIV experiments are conducted in two sets.

1. **Constant impulse.** Here the impulse given by piston cylinder mechanism is constant for all the solutions used. The properties of vortex rings in different fluids is then compared. Three cases, one for each impulse range is used in our experiments. (1) L100 V100 - Low impulse (I = 0.02827 $kgms^{-1}$) (2) L100 V500 - Medium impulse (I = 0.14135 $kgms^{-1}$) (3) L100 V1000 -High impulse (I = 0.2827 $kgms^{-1}$).

2. **Constant initial Reynolds number.** Since vortex rings is a transient flow, Reynolds number defined as, $Re = \frac{\Gamma}{\nu}$, keeps changing. Experiments are carried out with same initial Reynolds number. Properties of vortex rings generated in different fluids with same initial Reynolds number are then compared.

3.2.1 Method of calculation of different properties

In each case, atleast five runs have been carried out. The average of five runs is plotted in the figures, along with error bar. Error bar corresponds to one σ standard deviation, which has a confidence level of 68 %. Spline fit is used for plots involving distance on x-axis.

Circulation

Vorticity field was obtained from PIV velocity data. A cutoff on vorticity was put to isolate the ring from the ambient. Vorticity multiplied by the cell area is then summed over the isolated region (having vorticity higher than the cutoff). Cutoff vorticity is found by carrying out multiple trials. Cutoff vorticity of 10 s^{-1} is shown to isolate the ring region from the ambient for all the solutions to a very good extent. This method of using cutoff vorticity and then calculating circulation and enstrophy is reported by several researchers in literature (Fabris et al., 1996; Olsthoorn et al., 2014; Palacios-Morales et al., 2015; Palacios-Morales and Zenit, 2013; Weigand and Gharib, 1994). Circulation is calculated over positive vorticity core of the ring, since another core has the same circulation but with an opposite sign.

Enstrophy

Enstrophy is given by, $\int \omega^2 dA$. Enstrophy is calculated over the whole isolated vortex ring area (over both positive and negative cores). Vorticity is squared and multiplied by the cell area, and then summed over the isolated ring area.

Kinetic Energy

Kinetic energy is calculated over the whole field, using velocity field.

Peak vorticity, Distance Traveled, Diameter and Trajectory

Maximum and minimum vorticity location are determined from vorticity field. Tracing these points with time, gives distance traveled by vortex ring as a function of time. Distance between maximum and minimum vorticity locations gives diameter of the ring. Location of peak vorticity points can also be used to get trajectory. This methodology is earlier used by Fabris et al. (1996); Olsthoorn et al. (2014); Weigand and Gharib (1994) etc.

Plotting properties as a function of distance

In experiments, all different properties are measured as a function of time. Using the location of vortex ring at different time instants, these properties are then converted to a function of distance. Further spline fitting was done on data of all the five experiments. Accuracy of fit using splines is demonstrated in figure 3.6 and 3.7. All plots with distance over x-axis presented in later sections are spline curves fitted over experimental data

(Note: No fitting is used for data plotted as a function of time and non-dimensional time). Error bars represent one σ standard deviation.

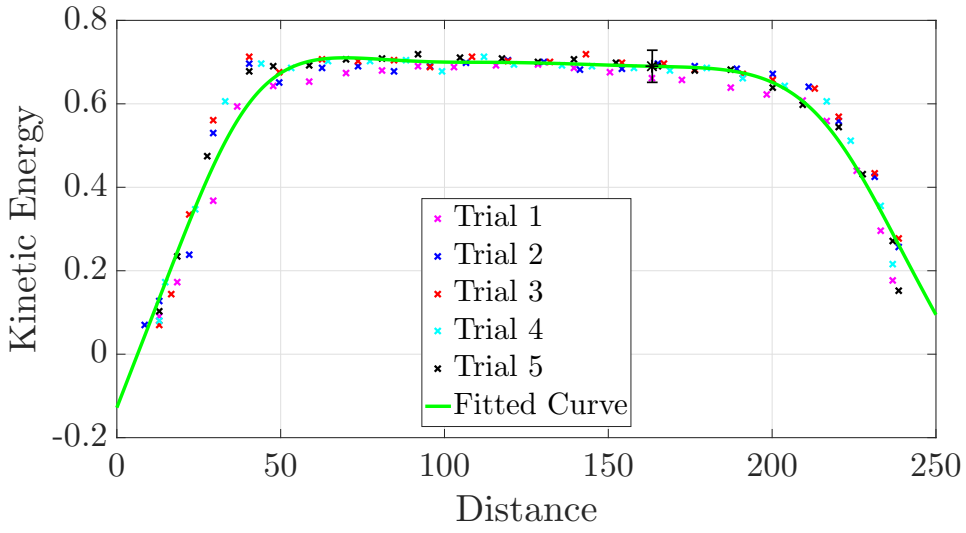

Fig. 3.6 Figure showing accurate fit using spline over data of all five experiments.

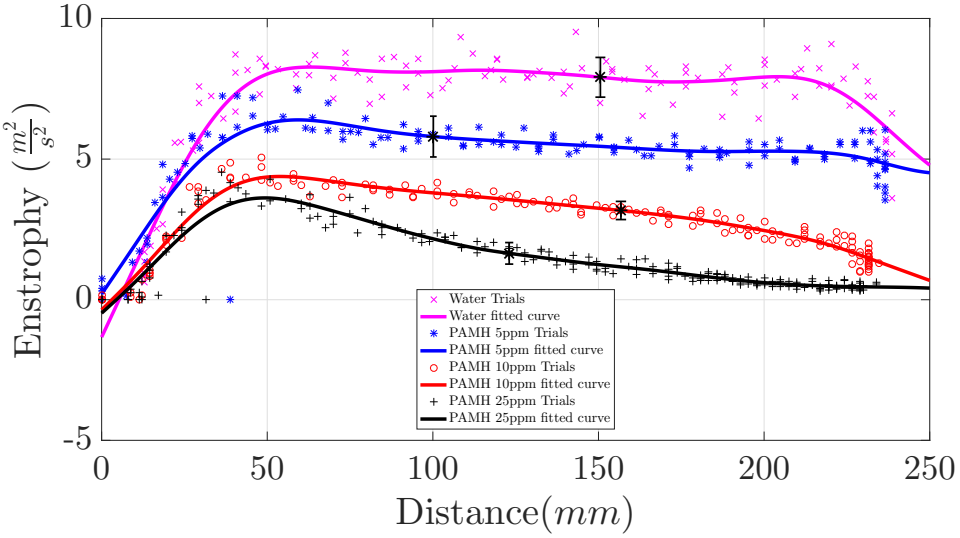

Fig. 3.7 Figure showing accurate fit using spline over data of all solutions.

PIV results obtained for different water cases is explained in section 3.3, since water forms the base case for all our polymer solution studies. In later section, PIV results of polymer solution are compared with that of water for constant impulse cases. Further down the chapter, results for constant Reynolds number experiments are explained.

3.3 Experiments in Water

Vortex ring impinging on wall experiments are carried out over a wide range of piston velocities from V 40 to V 1000, with constant stroke length L 100. Details of all water runs is given in table 3.1. Different flow properties calculated are presented in this section.

Table 3.1 Classification of experiments

Classification	**Stroke Length** (mm)	**Velocity** (mm/s)	**Name**	**approx** Re
Low impulse	100	40	L100 V40	4000
	100	86	L100 V86	8600
	100	94	L100 V94	9400
	100	100	L100 V100	10000
	100	200	L100 V200	20000
	100	300	L100 V300	30000
Medium impulse	100	400	L100 V400	40000
	100	429	L100 V429	42900
	100	471	L100 V471	47100
	100	500	L100 V500	50000
High impulse	100	857	L100 V857	85700
	100	943	L100 V943	94300
	100	1000	L100 V1000	100000

3.3.1 Circulation

Circulation is one of the most important properties of vortex ring. Re of a vortex ring is the ratio of circulation to kinematic viscosity of the solution. Circulation calculation methodology is explained in section 3.2.1. Figure 3.8, shows the three stages of circulation evolution in vortex ring impinging on wall experiments. First stage corresponds to formation of the ring. As the ring begins to form, its circulation increases, till the ring is completely formed. Many other properties of vortex ring also show the initial increase. Second stage corresponds to free shear movement of the ring. As shown in figure 3.8, during free shear movement for water rings, reduction in circulation is negligible. However at the end of free shear motion, reduction in circulation starts, which can be attributed to ring's interaction with wall. Hence, the last section of free shear motion is classified as stage 2b. In all future references, free shear motion refers to stage 2a only. Third and final stage corresponds to ring impinging on wall and final dissipation.

Even for low impulse cases, viscous dissipation of circulation during free shear motion is negligible (Refer figure 3.9a). From figure 3.9a and 3.9b, it is clear that evolution of circulation is qualitatively same for all impulses. Formation of vortex ring, is not affected from polymer addition or change in impulse. Also, impingement and dissipation stage is unaffected from polymer addition. Hence, formation stage (Stage 1) and Impingement and dissipation stage (Stage 3) is not considered in future discussions, unless something special is observed.

Circulation is non-dimensionalized ($\Gamma^* = \frac{\Gamma}{V \times L}$) using piston velocity times piston stroke-length. Variation of Γ^* as a function of piston velocity during free shear movement is plotted in figure 3.10. Initially non-dimensional circulation increases with piston velocity, and reaches maximum at around velocity of 500 mm/s. Further increase in velocity, however, reduces non-dimensional circulation of free shear vortex ring. Possible reason is that, at higher impulse, at the formation stage itself ring could be turbulent, resulting in loss of circulation. However, more experiments are needed to confirm the reasons. (Note: Non dimensional circulation shows this trend, absolute circulation monotonously increases with velocity). Though reduced Γ^* for higher impulse experiments is an interesting problem to answer, reduced Γ^* for low impulse could be an artifact of vorticity cut-off used in circulation calculation. For small impulse runs, considerable amount of vorticity falls below vorticity cut-off, thus not contributing to circulation calculation, hence, reduced Γ^* for low impulse experiments.

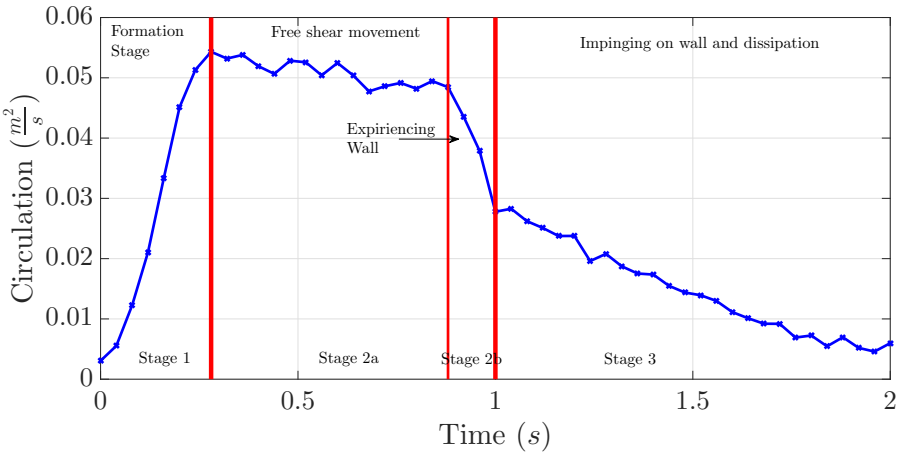

Fig. 3.8 Three stages of vortex ring wall impingement as captured using circulation plot for a typical vortex ring interacting with wall (L100-V500 case).

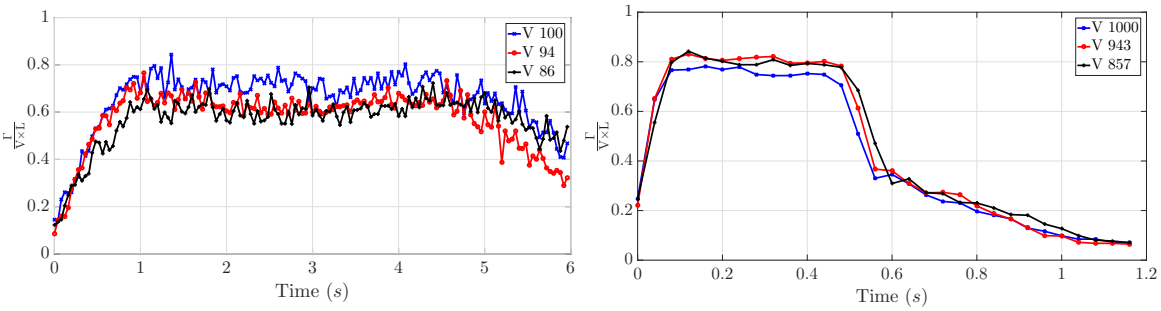

(a) Low impulse experiments

(b) High impulse experiments

Fig. 3.9 Non-dimensional circulation with time

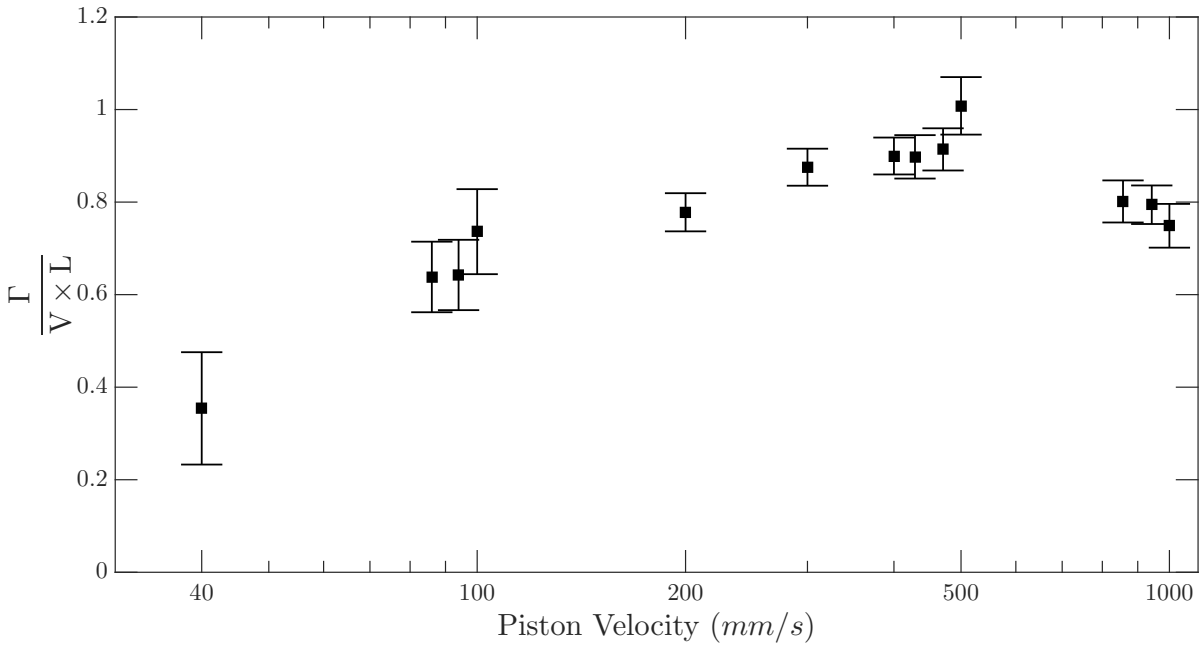

Fig. 3.10 Non-Dimensional circulation as a function of piston velocity

3.3.2 Enstrophy

Enstrophy evolution for vortex ring wall interaction experiments in water can again be classified into three stages, as it is done in the case of circulation (Refer figure 3.11, 3.13 and 3.12). Apart from stage 2b, enstrophy variation is qualitatively similar for all the experiments. However, in stage 2b, changes are observed for low impulse runs from that of medium and high impulse runs. As vortex ring starts to interact with the wall, its enstrophy reduces drastically for medium and high impulse runs (Refer figure 3.12 and 3.13). However, for low impulse runs, during vortex wall interaction and for a small time after ring impingement, enstrophy of the field increases. This increase in enstrophy is not observed in the case of medium and high impulse experiments.

Similar increase in enstrophy was also observed in vortex ring wall interaction experiments by Chu et al. (1995, 1993); Fabris et al. (1996); Olsthoorn et al. (2014)(For details, refer 1.4). According to Fabris et al. (1996), as vortex ring approaches the wall it undergoes vortex stretching, which causes enstrophy to increase. Chu et al. (1993) related enstrophy to dissipation of kinetic energy. As vortex ring impinges on the wall, there is a huge dissipation of kinetic energy which causes enstrophy generation.

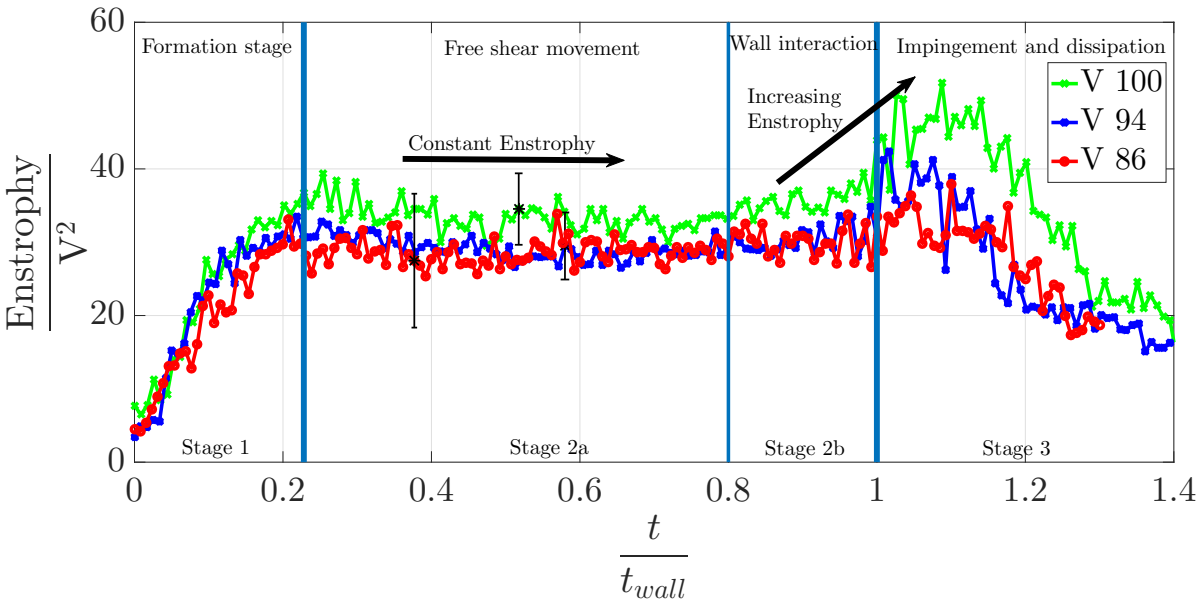

Fig. 3.11 Enstrophy evolution for vortex ring wall impingement for low impulse cases.

However, reason for absence of such an increase in enstrophy in high and medium impulse cases, is still not known. Enstrophy in our cases is calculated over the entire

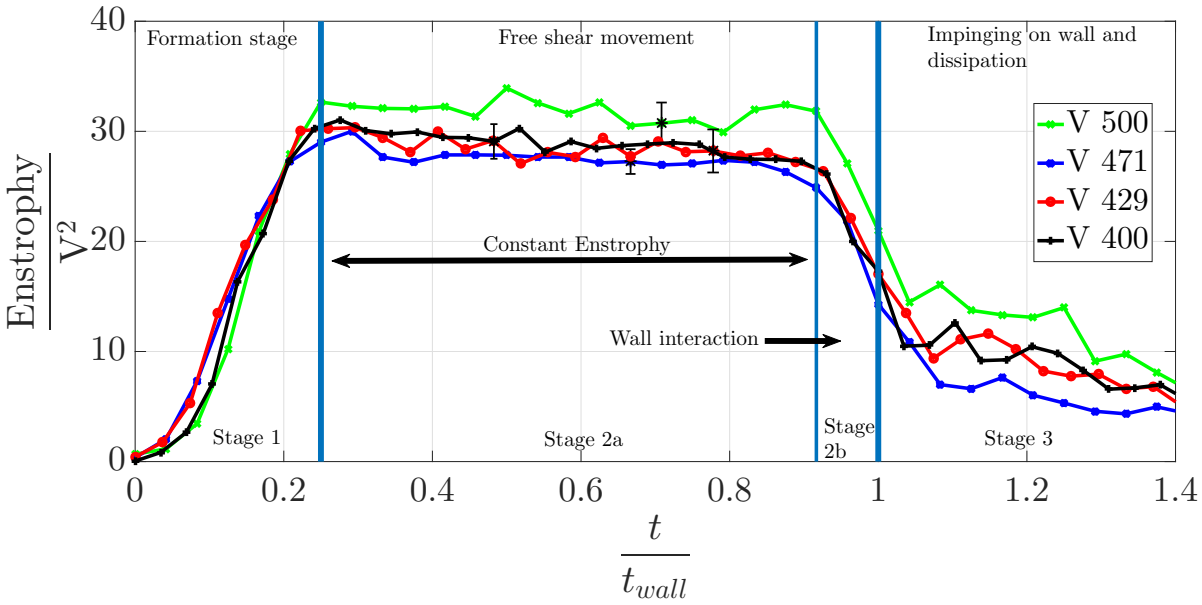

Fig. 3.12 Enstrophy evolution for vortex ring wall impingement for medium impulse cases.

field, as it is done in other reported works too. Hence, as the boundary layer appears, it also contributes to enstrophy. Because of experimental limitations and limited resolution, the contribution of boundary layer might be underestimated at medium and high impulse cases.

$$\delta \propto \frac{1}{\sqrt{Re}}$$

for laminar boundary layer, and

$$\delta \propto \frac{1}{\sqrt[5]{Re}}$$

for turbulent boundary layer over a flat plate. Hence as the Re increases boundary layer becomes thinner and thinner, making it difficult to resolve experimentally, which could be a possible reason for the above observed difference.

Apart from stage 2b, other stages show similar behavior in all the experiments. Stage 1 corresponds to formation of the ring, and the enstrophy of the field increases as the ring is getting formed. During free shear movement, dissipation of enstrophy due to viscosity is negligible. Through stage 3, as the vortex ring breaks down into small structures, because of viscosity, enstrophy gets dissipated. Enstrophy is non-dimensionalized using square of piston velocity. Non-dimensional enstrophy as a function of piston velocity is shown in figure 3.14. From figure it is clear that, the enstrophy reduces considerably for

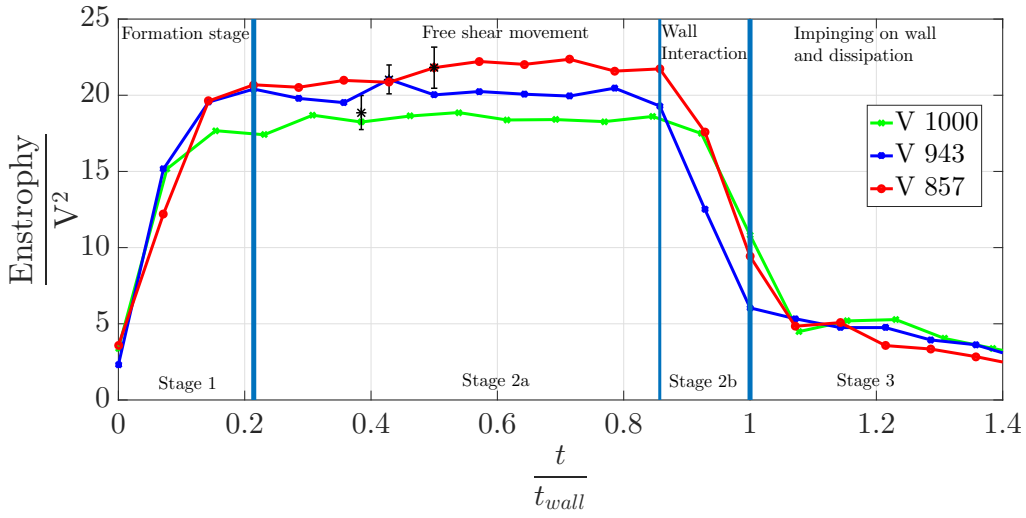

Fig. 3.13 Enstrophy evolution for vortex ring wall impingement for high impulse cases.

higher impulse cases, similar to the observations in circulation. The reason is not clear yet.

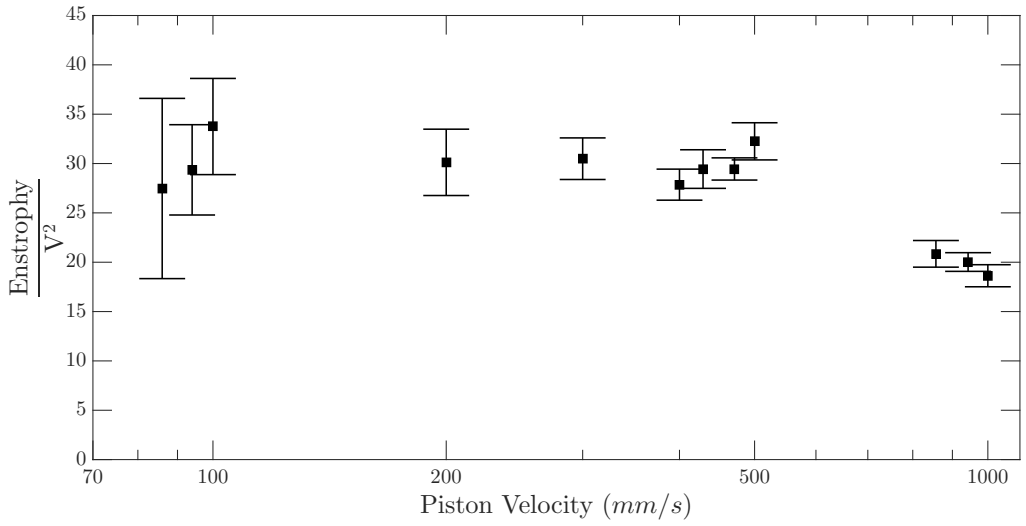

Fig. 3.14 Non-Dimensional enstrophy as a function of piston velocity. Enstrophy plotted corresponds to free shear motion.

3.3.3 Kinetic Energy

Kinetic energy of whole field also shows three distinct behavior corresponding to three stages of vortex ring wall interaction. During formation stage kinetic energy increases. During free shear movement, kinetic energy remains constant for medium and high impulse experiments, whereas a little increase in kinetic energy is observed in first half of free shear movement in low impulse experiments. A small dip in kinetic energy in the formation stage could be attributed to the formation of stopping vortex at the exit of the nozzle. Dissipation of kinetic energy due to viscosity is negligible during free shear movement.

Kinetic energy falls steeply during wall interaction. In a traveling vortex ring, maximum kinetic energy is at the center of the ring, since that is the location of maximum velocity. Presence of wall blocks this high velocity region, as ring approaches the wall, causing a steep reduction in kinetic energy.

Vortex rings induce a velocity field even upstream to their location. The presence of wall obstructs this velocity region even before it interacts with the vortex ring, causing a steep reduction in field kinetic energy. Hence, even before circulation and enstrophy, kinetic energy is affected by the presence of wall. Hence, stage 2b is wider in case of kinetic energy as compared to circulation and enstrophy. Third and the final stage involves, vortex ring breaking into small vortex structures and finally dissipating out because of viscosity, which is similar in all the experiments.

Kinetic energy is non-dimensionalized using $\frac{1}{2}\rho AV^2$. Non-dimensional kinetic energy for all the experiments is shown in figure 3.18. There is a distinct pattern in non-dimensional kinetic energy. All low impulse experiments have nearly the same non-dimensional kinetic energy (except for L100 V40), which is different from that of the medium impulse experiments. High impulse runs have considerably small non-dimensional kinetic energy. Similar reduction in non-dimensional circulation and enstrophy was also observed for high impulse runs, which suggests some kind of vortex ring saturation. However, more detailed experiments are needed to understand the reasons behind this.

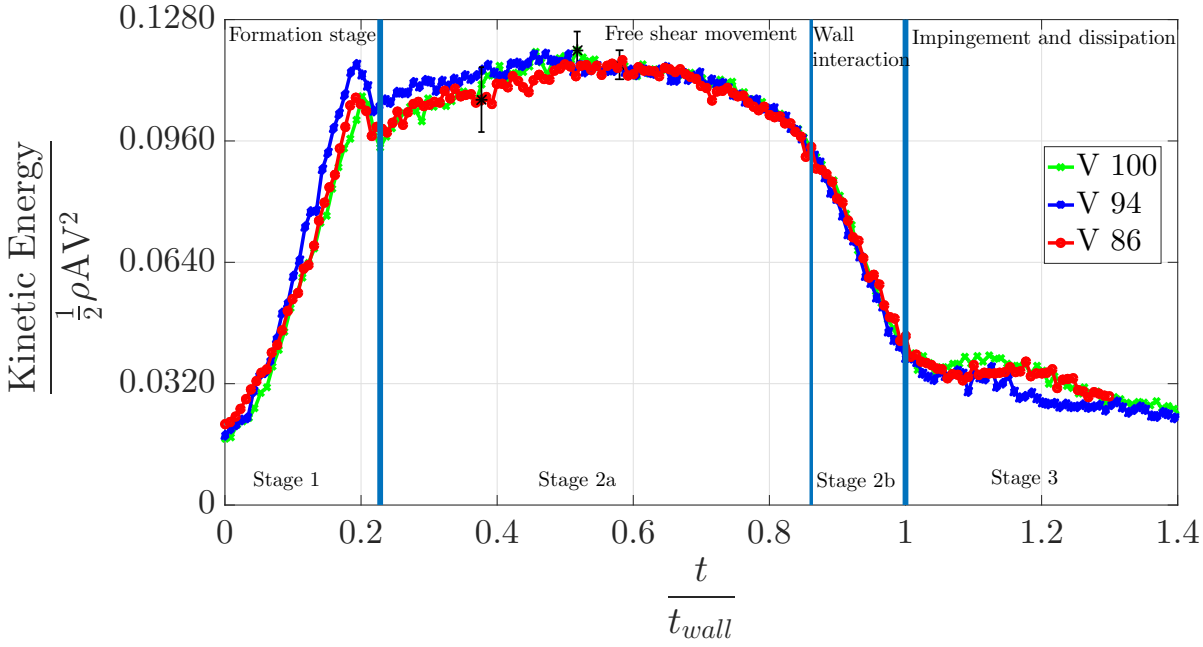

Fig. 3.15 Non-Dimensional kinetic energy for low impulse experiments.

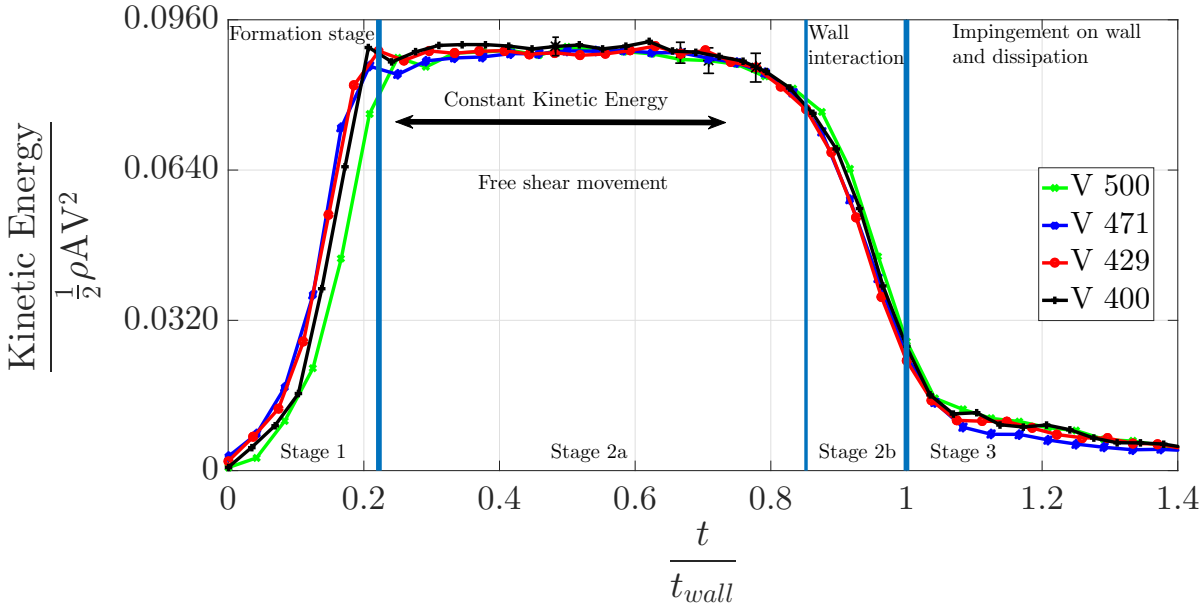

Fig. 3.16 Non-Dimensional kinetic energy for medium impulse experiments.

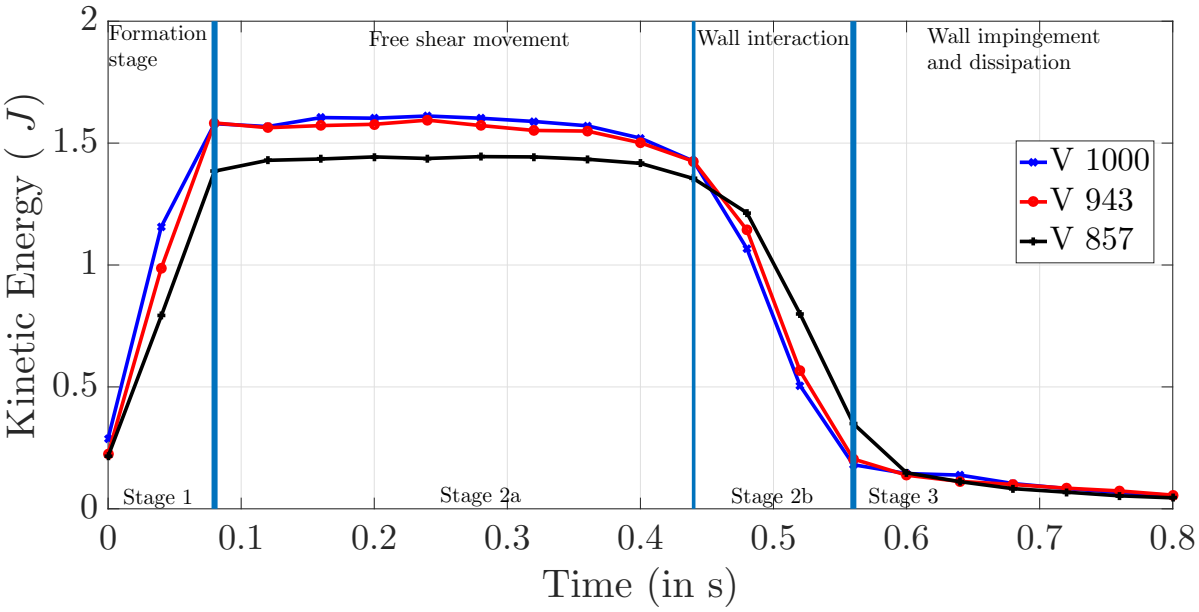

Fig. 3.17 Kinetic energy for high impulse experiments.

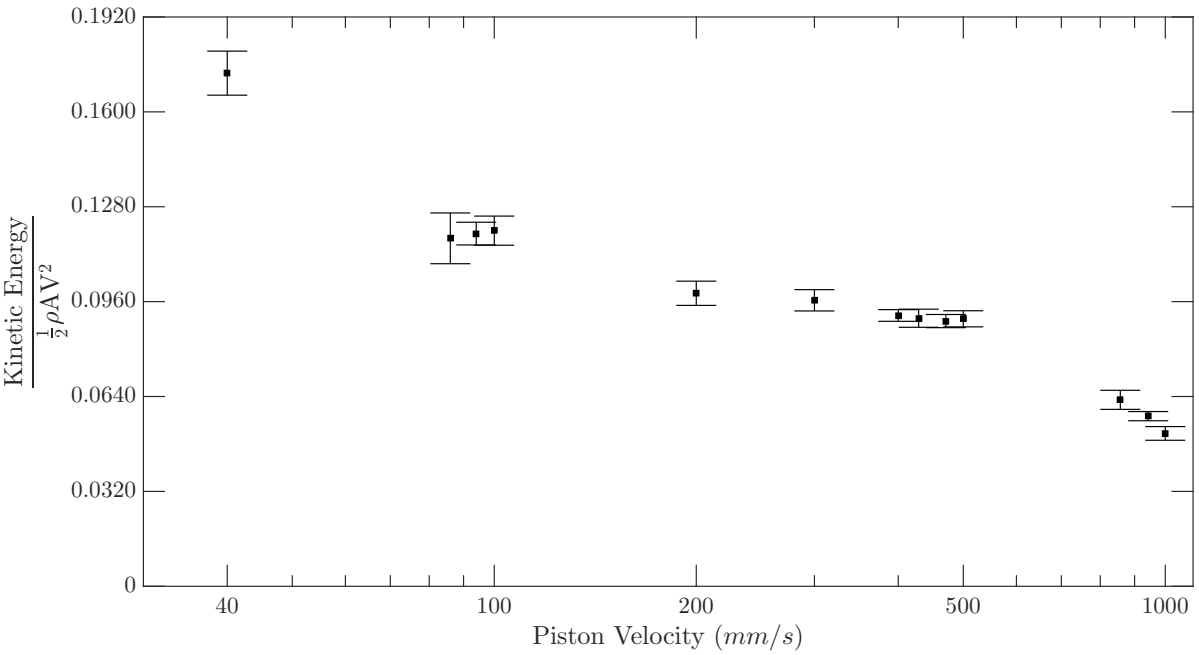

Fig. 3.18 Non-Dimensional kinetic energy for all the experiments. Kinetic energy plotted corresponds to maximum kinetic energy observed during free shear motion.

3.3.4 Peak vorticity

Location of peak vorticity is tracked to get position vs time data for vortex rings. Value of peak vorticity also shows some interesting features. From figure 3.19, 3.20 and 3.21, it is clear that, peak vorticity also shows three distinct features. Stage 1 and stage 3 are similar for all the experiments carried out. However, differences are observed in stage 2. For low impulse cases during free shear motion, peak vorticity reduces (Refer figure 3.19). This reduction can be attributed to diffusion of vorticity because of viscosity. Also, for low impulse cases, as vortex ring approaches the wall, peak vorticity increases, which can be attributed to vortex stretching. Similar increase in peak vorticity was observed by Fabris et al. (1996).

However, at medium and high impulse experiments, there is no reduction in peak vorticity during free shear motion (Refer figure 3.20 and 3.21). This is because vortex ring travels from nozzle to wall in a short time, and in that short time viscosity seems to have minimum effects. In stage 2b, for high and medium impulse experiments, there is no increase in peak vorticity. Even though both medium and high impulse rings undergo vortex stretching near wall, no increase in peak vorticity is observed, instead a reduction in peak vorticity is observed. Reason for this anomalous behavior is not yet known.

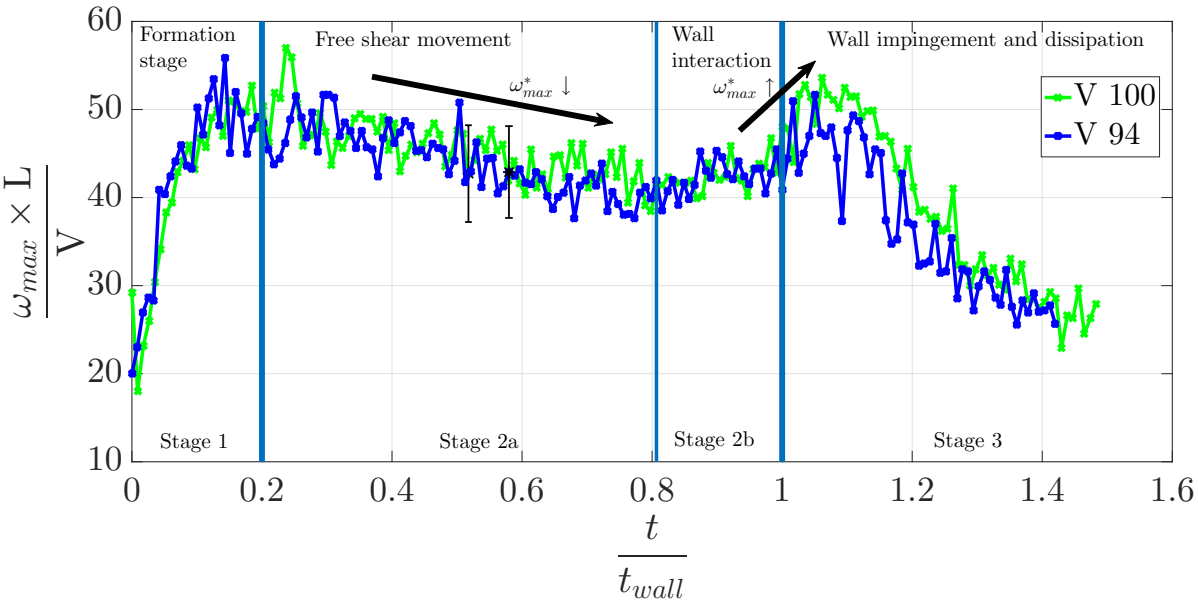

Fig. 3.19 Peak vorticity for low impulse experiments

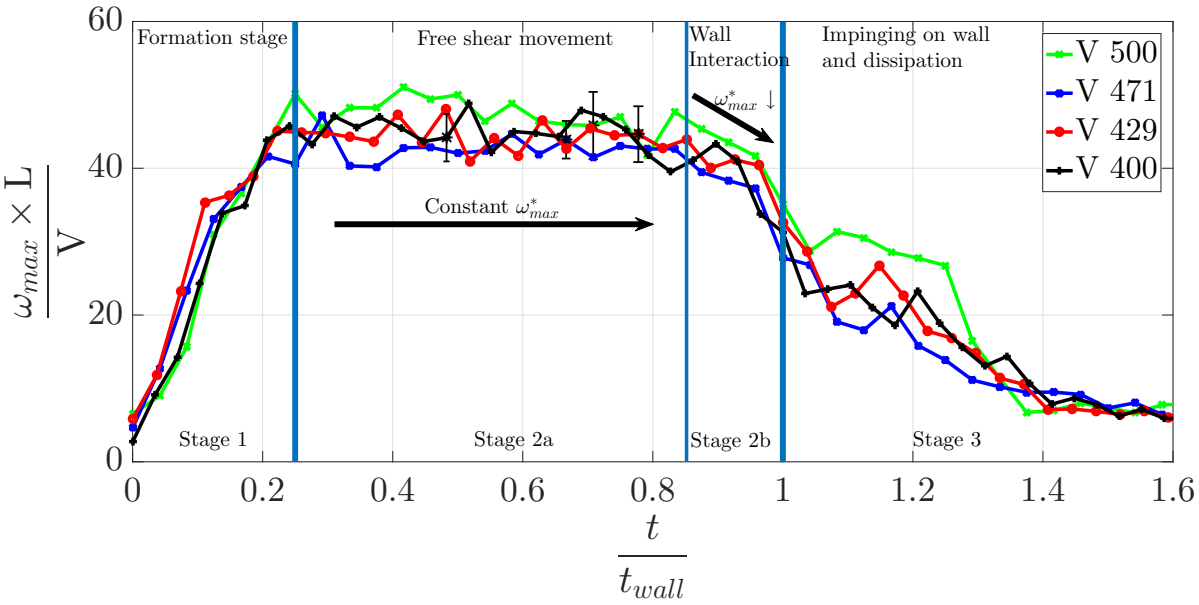

Fig. 3.20 Peak vorticity for medium impulse experiments

Peak vorticity is non-dimensionalised using $\frac{V}{L}$. Non-dimensional peak vorticity for all experiments is plotted in figure 3.22. As observed in enstrophy and kinetic energy plots, non-dimensional peak vorticity too is considerably small for high impulse experiments compared to low and medium impulse experiments, reinforcing the reasoning that there is some kind of vortex ring saturation at high impulse runs.

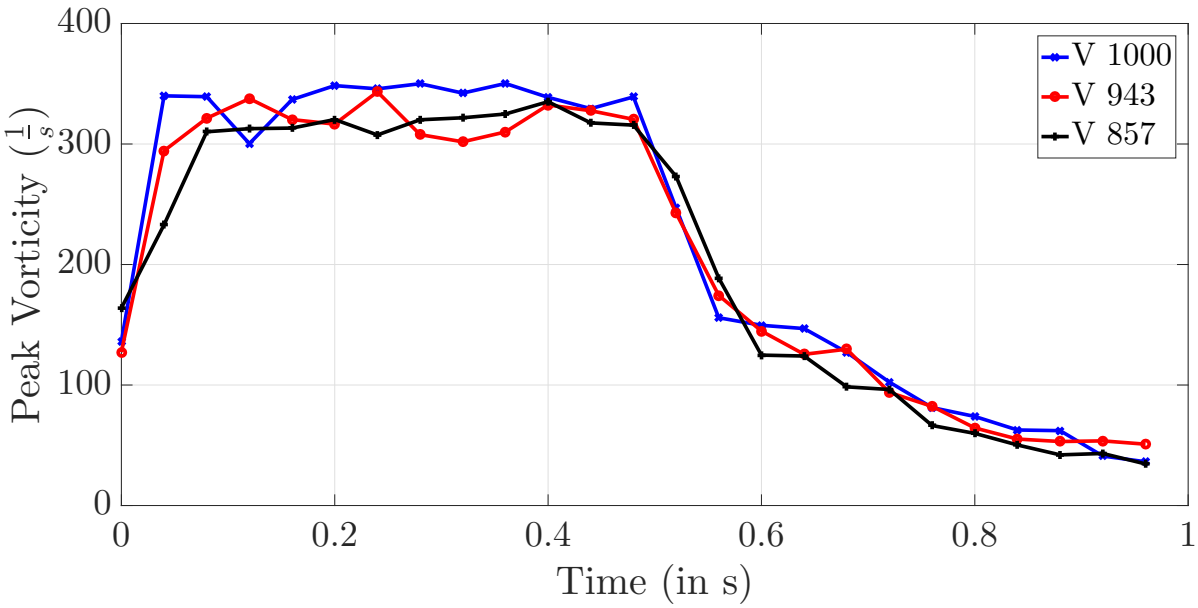

Fig. 3.21 Peak vorticity for high impulse experiments

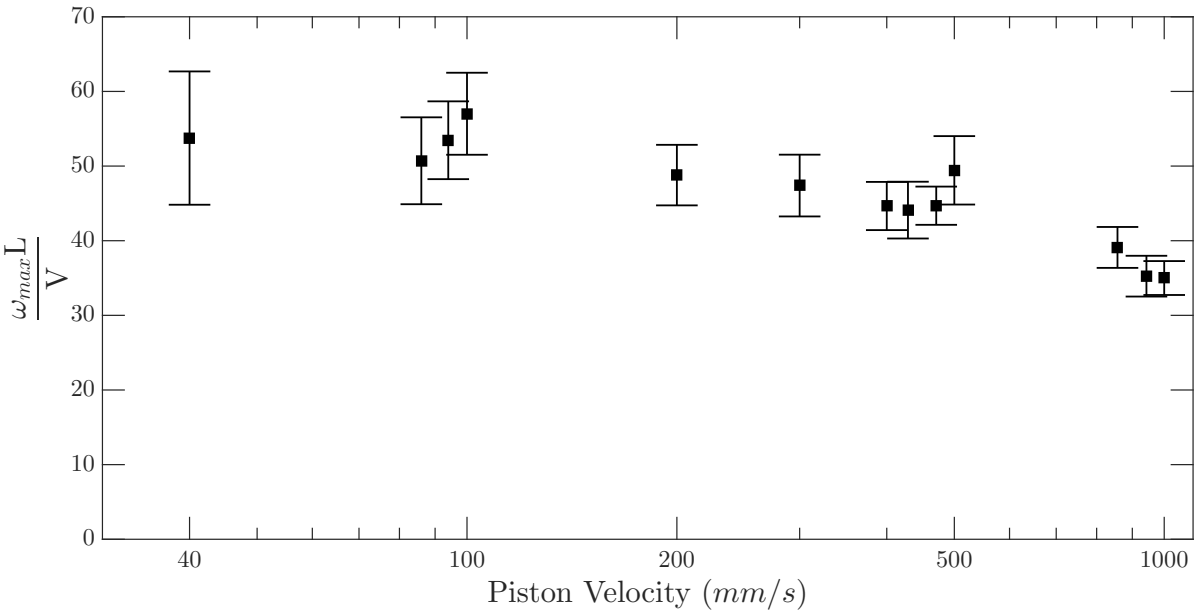

Fig. 3.22 Peak vorticity for all experiments

3.3.5 Distance vs Time

Distance traveled as a function of time is an important property of vortex rings. It is a function of translational velocity which in turn is a function of circulation, vorticity distribution, core diameter and ring diameter. Hence any significant changes in any property of vortex ring, will effect distance versus time plots. Also, this is a property which can be visualized with ease, without much of data analysis. Less amount of data analysis involved, makes distance versus time plots more foolproof.

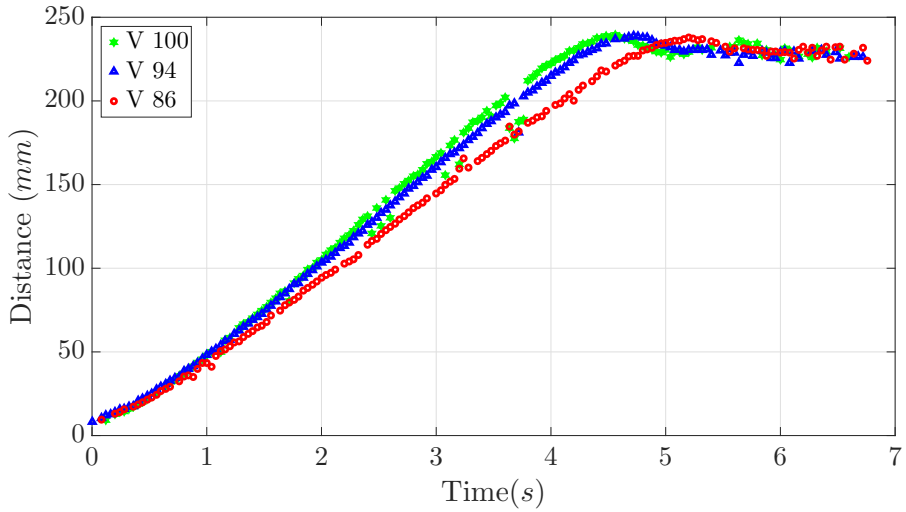

(a) Dimensional Time

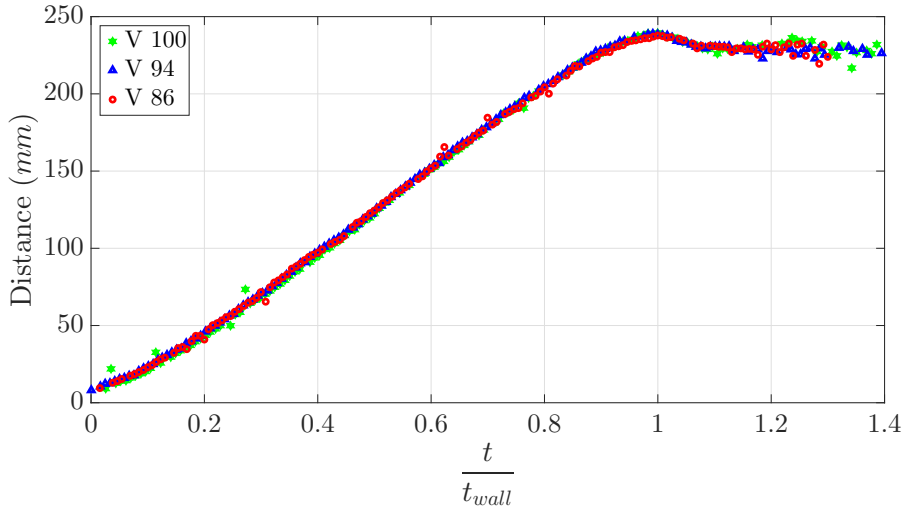

(b) Time is non-dimensionalized using t_{wall}

Fig. 3.23 Distance traveled by vortex ring as a function of time for low impulse experiments.

Figure 3.23a shows distance traveled by vortex ring. As the piston impulse increases, vortex rings reach the wall in a shorter time. Also, translational velocity of vortex rings is a function of piston velocity. However, when time axis is non-dimensionalised by t_{wall}, all plots collapse to a single curve (Refer figure 3.23b). This shows that, non-dimensionalising time by t_{wall} is valid throughout vortex ring wall interaction, not just in near wall region.

There is no distinct formation stage observed in distance plots as shown in figure 3.23. Stage 1 and Stage 2a show linear relation between distance traveled and time, which implies constant translational velocity. Translational velocity of vortex ring during free shear movement calculated from distance versus time plots, show some interesting behavior (Refer figure 3.24). For low impulse experiments $\frac{U}{V} \approx 0.58$ (U is translational velocity of vortex ring, V is piston velocity). For medium impulse experiments $\frac{U}{V} \approx 0.56$. However for high impulse experiments this ratio starts to drastically reduce, reaching $\frac{U}{V} = 0.46$ for V 1000 case. This reduction in non-dimensional translational velocity again shows some kind of saturation at higher impulse.

As the vortex ring approaches the wall, it starts to slow down and finally stops. Distance from wall where the ring stops is nearly the same for all water experiments. From figure 3.23, rebounding of vortex ring is clearly visible. Similar behavior is observed in all experiments (Refer figure 3.25 and 3.26).

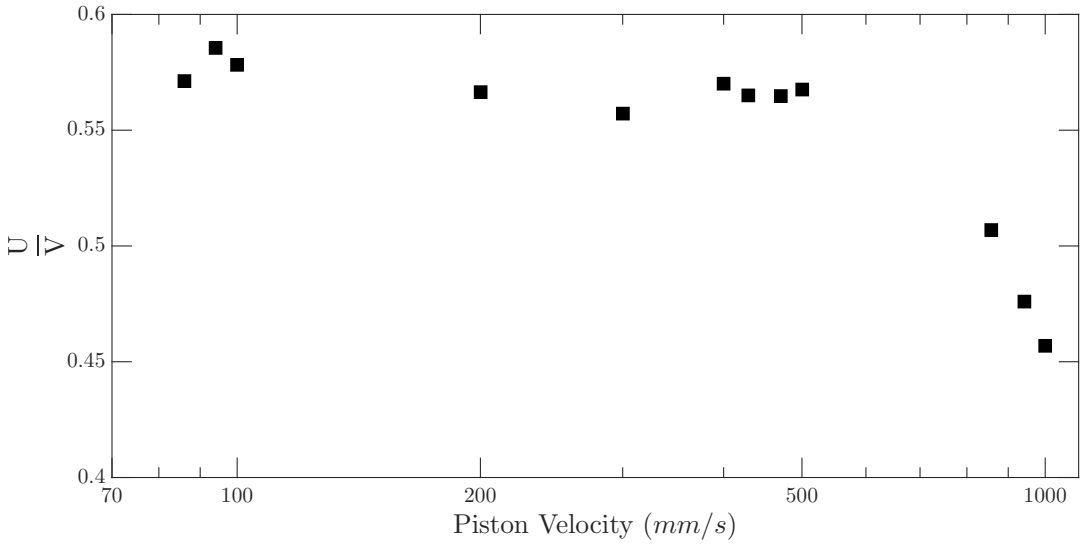

Fig. 3.24 Non-dimensional translational velocity of vortex rings for all experiments

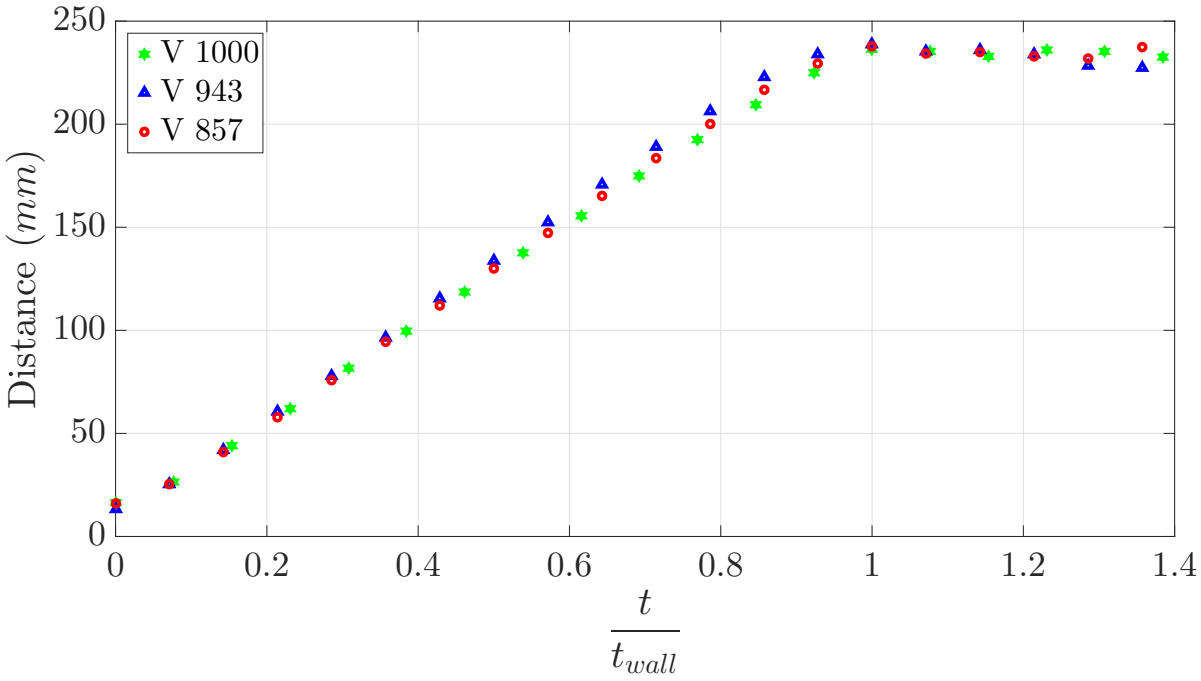

Fig. 3.25 Distance vs Time plot for medium impulse experiments

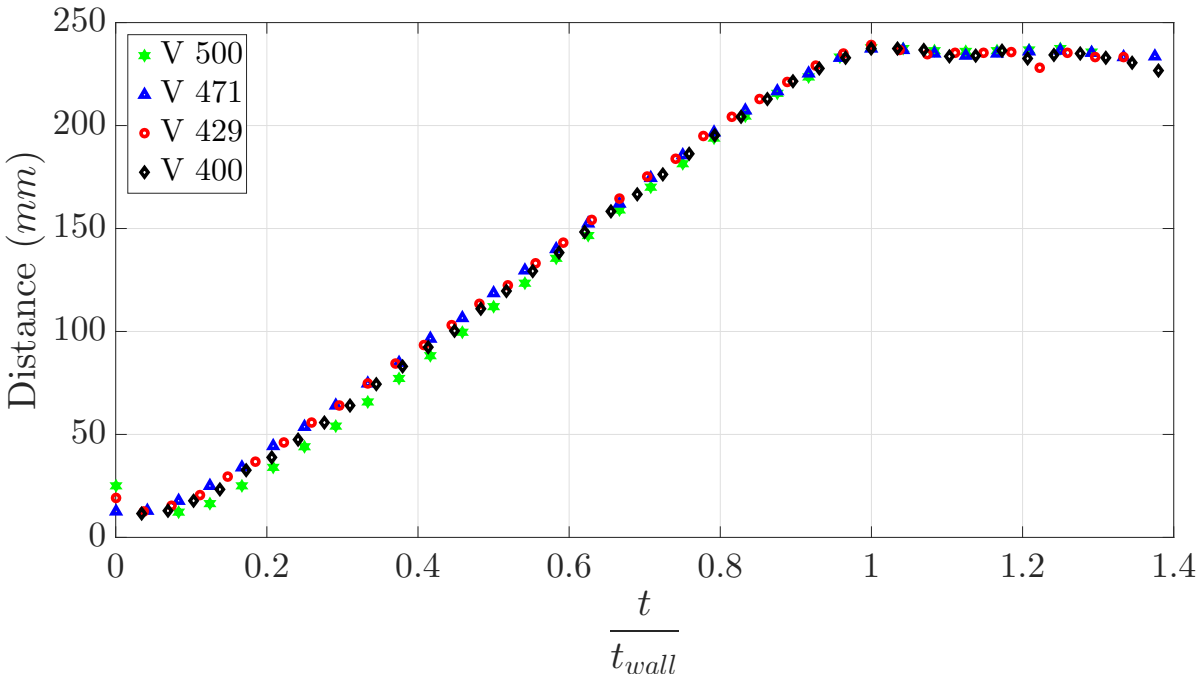

Fig. 3.26 Distance vs Time plot for high impulse experiments

3.3.6 Diameter

Diameter of vortex ring shows three stages of evolution. Figure 3.27 summarizes variation of diameter. During formation of the ring, for the initial short duration, diameter increases. However, throughout free shear motion, diameter remains constant for all experiments. During free shear movement $\frac{D_{ring}}{D_{nozzle}} = 1.4$, which is in agreement with Weigand and Gharib (1994). As the ring approaches wall, velocity of vortex ring reduces. Hence diameter suddenly starts to increase to conserve angular momentum, which is in agreement with earlier studies on vortex ring wall interaction (Chu et al., 1993; Doligalski et al., 1994; Fabris et al., 1996; Naguib and Koochesfahani, 2004; Orlandi and Verzicco, 1993; Walker et al., 1987). Diameter continues to increase during stage 3. Observations are very similar for all experiments in water.

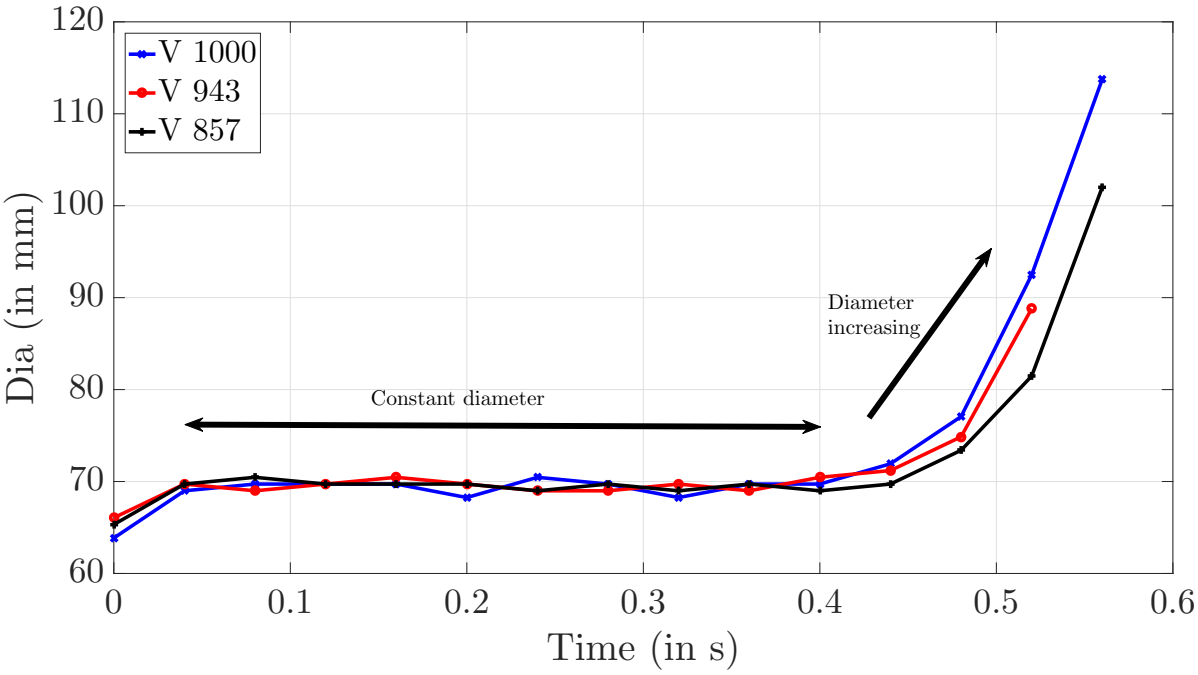

Fig. 3.27 Diameter of vortex ring

3.3.7 Core Size

Ratio of core radius (a) to ring radius (R) of vortex ring is an important property which determines behavior of vortex rings. In literature, vortex rings with $\frac{a}{R} \leq 0.3$ are referred to as thin core rings (Jha and Govardhan, 2015; Sullivan et al., 2008), and all other rings are referred as thick core vortex rings. Variation in vortex ring

core-size happens over three distinct stages, similar to other properties. Core size increases as vortex ring is getting formed. Changes in core size during free shear motion is negligible. After wall collision, as ring gets destroyed, vortex ring core area also reduces.

However, interesting changes in core size is observed as the piston velocity increases. As shown in figure 3.28, vortex ring core size increases with increase in piston velocity. Hence, vortex rings show a gradual transition from thin core to thick core with increase in piston velocity.

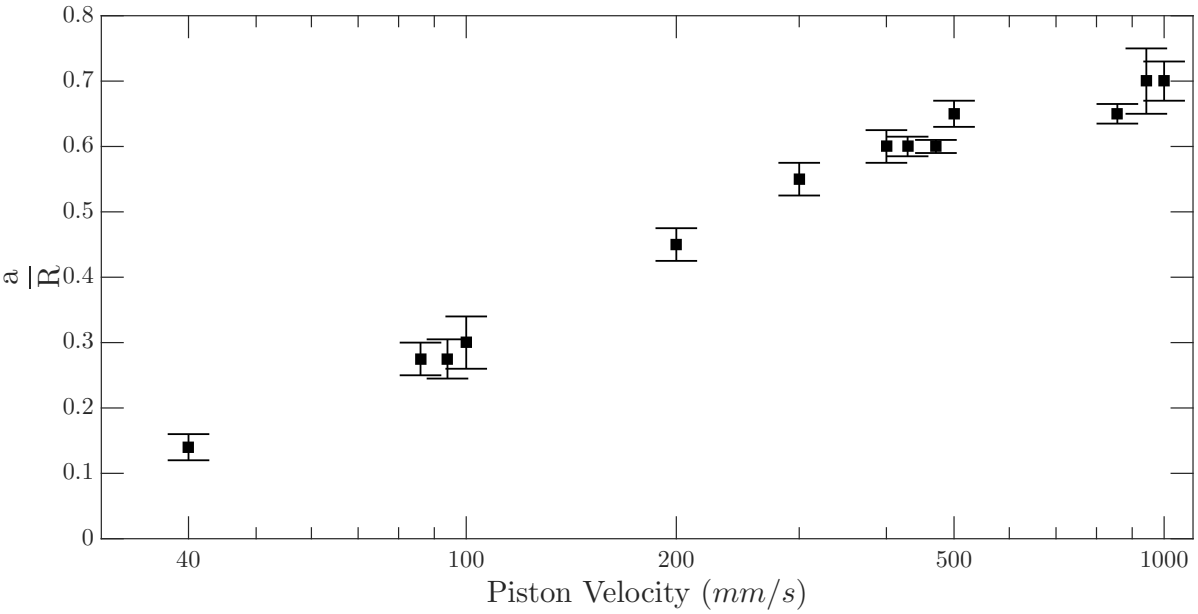

Fig. 3.28 $\frac{a}{R}$ for vortex rings as a function of piston velocity, showing gradual transition from thin core to thick core rings as piston velocity increased.

According to Norbury family of vortex rings (Norbury, 1973), for the same impulse provided, thick-core rings have higher $\frac{U}{V}$ than thin-core rings. But the opposite is observed in figure 3.24. However, it has to be kept in mind that in these experiments, impulse provided is different, hence, is not a fair comparison. (To have a fair comparison, we need to generate both thin and thick core rings from the same input impulse, and then compare their velocity). Along with it, there is an additional phenomena of increased turbulence intensity at higher impulses. Hence, the deviations observed in figure 3.24.

3.4 Constant Impulse Experiments in Polymer Solutions

In these experiments, impulse given by piston cylinder mechanism is same for all the solutions used. Properties of vortex rings in different polymer solutions is then compared with water. Same impulse here refers to same piston input i.e. same stroke length (L) and velocity (V) of piston movement. Hence, it should be noted that, circulation defined as, $\Gamma = L \times V$, will have the same value for vortex rings in all solutions at the initial stage. However, initial Reynolds number, defined as, $Re = \frac{\Gamma}{\nu}$, will have different values, because of difference in kinematic viscosities of polymer solutions. Constant initial Reynolds number experiments were also carried out, which are presented in section 3.5.

Three cases, one for each impulse range is used in our experiments. (1) L100 V100 - Low impulse (2) L100 V500 - Medium impulse (3) L100 V1000 - High impulse.

3.4.1 Circulation

Three stages of circulation evolution was described for water experiments in section 3.3.1. Similar to water experiments, polymer solutions also show three distinct stages for circulation, i.e. formation, free shear movement, wall interaction and dissipation (Refer figure 3.29, 3.30 and 3.31). Velocity of vortex ring in 10 and 25ppm of polymer solutions changes significantly during free shear motion and is smaller than water. Hence, eventhough the rings are generated with the same impulse, time it takes to impinge on wall will be different depending on the solution in which it is generated (From figure 3.29 it is clear that sharp reduction in circulation occurs at different time). Hence, three stages of circulation evolution will occur at different time intervals for different polymer solutions.

To overcome this, time axis is non-dimensionalized using t_{wall}, and the non-dimensional plot is shown in figure 3.30. However, velocity of translation is not constant. Hence, uniform scaling with t_{wall} is still not appropriate. Hence, plotting circulation as a function of distance is more appropriate (Refer figure 3.31). Enstrophy, kinetic energy and other properties also show distinct stages when plotted against distance, instead of time.

During formation stage for low impulse cases, though the impulse provided is same, vortex ring in PAMH 10ppm solution has considerably small circulation (Refer figure

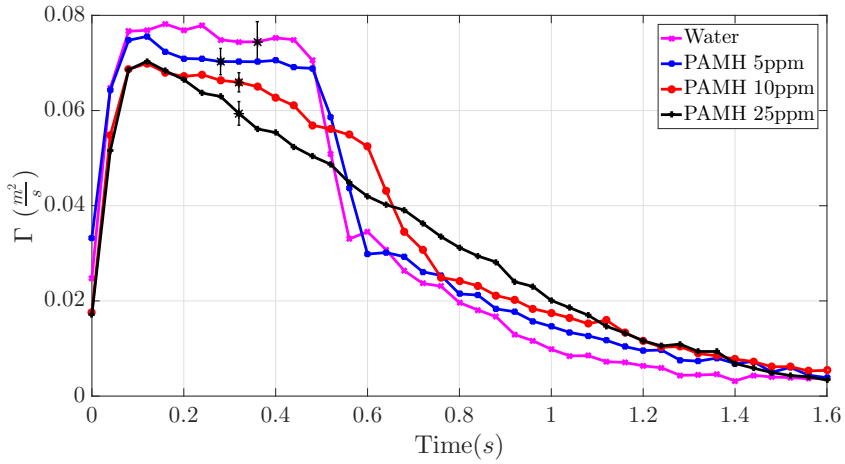

Fig. 3.29 Circulation vs Time for V1000 case

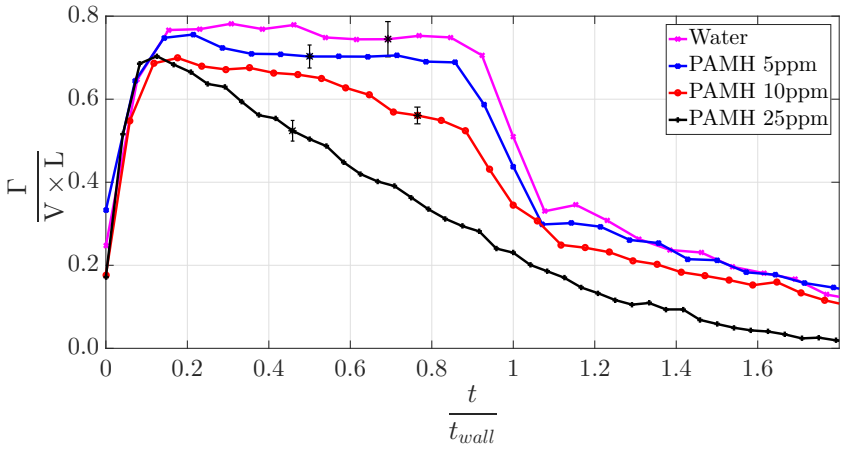

Fig. 3.30 Non-dimensional Circulation vs Time for V1000 case

3.32). However, for medium and high impulse cases, circulation of vortex ring at the end of formation stage in all the solutions is nearly the same (Refer figure 3.31). In low impulse experiments, time required for formation of ring is quite large, and during formation itself ring looses circulation due to increased viscosity of polymer solution, is a possible reason for this anomalous behavior at low impulse.

During free shear movement, circulation of vortex ring in water is nearly constant for all range of impulses. However, in polymer solutions, it varies depending on impulse and the solution concentration. Vortex rings in PAMH 25ppm solution show reduction in circulation in all the experiments as shown in figure 3.31 and 3.32. Vortex rings in PAMH 10ppm also show reduction in circulation during free shear motion, but to lesser extent as compared to PAMH 25ppm. However, vortex rings in PAMH 5ppm, show

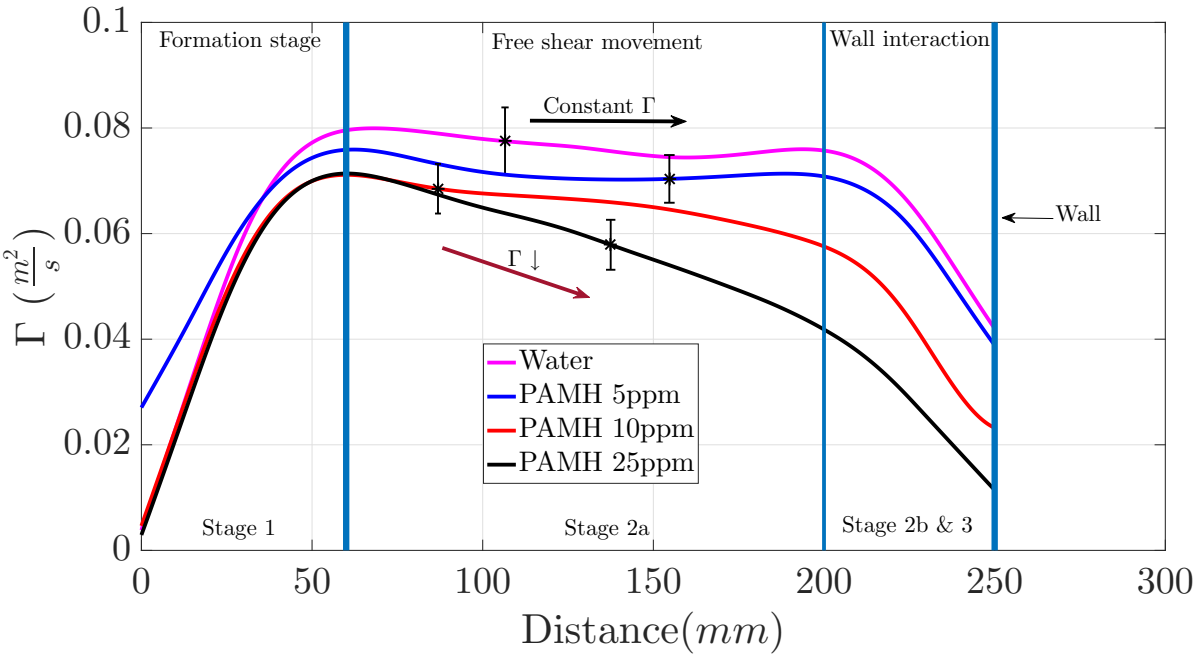

Fig. 3.31 Circulation vs Distance for V1000 case

reduction in circulation only for V100 case, and shows negligible reduction in circulation for V500 and V1000 cases.

Changes in circulation during free shear movement can be explained by the increased viscosity of polymer solutions. Traveling vortex ring is surrounded by ambient fluid which is at low shear rate and hence higher viscosity. η_0 of PAMH 25ppm solution is 20-60 times that of water, which causes higher viscous dissipation of circulation at the edges of the ring. This reduction in circulation makes the ring to move slower, thereby reducing shear rate inside the ring, which aids viscous dissipation further through increased viscosity. This mechanism of viscous dissipation of circulation could be the reason for reduction in circulation of PAMH 10ppm and PAMH 5ppm rings too. Also the rate of circulation reduction is more for higher viscosity solution. However, as the impulse increases, vortex rings travel faster, hence, time available for viscous dissipation reduces. This explains less reduction in circulation at V1000 compared to V100 experiments.

Elasticity is another additional property present in polymer solutions compared to water, hence, another contender for this reduction in circulation. However, elasticity is more prominent at high shear rates than low shear rates. If elasticity was the primary reason for reduction in circulation, V1000 should have shown greater reduction than V500 and V100 cases, because of higher shear rates involved. However, that is not the

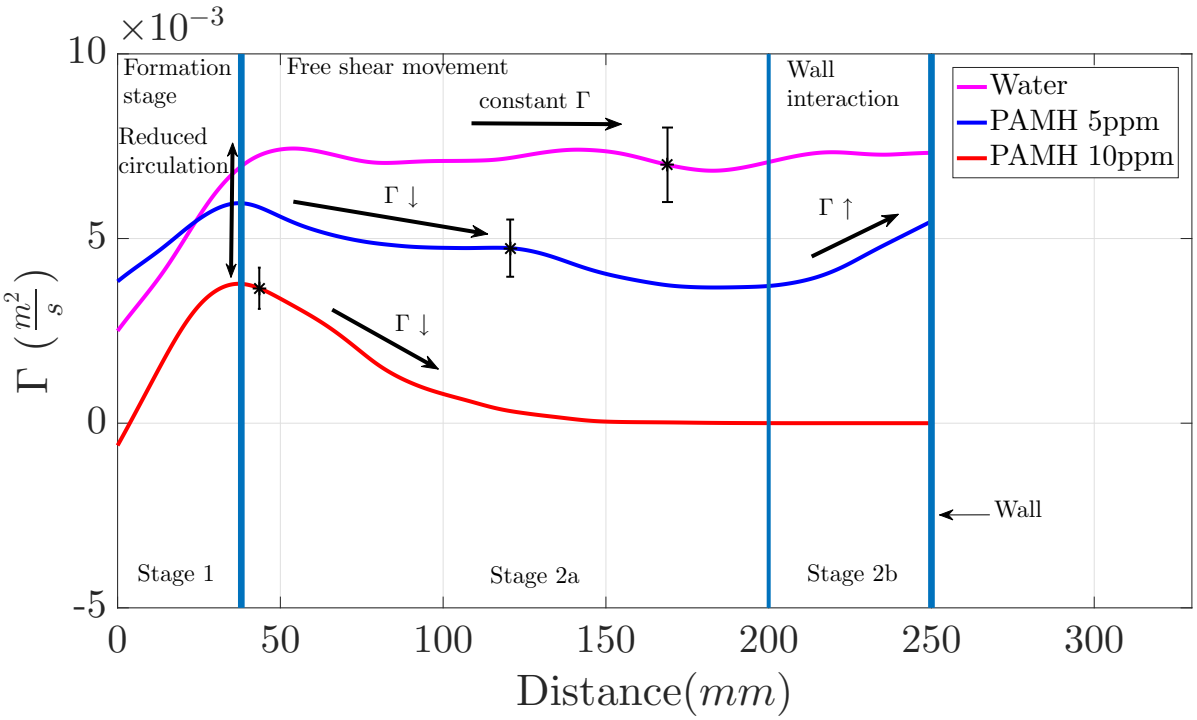

Fig. 3.32 Circulation vs Distance for V100 case

case, and reduction for V100 is far more significant than V1000 case, thereby ruling out the elasticity as the primary reason.

As the vortex ring approaches wall, circulation drastically reduces as the primary vortex ring breaks into smaller vortex structures, and finally gets dissipated because of viscosity. However, only exception for this behavior is seen in the case of PAMH 5ppm solution for V100 case, where circulation increased as the ring approaches wall (Refer figure 3.32). The reason for this is not clear.

Conclusion is that as the concentration of polymer solution increases, deviation from water also increases. Major difference is observed for PAMH 25ppm solution during free shear movement. PAMH 25ppm also showed deviation at formation stage for low impulse case. Near wall effects on vortex ring circulation is all similar to water except for PAMH 5ppm V100 case. Details of near wall measurements are limited by resolution of PIV experiments.

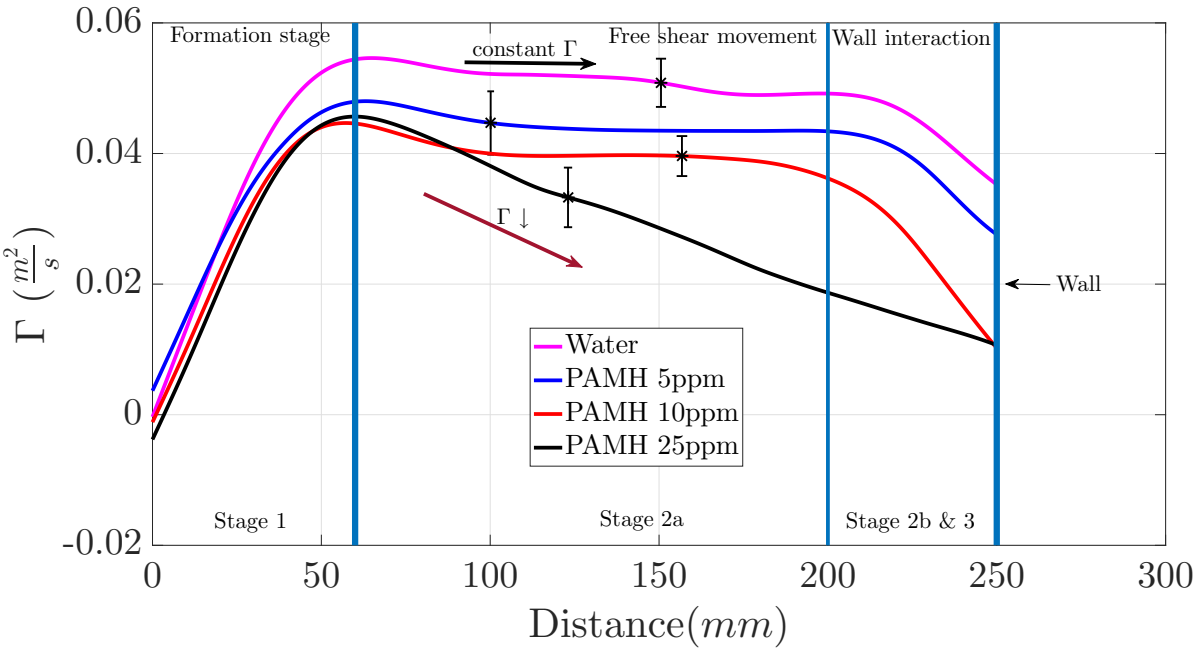

Fig. 3.33 Circulation vs Distance for V500 case

3.4.2 Enstrophy

Enstrophy behavior can be classified into three distinct stages for vortex ring wall interaction in polymer solutions too, as it was done in the case of water. Method of calculation of enstrophy is explained in section 3.2.1. At the end of formation stage, enstrophy values for vortex rings in polymer solutions are smaller than that of water for all the experiments (Refer figure 3.35a, 3.35b and 3.35c). However, circulation at the end of formation stage is nearly the same for polymer and water rings (except for PAMH 10ppm V100 case). Hence, difference in enstrophy though the circulation is same, implies that the vorticity distribution over the ring is different for polymer solutions as compared to water.

Reduction in enstrophy is used as a measure for drag reduction. Addition of polymers seems to modify the vorticity distribution inside vortex structures, which could have potential connection with polymer drag reduction phenomena. However, PIV experiments with better resolution is necessary to make a clear conclusion.

During free shear movement negligible reduction in enstrophy is observed for vortex rings in water as explained in section 3.3.2. However, significant reduction in enstrophy is observed for vortex rings in polymer solutions during free shear movement (Refer figure 3.35a, 3.35b and 3.35c). As the concentration of polymer solution increases, more reduction in enstrophy is observed. Also, the rate of reduction of enstrophy increases with concentration of polymer solution, i.e. PAMH 25ppm being the largest concentration shows the steepest reduction in enstrophy.

Reduction in enstrophy during free shear motion could again be attributed to increased viscosity of polymer solutions. Increased viscosity of polymer solutions cause faster dissipation of vorticity, which in turn reduces enstrophy. However, it is interesting to note that PAMH 5ppm whose increment in viscosity is very minute, also shows considerable reduction in enstrophy as compared to water (especially for V100 and V500 cases). Reason for this is given in section 3.4.7, where it is shown that the vorticity distribution in PAMH 5ppm solution is considerably different from that of water, though the viscosity increment is small.

Wall interaction stage (Stage 2b) shows a clear difference for V100 as compared to V500 and V1000 (Refer figure 3.35a, 3.35b and 3.35c). As vortex ring approaches the wall, its enstrophy increases for water and PAMH 5ppm solutions. (Vortex ring in PAMH 10ppm solution gets dissipated even before it reaches the wall, and there is no clear

formation of vortex ring for PAMH 25ppm solution for this piston input parameter). However, no such enstrophy increase is observed for V500 and V1000 cases. A possible reason is explained in section 3.3.2. As the Re increases, boundary layer gets thinner and thinner making it hard to resolve experimentally. Hence, underestimation of contribution of boundary layer for enstrophy calculations at higher Re could be a possible reason. However, the reduction in enstrophy during wall interaction is quite large, and reason is not clear yet.

After impinging on wall, vortex ring breaks down into smaller vortex structures. Hence enstrophy reduces drastically during stage 3, and finally gets dissipated by viscosity, similar to water experiments.

The conclusion is that, addition of polymer reduces enstrophy of vortex ring, even-though the circulation is same, by modifying vorticity distribution. Also presence of polymers cause reduction in enstrophy during free shear motion. Near wall increase in enstrophy is observed for V100 which can be attributed to vortex stretching. However, reason for reduction in enstrophy observed during wall interaction for V500 and V1000 is still not known.

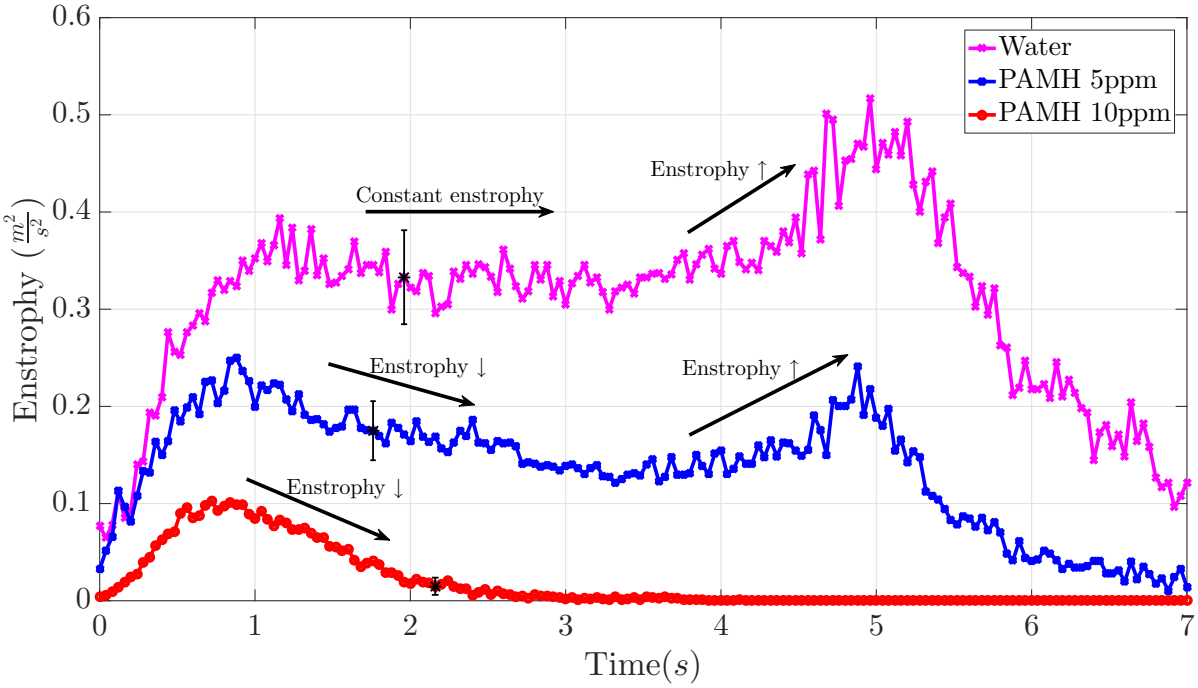

(a) V100 - Low impulse

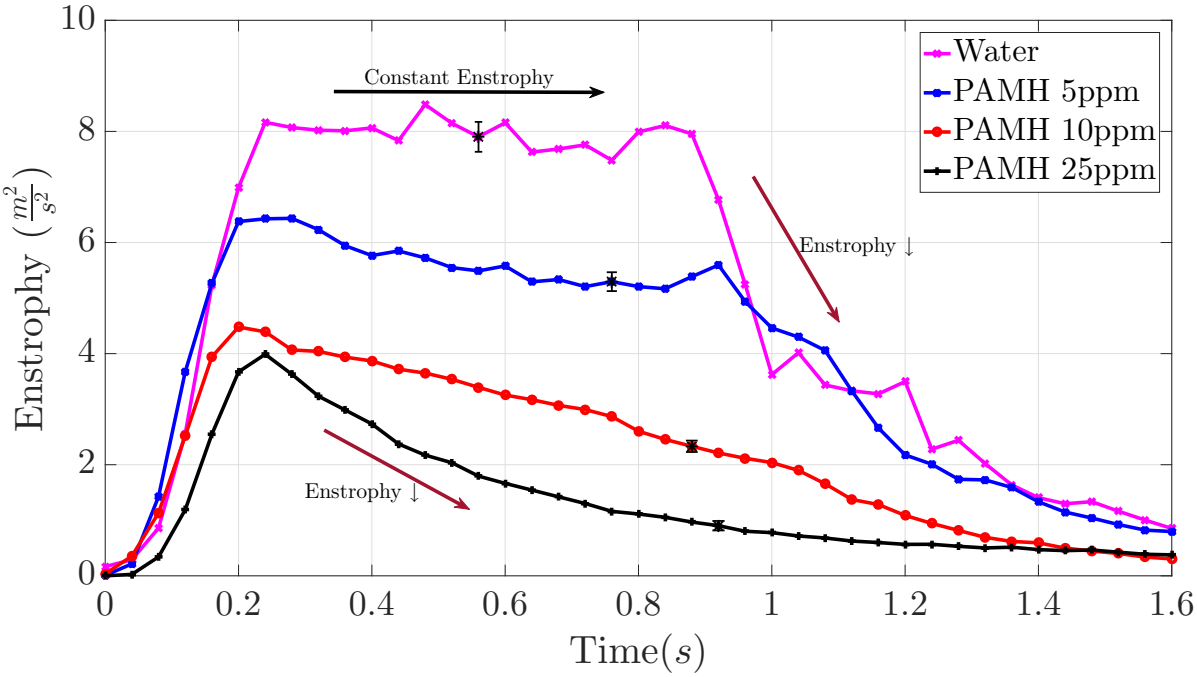

(b) V500 - Medium impulse

Fig. 3.34 Enstrophy vs Time

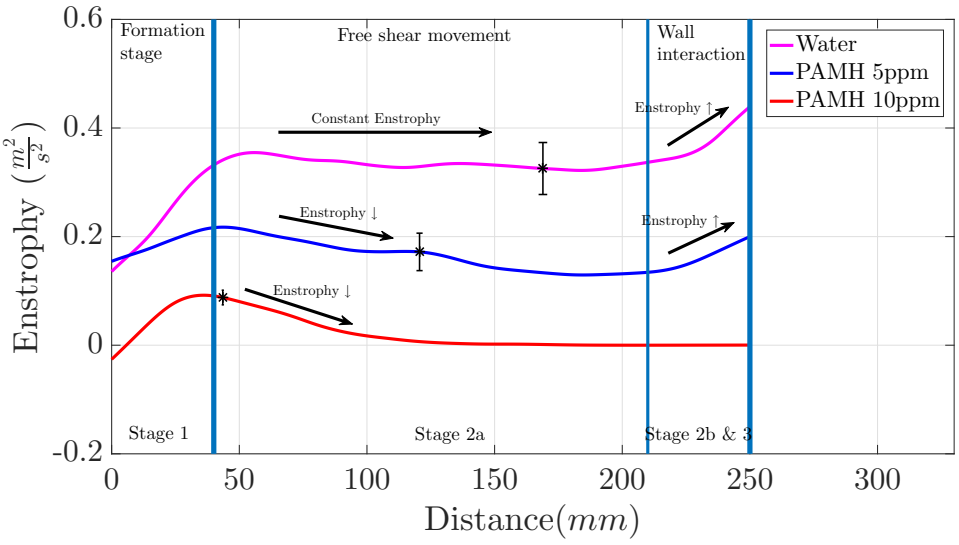

(a) V100 - Low impulse

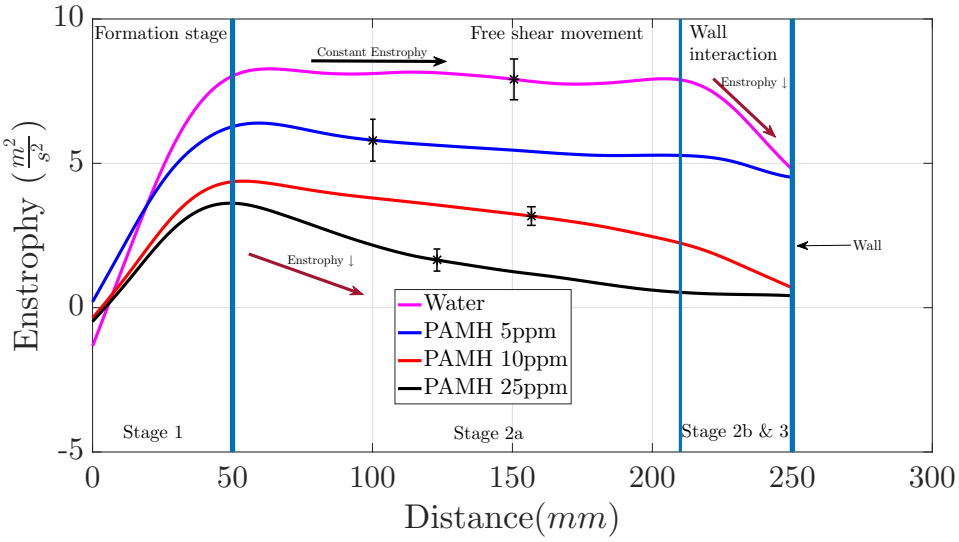

(b) V500 - Medium impulse

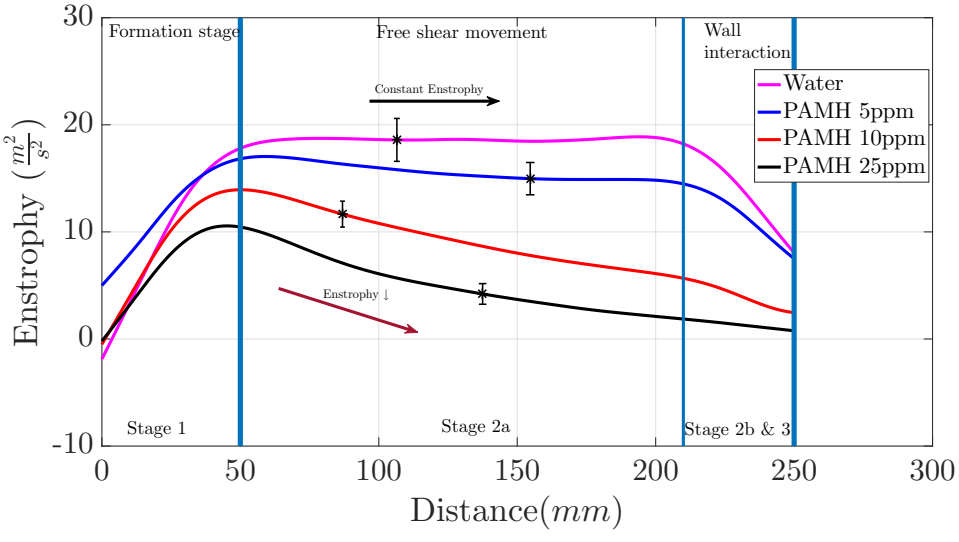

(c) V1000 - High impulse

Fig. 3.35 Enstrophy vs Distance

3.4.3 Kinetic Energy

Kinetic energy of the field shows three distinct behavior corresponding to three stages of vortex ring wall interaction in polymer solution, similar to water as explained in section 3.3.3. At the end of vortex ring formation stage, all solutions have nearly the same kinetic energy for V100 and V1000 cases (Refer figure 3.37a and 3.37c). A slight deviation is observed for V500, wherein PAMH 10ppm and PAMH 25ppm have slightly lesser kinetic energy (Refer figure 3.37b).

Negligible reduction in kinetic energy is observed during free shear motion for water case, as explained in section 3.3.3. However, PAMH 10 and 25 ppm solutions show considerable reduction in kinetic energy during free shear movement. PAMH 5ppm show reduction in kinetic energy for V100 case and behaves like water for V500 and V1000 cases. It is also observed that rate of kinetic energy reduction is directly proportional to solution concentration. All these observations can again be explained using increased viscosity of polymer solutions.

Increased viscosity of polymer solution speeds up dissipation of vorticity, thereby reducing the ring circulation. Vortex rings with reduced circulation will induce smaller velocity field, hence, reduced kinetic energy of the field. However, for smaller viscosities like PAMH 5ppm at high impulse, changes in circulation because of viscous dissipation during free shear movement is negligible. Hence, the reduction in kinetic energy is also negligible.

As vortex ring approaches wall, kinetic energy falls steeply for all solutions. After impinging on wall, vortex ring breaks down into smaller vortex structures, and finally gets dissipated because of viscosity.

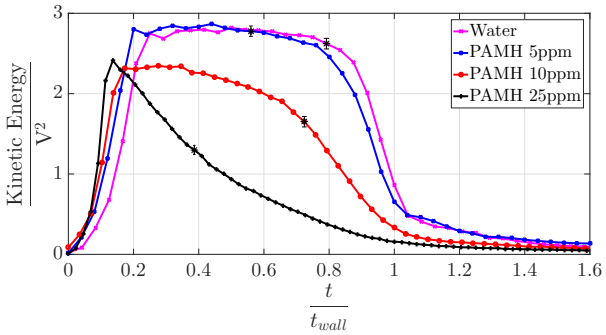

Fig. 3.36 Non-dimensional kinetic energy vs time for V500 case

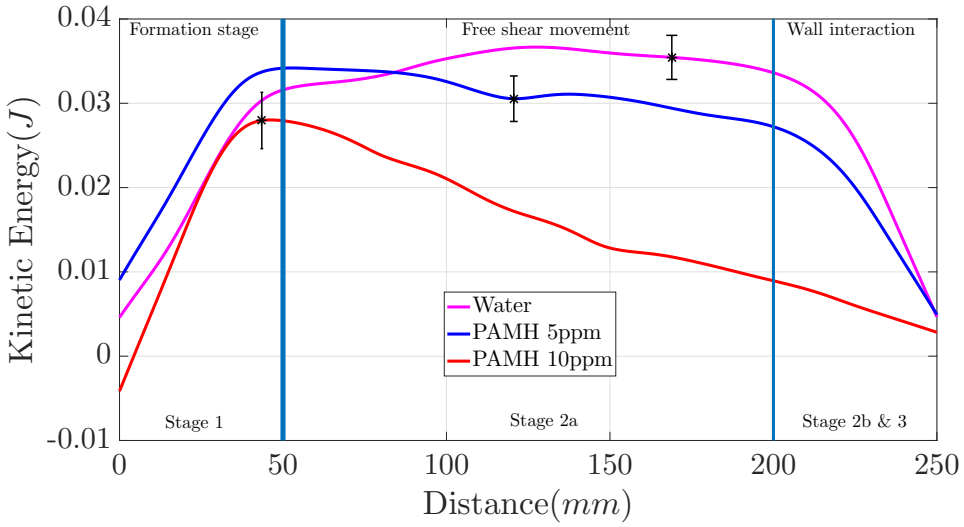

(a) V100 - Low impulse

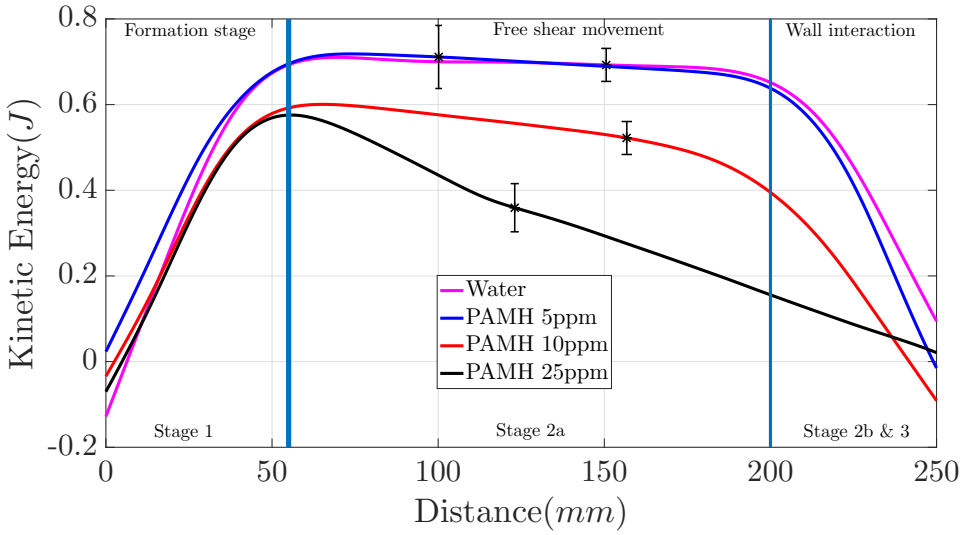

(b) V500 - Medium impulse

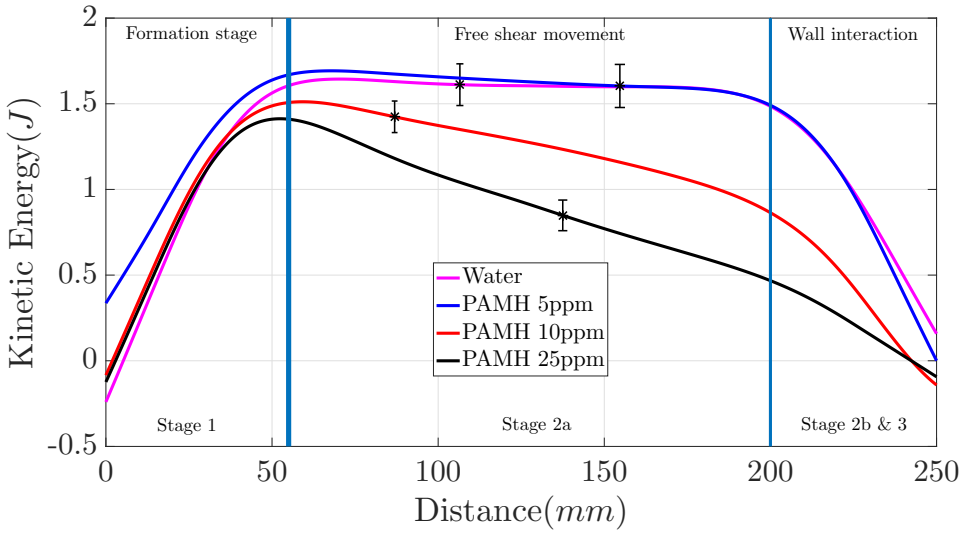

(c) V1000 - High impulse

Fig. 3.37 Kinetic energy of the field vs Distance

3.4.4 Peak vorticity

Peak vorticity occurs at the center of the ring. Hence, tracking peak vorticity is a way to track the ring and is used in earlier literatures (Fabris et al., 1996; Olsthoorn et al., 2014; Weigand and Gharib, 1994). However, peak vorticity value itself shows interesting behavior. At the end of formation stage, peak vorticity for polymer solutions is lesser than water for all experiments (Refer figure 3.38). More the concentration of polymer solution used, lesser is the peak vorticity value at the end of formation stage. However, circulation is nearly the same for water and polymer solutions at the end of formation stage. Reduced peak vorticity but with same circulation, implies a change in vorticity distribution in core of the ring in polymer solutions, which is corroborated in section 3.4.7. Water is shown to have higher peak vorticity than polymer solutions in all stages of vortex ring wall interaction.

In stage 2a, reduction in peak vorticity is observed for all experiments in all polymer solutions (Refer figure 3.38). However as the impulse increases or concentration of polymer solution reduces, changes in peak vorticity gets smaller. PAMH 5ppm, whose η_0 is just 1.1 times that of water also shows considerable reduction in peak vorticity compared to water, during formation and free shear movement.

A complex behavior is observed during stage 2b, where increase in peak vorticity is observed for PAMH 5ppm for V100 and V500 cases, but not for V1000 case. Water also shows similar behavior of increased peak vorticity for V100 case, and reduced peak vorticity for V500 and V1000 cases. However, other two polymer solutions, i.e. PAMH 10ppm and PAMH 25ppm doesn't show increase in peak vorticity during wall interaction in any experiment.

Increased peak vorticity is observed in earlier works of Chu et al. (1993); Fabris et al. (1996); Olsthoorn et al. (2014) also. And this increase in peak vorticity is attributed to vortex stretching, as the ring approaches the wall. However reason for such behavior only for few cases, and complete absence in few other cases is not yet known.

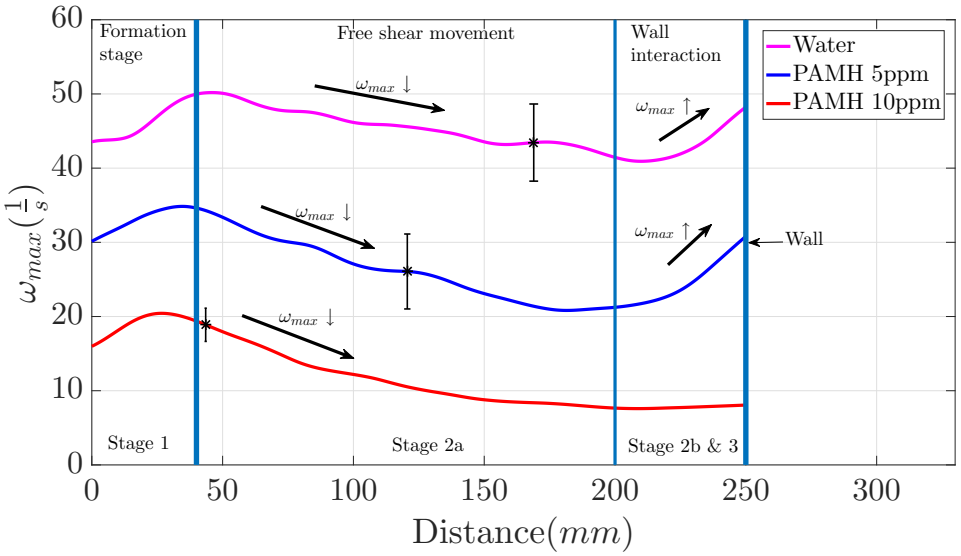

(a) V100 - Low impulse

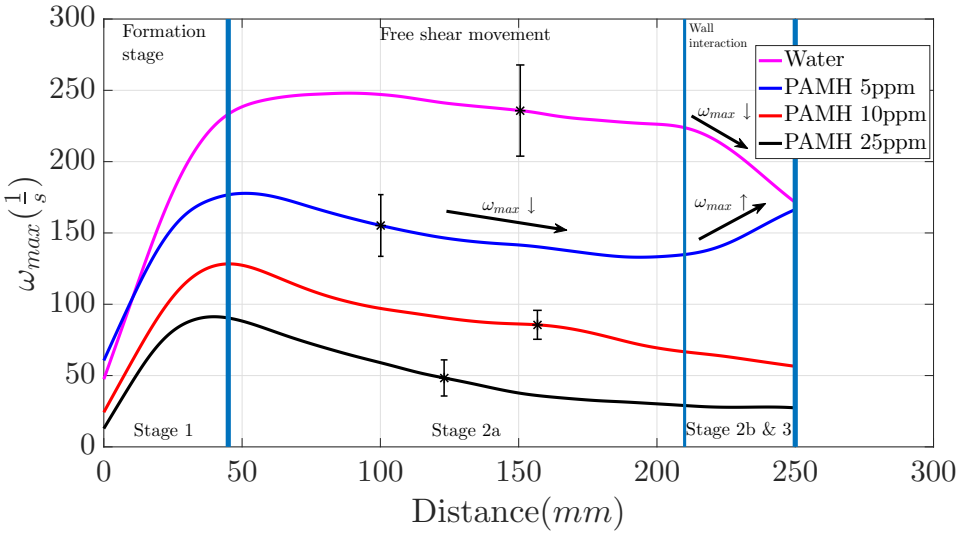

(b) V500 - Medium impulse

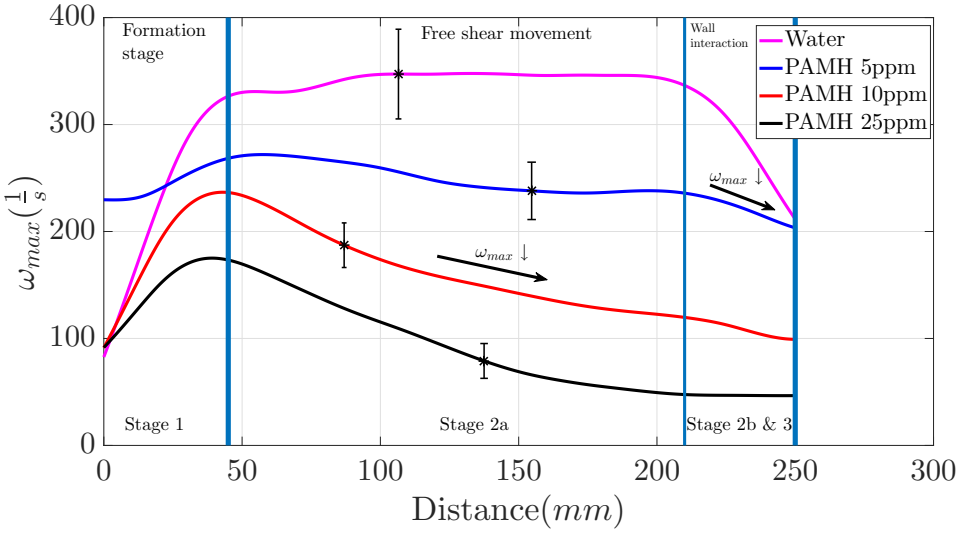

(c) V1000 - High impulse

Fig. 3.38 Peak vorticity vs Distance

After wall impingement, as vortex ring starts to break down, peak vorticity falls steeply. Conclusion for this section is that, polymer solutions show significant reduction in peak vorticity during formation stage itself, as compared to water, though circulation is nearly the same. Changes in vorticity distribution being the reason. Polymer solutions show greater reduction in peak vorticity during free shear movement. Increased viscosity of polymer solutions is a possible reason. However, in stage 2b two contradicting behavior of peak vorticity is observed for Water and PAMH 5ppm. Increase in peak vorticity can be explained using vortex stretching argument, but, absence of such an increase in certain cases, makes it hard to explain.

3.4.5 Distance vs Time

Distance vs time plots for water and its significance is explained in section 3.3.5. Differences between vortex rings in polymer solution to that in water are evident from distance plots. In all experiments, for first 100 mm (2D), vortex rings in all polymer solutions travel with same speed as that of water rings. The reason could be, for initial 100 mm rings are driven by inertia of the fluid pushed by piston, rather than vortex ring's self induced velocity. Hence, difference in circulation, vorticity distribution etc doesn't affect the translational velocity of vortex rings in polymer solutions for the first 100 mm distance from nozzle.

After the first phase of inertia driven movement, vortex rings travel by their self induced velocity. Since, PAMH 10ppm and 25ppm have considerably less circulation by that distance, as compared to water, self induced velocity is also smaller for these vortex rings. Hence, distance vs time plots for PAMH 10 and 25ppm start to show a deviation from that of water. However, PAMH 5ppm shows a very small difference for V100 and behaves exactly like water for V500 and V1000. Water rings travel with the same constant velocity throughout free shear movement. Reduction in velocity is observed for water rings as they approach the wall.

Distance at which polymer rings start to slow down, depends on polymer solution concentration and the impulse used. From figure 3.39, it is clear that, for PAMH 10 and 25ppm solutions velocity falls continuously after the initial phase. Continuous reduction in circulation is the reason for fall of velocity.

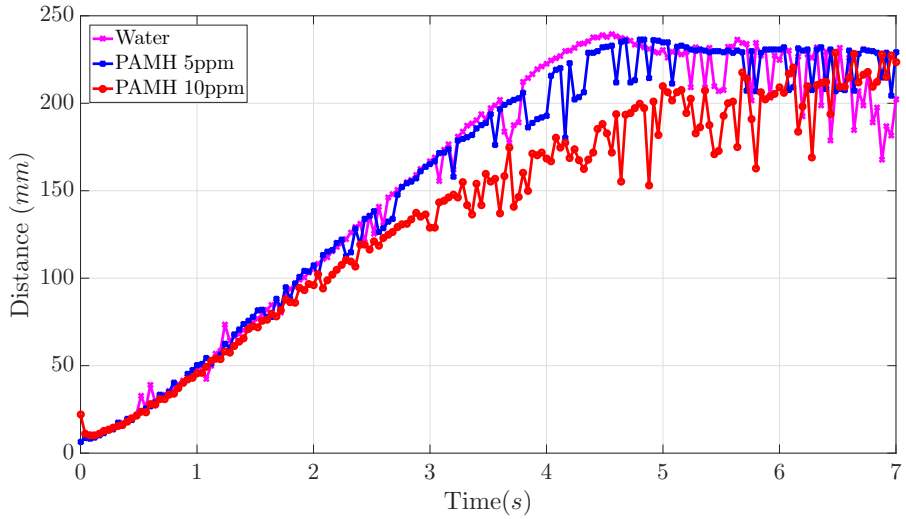

(a) V100 - Low impulse

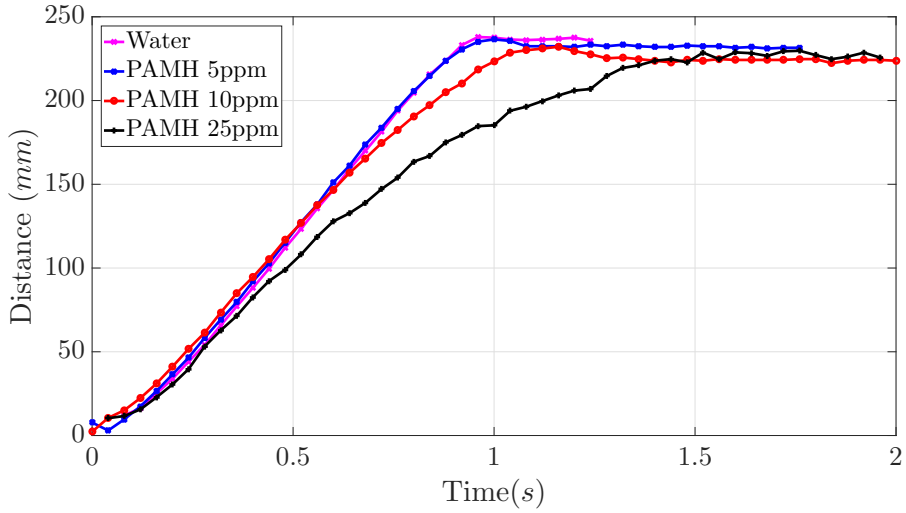

(b) V500 - Medium impulse

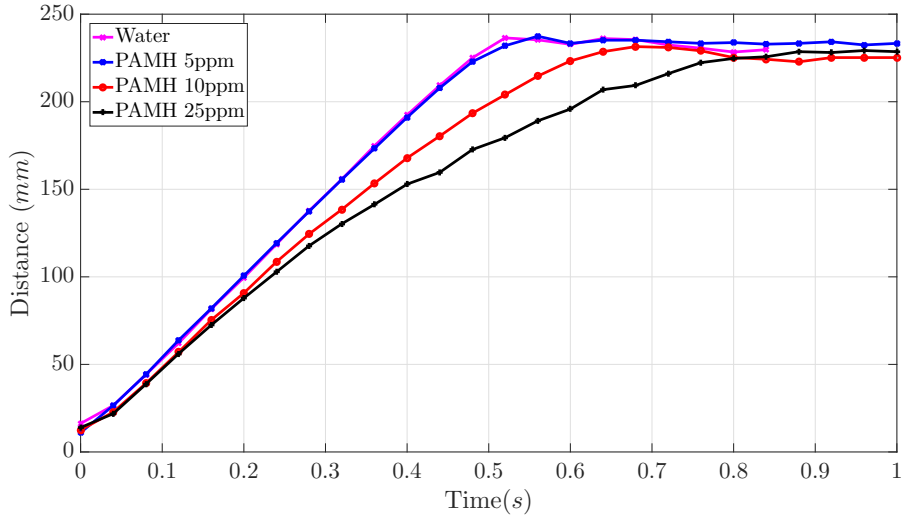

(c) V1000 - High impulse

Fig. 3.39 Distance vs Time

As vortex ring approaches the wall, there will be a growth of boundary layer which separates into secondary vortex ring. Interaction with boundary layer and secondary vortex ring makes the primary ring to bounce back, which is captured in distance plots. Distance from wall, where primary vortex ring rebounds is nearly the same for all polymer solutions and water.

Non-dimensionalising the time by t_{wall} is shown to collapse all distance plots for water (Refer figure 3.23). However, it doesn't work for polymer solutions as shown in figure 3.40. Which implies that linear scaling by t_{wall} is insufficient, since distance traveled by vortex rings in PAMH 10 and 25 ppm solutions is a nonlinear function of time.

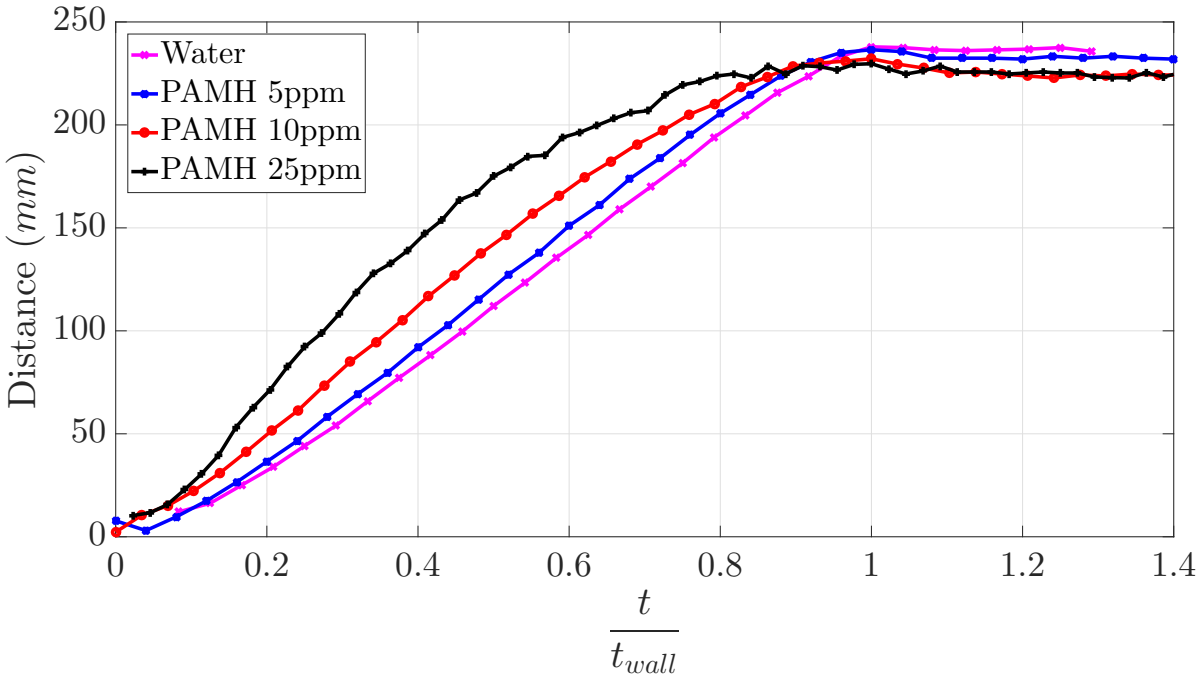

Fig. 3.40 Distance vs Non-dimensional time for V500 case

3.4.6 Diameter

Diameter variation for vortex ring wall interaction in water is presented in section 3.3.6. During free shear motion no increase in diameter is observed for water and PAMH 5ppm solutions (Refer figure 3.41 and 3.42). However, a slight increase in diameter is observed for PAMH 10 and 25ppm solutions at the end of free shear motion. This increase in diameter is also associated with the reduction in circulation and velocity of the ring.

Drastic increase in diameter, as vortex ring approaches the wall is observed in all polymer solutions and in water for all experiments.

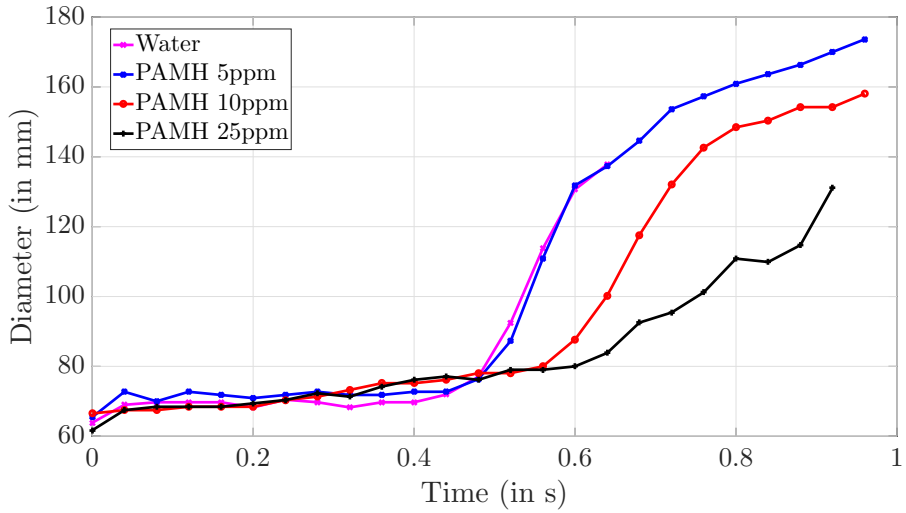

Fig. 3.41 Diameter vs Time for V1000 case. Vortex rings in polymer solutions reach wall at different time. Hence steep increase in diameter, which indicates wall interaction, occurs at different times.

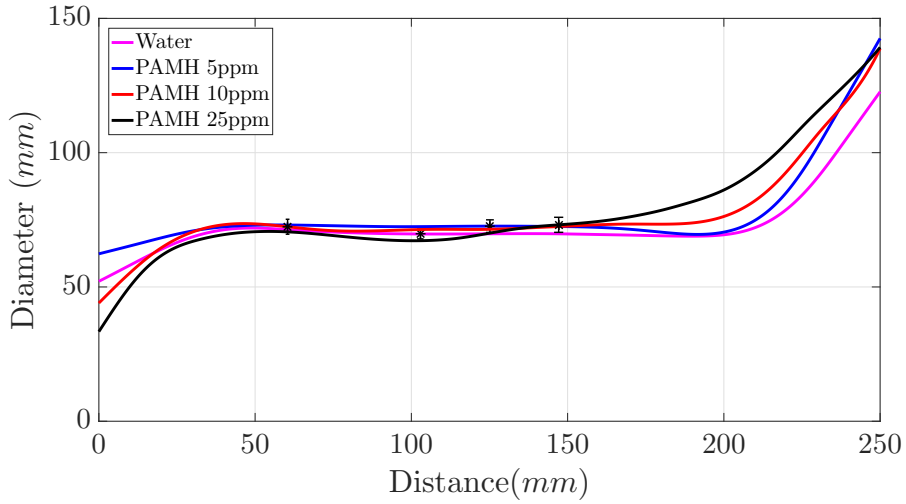

Fig. 3.42 Diameter vs Distance for V500 case.

3.4.7 Core vorticity distribution

Addition of polymers change the vorticity distribution inside the core of the vortex ring. Figure 3.43 shows vorticity distribution over one half of the ring in 3D. In figure 3.43, z-axis corresponds to vorticity, whereas x and y axis corresponds to co-ordinates of the plane. From figure 3.43, it is clear that, vorticity distribution inside the core of the ring is different even for the smallest concentration of polymer added. In polymer solution, lesser vorticity levels constitute larger areas, thereby giving a short but fat ring, whereas in water, ring remains thin and tall in nature.

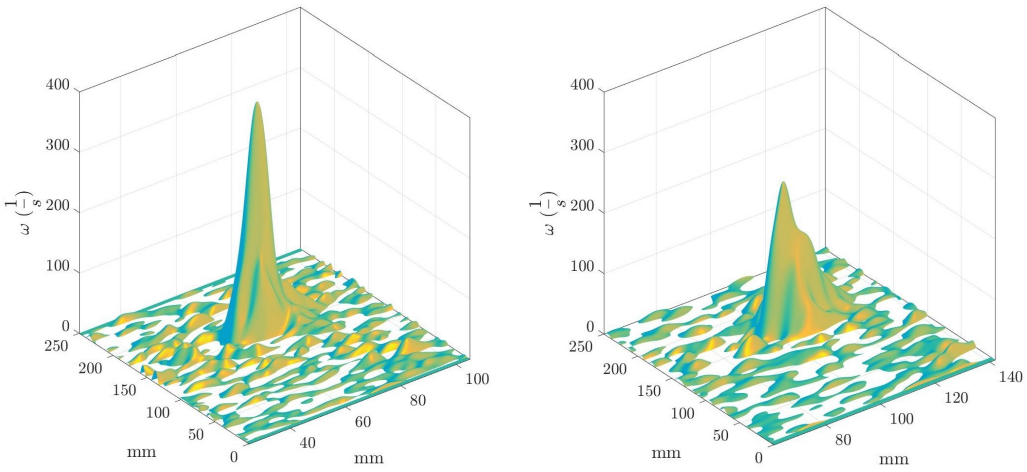

(a) Water (b) PAMH 5ppm

Fig. 3.43 Vorticity distribution shown in 3D over one half of the vortex ring for Water and PAMH 5ppm solution at the same time instant for L100 V1000 case.

Presence of lesser vorticity levels over larger area could be clearly demonstrated, if the vorticity plotted on the z-axis is normalized with peak vorticity. Figure 3.44 shows normalized vorticity profiles for PAMH 5ppm and water, which clearly shows the increased thickness for intermediate $\frac{\omega}{\omega_{max}}$ values.

Difference in vorticity distribution gets amplified as polymer concentration increases, or as the impulse reduces, which is clearly shown in figure 3.45. This drastic modification in vorticity distribution though the impulse provided is same, is the reason for reduction in enstrophy, peak vorticity and circulation observed in PAMH 10ppm case. Also differences are more clear with front and side views of the 3D plot (Refer figure 3.46).

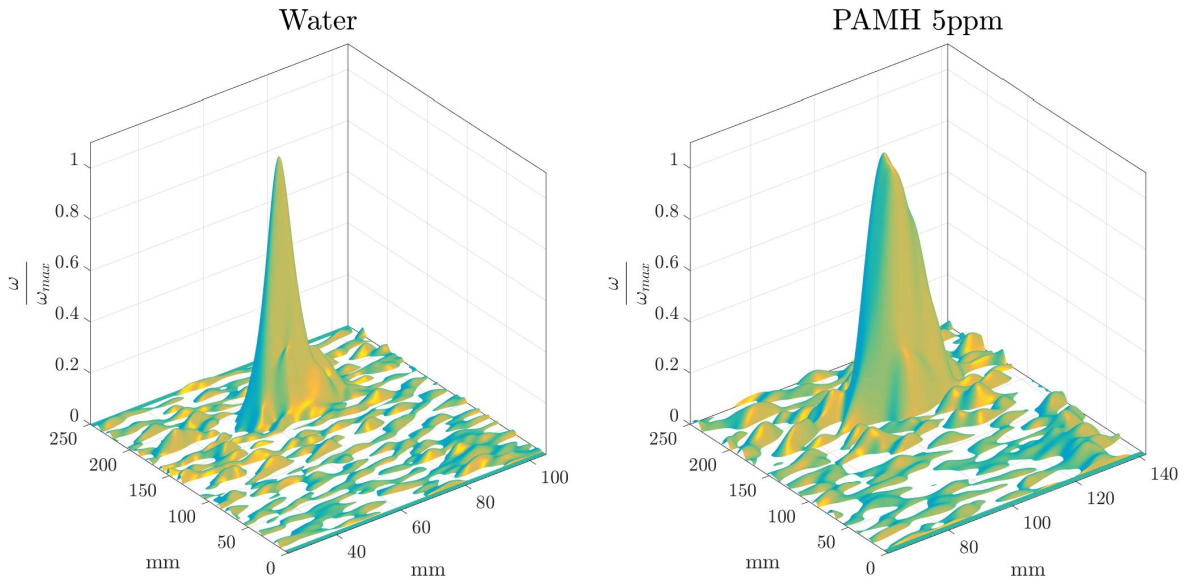

Fig. 3.44 Normalized vorticity distribution shown in 3D over one half of the vortex ring for Water and PAMH 5ppm solution at the same time instant for L100 V1000 case. Increased thickness at intermediate $\frac{\omega}{\omega_{max}}$ signifies presence of lesser vorticity levels over larger area.

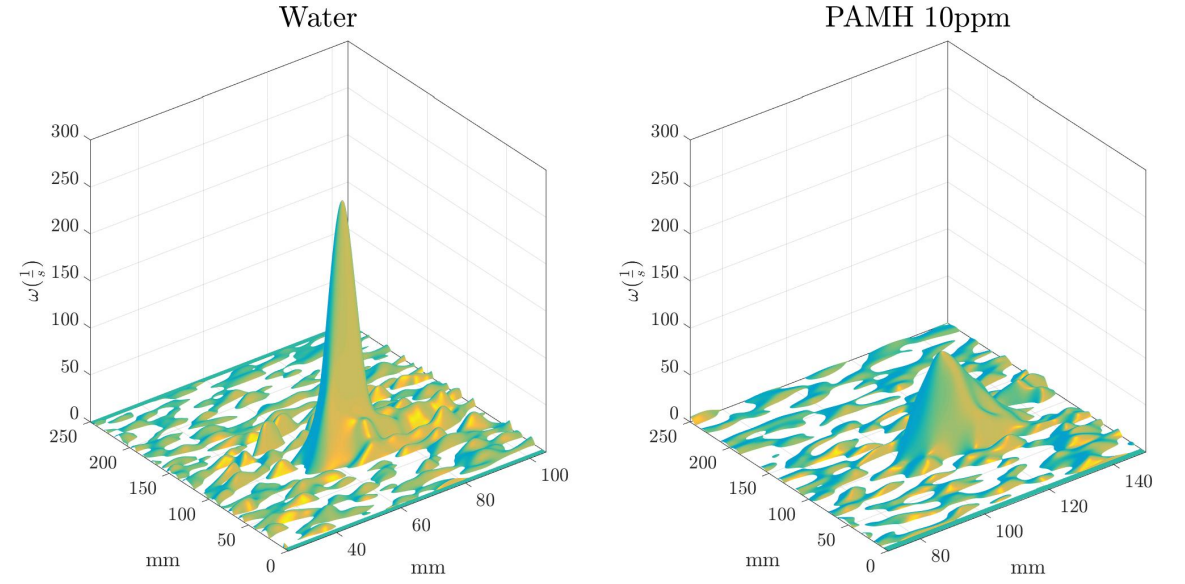

Fig. 3.45 Vorticity distribution shown in 3D over one half of the vortex ring for Water and PAMH 10ppm solutions at the same time instant for L100 V500 case. Drastic reduction in peak vorticity along with clear changes in vorticity distribution is visible.

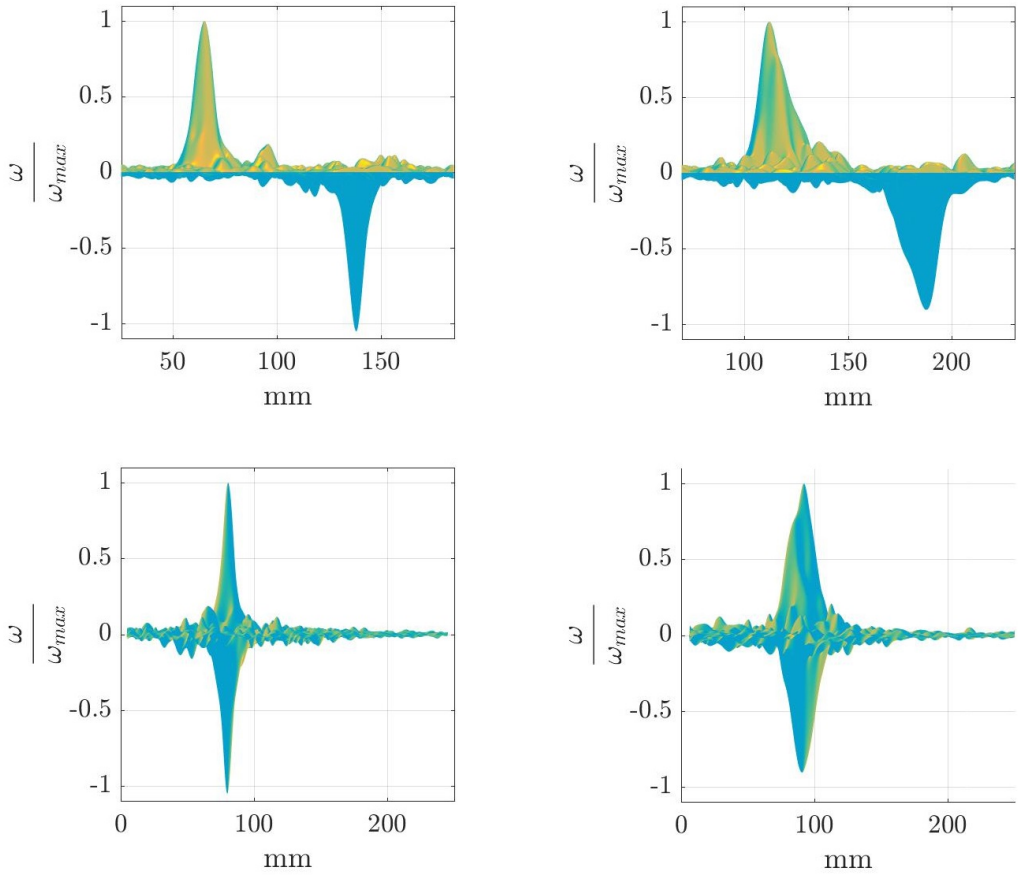

(a) Water (b) PAMH 10ppm

Fig. 3.46 3D Vorticity distribution over the vortex ring for Water and PAMH 10ppm solutions at the same time instant for L100 V500 case shown in front and side view. Top - Front view, Bottom - Side view.

In constant viscosity solution, vorticity evolution will be through a series of self-similar Gaussian profiles. Hence, normalized vorticity profile looks the same for all water runs at all time instants. However, presence of shear thinning viscosity will break this Gaussian self-similarity (However, there could be another self-similar law different from Gaussian). Hence, vorticity profiles will differ in shape from that of initial profile and from their water counterpart. Difference in normalized vorticity profile of PAMH 5 & 10ppm with that of water, as shown in figure 3.44 and 3.46, could be largely attributed to shear-thinning viscosity.

This change in vorticity distribution could be the main reason behind all the changes observed in circulation, enstrophy and peak vorticity in polymer solutions from that of water, for constant impulse experiments.

3.5 Constant Reynolds Number Experiments

Behavior of Newtonian vortex ring mainly depends on three parameters, (1) Reynolds number (2) Ratio of core diameter to ring diameter (3) Normalized vorticity profile. In theory, if these three parameters are matched for vortex rings in two different solutions, then further evolution of those rings is same in non-dimensional co-ordinates (In dimensional co-ordinates they might still show differences). However, this is only for vortex rings, where viscous and inertial forces are the only two dominant forces. If any other force is dominant, such as elastic force, then additional parameters are needed.

Reynolds number for vortex rings is defined as $Re = \frac{\Gamma}{\nu}$. Polymer solutions show shear dependent viscosity with two viscosity plateaus, making it difficult to measure Re_p directly. However, based on two viscosity plateau values, two Reynolds numbers can be defined, which are represented as Re_0 and Re_∞. Re_0 and Re_∞ together envelop actual Re_p, and forms the limiting Reynolds numbers for polymer solutions.

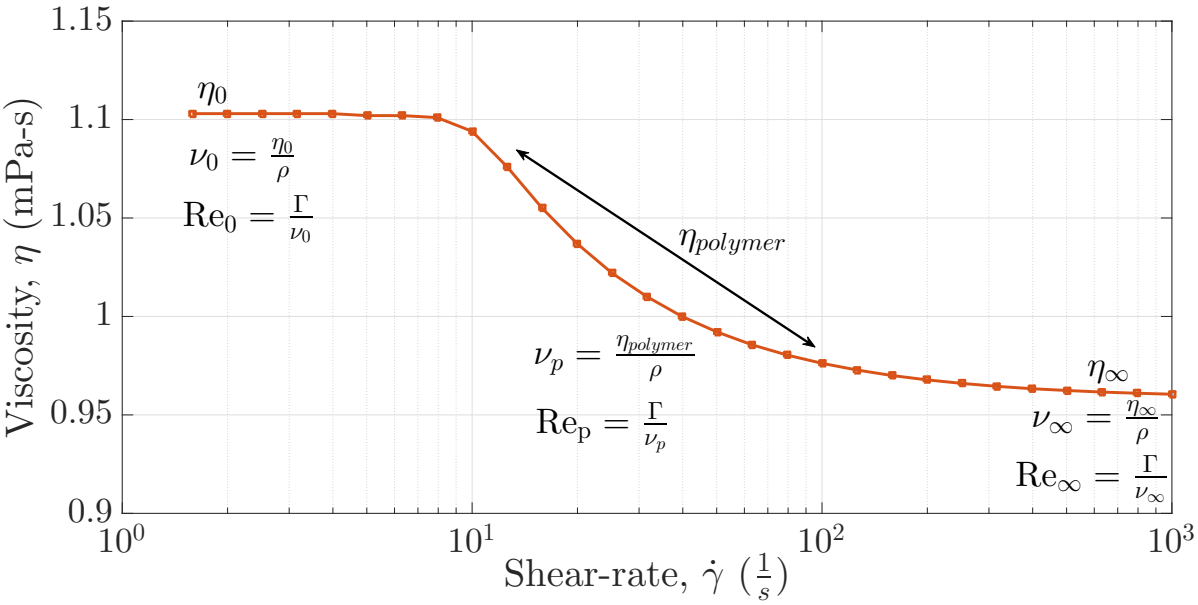

Fig. 3.47 Reynolds number defined for polymer solutions.

Vortex ring experiments are conducted at Re_0 and Re_∞ in water. Since, water has lesser kinematic viscosity, Re_0 and Re_∞ are achieved by varying circulation, which in turn is achieved by varying piston velocity (Note: $\Gamma = \mathrm{L} \times \mathrm{V}$. V can be varied to get the required Γ). Stroke-length for all experiments is kept constant at 100 mm, in order to keep $\frac{L}{D}$ ratio same for all experiments. As given in table 2.2, η_0 and η_∞ varies over a

Polymer solution	η_0 (mPa-s)	η_∞ (mPa-s)	In polymer solution	In water	
			V (mm/s)	V (To match Re_0) (mm/s)	V (To match Re_∞) (mm/s)
5ppm	1.05	0.95	100	86	94
			500	429	471
			1000	857	943
10 ppm	2.25	0.955	100	40	94
			500	200	471
			1000	400	943
25ppm	40	0.95	500	11.25	471
			1000	22.50	943

Table 3.2 Input parameters for *Re* matched experiments. Input piston velocity in water is systematically varied to get the required Reynolds number. V corresponds to input piston velocity. Stroke-length L is kept constant at 100 *mm* for all experiments.

small range of values. Values of η_0 and η_∞ taken from this range to calculate Re_0 and Re_∞ are given in table 3.2, along with all the other parameters of *Re* matched experiments.

As shown in table 3.2, L100 V100 experiment of PAMH 5ppm will be compared with L100 V86 and L100 V94 of water experiments. Similarly other experiments in polymer solutions are compared with their respective water counterparts. Because of very low velocities involved, *Re* matched experiments couldn't be conducted for PAMH 25ppm.

Re matched experiments are plotted in non-dimensional co-ordinates (In dimensional co-ordinates, they don't show any general evolution). Also, this *Re* dependent evolution is only applicable during vortex ring free shear movement, with fully formed vortex ring as the starting point (i.e fully formed vortex ring is considered even at time t = 0). Hence, analysis of vortex formation stage and wall interaction stage is inherently absent in *Re* matched experiments.

Properties such as circulation, Enstrophy, Kinetic Energy and Peak vorticity are normalized by their initial values (values at time t=0, i.e values corresponding to vortex ring just after formation stage). There exists two ways of non-dimensionalising time. (1) Using inertial time scale

$$t^* = t \times \frac{\Gamma_0}{2\pi R_0^2}$$

(2) Using viscous time scale

$$t^* = t \times \frac{\nu}{2\pi R_0^2}$$

where, t is dimensional time, Γ_0 is initial circulation, R_0 is initial vortex ring radius and ν is kinematic viscosity of the solution. Since all our vortex ring experiments are at $Re \geq 1000$, inertial force is the dominant force. Hence, inertial time scale is used for non-dimensionalising time, which is shown to collapse data better than viscous time scale.

Using predetermined quantities like Γ_{slug} and R_{Nozzle} while non-dimensionalising, instead of using measured quantities like Γ_0 and R_0, is shown to have negligible changes as presented in figure 3.48 (Note: $\Gamma_{slug} = \mathrm{L} \times \mathrm{V}$). Hence, in all plots, Γ_0 and R_0 itself is used in non-dimensionalisation.

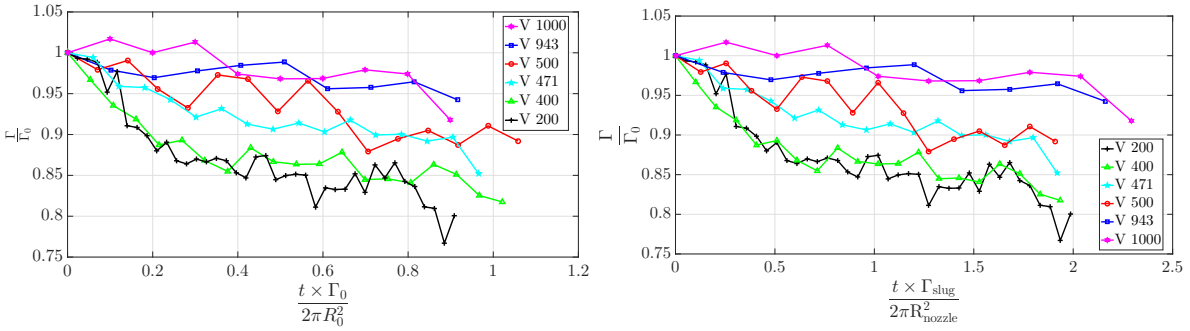

Fig. 3.48 Using measured and predetermined quantities for Non-dimensionalisation. Both ways of non-dimensionalisation show similar behaviour.

3.5.1 Circulation

Variation of circulation as a function of non-dimensional time for limiting value of Re can be intuitively obtained. For $Re \to \infty$, viscous effects are absent, hence, vorticity won't diffuse, there by $\frac{\Gamma}{\Gamma_0}$ remains constant throughout the duration of the experiment. On the other hand, for $Re \to 0$, vorticity will diffuse instantly, thereby reducing core circulation to zero. For all finite Re, circulation evolution falls in between these two limits, as shown in figure 3.49.

Validity of this argument is checked on water and all polymer solutions. As shown in figure 3.50, experiments with higher Re show slower reduction in $\frac{\Gamma}{\Gamma_0}$ than the ones with lower Re. Very similar behavior is observed in all polymer solutions (Refer figure 3.51)

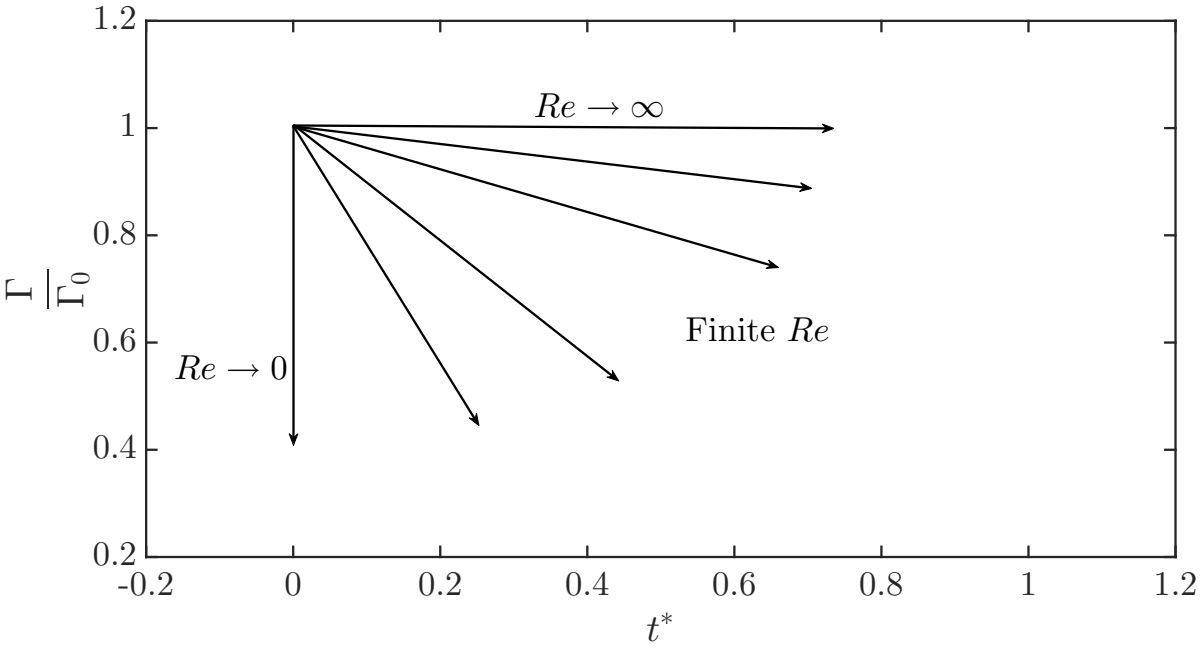

Fig. 3.49 Vortex ring circulation variation in non-dimensional co-ordinates as expected from theory.

for varying Re.

In figure 3.52 and 3.53, polymer experiments are compared with their corresponding Re matched water counterparts. From figure it is clear that, Γ^* of polymer experiment falls in between that of Re_0 and Re_∞ experiments, which are conducted in water. This suggests that, earlier observed reduction in circulation in polymer solutions for constant impulse experiments could be because of reduced Re associated with polymer experiments (which could be attributed to increased viscosity of polymer solutions). And very similar reduction in circulation could even be obtained for water, given Re is sufficiently small.

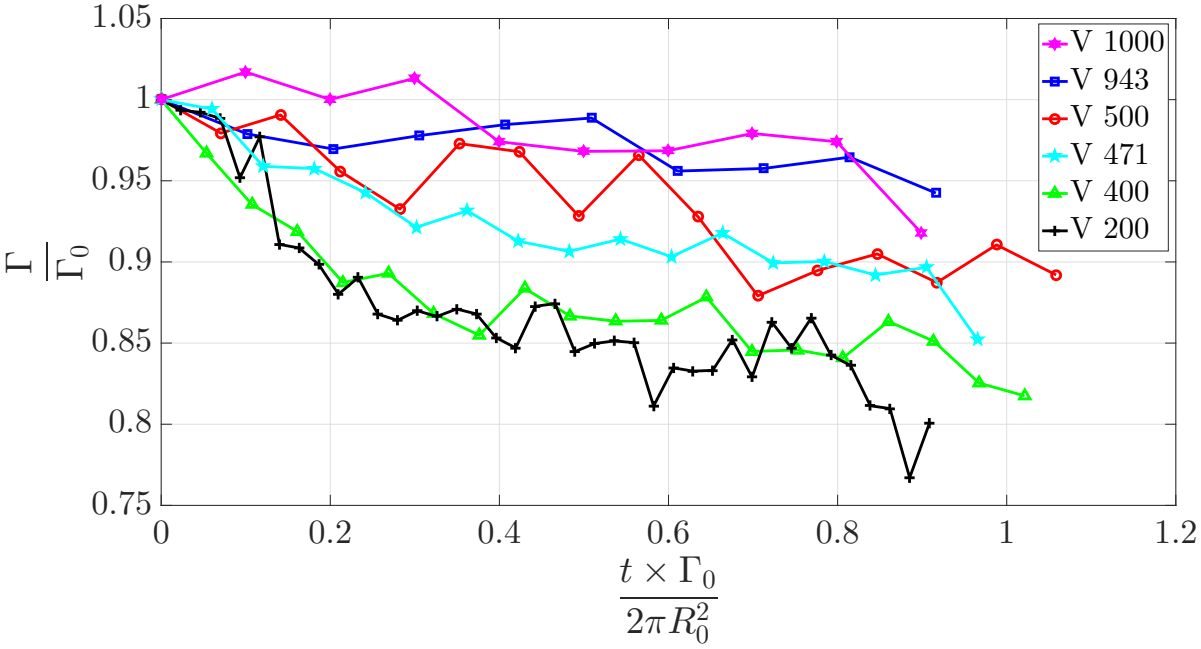

Fig. 3.50 Vortex ring circulation variation in non-dimensional co-ordinates for different *Re* water experiments. Stroke length of piston input is kept constant at 100 *mm*. *Re* corresponding to these experiments is given in table 3.1.

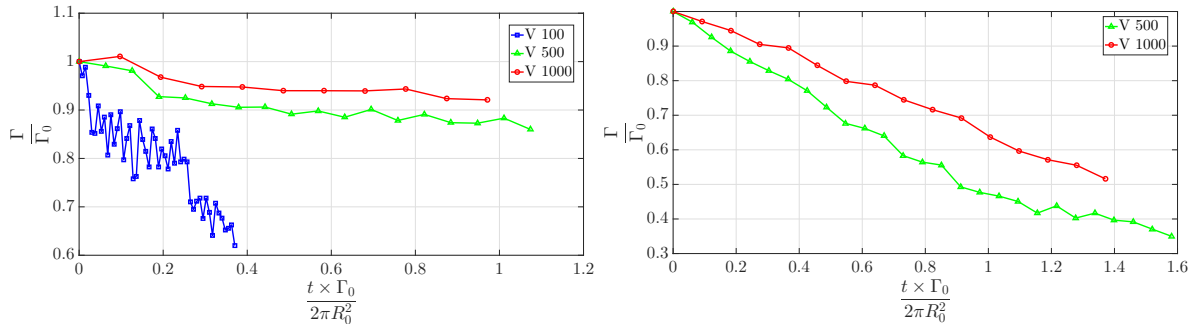

(a) PAMH 5ppm

(b) PAMH 25ppm

Fig. 3.51 Vortex ring circulation variation in non-dimensional co-ordinates for different *Re* experiments in PAMH 5ppm and PAMH 25ppm. Higher input piston velocity implies higher *Re*.

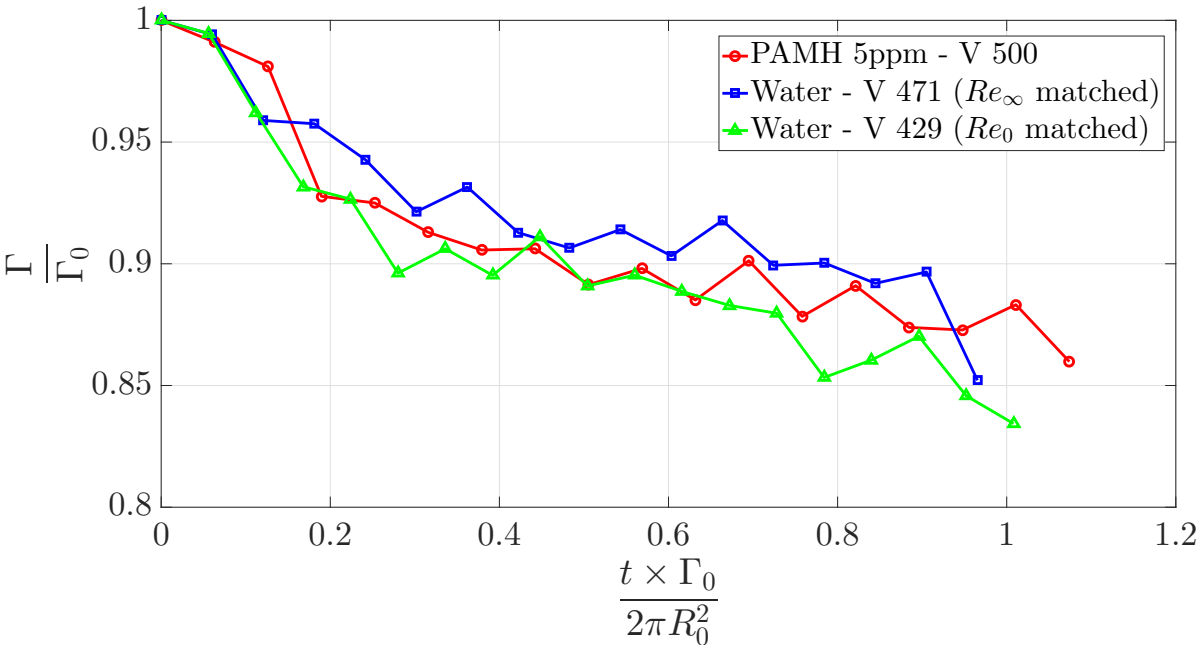

Fig. 3.52 Comparison of vortex ring circulation variation in non-dimensional co-ordinates for PAMH 5ppm experiment with its Re matched water experiments.

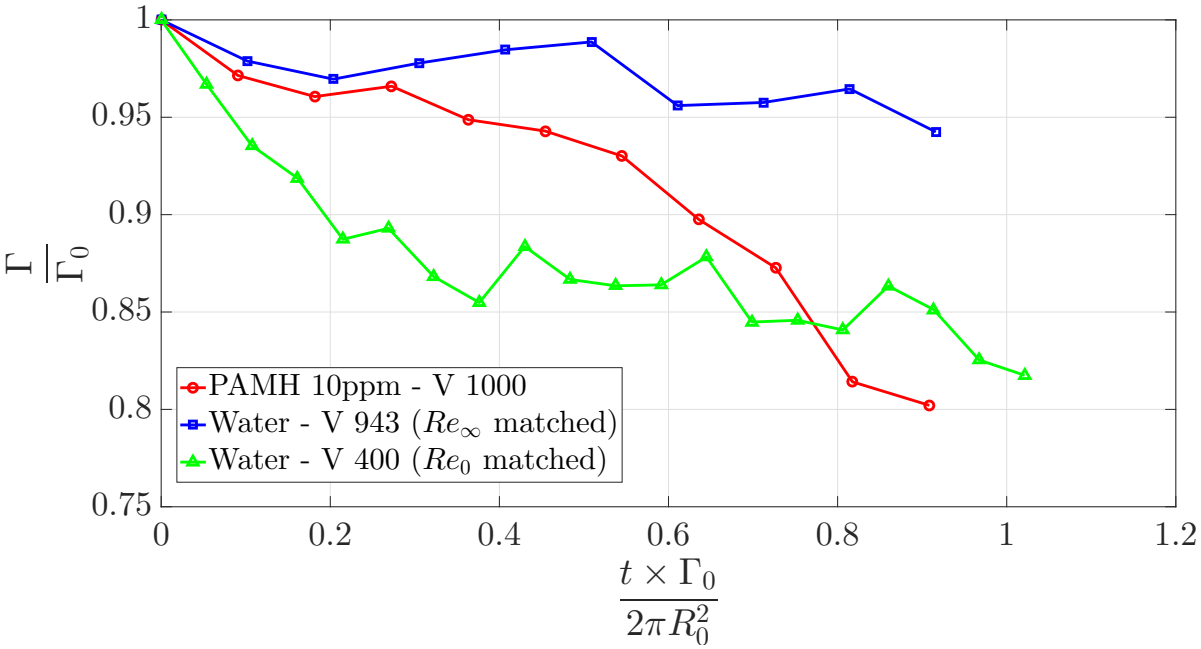

Fig. 3.53 Comparison of vortex ring circulation variation in non-dimensional co-ordinates for PAMH 10ppm experiment with its Re matched water experiments.

3.5.2 Enstrophy

Enstrophy changes can't be generalized by just a single parameter i.e. Re, as it was possible in the case of circulation. The reason is, enstrophy being non-conserved quantity depends highly on vorticity distribution. For example, two vortex rings in the same solution, with different vorticity distribution, but with same circulation (hence same Re), can have entirely different enstrophy. Above this, modified self similarity law for vortex ring vorticity distribution of shear thinning liquids is another hurdle for generalization of enstrophy by just a single parameter i.e. Re. Hence, matching Re doesn't necessitates a particular way of enstrophy evolution.

Inline with the above argument, no general Re dependent behavior is observed among different experiments of either water or polymer solutions. Figure 3.54 shows enstrophy variation for PAMH 10ppm with its Re matched water experiments. As it can be seen from figure, polymer ring looses enstrophy very quickly, though its limiting Re experiments in water doesn't show such a behaviour. This major difference comes from stark difference in vorticity distribution in polymer solutions, which is different altogether from water experiments even at limiting Re, as shown in figure 3.55(Refer section 3.4.7).

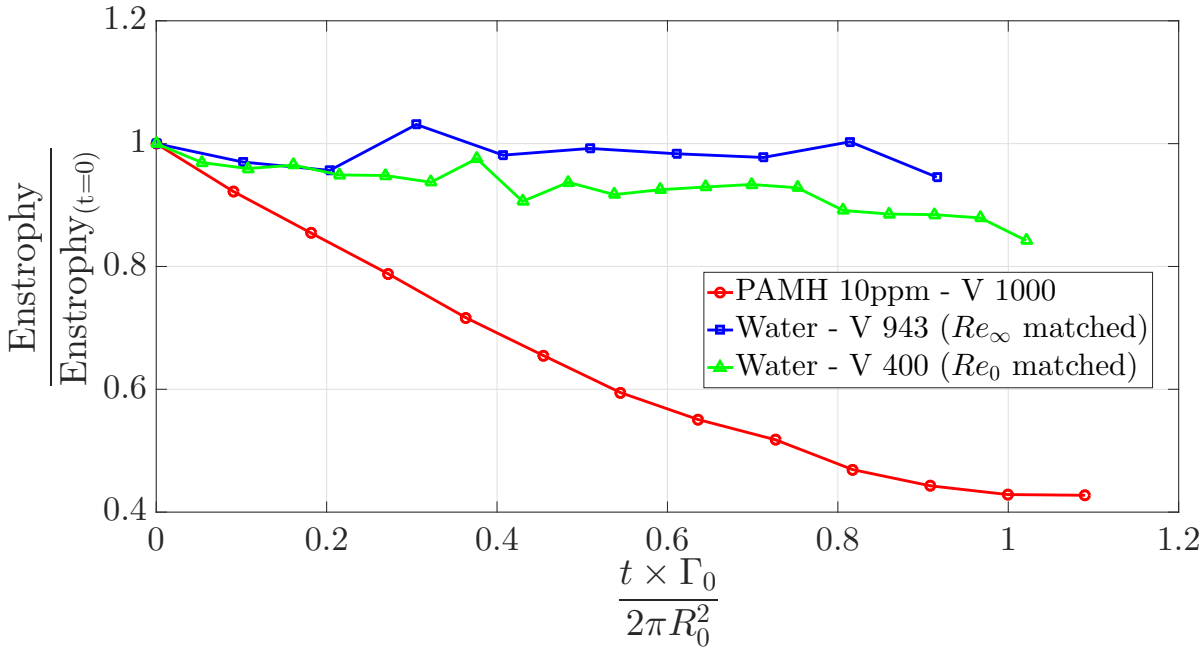

Fig. 3.54 Comparison of vortex ring enstrophy variation in non-dimensional co-ordinates for PAMH 10ppm experiment with its Re matched water experiments.

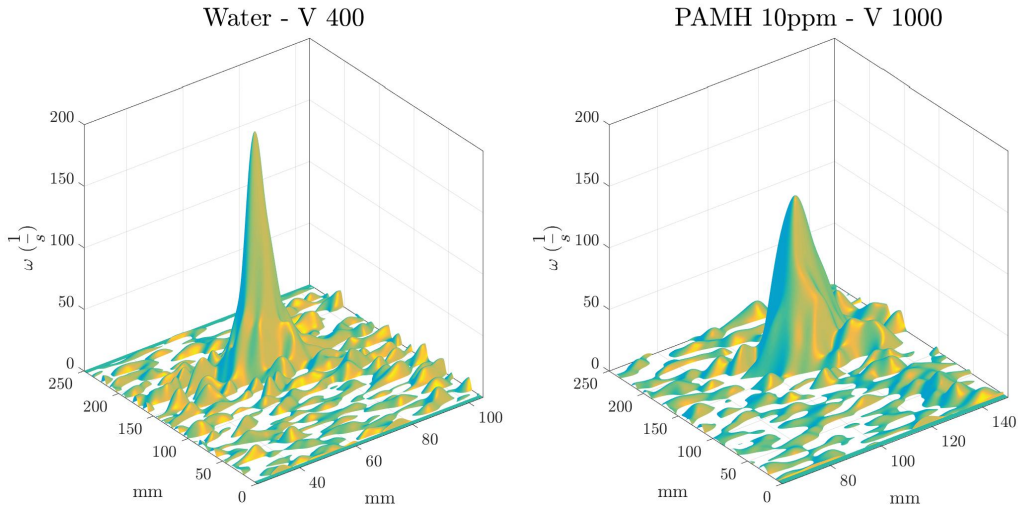

Fig. 3.55 Comparison of vorticity distribution over one half of the ring for PAMH 10ppm - V 1000 experiment with its Re_0 matched water experiment - V400. Vorticity distribution over polymer ring is different even from its Re_0 matched experiment in water.

3.5.3 Peak vorticity

Peak vorticity evolution has lot of similarities with enstrophy evolution. As explained in earlier section, single parameter, i.e. Re is not sufficient enough to capture the whole evolution in non-dimensional co-ordinates, because of modification of self-similarity. No general Re dependent behavior is observed among different experiments of either water or polymer solutions.

Figure 3.56, shows variation of peak vorticity for polymer solution along with its Re matched water experiments. From figure, it is clear that peak vorticity reduction is quicker in polymer solution, even when compared with its Re_0 matched water experiment. Very similar behaviour is seen in other Re matched experiments also. The reason being, modification in self similarity law because of shear thinning viscosity. Also from figure 3.55, it can be noticed that water vortex ring has higher peak vorticity compared to polymer solution ring, even-though water ring has lesser Re and lesser circulation compared to polymer solution.

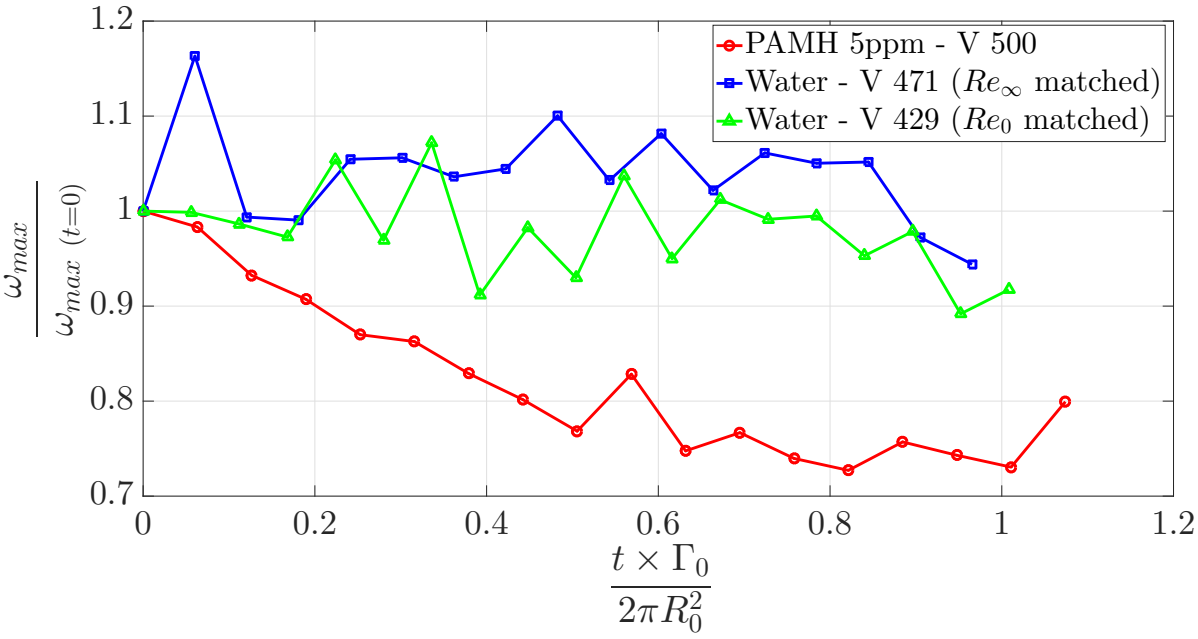

Fig. 3.56 Comparison of peak vorticity variation in non-dimensional co-ordinates for PAMH 5ppm experiment with its *Re* matched water experiments.

3.5.4 Kinetic Energy

Kinetic energy is obtained from velocity field, which in turn is determined by vortex ring strength and its vorticity distribution. Reduction in kinetic energy because of viscous dissipation for water experiments for a range of *Re* is fairly small (Refer figure 3.57). However, in polymer solutions, considerable reduction is observed (Refer section 3.4.3). This reduction in kinetic energy becomes more pronounced at low impulses or as concentration of polymer solution increases.

In figure 3.58, kinetic energy changes in PAMH 5ppm vortex ring is compared with its *Re* matched water vortex rings. For vortex rings in PAMH 5ppm solution, no significant difference is observed from their *Re* matched water counterparts. However, for higher concentration of polymer solutions, even in *Re* matched experiments, differences are observed. As it is clear from figure 3.59, kinetic energy reduction for PAMH 10ppm rings is considerably large compared to its *Re* matched water experiments. The exact reason for this behaviour is not yet known, however, drastic modification in vorticity distribution for vortex rings in PAMH 10ppm compared to water is a possible reason.

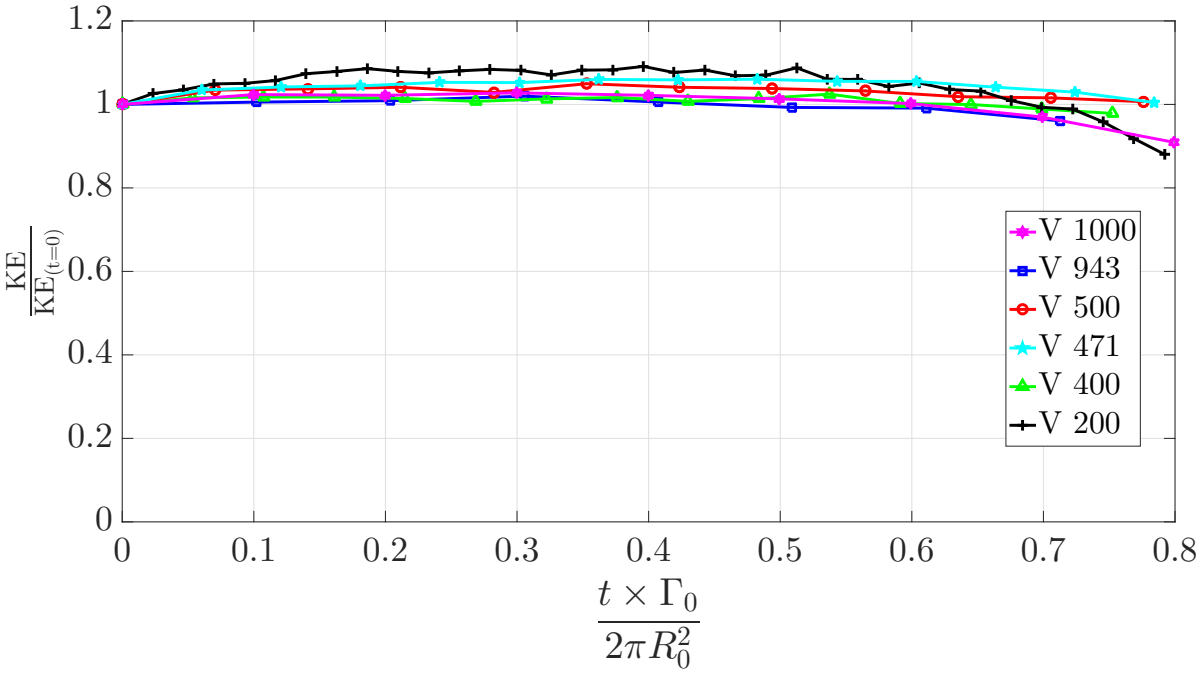

Fig. 3.57 Comparison of kinetic energy in non-dimensional co-ordinates among water experiments.

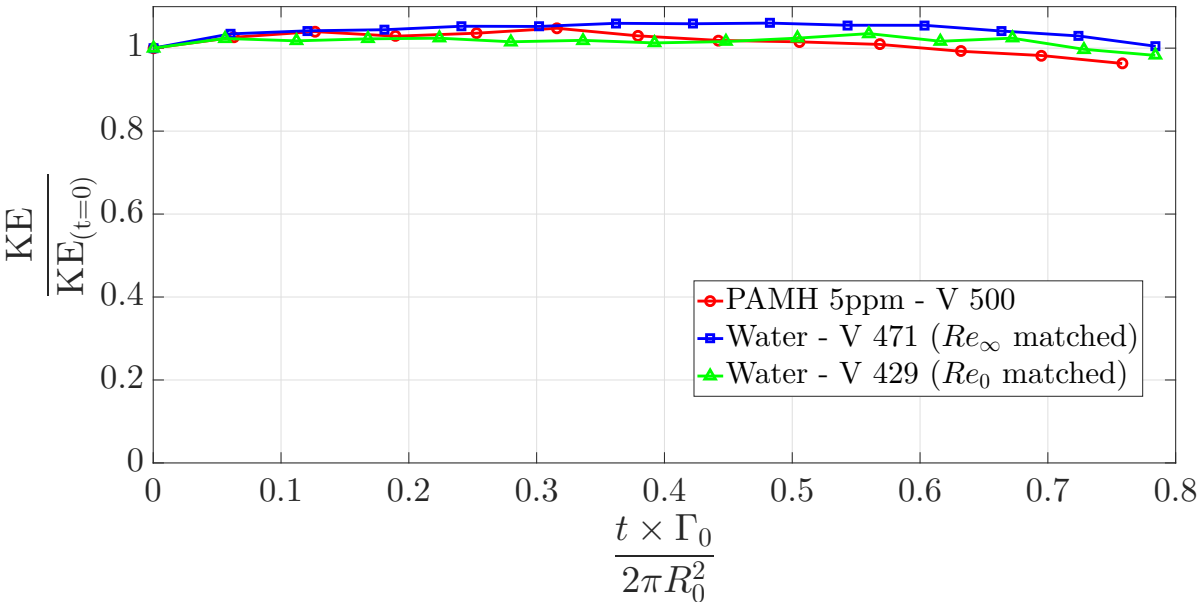

Fig. 3.58 Comparison of kinetic energy in non-dimensional co-ordinates for PAMH 5ppm solution with its Re matched water experiments.

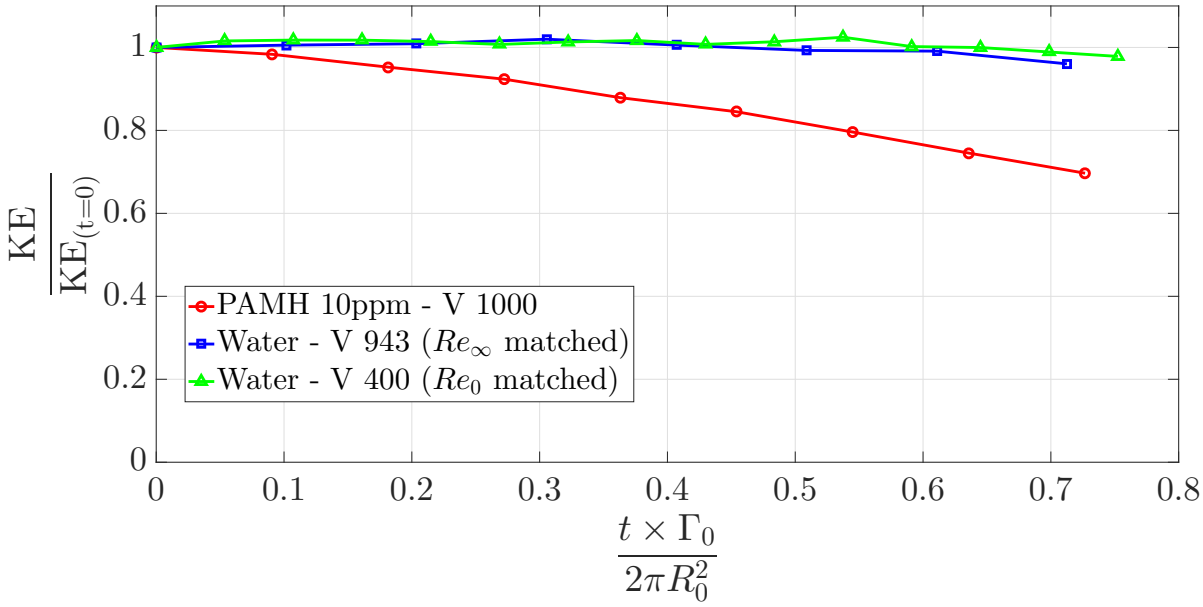

Fig. 3.59 Comparison of kinetic energy in non-dimensional co-ordinates for PAMH 10ppm solution with its Re matched water experiments. Significant reduction in kinetic energy is observed for PAMH 10ppm even when compared with lower limit of Reynolds number i.e. Re_0 experiment in water.

3.6 Formation Number

In a seminal work Gharib et al. (1998) showed that there exists a saturation of circulation for vortex rings generated using piston cylinder mechanism. Piston cylinder mechanism is widely used for generation of vortex rings. Slug of fluid pushed out by piston motion, curls up to form vortex ring. Hence, as the amount of fluid pushed out increases, vortex ring also grows in size and circulation. However, Gharib et al. (1998) showed that vortex ring can't grow indefinitely and there exists a limiting circulation which is obtained at $L \approx 4 \times D$ (L = stroke-length of piston, D = nozzle dia). Hence, the fluid pushed out after this limiting stroke-length won't get entrained inside the ring, and follows the ring as a trailing jet. This limiting non-dimensional stroke-length is famously called Formation Number (or $\frac{L}{D}$ ratio).

As explained in section 1.2, existence of saturation in circulation has attracted lot of attention in fluid dynamics community, because of its applications in underwater vehicles and bio-inspired propulsion. Interestingly, limiting $\frac{L}{D}$ doesn't exist for vortex pairs, which is 2D Cartesian analogue of vortex rings (Afanasyev, 2006; Gao and Yu, 2016; Pedrizzetti, 2010). Krueger et al. (2006) showed that formation number varies if background co-flow or counter-flow is present during vortex ring formation. Dabiri and Gharib (2005) studied effect of temporally varying nozzle exit diameter on vortex ring formation number.

A set of experiments were conducted with varying $\frac{L}{D}$ ratio in different polymer solutions, to check the effect of non-newtonian properties on vortex ring formation number. Figure 3.61, 3.62 and 3.63 shows vorticity field for vortex ring experiments in PAMH 5, 10 and 25 ppm experiments with varying L/D ratio. Figures from left to right shows time evolution of vorticity field for that particular case. In all solutions, piston velocity is kept constant at 500 mm/s, as piston stroke-length is varied to get different $\frac{L}{D}$ ratios.

Figure 3.60 shows effect of formation number on vortex formation in water solution. When $\frac{L}{D} \leq 4$, an isolated vortex ring without a trailing jet is formed. However, for $\frac{L}{D} \geq 4$ a clear trailing jet is seen behind the vortex ring. These observations are in line with those of Gharib et al. (1998).

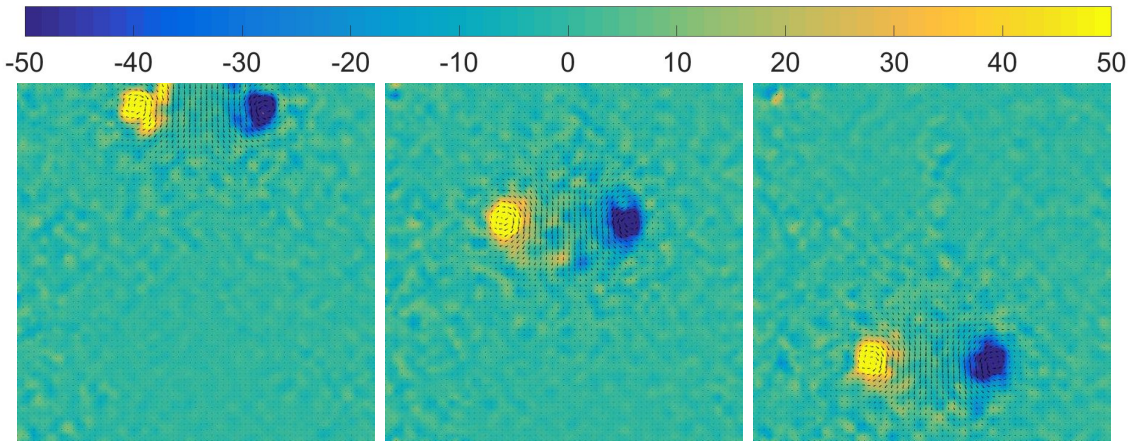

(a) L/D = 2.88

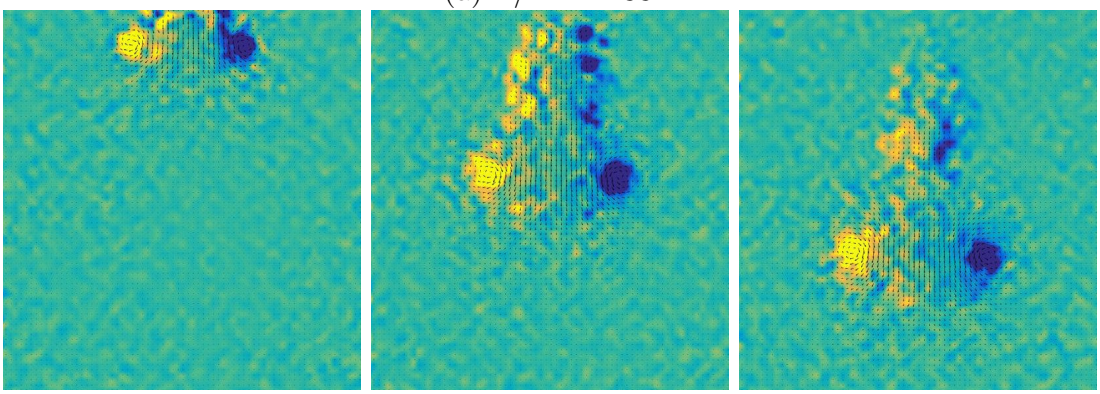

(b) L/D = 5.76

Fig. 3.60 Vorticity field for Water rings for two different L/D ratios. Vorticity scale shown above is used for figure 3.60, 3.61, 3.62 and 3.63

From figure 3.61, 3.62 and 3.63, it is clear that there is no difference in formation number for polymer vortex rings. As long as $\frac{L}{D} \leq 4$, an isolated vortex ring is formed in polymer solutions too. A trailing jet is seen only for experiments with $\frac{L}{D} \geq 4$. Figure 3.64 clearly shows that the primary vortex ring's circulation saturates, although total circulation increases for $\frac{L}{D} \geq 4$.

Hence, addition of polymers which is earlier shown to change vorticity distribution, circulation, enstrophy etc, doesn't have any effect on formation number (Note: Structure of vortex rings in PAMH 25ppm solution is clearly different from water rings). Vorticity strength of the trailing jet increases with increase in $\frac{L}{D}$ ratio. Hence, trailing jet is more clearly observed at higher L/D ratios.

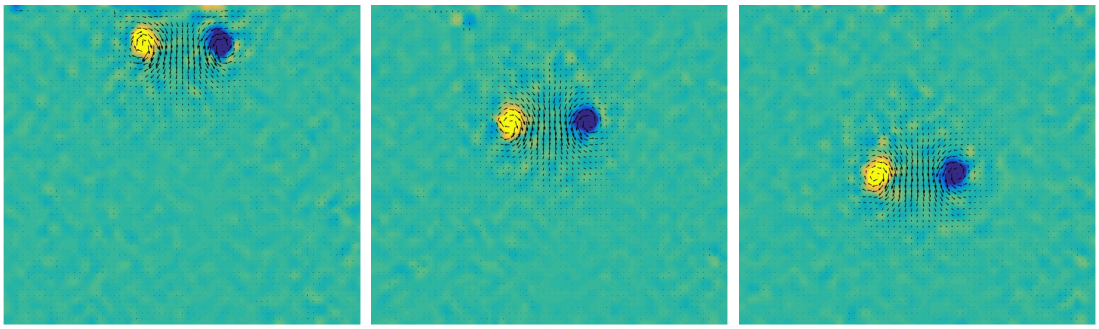

(a) L/D = 1.44

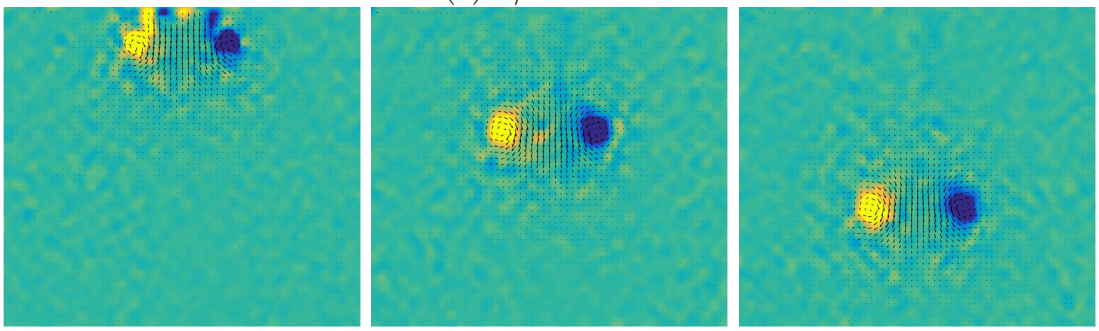

(b) L/D = 2.88

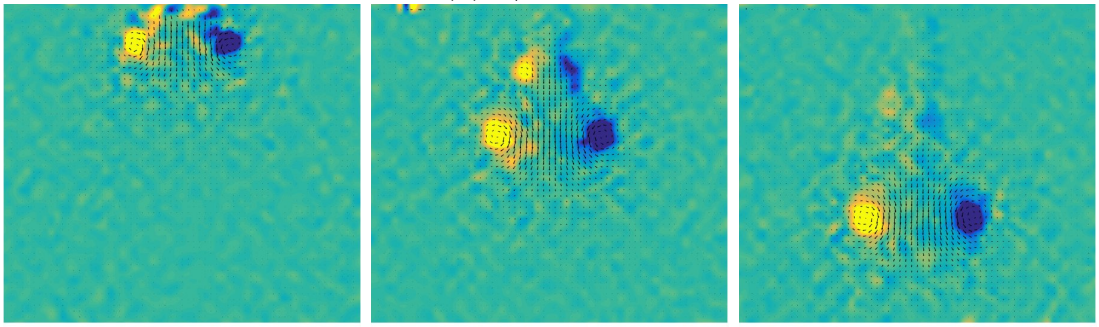

(c) L/D = 4.32

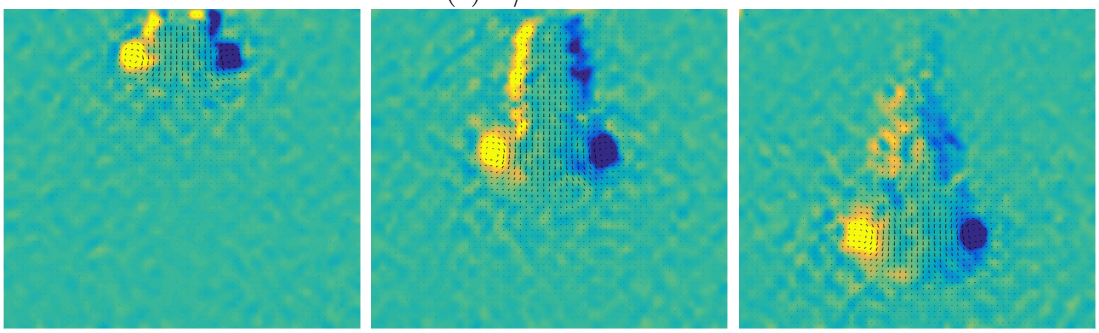

(d) L/D = 5.76

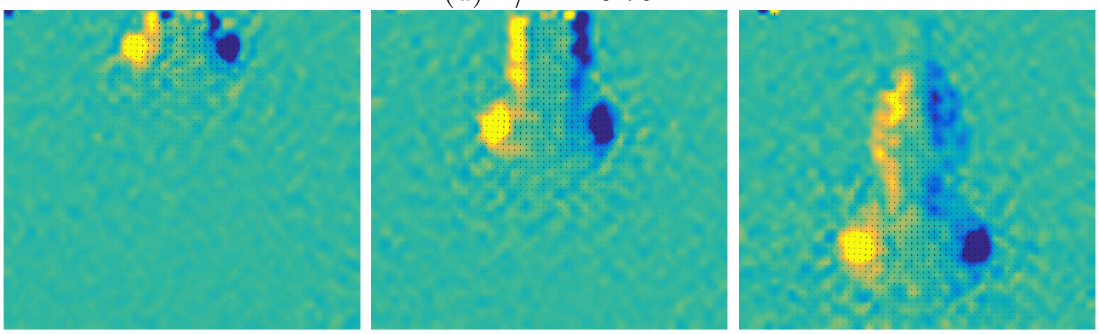

(e) L/D = 7.2

Fig. 3.61 Vorticity field for PAMH 5 ppm rings for different L/D ratios.

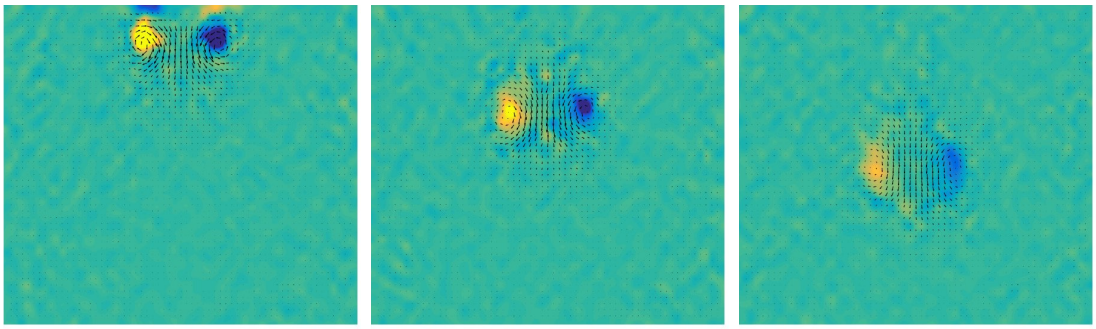

(a) L/D = 1.44

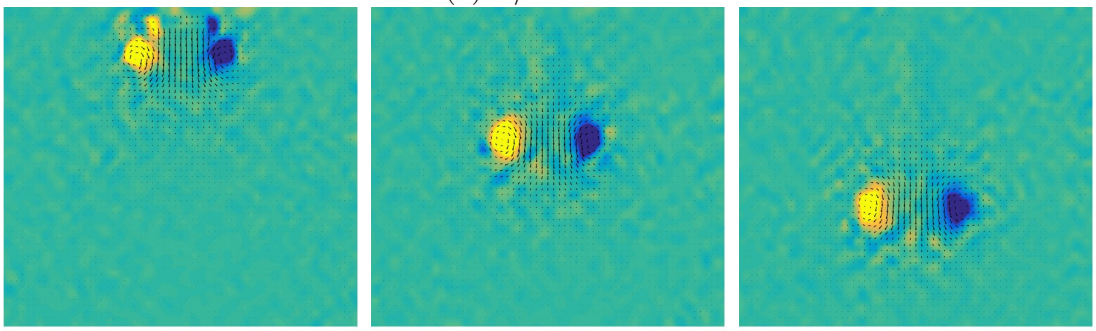

(b) L/D = 2.88

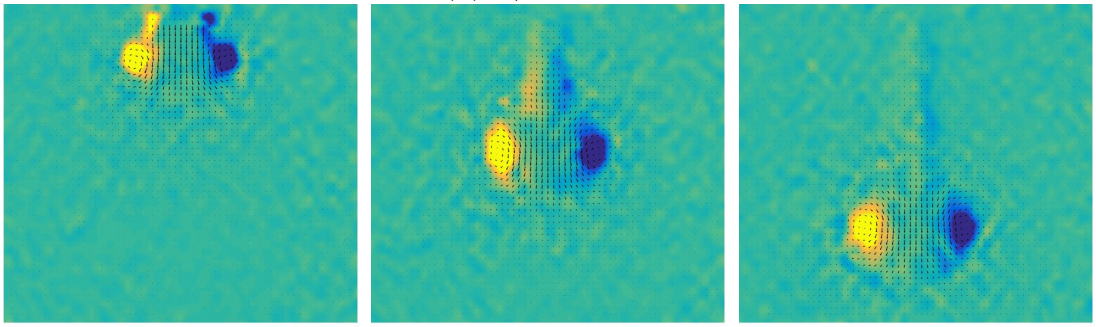

(c) L/D = 4.32

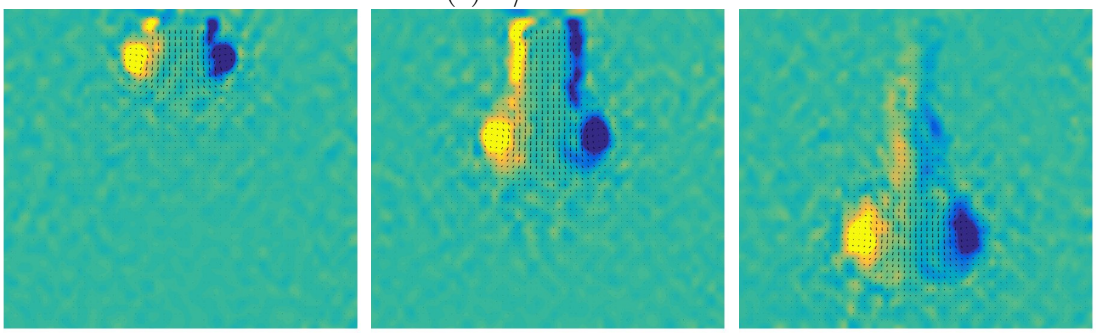

(d) L/D = 5.76

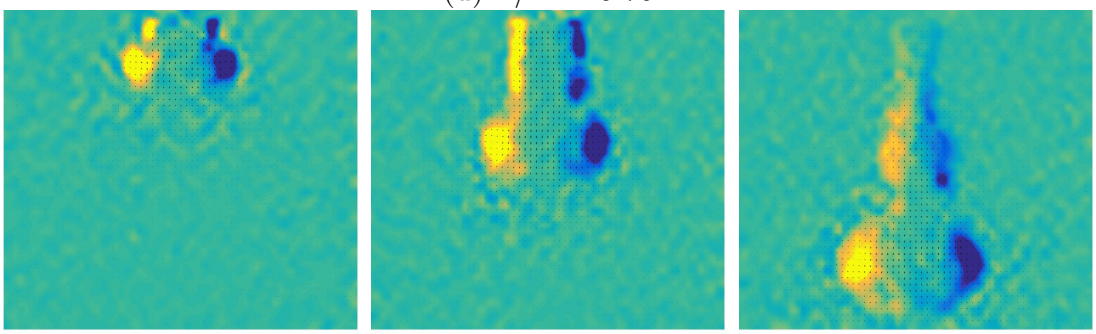

(e) L/D = 7.2

Fig. 3.62 Vorticity field for PAMH 10 ppm rings for different L/D ratios.

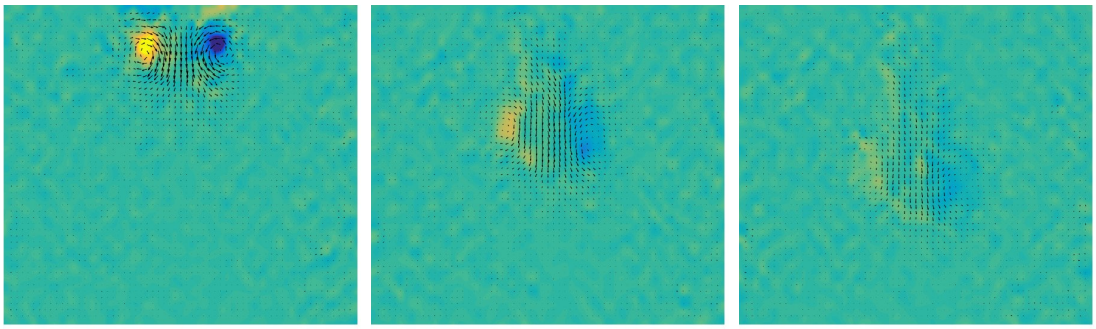

(a) L/D = 1.44

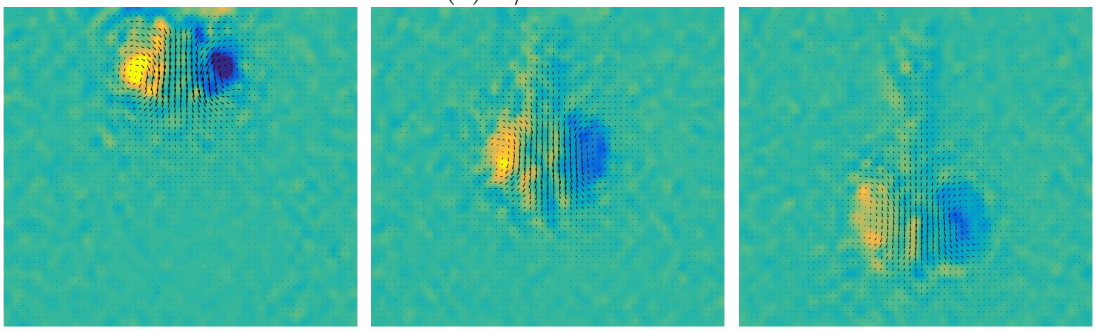

(b) L/D = 2.88

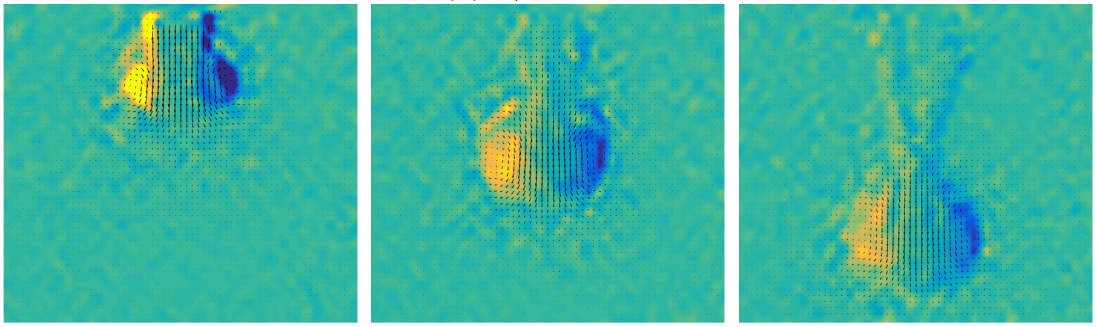

(c) L/D = 4.32

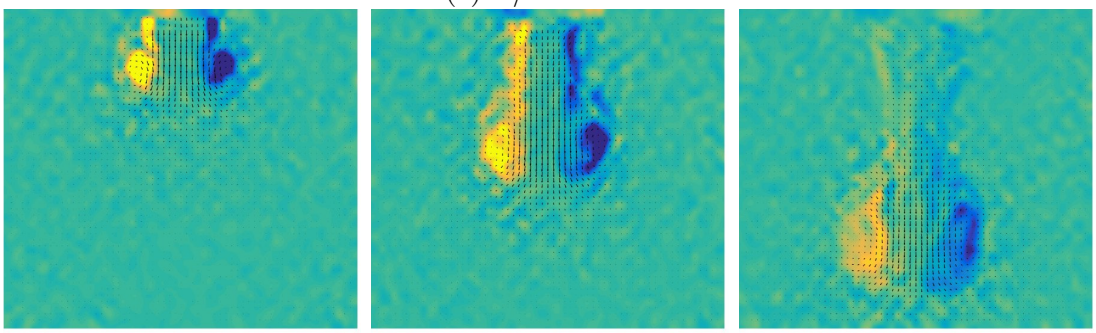

(d) L/D = 5.76

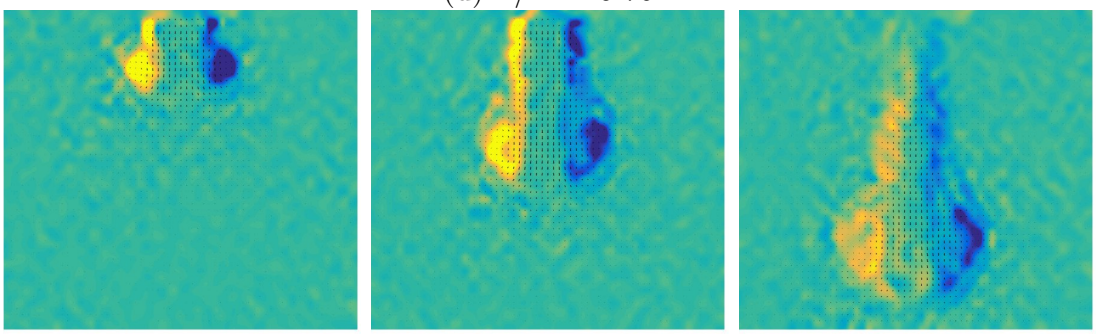

(e) L/D = 7.2

Fig. 3.63 Vorticity field for PAMH 25 ppm rings for different L/D ratios.

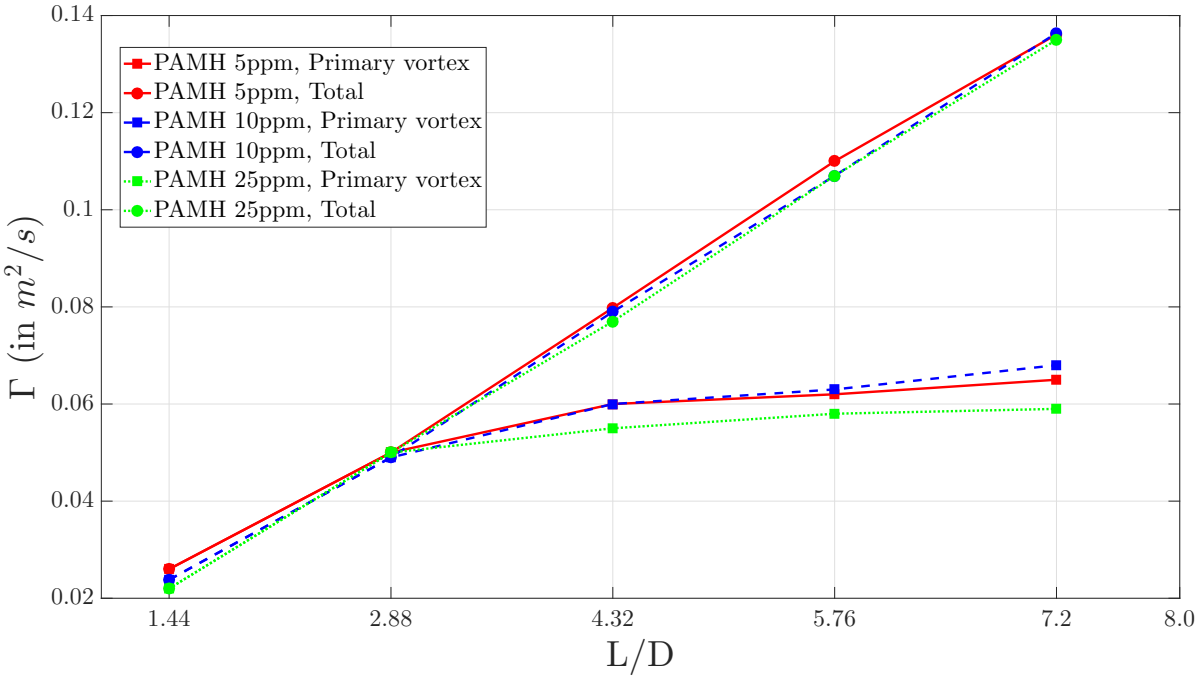

Fig. 3.64 Comparison of primary vortex ring circulation to total circulation.

Linden and Turner (2001) and Mohseni and Gharib (1998) proposed an argument for existence of formation number using limiting member of Norbury family vortex rings i.e. Hill's spherical vortex. According to this model, as piston stroke-length increases, vortex ring core diameter also increases. This increase in core-diameter will cause the ring to move from thin core to thick core then finally reach Hill's spherical vortex (Norbury, 1973). Once, Hill's spherical vortex state is reached, vortex ring can't take any more circulation, causing the formation of trailing jet. Using this model, Linden and Turner (2001); Mohseni and Gharib (1998) found formation number to be approximately 4. It is clear from our experiments that vortex ring core size increases, with increase in stroke-length. However, vortex rings are still far from Hill's spherical vortex state when formation number is reached , or when trailing jet appears. Very similar observation could be made from earlier work of Gharib et al. (1998). This suggests that, possible reason for formation number could be different from this norbury family of rings. Other arguments available in literature for existence of formation number involve Kelvin-Helmholtz variational principle (Gharib et al., 1998), and perturbation response of vortex rings (Kaplanski and Rudi, 2005; O'Farrell and Dabiri, 2012, 2014).

Chapter 4

Conclusion

Vortex ring experiments were conducted in water and PAMH solution with three different concentrations of 5, 10 and 25ppm. Vortex rings were generated using standard piston cylinder mechanism. Dye visualisation and Planar Laser Induced Florescence were used for qualitative flow visualization. Particle Image Velocimetry was used for quantitative flow field measurement. PIVLab based MATLAB code was developed for carrying out PIV analysis. Circulation, enstrophy, kinetic energy, peak vorticity, distance traveled, diameter and vorticity distribution are the quantitatively measured vortex ring properties.

Series of polymer solution measurements were carried out to characterize rheological properties. Oscillatory rheometry, which is predominantly used for characterization of viscoelasticity, fails because of lesser concentration used in our polymer solutions. Hence, rotational rheometry measurements along with carreau-yasuda model is used for polymer characterization. Viscometric measurements and dynamic light scattering experiments were also conducted. All the three polymer solutions used in our experiments show shear thinning behaviour along with elasticity. Concentrations of polymer solutions are carefully chosen to cover a wide range of viscosities and carreau-yasuda relaxation time.

Experiments are conducted in water covering wide range of Re, from 4000 to 100000. A kind of saturation is observed in different properties of water vortex rings at higher Re, which could be attributed to enhanced turbulent eddy viscosity at higher Re. Increase in core-diameter with increase in piston input velocity is observed in experiments. Salient features of vortex ring wall interaction, such as, boundary layer development over the wall, separation of boundary layer into secondary and tertiary vortex rings, combined movement of primary and secondary vortex rings are clearly captured using both PIV

and PLIF techniques.

Two different sets of experiments were carried out for polymer solutions, one with matched input impulse and another with matched Reynolds number, with their water couterparts. Three distinct stages were observed in vortex ring wall interaction experiments, both in water and polymer solutions. (1) Formation stage (2) Free shear movement (3) Wall interaction and dissipation are the three stages. Formation stage is nearly unaffected by polymer addition. Different properties measured show deviation during free shear stage for polymer solutions when compared to water. Larger deviation is observed for higher concentration solutions. Though measurements at wall interaction stage are restricted by PIV resolution, certain deviations from water case are observed.

Polymer solutions show shear thinning behavior, without a fixed viscosity. Hence a methodology is developed to carry out *Re* matched experiments. This involves, calculating the upper and lower limiting Reynolds numbers of polymer vortex ring, and then carrying out experiments in water with those Reynolds numbers. Different properties are then plotted in suitable non-dimensional co-ordinates to demonstrate the possible viscosity contribution to the changes observed in polymer solutions.

Reduction in circulation, enstrophy, kinetic energy and peak vorticity is consistently observed for polymer solutions during free shear movement for all range of impulses used. Changes in vorticity distribution is the main cause for such a reduction. Shear thinning viscosity of polymer solutions breaks self-similarity of vorticity evolution and can cause changes in vorticity distribution. Hence, shear dependent viscosity of polymer solutions could be the main reason for all the changes observed through modification of vorticity distribution. Also, theoretically it is possible to explain all the changes without even appealing to elastic effects. Though polymer solutions are known to have elasticity, contribution of elasticity to the changes observed couldn't be quantified at this point of time.

A set of experiments were carried out to check the effect of polymers on formation number. However, formation number of approximately 4 is observed even in polymer solutions. In conclusion, presence of polymers has effect on many properties of vortex ring, through modification in vorticity distribution, and has no effect on few other properties like formation number. Connecting these observations on individual vortex ring with

the larger picture of turbulent flows will give better understanding of this long-standing conundrum i.e. polymer drag reduction.

References

Adrian, R. J. (2005). Twenty years of particle image velocimetry. *Experiments in fluids*, 39(2):159–169.

Adrian, R. J. and Westerweel, J. (2011). *Particle image velocimetry*. Number 30. Cambridge University Press.

Afanasyev, Y. (2006). Formation of vortex dipoles. *Physics of fluids*, 18(3):037103.

Allen, J. and Auvity, B. (2002). Interaction of a vortex ring with a piston vortex. *Journal of Fluid Mechanics*, 465:353–378.

Allen, J., Jouanne, Y., and Shashikanth, B. (2007). Vortex interaction with a moving sphere. *Journal of Fluid Mechanics*, 587:337–346.

ANSYS (2018). Ansys® academic research mechanical, release 18.1.

Bentata, O. (2013). *Étude expérimentale d'un anneau tourbillonnaire en fluide newtonien et non newtonien en régime faiblement inertiel*. PhD thesis.

Benzi, R. and Ching, E. S. (2018). Polymers in fluid flows. *Annual Review of Condensed Matter Physics*, 9:163–181.

Berman, N. S. (1978). Drag reduction by polymers. *Annual Review of Fluid Mechanics*, 10(1):47–64.

Bewersdorff, H., Gyr, A., Hoyer, K., and Tsinober, A. (1993). An investigation of possible mechanisms of heterogeneous drag reduction in pipe and channel flows. *Rheologica acta*, 32(2):140–149.

Cadot, O., Bonn, D., and Douady, S. (1998). Turbulent drag reduction in a closed flow system: Boundary layer versus bulk effects. *Physics of Fluids*, 10(2):426–436.

Cater, J. E., Soria, J., and Lim, T. (2004). The interaction of the piston vortex with a piston-generated vortex ring. *Journal of Fluid Mechanics*, 499:327–343.

Chandra, B., Shankar, V., and Das, D. (2018). Onset of transition in the flow of polymer solutions through microtubes. *Journal of Fluid Mechanics*, 844:1052–1083.

Choueiri, G. H., Lopez, J. M., and Hof, B. (2018). Exceeding the asymptotic limit of polymer drag reduction. *Phys. Rev. Lett.*, 120:124501.

Chu, C.-C., Wang, C.-T., and Chang, C.-C. (1995). A vortex ring impinging on a solid plane surface—vortex structure and surface force. *Physics of Fluids*, 7(6):1391–1401.

Chu, C.-C., Wang, C.-T., and Hsieh, C.-S. (1993). An experimental investigation of vortex motions near surfaces. *Physics of Fluids A: Fluid Dynamics*, 5(3):662–676.

Dabiri, J. O. (2009). Optimal vortex formation as a unifying principle in biological propulsion. *Annual review of fluid mechanics*, 41:17–33.

Dabiri, J. O. and Gharib, M. (2005). Starting flow through nozzles with temporally variable exit diameter. *Journal of Fluid Mechanics*, 538:111–136.

Das, D., Bansal, M., and Manghnani, A. (2017). Generation and characteristics of vortex rings free of piston vortex and stopping vortex effects. *Journal of Fluid Mechanics*, 811:138–167.

Das, D., Manghnani, A., Bansal, M., and Sohoni, P. (2016). Axial interaction of a vortex ring with a cylinder. *Journal of Fluid Mechanics*, 809:1–30.

De Angelis, E., Casciola, C. M., L'vov, V. S., Pomyalov, A., Procaccia, I., and Tiberkevich, V. (2004). Drag reduction by a linear viscosity profile. *Phys. Rev. E*, 70:055301.

De Gennes, P. G. (1990). Introduction to polymer dynamics.

Den Toonder, J., Hulsen, M., Kuiken, G., and Nieuwstadt, F. (1997). Drag reduction by polymer additives in a turbulent pipe flow: numerical and laboratory experiments. *Journal of Fluid Mechanics*, 337:193–231.

Deng, Z., Richmond, M. C., Guensch, G. R., and Mueller, R. P. (2004). Study of fish response using particle image velocimetry and high-speed, high-resolution imaging. Technical report, Pacific Northwest National Lab.(PNNL), Richland, WA (United States).

Didden, N. (1979). On the formation of vortex rings: rolling-up and production of circulation. *Zeitschrift für angewandte Mathematik und Physik ZAMP*, 30(1):101–116.

Doligalski, T., Smith, C., and Walker, J. (1994). Vortex interactions with walls. *Annual Review of Fluid Mechanics*, 26(1):573–616.

Dubief, Y., Terrapon, V. E., White, C. M., Shaqfeh, E. S., Moin, P., and Lele, S. K. (2005). New answers on the interaction between polymers and vortices in turbulent flows. *Flow, turbulence and combustion*, 74(4):311–329.

Fabris, D., Liepmann, D., and Marcus, D. (1996). Quantitative experimental and numerical investigation of a vortex ring impinging on a wall. *Physics of Fluids*, 8(10):2640–2649.

Fraenkel, L. E. (1972). Examples of steady vortex rings of small cross-section in an ideal fluid. *Journal of Fluid Mechanics*, 51(1):119–135.

Fukumoto, Y. and Moffatt, H. (2000). Motion and expansion of a viscous vortex ring. part 1. a higher-order asymptotic formula for the velocity. *Journal of Fluid Mechanics*, 417:1–45.

Gao, L. and Yu, S. (2010). A model for the pinch-off process of the leading vortex ring in a starting jet. *Journal of Fluid Mechanics*, 656:205–222.

Gao, L. and Yu, S. (2016). Formation of leading vortex pair in two-dimensional starting jets. *AIAA Journal*, 54(1):1364–1369.

Garg, P., Chaudhary, I., Khalid, M., Shankar, V., and Subramanian, G. (2018). Viscoelastic Pipe Flow is Linearly Unstable. *Physical Review Letters*, 121(2):024502.

Gharib, M., Rambod, E., Kheradvar, A., Sahn, D. J., and Dabiri, J. O. (2006). Optimal vortex formation as an index of cardiac health. *Proceedings of the National Academy of Sciences*, 103(16):6305–6308.

Gharib, M., Rambod, E., and Shariff, K. (1998). A universal time scale for vortex ring formation. *Journal of Fluid Mechanics*, 360:121–140.

Glezer, A. and Coles, D. (1990). An experimental study of a turbulent vortex ring. *Journal of Fluid Mechanics*, 211:243–283.

Graham, M. D. (2004). Drag Reduction in Turbulent Flow of Polymer Solutions. *The British Society of Rheology*, 2004:143–170.

Groisman, A. and Steinberg, V. (2000). Elastic turbulence in a polymer solution flow. *Nature*, 405(6782):53–55.

Gyr, A., Bewersdorff, H.-W., Bühler, J., and Papantoniou, D. (1992). The interaction of polymer additives with vorticity (a case study on vortex rings). *Journal of Non-Newtonian Fluid Mechanics*, 43(2-3):179–194.

Jha, N. K. and Govardhan, R. (2015). Interaction of a vortex ring with a single bubble: bubble and vorticity dynamics. *Journal of Fluid Mechanics*, 773:460–497.

Joseph, D. D. (1990). Fluid dynamics of viscoelastic liquids.

Kaplanski, F. B. and Rudi, Y. A. (2005). A model for the formation of "optimal" vortex rings taking into account viscosity. *Physics of Fluids*, 17(8):087101.

Krueger, P. S., Dabiri, J. O., and Gharib, M. (2006). The formation number of vortex rings formed in uniform background co-flow. *Journal of Fluid Mechanics*, 556:147–166.

Lim, T. (1989). An experimental study of a vortex ring interacting with an inclined wall. *Experiments in Fluids*, 7(7):453–463.

Linden, P. and Turner, J. (2001). The formation of 'optimal'vortex rings, and the efficiency of propulsion devices. *Journal of Fluid Mechanics*, 427:61–72.

Lumley, L. (1969). DRAG REDUCTION BY ADDITIVESl. *Annual Review of Fluid Mechanics*, 1(33):367–387.

L'vov, V. S., Pomyalov, A., Procaccia, I., and Tiberkevich, V. (2004). Drag reduction by polymers in wall bounded turbulence. *Phys. Rev. Lett.*, 92:244503.

L'Vov, V. S., Pomyalov, A., Procaccia, I., and Tiberkevich, V. (2004). Drag reduction by polymers in wall bounded turbulence. *Physical Review Letters*, 92(24):1–4.

Marhefka, J. and Kameneva, M. (2016). Natural Drag-Reducing Polymers: Discovery, Characterization and Potential Clinical Applications. *Fluids*, 1(2):6.

Marhefka, J., Zhao, R., Wu, Z., Velankar, S., Antaki, J., and Kameneva, M. (2009). Drag reducing polymers improve tissue perfusion via modification of the rbc traffic in microvessels. *Biorheology*, 46(4):281–292.

Maxworthy, T. (1972). The structure and stability of vortex rings. *Journal of Fluid Mechanics*, 51(1):15–32.

Maxworthy, T. (1977). Some experimental studies of vortex rings. *Journal of Fluid Mechanics*, 81(3):465–495.

McComb, W. and Rabie, L. (1979). Development of local turbulent drag reduction due to nonuniform polymer concentration. *The Physics of Fluids*, 22(1):183–185.

Mendoza-Fuentes, A., Montiel, R., Zenit, R., and Manero, O. (2009). On the flow of associative polymers past a sphere: Evaluation of negative wake criteria. *Physics of fluids*, 21(3):033104.

Min, T., Yoo, J. Y., Choi, H., and Joseph, D. D. (2003). Drag reduction by polymer additives in a turbulent channel flow. *Journal of Fluid Mechanics*, 486:213–238.

Mohseni, K. and Gharib, M. (1998). A model for universal time scale of vortex ring formation. *Physics of Fluids*, 10(10):2436–2438.

Mohseni, K., Ran, H., and Colonius, T. (2001). Numerical experiments on vortex ring formation. *Journal of Fluid Mechanics*, 430:267–282.

Naguib, A. M. and Koochesfahani, M. M. (2004). On wall-pressure sources associated with the unsteady separation in a vortex-ring/wall interaction. *Physics of Fluids*, 16(7):2613–2622.

Naitoh, T., Sun, B., and Yamada, H. (1995). A vortex ring travelling across a thin circular cylinder. *Fluid Dynamics Research*, 15(1):43.

New, T. and Zang, B. (2017). Head-on collisions of vortex rings upon round cylinders. *Journal of Fluid Mechanics*, 833:648–676.

Norbury, J. (1973). A family of steady vortex rings. *Journal of Fluid Mechanics*, 57(3):417–431.

O'Farrell, C. and Dabiri, J. O. (2012). Perturbation response and pinch-off of vortex rings and dipoles. *Journal of Fluid Mechanics*, 704:280–300.

O'Farrell, C. and Dabiri, J. O. (2014). Nested contour dynamics models for axisymmetric vortex rings and vortex wakes. *Journal of Fluid Mechanics*, 748:521–548.

Olsthoorn, J., Stastna, M., and Steinmoeller, D. (2014). On the dynamics of vortex-wall interaction in low viscosity shear thinning fluids. *Physics of Fluids*, 26(1):013101.

Orlandi, P. and Verzicco, R. (1993). Vortex rings impinging on walls: axisymmetric and three-dimensional simulations. *Journal of Fluid Mechanics*, 256:615–646.

Osswald, R. (2014). Polymer rheology.

Palacios-Morales, C., Barbosa, C., Solorio, F., and Zenit, R. (2015). Negative vortices: The formation of vortex rings with reversed rotation in viscoelastic liquids. *Physics of Fluids*, 27(5):051703.

Palacios-Morales, C. and Zenit, R. (2013). The formation of vortex rings in shear-thinning liquids. *Journal of Non-Newtonian Fluid Mechanics*, 194:1–13.

Pedrizzetti, G. (2010). Vortex formation out of two-dimensional orifices. *Journal of Fluid Mechanics*, 655:198–216.

Prasad, A. K. (2000). Particle image velocimetry. *CURRENT SCIENCE-BANGALORE-*, 79(1):51–60.

Procaccia, I., L'Vov, V. S., and Benzi, R. (2008). Colloquium: Theory of drag reduction by polymers in wall-bounded turbulence. *Reviews of Modern Physics*, 80(1):225–247.

Ptasinski, P., Boersma, B., Nieuwstadt, F., Hulsen, M., Van den Brule, B., and Hunt, J. (2003). Turbulent channel flow near maximum drag reduction: simulations, experiments and mechanisms. *Journal of Fluid Mechanics*, 490:251–291.

Raffel, M., Willert, C. E., Scarano, F., Kähler, C. J., Wereley, S. T., and Kompenhans, J. (2018). *Particle image velocimetry: a practical guide*. Springer.

Ren, H. and Xu, C. (2014). Three-dimensional numerical simulation of a vortex ring impacting a bump. *Theoretical and Applied Mechanics Letters*, 4(3).

Reynolds, O. (1876). On the resistance encountered by vortex rings, and the relation between the vortex rings and streamlines of a disk. *Nature*, 14:477–479.

Ryskin, G. (1987). Turbulent drag reduction by polymers: A quantitative theory. *Phys. Rev. Lett.*, 59:2059–2062.

Saffman, P. G. (1981). Vortex dynamics.

Samanta, D., Dubief, Y., Holzner, M., Schäfer, C., Morozov, A. N., Wagner, C., and Hof, B. (2013). Elasto-inertial turbulence. *Proceedings of the National Academy of Sciences*, 110(26):10557–10562.

Shariff, K. and Leonard, A. (1992). Vortex rings. *Annual Review of Fluid Mechanics*, 24(1):235–279.

Shashank, H. J. (2019). Experiments on instability in polyemric pipe flow and vortex rings. PhD thesis (under preparation).

Shusser, M. and Gharib, M. (2000). Energy and velocity of a forming vortex ring. *Physics of Fluids*, 12(3):618–621.

Smith, D. E. and Chu, S. (1998). Response of flexible polymers to a sudden elongational flow. *Science*, 281(5381):1335–1340.

Soto, E., Goujon, C., Zenit, R., and Manero, O. (2006). A study of velocity discontinuity for single air bubbles rising in an associative polymer. *Physics of Fluids*, 18(12):121510.

Sreenivasan, K. R. and White, C. M. (2000). The onset of drag reduction by polymer additives, and drag reduction asymptote. *J.\,Fluid Mech.*, 409:149–164.

Srinivas, S. and Kumaran, V. (2017). Effect of viscoelasticity on the soft-wall transition and turbulence in a microchannel. *Journal of Fluid Mechanics*, 812:1076–1118.

Sullivan, I. S., Niemela, J. J., Hershberger, R. E., Bolster, D., and Donnelly, R. J. (2008). Dynamics of thin vortex rings. *Journal of Fluid Mechanics*, 609:319–347.

Tabor, M. and De Gennes, P. (1986). A cascade theory of drag reduction. *EPL (Europhysics Letters)*, 2(7):519.

Thielicke, W. (2014). The flapping flight of birds. *Diss. University of Groningen*.

Thielicke, W. and Stamhuis, E. (2014). Pivlab–towards user-friendly, affordable and accurate digital particle image velocimetry in matlab. *Journal of Open Research Software*, 2(1).

Tinaikar, A., Advaith, S., and Basu, S. (2018). Understanding evolution of vortex rings in viscous fluids. *Journal of Fluid Mechanics*, 836:873–909.

van Doorn, E., White, C. M., and Sreenivasan, K. (1999). The decay of grid turbulence in polymer and surfactant solutions. *Physics of Fluids*, 11(8):2387–2393.

Verzicco, R., Flor, J., Van Heijst, G., and Orlandi, P. (1995). Numerical and experimental study of the interaction between a vortex dipole and a circular cylinder. *Experiments in fluids*, 18(3):153–163.

Virk, P. S. (1975). Drag reduction fundamentals. *AIChE Journal*, 21(4):625–656.

Virk, P. S., Merrill, E. W., Mickley, H. S., Smith, K. A., and Mollo-Christensen, E. L. (1967). The Toms phenomenon: turbulent pipe flow of dilute polymer solutions. *J . Fluid Me&*, 30(2):305–328.

Vonlanthen, R. and Monkewitz, P. A. (2013). Grid turbulence in dilute polymer solutions: Peo in water. *Journal of Fluid Mechanics*, 730:76–98.

Walker, J., Smith, C., Cerra, A., and Doligalski, T. (1987). The impact of a vortex ring on a wall. *Journal of Fluid Mechanics*, 181:99–140.

Warholic, M. D., Massah, H., and Hanratty, T. J. (1999). Influence of drag-reducing polymers on turbulence: effects of Reynolds number, concentration and mixing. *Experiments in Fluids*, 27(5):461–472.

Weigand, A. and Gharib, M. (1994). On the decay of a turbulent vortex ring. *Physics of fluids*, 6(12):3806–3808.

Westerweel, J. (1997). Fundamentals of digital particle image velocimetry. *Measurement science and technology*, 8(12):1379.

White, C., Somandepalli, V., and Mungal, M. (2004). The turbulence structure of drag-reduced boundary layer flow. *Experiments in fluids*, 36(1):62–69.

White, C. M. and Mungal, M. G. (2008). Mechanics and Prediction of Turbulent Drag Reduction with Polymer Additives. *Annual Review of Fluid Mechanics*, 40(1):235–256.

Willert, C. E. and Gharib, M. (1991). Digital particle image velocimetry. *Experiments in fluids*, 10(4):181–193.

Yang, S.-Q. (2009). Drag Reduction in Turbulent Flow With Polymer Additives. *Journal of Fluids Engineering*, 131(5):051301.

Zhang, Y. and Muller, S. J. (2018). Unsteady sedimentation of a sphere in wormlike micellar fluids. *Physical Review Fluids*, 3(4):043301.

Appendix A

Experiments with near wall area magnified

A set of experiments were conducted, wherein field of view of camera was focused into a small region near the wall. Motivation for these experiments was to capture the boundary layer and formation of secondary vortex ring with better resolution. Macro 105 mm focal length lens was used for these experiments. However, particle density was found to be a limiting factor for these experiments. Even particle density of 6 gm in 1200 liters, was found to be insufficient to carry out PIV at such high zoomed in field of view. And particle density can't be increased further, since higher particle density attenuates laser sheet considerably. Also, at such high zoomed in camera recording, vortex ring enters and leaves the field of view in 1-2 frames. Hence, only a few velocity field can be obtained. Because of these limitations, boundary layer could not be resolved in any of these experiments.

However, a set experiments were conducted with intermediate field of view (Field of view is small compared to earlier full field experiments, but larger than the above explained boundary layer resolved experiments). Resolution of primary ring is better in these experiments compared to earlier full field experiments. All the properties are calculated for these near wall experiments also, and found to be in good agreement with earlier full field experiments. This proves, that the results presented in chapter 3 are resolution independent.

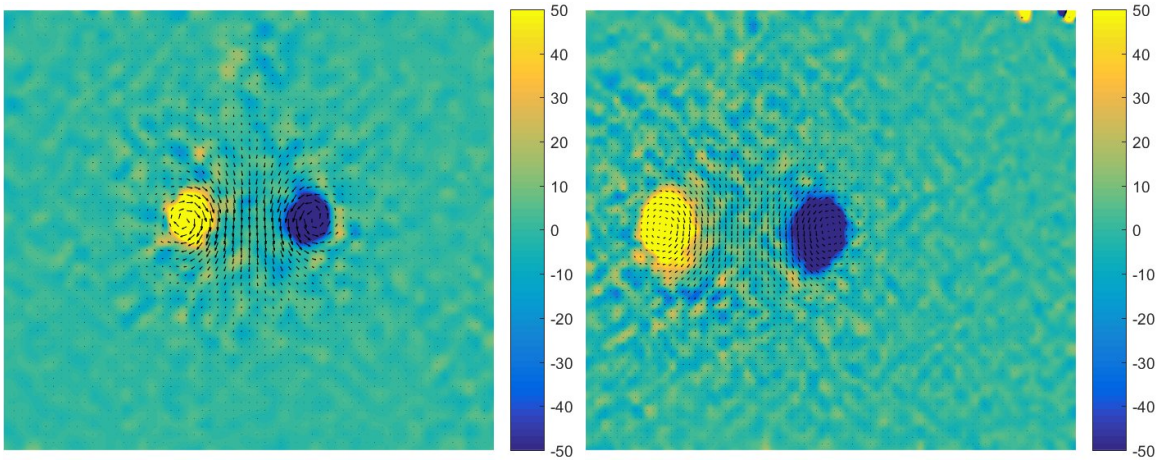

(a) Full field experiment (b) Near wall zoomed experiment

Fig. A.1 Velocity field obtained from PIV experiments with two fields of interest.

Appendix B

Reynolds stress

It is widely observed in polymer drag reduction literature that addition of polymers affects Reynolds stress (Refer figure 1.5 and 1.9b). Reduction in Reynolds stress is also proposed as a reason for turbulent drag reduction. Motivated by this, Reynolds stress was calculated in our vortex ring experiments using ensemble averaging. Five experiments for each case were considered for Reynolds stress calculations.

Reynolds shear stress field was calculated in our experiments. Methodology followed is given below.

1. u and v velocity fields for a given time step were averaged over all the five runs to get $\overline{u}$ and $\overline{v}$.
2. For each run, at a given time step, u' and v' were calculated by subtracting u, v from $\overline{u}$, $\overline{v}$ velocity fields respectively.
3. $u'v'$ quantity was calculated for each run.
4. Quantity $u'v'$ was summed over all the five runs for the particular time step to get $\overline{u'v'}$. -$\overline{u'v'}$ gives Reynolds shear stress field for the particular time step.
5. Same procedure was carried out for all the time steps.

Figure B.1 shows Reynolds stress at three different time instants. Color-scheme used for all the plots is given below.

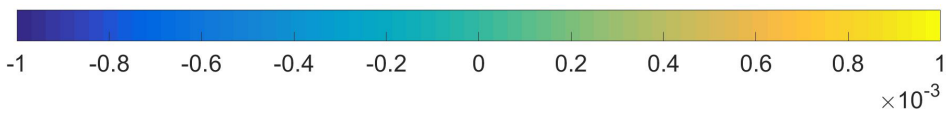

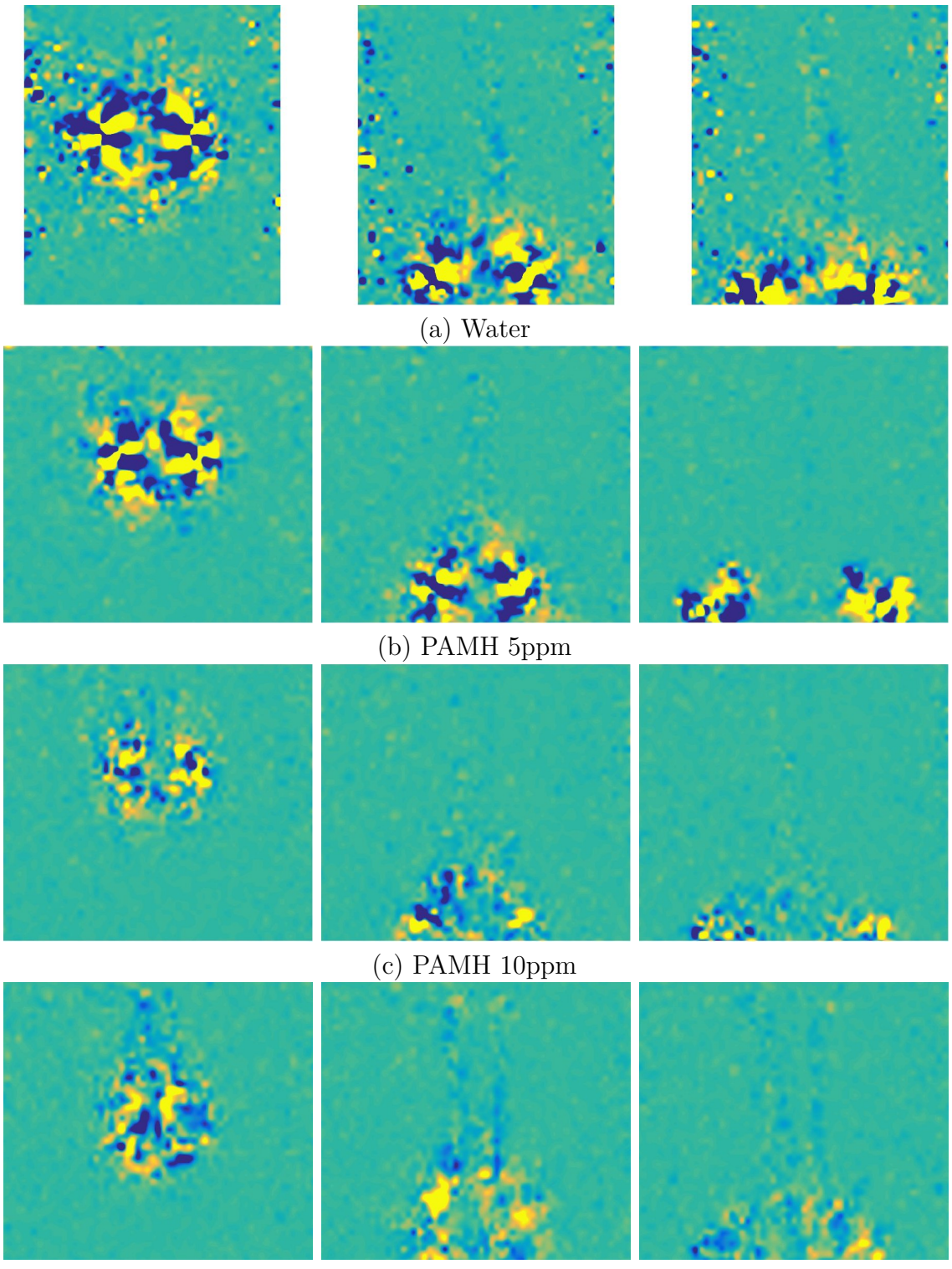

(a) Water

(b) PAMH 5ppm

(c) PAMH 10ppm

(d) PAMH 25ppm

Fig. B.1 Reynolds shear stress field for water and polymer vortex rings (L100 V500 case).

Figure B.1 shows Reynolds stress at three different time instants for water and polymer solutions for L100 V500 case. Though it is hard to conclusively conclude anything, it seems that Reynolds stress patches gets smaller and smaller with increase in polymer concentration. Also it seems that intensity of Reynolds stress reduces with increase in polymer concentration. In higher concentration polymer solutions (i.e. in PAMH 10 & 25ppm), velocity associated with vortex ring and the field itself is smaller, and this could be a possible reason for reduction in Reynolds stress observed.

However, more experiments are needed to confirm above observations. Also, ensemble averaging has to be carried out with more runs for accurate results. Experiments have to be carried out at higher frequency, than the current 25 Hz for better time resolution.

Appendix C

Synthetic Dye Visualization

Synthetic dye visualization is a technique in which artificial dye particles are put in the velocity field obtained by the PIV measurements. At every time instant particles are displaced according to their local velocity, which is obtained from PIV velocity field, and their new position is updated. PIV measurements being instantaneous, sometimes fail to capture time integrated effects. Hence, by Lagrangian tracking of particles, it is possible to observe such time integrated effects, which otherwise would have missed in instantaneous velocity fields of PIV.

This technique was implemented in multiple ways. One among them was putting particles right on top of the ring, just after formation of ring and observe their movement (Refer figure C.1). However, all particles move out of the ring and accumulate at the circumference. The reason is, at any given time instant, velocity vector is tangential to actual particle path, and contributes to slight outward movement.

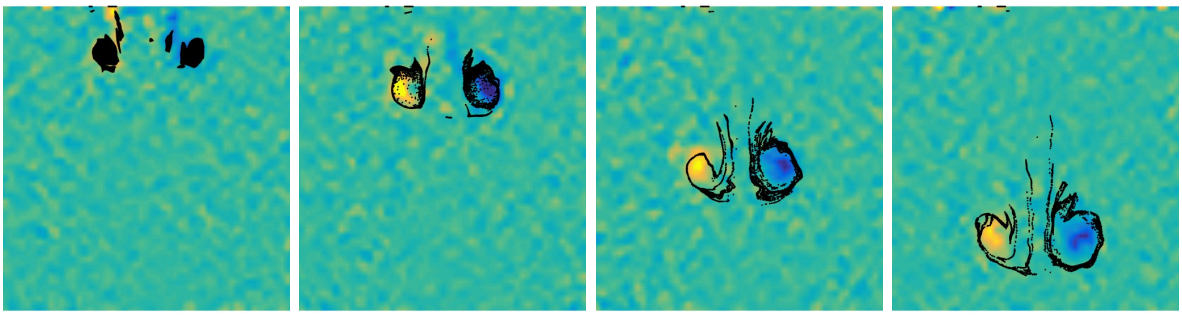

Fig. C.1 Synthetic dye visualization with particles put on top of the vortex ring. PAMH 5ppm solution, L100 V100 case.

In another method, particles were kept in straight line just ahead of the ring, and their movement was observed (Refer figure C.2). Patterns observed in these kind of simulations depend extremely on initial condition of particles. Also no considerable difference was observed between water and polymer solution experiments.

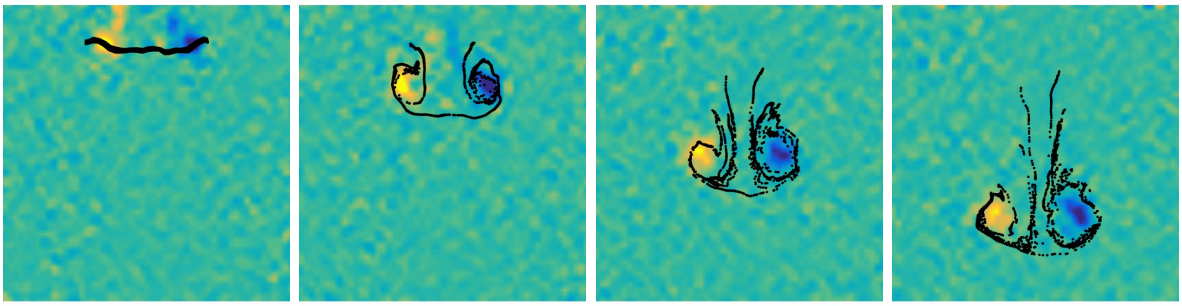

Fig. C.2 Synthetic dye visualization with particles put in a straight line just ahead of vortex ring. PAMH 5ppm solution, L100 V100 case.

Attempts were done to capture boundary layer instability waves, and secondary ring by putting particles near wall (Refer figure C.3). However, no conclusive observations could be made. The reason is, velocity profile inside the boundary layer itself is not clearly resolved, and using this velocity for particle movement would give erroneous results. Coarse time resolution (i.e. 25 Hz) is another important limitation.

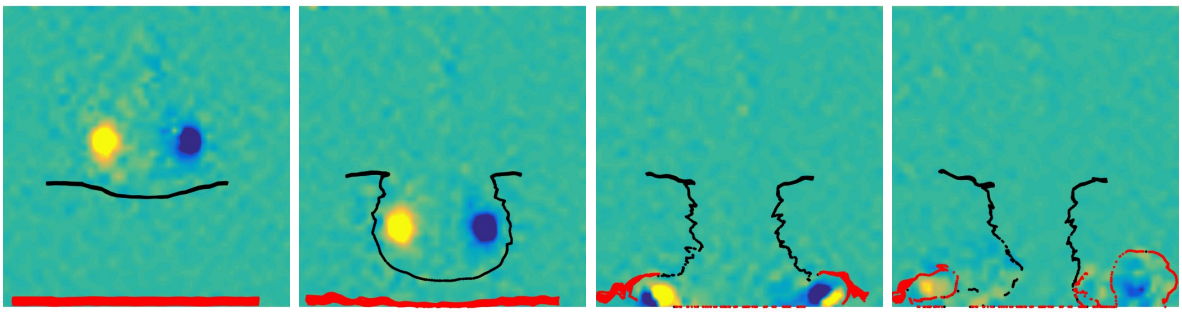

Fig. C.3 Synthetic dye visualization with particles put near the wall. PAMH 5ppm solution, L100 V500 case.

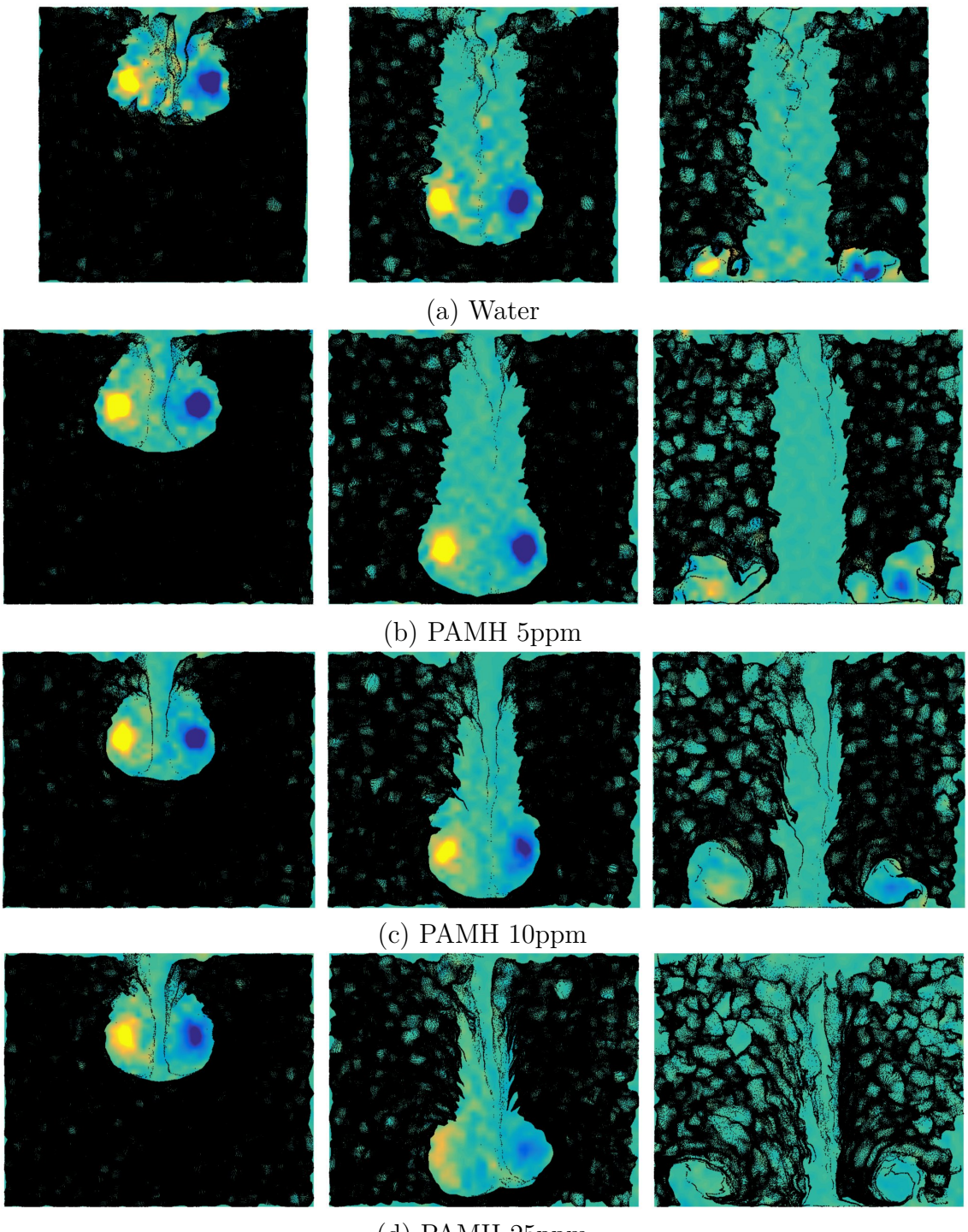

(a) Water

(b) PAMH 5ppm

(c) PAMH 10ppm

(d) PAMH 25ppm

Fig. C.4 Synthetic dye visualization for water and different polymer solutions - L100 V500 case.

In a final attempt, particle were placed throughout the domain, and all the particles were tracked throughout the duration (Refer figure C.4). Clustering of particles seems to be happening in ambient, which could be because of 3rd dimensional movement. No significant changes was observed among different solutions as far as vortex ring is concerned. However, wake behind the ring seems to be quite different for water when compared to polymer solutions. Water has wider wake with clear wake-ambient boundary, whereas higher concentration polymer solutions i.e. PAMH 10 & 25ppm have narrow wake with blurred wake-ambient boundary.

Single particle trajectory for PAMH 5ppm L100 V100 case is shown in figure C.5. Very similar trajectories were observed for particles in water and other polymer solutions also.

Fig. C.5 Particle trajectory over the total duration for PAMH 5ppm solution, L100 V500 case, as captured using synthetic dye visualization.

Appendix D

Theoretical calculations

Theoretical calculations were carried out, during our efforts to build a simple model which can capture larger behaviour seen in our experiments. Many properties of vortex rings are analytically calculated, although with oversimplifying assumptions (Fukumoto and Moffatt, 2000; Saffman, 1981; Sullivan et al., 2008; Tinaikar et al., 2018). In our study we calculate the variation of circulation, enstrophy and vorticity profile as a function of time. Effect of Reynolds number and viscosity of the solution is found.

Circulation, being a conserved quantity, will have the same value at all times (even at $Re = 0$) if calculated over infinitely large domain. However, in all practical situations, circulation reduces with time, given time is long enough. This is mainly because in all practical situations, circulation is calculated over finite domain size. Another way of calculating circulation involves threshold vorticity. Only vorticity above the threshold is considered for circulation calculation. Both these ways of calculating circulation can generate artificial results, if not used properly. Our motivation is to check evolution of different properties with these two methods of calculation.

Vorticity distribution inside the core of the ring is assumed to be 2D Gaussian. This vorticity distribution undergoes viscous diffusion, which causes further changes in vortex ring properties. However, at $t = 0$ this Gaussian distribution becomes Dirac-delta function. Hence, $t = 0$ is a singularity in our calculations.

Vorticity distribution is given by,

$$\omega(r,t) = \frac{\Gamma_0}{4\pi\nu t} e^{(\frac{-r^2}{4\nu t})} \tag{D.1}$$

Hence, at time $t = 0$, vorticity distribution is a dirac-delta function.

$$\omega(r, t = 0) = \Gamma_0 \delta(r = 0) \tag{D.2}$$

Circulation is calculated as,

$$\Gamma(t) = \int_{r=0}^{r=a} \omega(r, t) dA = \int_{r=0}^{r=a} \omega(r, t) 2\pi r dr \tag{D.3}$$

However, if circulation is calculated over infinitely large domain, then it is independent of time and is a constant

$$\Gamma(t) = \int_{r=0}^{r=\infty} \omega(r, t) dA = constant \tag{D.4}$$

Now, consider finite circular domain with radius a, over which circulation is calculated. Vorticity diffusing out of this finite domain won't contribute to circulation calculation anymore. This correction brings circulation calculation a step closer to practical situations.

$$\Gamma(t) = \int_{r=0}^{r=a} \omega(r, t) dA = \int_{r=0}^{r=a} \frac{\Gamma_0}{4\pi\nu t} e^{(\frac{-r^2}{4\nu t})} 2\pi r dr \tag{D.5}$$

However, the quantity of interest is $\frac{\Gamma(t)}{\Gamma(t=0)}$. From integrating equation D.2, we get $\Gamma(t = 0) = \Gamma_0$. Hence,

$$\frac{\Gamma(t)}{\Gamma(t = 0)} = \int_{r=0}^{r=a} \frac{2\pi r}{4\pi\nu t} e^{(\frac{-r^2}{4\nu t})} dr \tag{D.6}$$

Equation D.6 is integrated numerically to get time variation of $\frac{\Gamma(t)}{\Gamma(t=0)}$. Since, $t = 0$ is a singular point, numerical integration is calculated from $t = 0.1$. We particularly have considered three cases.

- Same Re vortex rings at different ν.
- Different Re vortex rings at same ν.

Reynolds number is defined as $Re = \Gamma_0/\nu$. Hence, Γ_0 can be independently changed to obtain any of the above two cases.

- Same Re and ν vortex rings, but with different domain size of circulation calculation.

Figure D.1 shows evolution of $\Gamma^* = \frac{\Gamma}{\Gamma_0}$ as a function of dimensional time. From figure it is clear that, when circulation is calculated over finite domain, higher reduction in circulation is observed for the solution with larger viscosity. And for a given viscosity same amount of reduction is observed at all Re. As the size of the domain over which

circulation is calculated gets bigger, slower reduction in circulation is observed. Final observation is in-line with what was explained earlier, as the calculation domain size increases reduction in circulation gets smaller, and when domain becomes infinitely large, no reduction in circulation is observed.

Equation D.6 gives evolution of circulation with dimensional time. As explained in section 3.5, time can be non-dimensionalized as $t^* = t\frac{\Gamma_0}{2\pi R^2}$. Hence, by replacing t by $t^*\frac{2\pi R^2}{\Gamma_0}$, we get circulation evolution equation in non-dimensional time. i.e.

$$\frac{\Gamma(t^*)}{\Gamma(t^*=0)} = \int_{r=0}^{r=a} \frac{rRe}{4\pi R^2 t^*} exp\left(\frac{-r^2 Re}{8\pi R^2 t^*}\right) dr \tag{D.7}$$

Figure D.2 shows evolution of circulation in non-dimensional time co-ordinates as given by equation D.7. Figure D.2a shows that in non-dimensional co-ordinates all Re matched vortex rings show exactly the same circulation evolution, independent of viscosity. This is in-line with the explanation given in section 3.5. Figure D.2b shows that for a given solution, reduction in circulation depends on Re. This expected behaviour is also shown in figure 3.49. Hence, figure D.1 and figure D.2 together shows the evolution circulation over finite area domains. Later we compare it with evolution of circulation using vorticity threshold.

Enstrophy (E) is another property of vortex ring which is often used. Enstrophy over a finite domain is calculated as,

$$E(t) = \int_{r=0}^{r=a} (\omega(r,t))^2 dA = \int_{r=0}^{r=a} (\omega(r,t))^2 2\pi r dr \tag{D.8}$$

where a is the radius of the domain over which enstrophy is calculated. Now, substituting expression for $\omega(r,t)$ from equation D.1, we get,

$$E(t) = \int_{r=0}^{r=a} \frac{\Gamma_0^2}{16\pi^2\nu^2 t^2} exp\left(\frac{-r^2}{2\nu t}\right) 2\pi r dr \tag{D.9}$$

However, the required quantity is $\frac{E(t)}{E(t=0)}$. From equation D.2, $E(t=0) = \Gamma_0^2$. Hence,

$$\frac{E(t)}{E(t=0)} = \int_{r=0}^{r=a} \frac{r}{8\pi\nu^2 t^2} exp\left(\frac{-r^2}{2\nu t}\right) dr \tag{D.10}$$

Equation D.10 is numerically calculated to get time evolution of enstrophy. Similar to circulation calculation starts from $t = 0.1$, since $t = 0$ is a singularity.

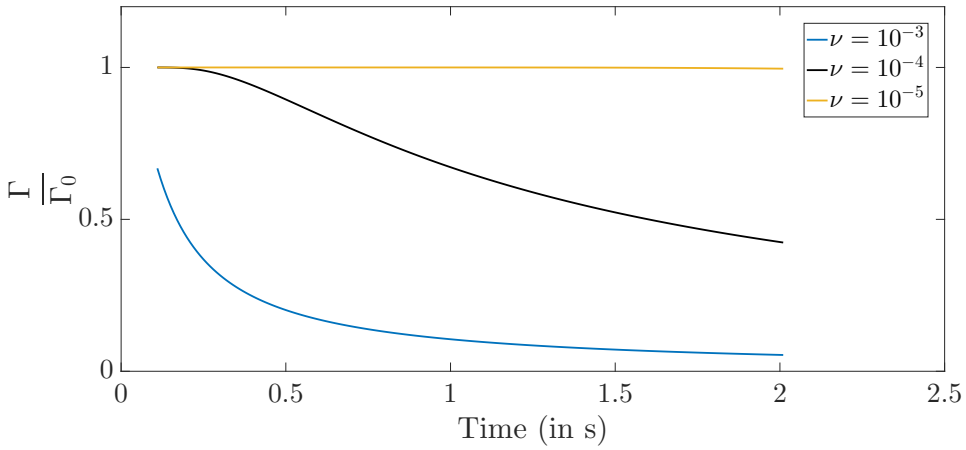

(a) Effect of viscosity at constant Re ($Re = 10000$, $a = 0.6 \times$ R)

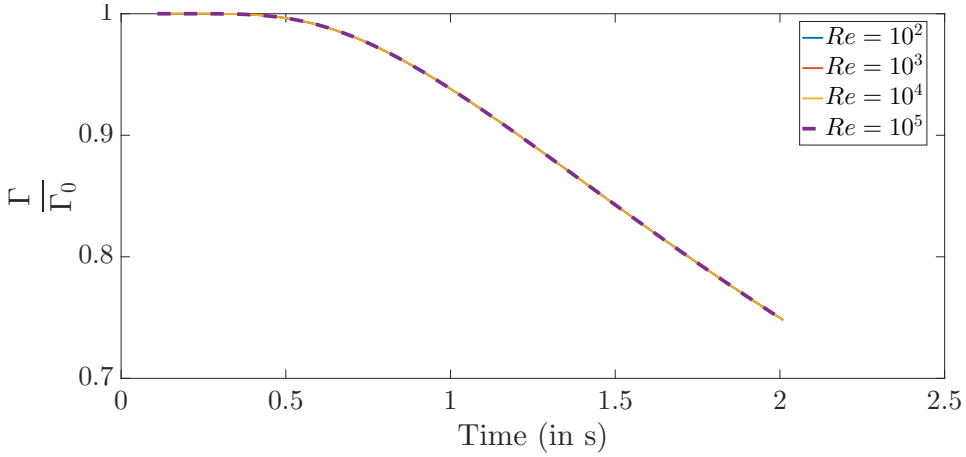

(b) Effect of Re at constant ν ($\nu = 10^{-5}$, $a = 0.6 \times$ R)

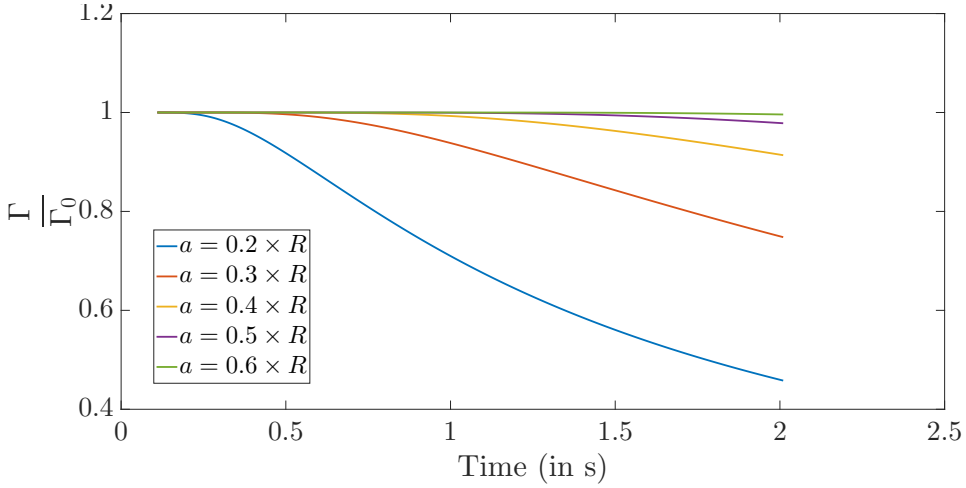

(c) Effect of calculation domain area at constant ν and constant Re ($\nu = 10^{-5}$, $Re = 10000$)

Fig. D.1 Circulation evolution calculated over finite area domain for three different cases. Note that time plotted here is dimensional time. R corresponds to radius of vortex ring i.e. 0.035 m. a corresponds to the radius of domain over which circulation is calculated. Since, time $t = 0$ is a singular point, numerical integration can't be performed at $t = 0$. Hence, plots starts from $t = 0.1$.

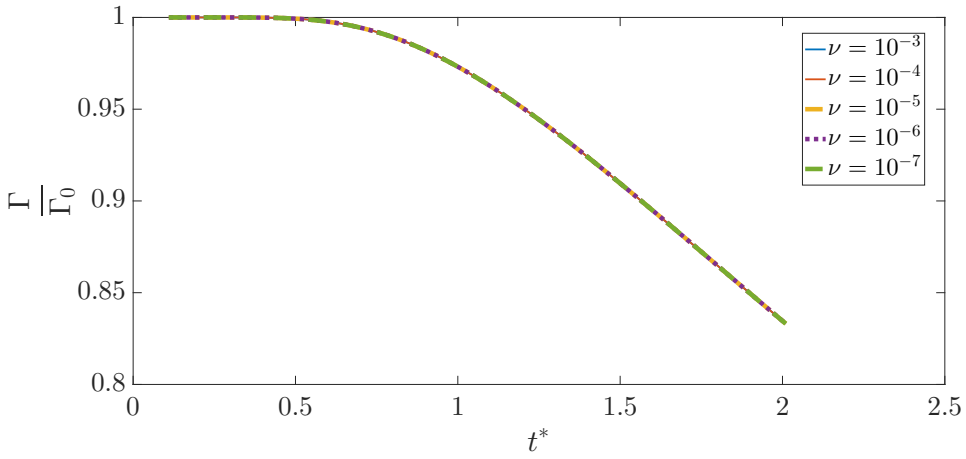

(a) Effect of viscosity at constant Re ($Re = 1000$, $a = 0.3 \times$ R)

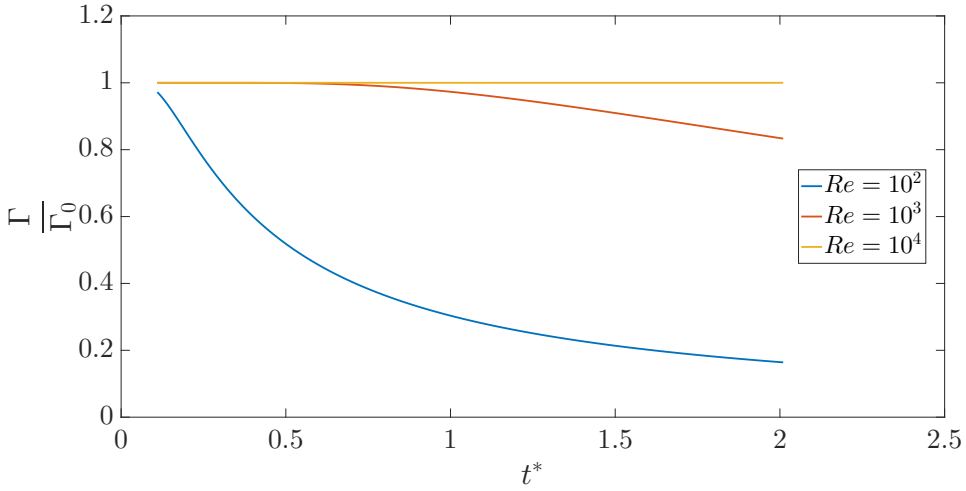

(b) Effect of Re at constant ν ($\nu = 10^{-5}$, $a = 0.3 \times$ R)

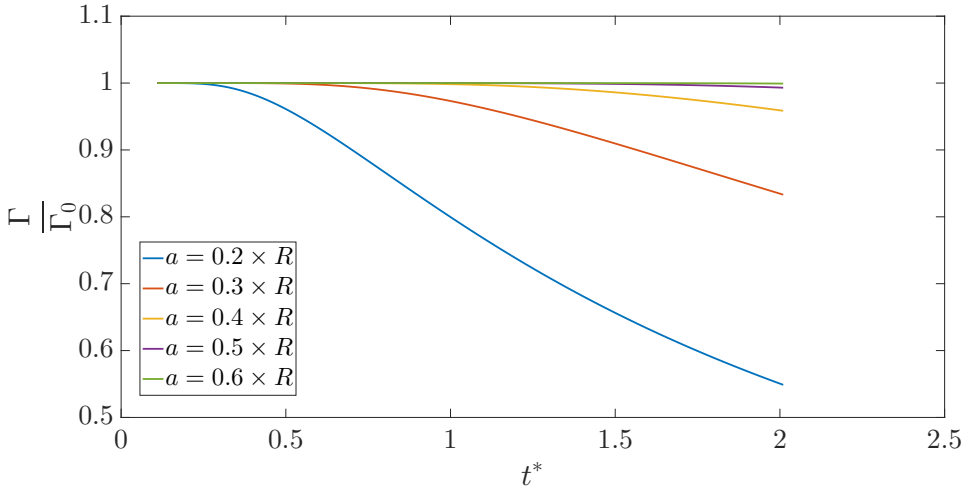

(c) Effect of calculation domain area at constant ν and constant Re ($\nu = 10^{-5}$, $Re = 1000$)

Fig. D.2 Circulation evolution calculated over finite area domain for three different cases as a function of non-dimensional time. R corresponds to radius of vortex ring i.e. 0.035 m. a corresponds to the radius of domain over which circulation is calculated.

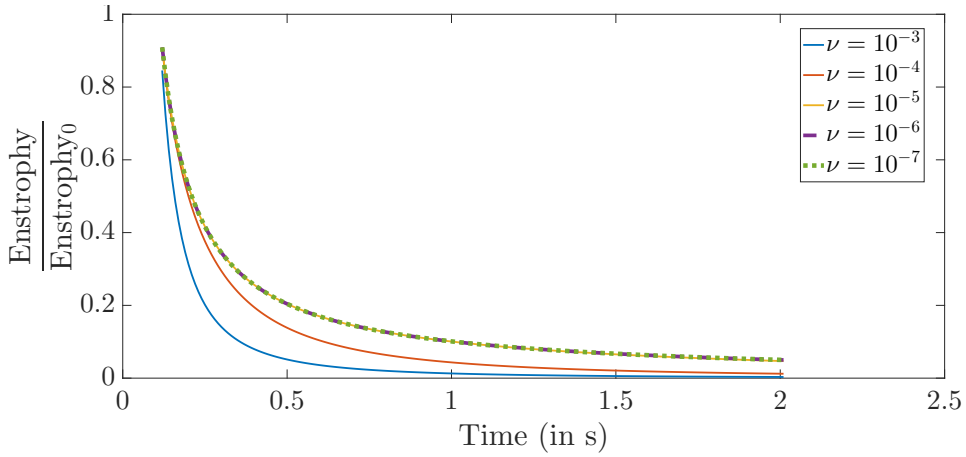

(a) Effect of viscosity at constant Re ($Re = 1000$, $a = 0.3 \times \mathrm{R}$)

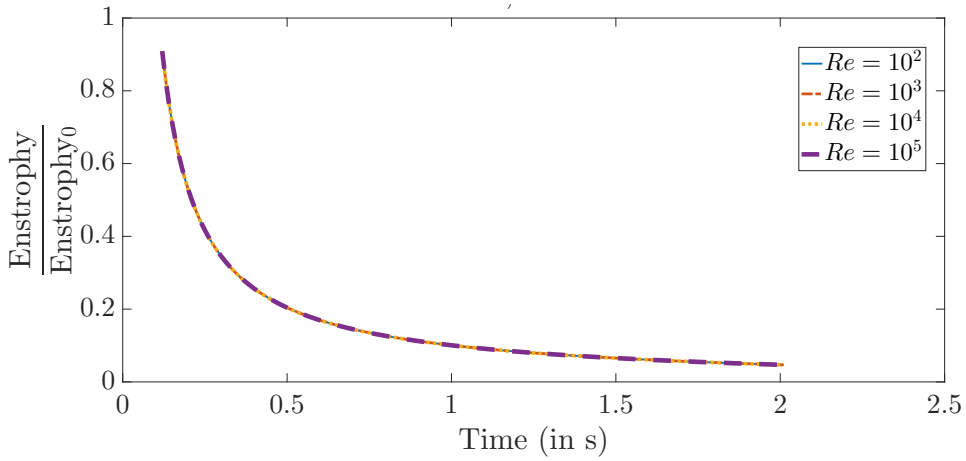

(b) Effect of Re at constant ν ($\nu = 10^{-5}$, $a = 0.3 \times \mathrm{R}$)

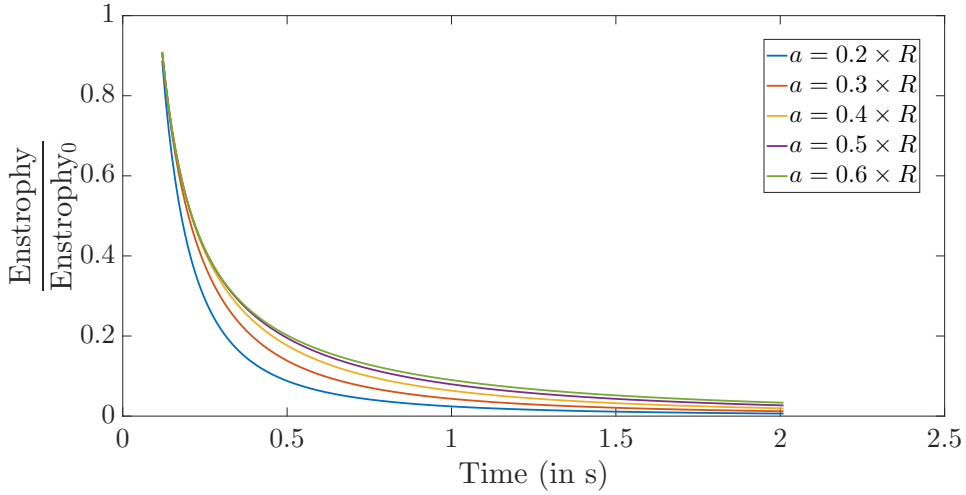

(c) Effect of calculation domain area at constant ν and constant Re ($\nu = 10^{-5}$, $Re = 1000$)

Fig. D.3 Enstrophy evolution calculated over finite area domain for three different cases as a function of dimensional time.

From figure D.3a, it is clear that for a particular Re, reduction in enstrophy is more for solutions of higher viscosity in dimensional time co-ordinates. Whereas, for a particular viscosity, changing Re doesn't have any effect (Refer figure D.3b). Changing area of the domain has the same effect as it was in the case of circulation. Smaller domains show faster reduction in enstrophy, since more and more vorticity diffuses out of the domain quickly.

Replacing t with $t^* \frac{2\pi R^2}{\Gamma_0}$ will give below equation, which will describe enstrophy evolution in non-dimensional co-ordinates.

$$\frac{E(t^*)}{E(t^*=0)} = \int_{r=0}^{r=a} \frac{rRe^2}{32\pi^3 R^4 (t^*)^2} exp\left(\frac{-r^2 Re}{4\nu t^* R^2}\right) dr \tag{D.11}$$

Numerical solution of equation D.11 for two different cases is given in figure D.4.

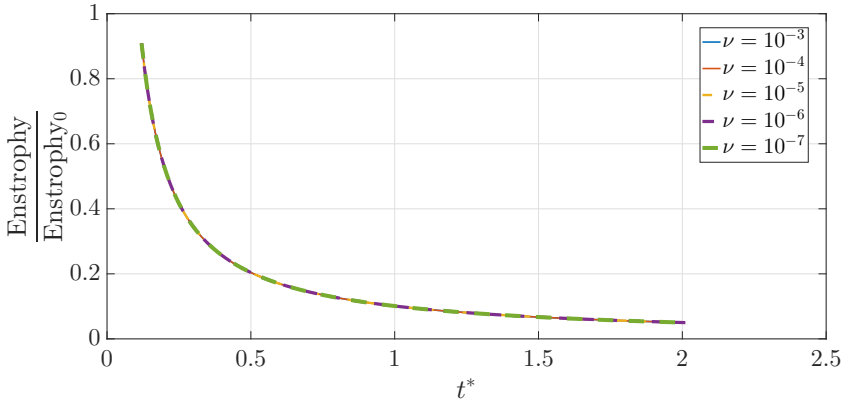

(a) Effect of viscosity at constant Re ($Re = 10000$, $a = 0.3 \times \mathrm{R}$)

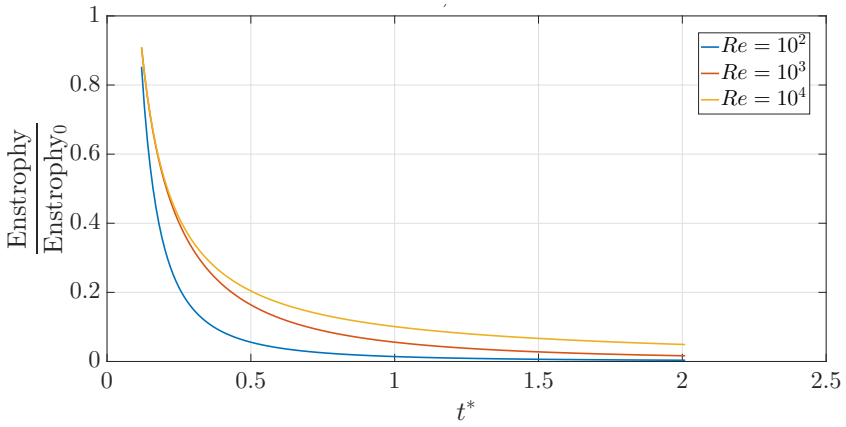

(b) Effect of Re at constant ν ($\nu = 10^{-5}$, $a = 0.3 \times \mathrm{R}$)

Fig. D.4 Enstrophy evolution calculated over finite area domain for three different cases as a function of non-dimensional time.

Figure D.4a shows that for Re matched vortex rings, enstrophy evolution is independent of ν in non-dimensional time co-ordinates. However, for a particular viscosity, reduction in Re will cause faster reduction in enstrophy in non-dimensional time.

In all the above calculations, domain size was constant throughout the duration of vortex ring evolution. However, another method very frequently used involves vorticity threshold (Fabris et al., 1996; Gharib et al., 1998; Weigand and Gharib, 1994). Since, the threshold vorticity occurs at different distances at different time instants, domain size for calculations keeps changing with time. Hence, a used in equation (D.6), (D.7), (D.10) and (D.11), is a time dependent quantity. A MATLAB code was developed, which first determines the location of vorticity cutoff from the center of the ring (i.e. a), then evaluates (D.6), (D.7), (D.10) and (D.11).

Figure D.5 shows circulation evolution in dimensional time. From figure D.5a, it is clear that as long as Re is kept constant, varying ν doesn't have any effect on circulation evolution in dimensional time. And for a particular ν, vortex rings with lower Re, loose circulation faster (Refer figure D.5b). These two observations are in stark difference with the observations made using fixed domain area (Refer D.1). Higher vorticity cutoff will show larger reduction in circulation and vice versa, which is fairly intuitive (Refer figure D.5c).

However, when circulation is plotted against non-dimensional time, very different behavior is seen (Refer figure D.6). Figure D.6a shows that, vortex rings in lower viscosity solution undergo more reduction in circulation though Re is matched in t^* co-ordinates. The reason is, solution with lower viscosity will have lower circulation to get the same Re. Hence, vorticity levels falls below threshold vorticity quickly, causing reduction in circulation. For vortex rings in a particular ν, reduction Re causes faster in circulation. And effect of vorticity threshold is exactly same as in the case of dimensional time.

Enstrophy variation calculated using vorticity cutoff method is shown in figure D.7 and D.8. Behavior of enstrophy is in sync with that of circulation. For Re matched vortex rings, ν is immaterial in dimensional co-ordinates. However, in non-dimensional co-ordinates, vortex ring in lesser viscosity solution shows faster reduction in enstrophy. For a particular ν solution, lesser Re shows faster reduction in enstrophy both in t and t^* co-ordinates. Vorticity cutoff has the same effect on enstrophy as it had on circulation.

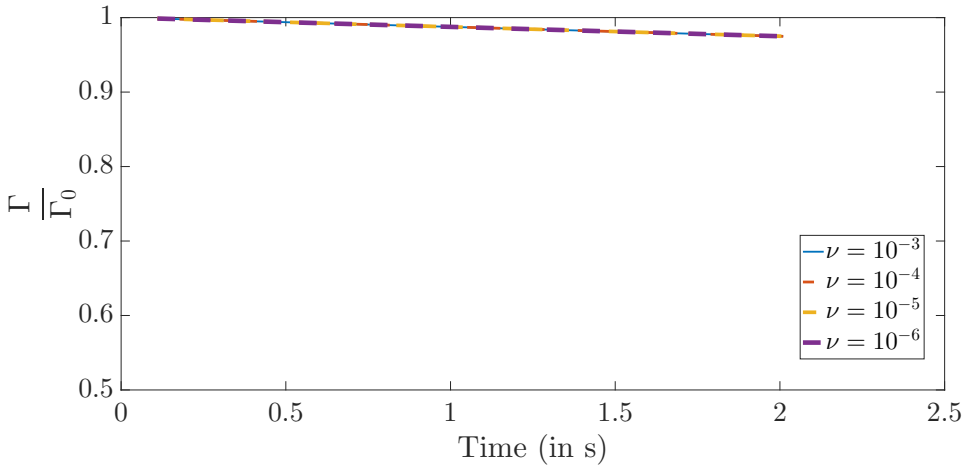

(a) Effect of viscosity at constant Re ($Re = 10000$, $\omega_{cutoff} = 10$)

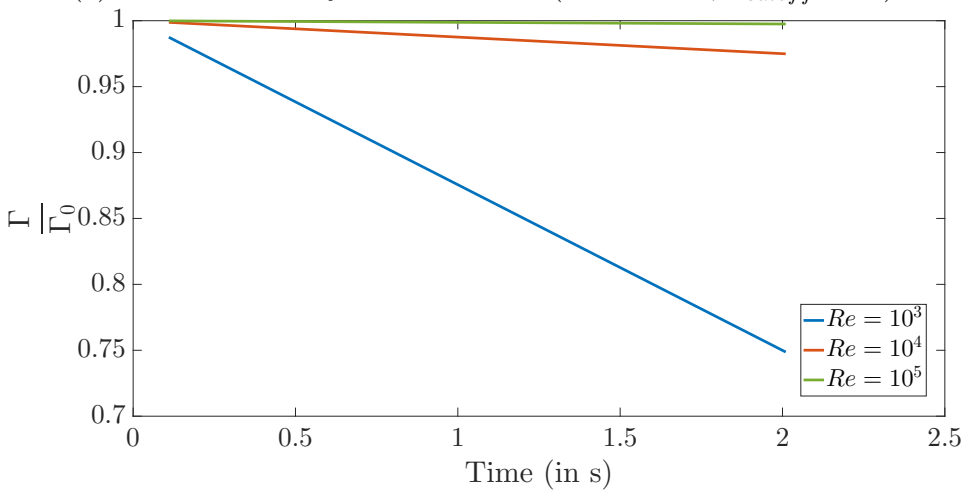

(b) Effect of Re at constant ν ($\nu = 10^{-5}$, $\omega_{cutoff} = 10$)

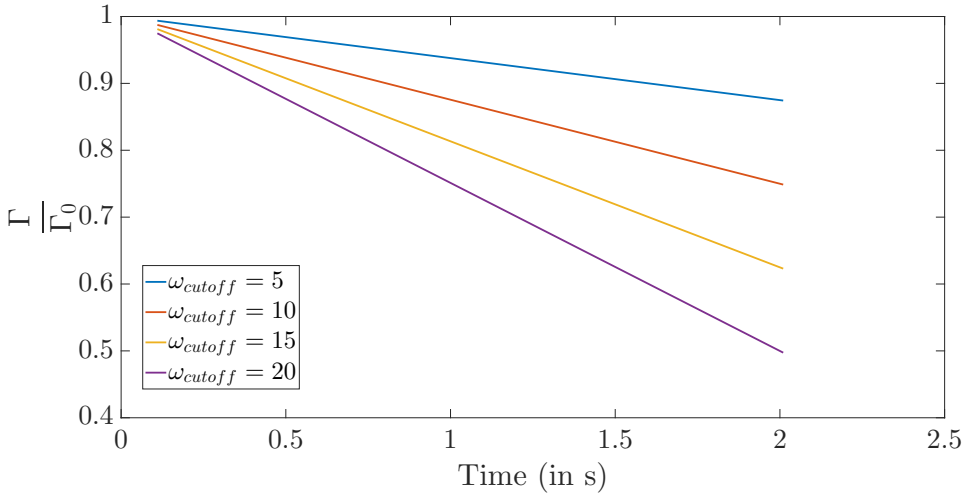

(c) Effect of cutoff vorticity at constant ν and constant Re ($\nu = 10^{-5}$, $Re = 1000$)

Fig. D.5 Circulation evolution calculated using vorticity cutoff for three different cases as a function of dimensional time.

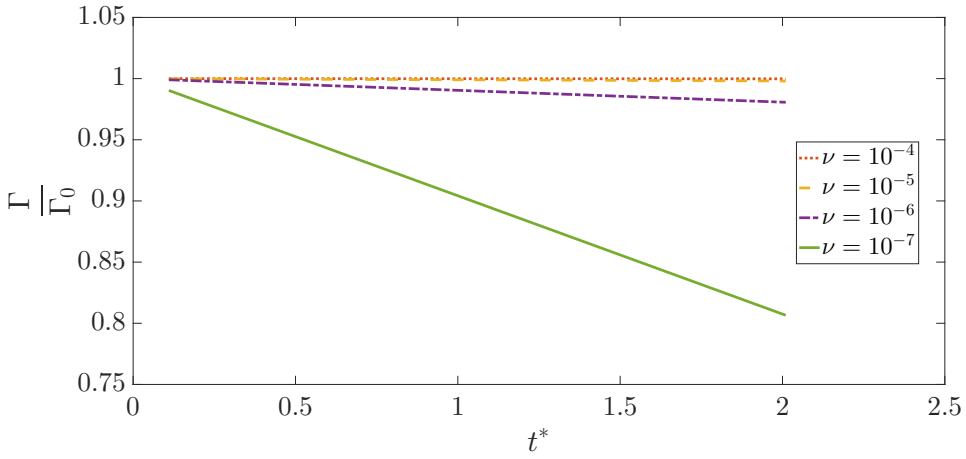

(a) Effect of viscosity at constant Re ($Re = 10000$, $\omega_{cutoff} = 10$)

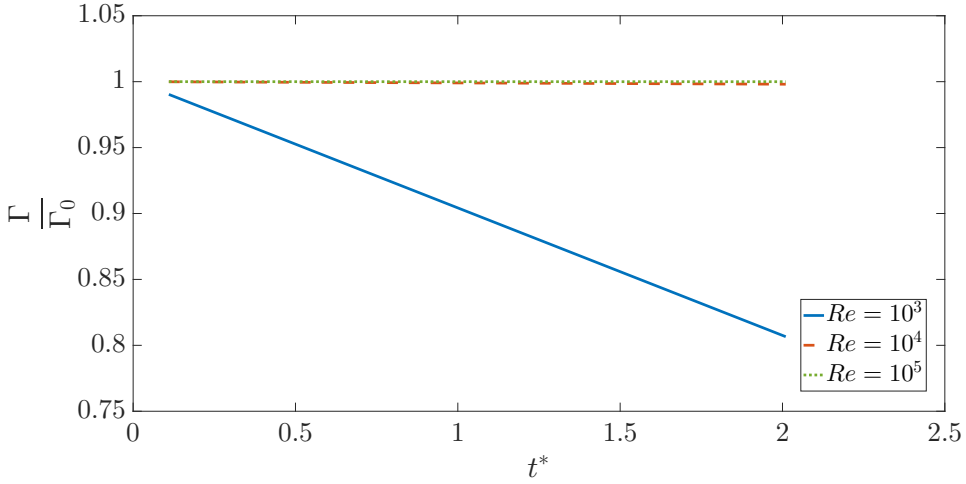

(b) Effect of Re at constant ν ($\nu = 10^{-5}$, $\omega_{cutoff} = 10$)

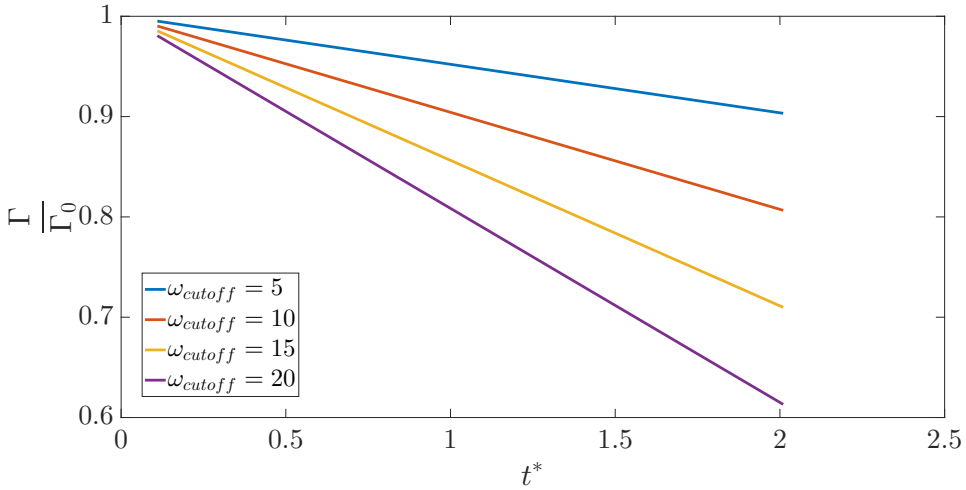

(c) Effect of cutoff vorticity at constant ν and constant Re ($\nu = 10^{-5}$, $Re = 1000$)

Fig. D.6 Circulation evolution calculated using vorticity cutoff for three different cases as a function of non-dimensional time.

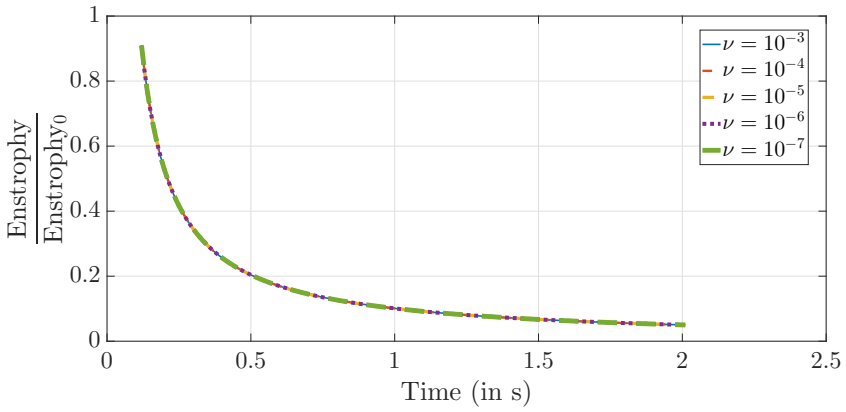

(a) Effect of viscosity at constant Re ($Re = 10000$, $a = 0.3 \times \mathrm{R}$)

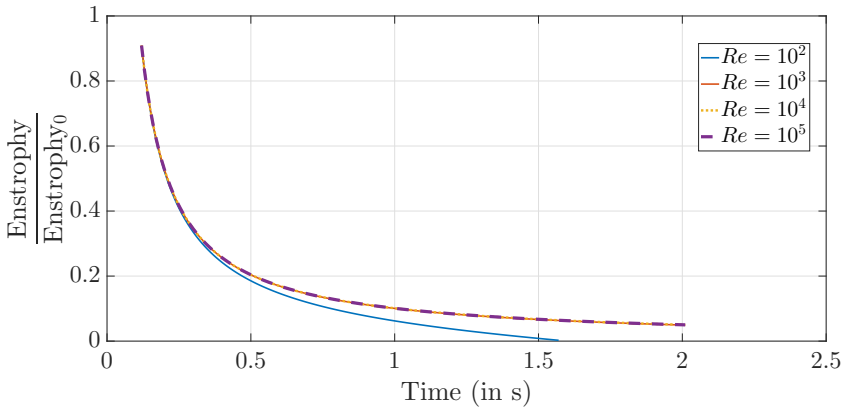

(b) Effect of Re at constant ν ($\nu = 10^{-5}$, $a = 0.3 \times \mathrm{R}$)

Fig. D.7 Enstrophy evolution calculated using vorticity cutoff for three different cases as a function of dimensional time.

In this section, an attempt has been made to calculate circulation and enstrophy as a function of time analytically. As explained earlier, for a infinitely large domain, circulation doesn't change with time. However, when calculations are done on finite domain, reduction in circulation is observed. Two ways of calculating circulation and enstrophy are used, (1) Over finite area domain (2) Using vorticity cutoff. Integrals of equation (D.6), (D.7), (D.10) and (D.11) are evaluated numerically. Effect of varying Re at constant ν and effect of varying ν at constant Re are calculated. Results are plotted in both t and t^* co-ordinates.

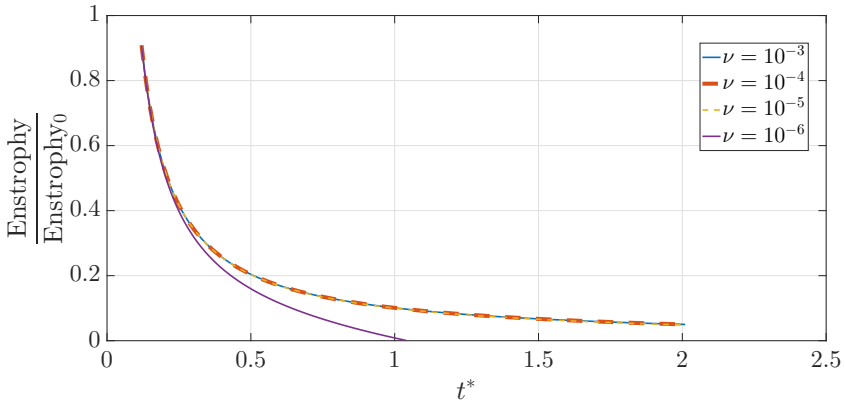

(a) Effect of viscosity at constant Re ($Re = 10000$, $a = 0.3 \times \mathrm{R}$)

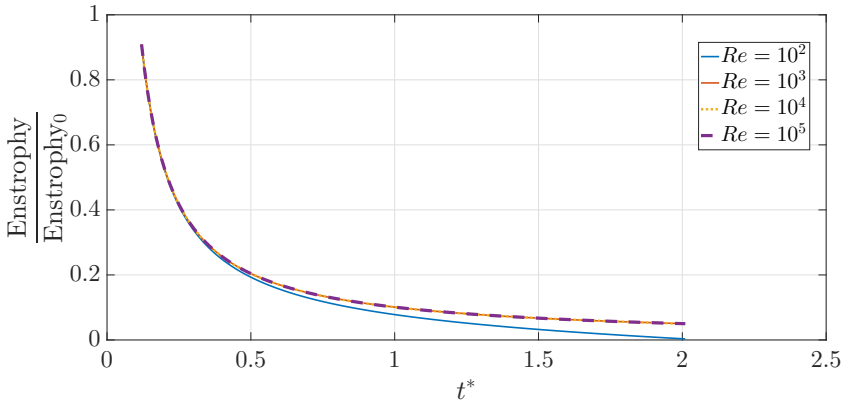

(b) Effect of Re at constant ν ($\nu = 10^{-5}$, $a = 0.3 \times \mathrm{R}$)

Fig. D.8 Enstrophy evolution calculated using vorticity cutoff for three different cases as a function of non-dimensional time.

Appendix E

ANSYS Simulations

ANSYS simulations were carried out to examine formation number in vortex rings. As explained in section 3.6, there exists a critical stroke-length of piston input, above which it is not possible to generate an isolated vortex ring (Gharib et al., 1998). As shown in Gharib et al. (1998), circulation of vortex ring increases as the stroke-length increases till critical stroke-length is reached. Vortex ring circulation saturates at formation number, and thereafter, increase in stroke-length will not cause any increase in ring circulation, and leads to formation of trailing jet.

Linden and Turner (2001) explained this phenomena using transformation in vortex ring from thin core → thick core → Hills's spherical vortex, as the stroke-length of piston is increased. According to this argument, when stroke-length of piston input is much lesser than formation number, thin core vortex rings are generated. However, as the stroke-length increases, core of vortex ring also increases. And at the critical stroke-length Hill's spherical vortex rings are generated. Hereafter, vortex ring won't be able to accommodate anymore fluid inside the core, hence all the fluid pushed by piston movement beyond critical stroke-length follow primary ring as a trailing jet. Very similar argument is presented by Mohseni and Gharib (1998). Gao and Yu (2010) approximated leading vortex as a Norbury vortex ring. By applying Kelvin-Benjamin variational principle, formation time and time for separation of leading vortex from trailing jet was obtained.

In our experiments, we observed that the core of vortex ring increases with increase in piston velocity also (Refer section 3.3.7). Hence, if thin core → thick core → Hills's spherical vortex transformation is the reason for existence of formation number, then there must exist a formation number with respect to piston velocity also. To check the validity of our arguments for existence of formation number in velocity, ANSYS

simulations were carried out. ANSYS Student 19.1 workbench is used with student license for simulations. Fluid equations are solved using Fluent flow-solver. Post-processing is carried out using CFD-post available inside ANSYS workbench (ANSYS, 2018).

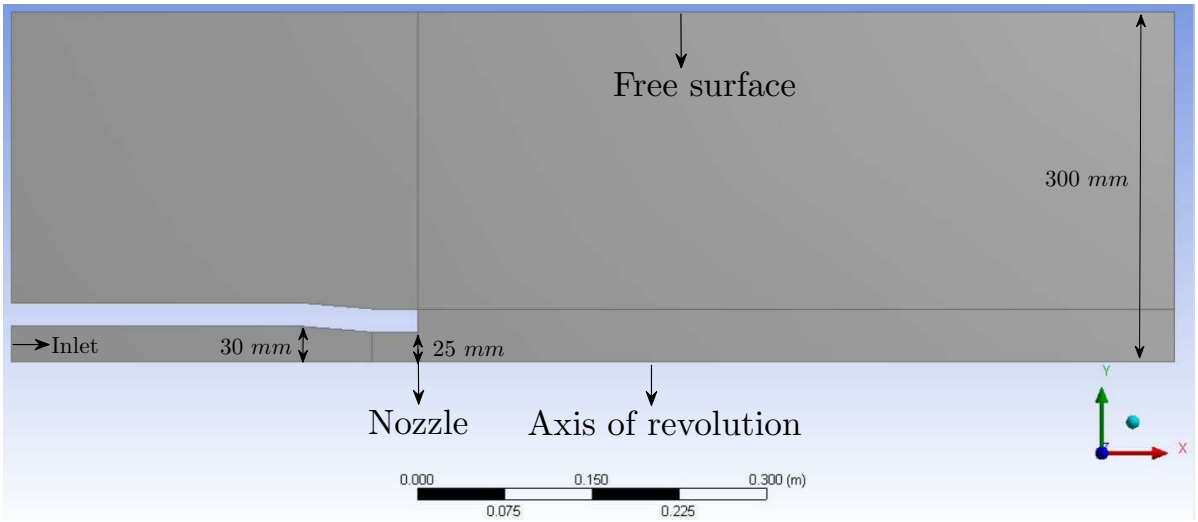

Fig. E.1 Geometry used in ANSYS simulations. 2D axisymmetric simulations are carried out using ANSYS. Images used courtesy of ANSYS, Inc.

2D axisymmetic simulations were carried out using ANSYS. Geometry is designed to match experimental setup (Refer figure E.1). Regular square mesh with 170,000 cells was used for simulations. Mesh independence was tested with four different mesh sizes. Pressure based solver was used for solving 2D axisymmetric Navier-Stokes equation. PISO scheme was used for pressure-velocity coupling. Second order implicit formulation was used for time marching, with time step of 0.001 s. Laminar simulation was carried out. Fluid used in simulation was water with $\rho = 998.2 kg/m^3$ and $\mu = 0.001003 Pa - s$. Standard initialization with pressure, axial velocity and radial velocity equal to zero was used.

Axis boundary condition is used for axis of symmetry. Pressure-outlet boundary condition with zero gauge pressure is used for free surface. Time varying inlet flow is necessary to simulate piston movement. A user defined function was written for time dependent inlet flow boundary condition. All the other boundaries have no slip wall boundary condition.

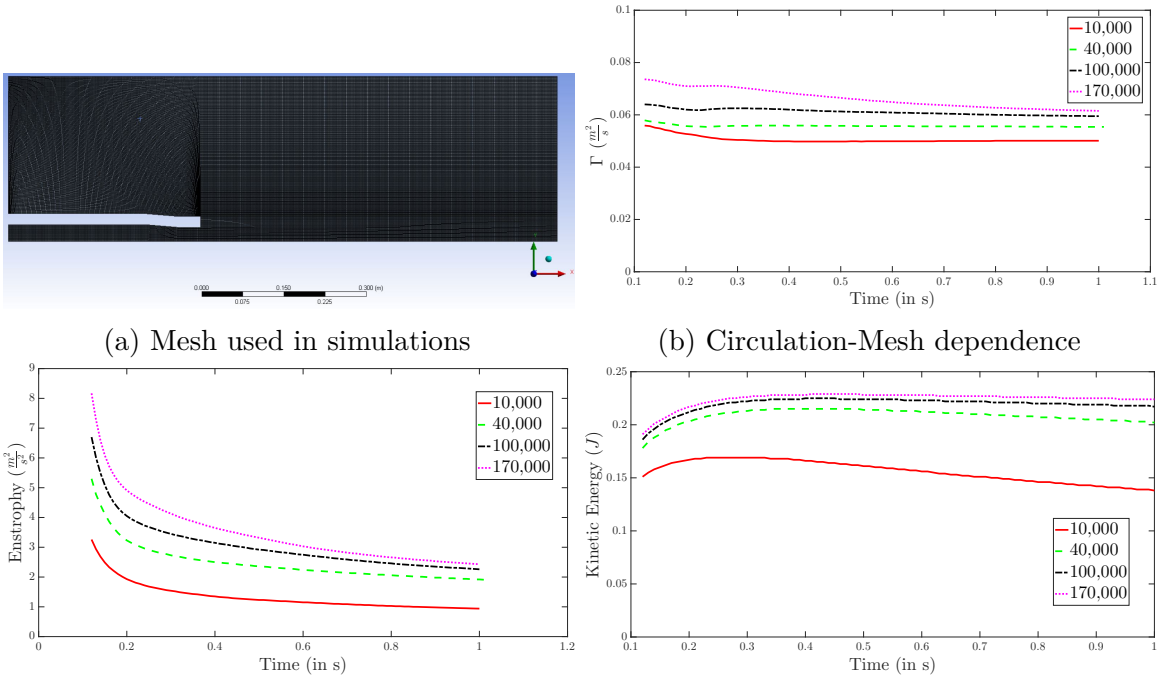

(a) Mesh used in simulations

(b) Circulation-Mesh dependence

(c) Enstrophy-Mesh dependence

(d) Kinetic Energy-Mesh dependence

Fig. E.2 Mesh used in simulations and the effect of number of mesh cells on few different properties. Images used courtesy of ANSYS, Inc.

Results of ANSYS simulation are given below. In all the figures vorticity magnitude is plotted. Vorticity scale used in all the figures is given below.

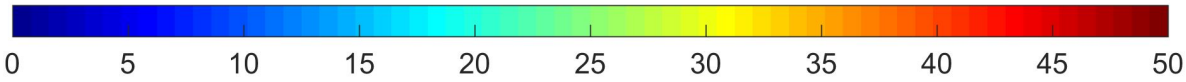

First simulations were carried out to check whether the simulations are capable of capturing classical formation number, when stroke length is increased. Figure E.3 shows vortex evolution for two different L/D ratios. It is clear from figure that, for L/D $\leq$ 4, an isolated vortex ring is formed, whereas for L/D $>$ 4 a trailing jet with multiple secondary vortex rings appears. This observation is is very good agreement with Gharib et al. (1998). Primary ring remains the same upon further increase in stroke-length beyond formation number, and the trailing jet gets the additional circulation, which results in more vorticity patches (Refer figure E.5).

Figure E.4 shows effect of increasing velocity for L/D $<$ 4. From figure E.4 and E.3a, it is clear that, increasing velocity increases the core thickness, which was earlier observed in experiments also (Refer figure 3.28). However, there is no sign of trailing jet, though

the rings are nearly Hill's spherical vortices. However, wake behind the ring is clearly visible, which implies that there is significant dumping of vorticity from the core of the ring to wake. Also wake strength increases with increase in piston velocity as it is evident from figure E.4. Difference between wake and the trailing jet is demonstrated in figure E.6.

Hence, absence of trailing jet though the ring is nearly Hill's spherical vortex raises questions over arguments of Linden and Turner (2001). When trailing jet appears from increasing stroke-length beyond formation number, primary vortex ring is still far from Hill's spherical vortex. Hence, reaching Hill's spherical state is not the driving mechanism for existence of vortex ring formation number. Recent studies on this are directed towards perturbation response of vortex rings O'Farrell and Dabiri (2012, 2014), which could be a possible reason for existence of this phenomena.

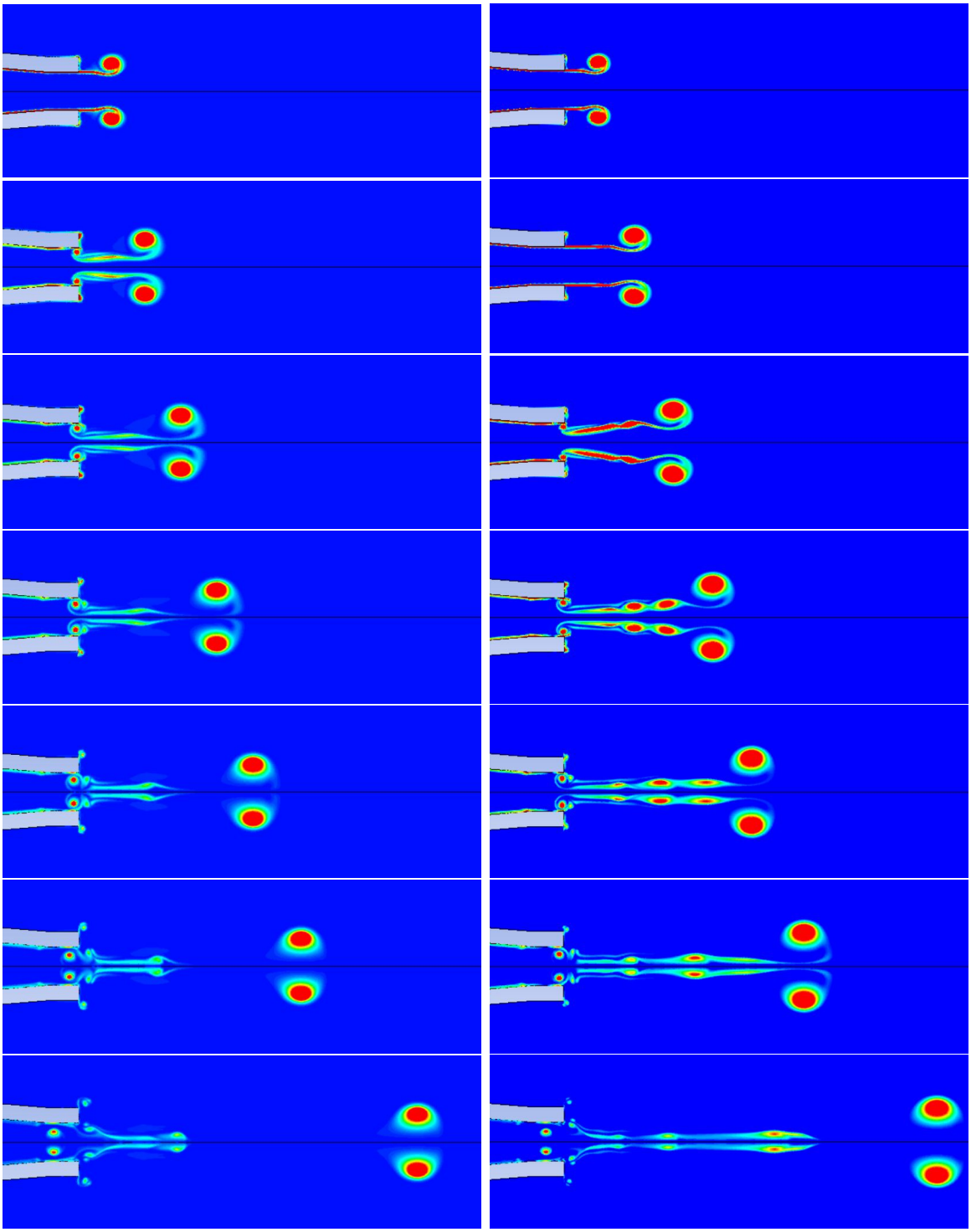

(a) L100 V500, L/D = 2.88 (b) L200 V500, L/D = 5.76

Fig. E.3 Effect of increasing stroke-length on vortex ring evolution. Images used courtesy of ANSYS, Inc.

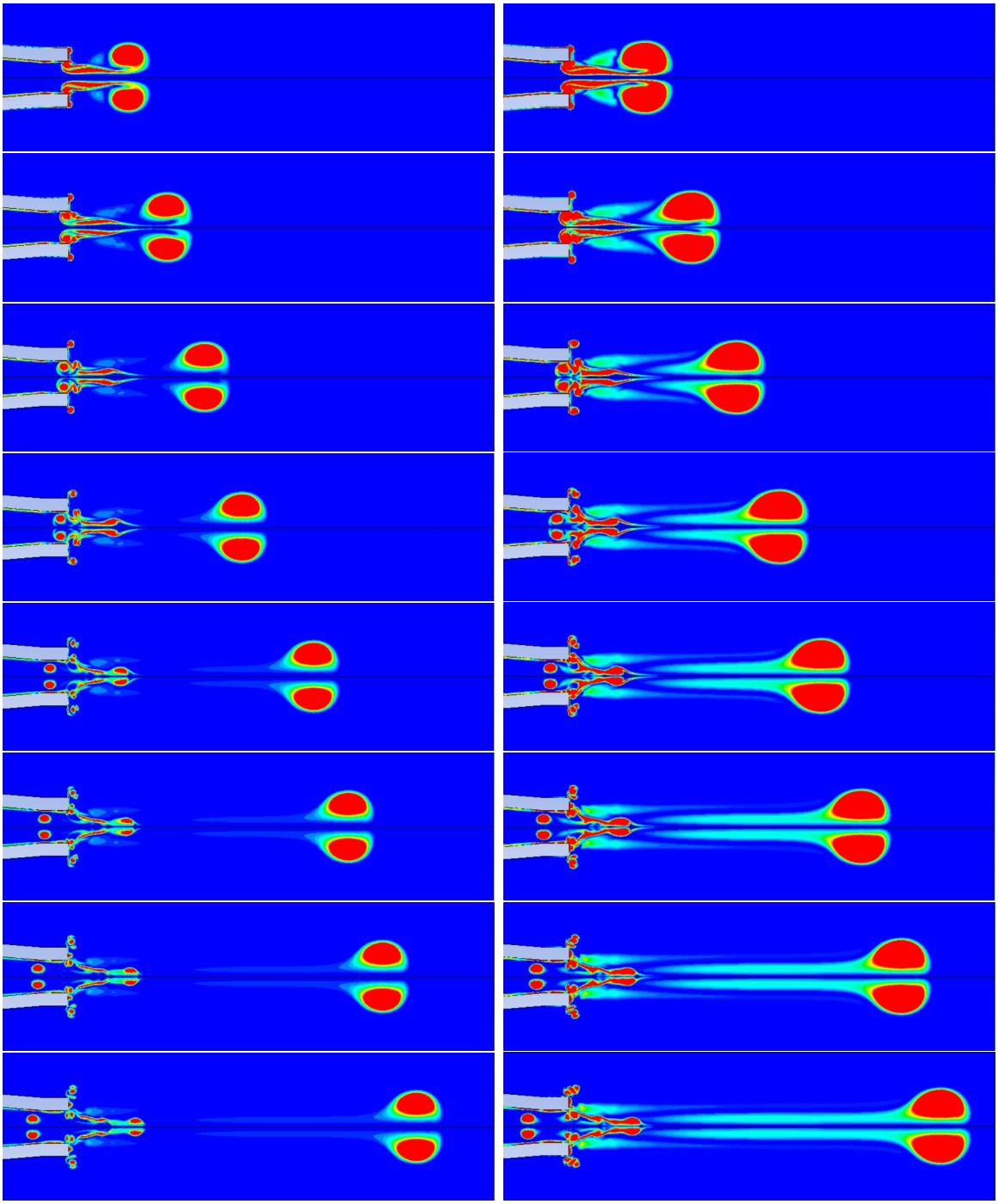

(a) L100 V2000, L/D = 2.88 (b) L100 V5000, L/D = 2.88

Fig. E.4 Effect of increasing velocity on vortex ring formation. Images used courtesy of ANSYS, Inc.

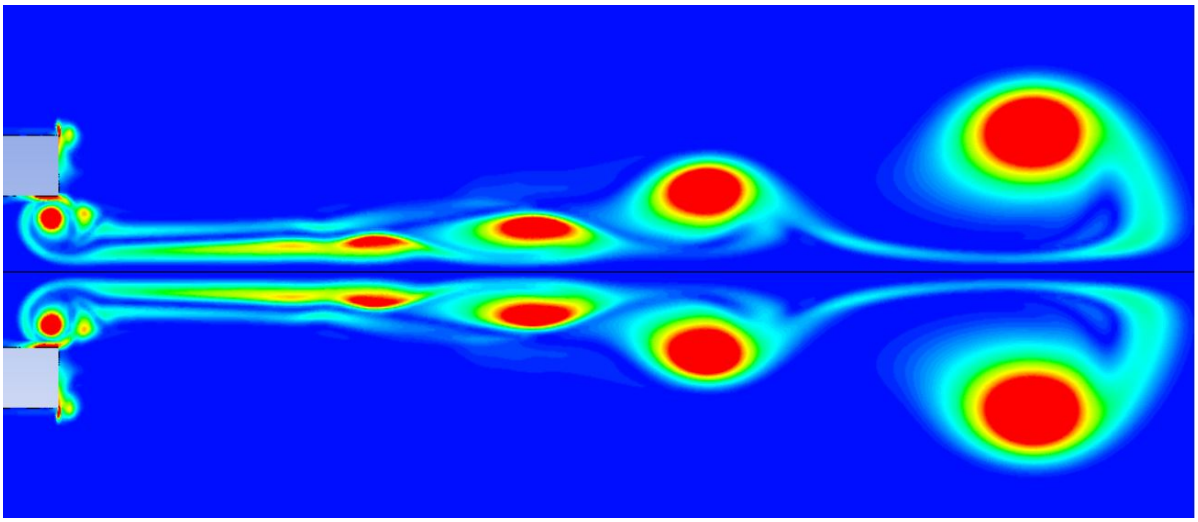

Fig. E.5 Trailing jet behind primary vortex ring for L300 V500 case. Images used courtesy of ANSYS, Inc.

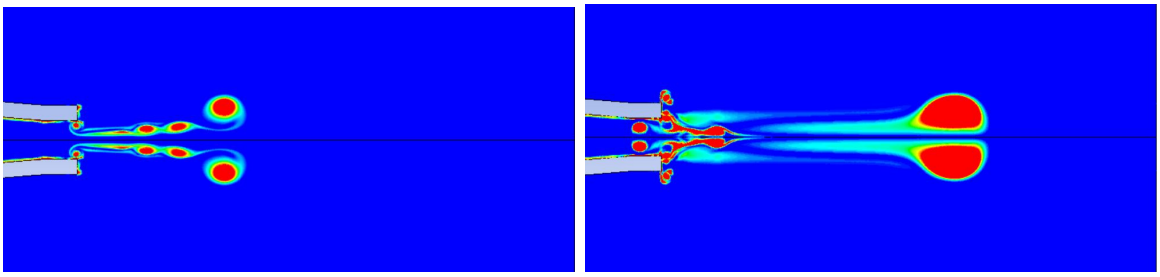

(a) L200 V500, L/D = 5.76 (b) L100 V5000, L/D = 2.88

Fig. E.6 Difference in trailing jet and wake for two vortex ring cases. Images used courtesy of ANSYS, Inc.

Interestingly, no trailing jet is observed, when simulations are carried out in 2D Cartesian co-ordinates, which corresponds to vortex pairs (Refer figure E.7). From figure it is clear that, the shear layer feeding to the vortex pair gets broken into multiple small secondary vortex patches. However, as they move down, they get entrained into the primary vortex pair. Hence, for all L/D only a single vortex pair forms. Hence, no formation number exists in vortex pair, though it is a planar analogue of vortex rings.

Effect of increasing velocity on vortex pair formation is also carried out. As shown in figure E.8, increasing velocity doesn't show any trailing jet for vortex pair also. However, vortex pairs formed from increasing velocity have thicker core, with cores are in contact at the centerline. Simulations are carried out in fluids with carreau shear-thinning viscosity profile. Reduction in circulation, enstrophy, kinetic energy and peak vorticity in shear-thinning fluids is found to be more than that of Newtonian solution. Though results qualitatively match with experiments, better schemes have to be used to get quantitatively accurate solution.

In this section, ANSYS simulations were carried out to test formation number and its dependence on piston velocity. From simulations it is clear that formation number is nearly independent of velocity. No saturation in circulation is observed for vortex rings, as velocity is increased. Which implies that the saturation in circulation, enstrophy, kinetic energy etc observed in section 3.3, could be mainly because of increased turbulent dissipation rather than formation number effects. However,as the velocity is increased core of the vortex ring increases and finally reaches Hill's spherical vortex stage. Absence of trailing jet even though ring generated is nearly Hill's spherical vortex casts doubts on the arguments of Linden and Turner (2001). There is no trailing jet in the case of vortex pairs, though it is 2D Cartesian analogue of vortex ring.

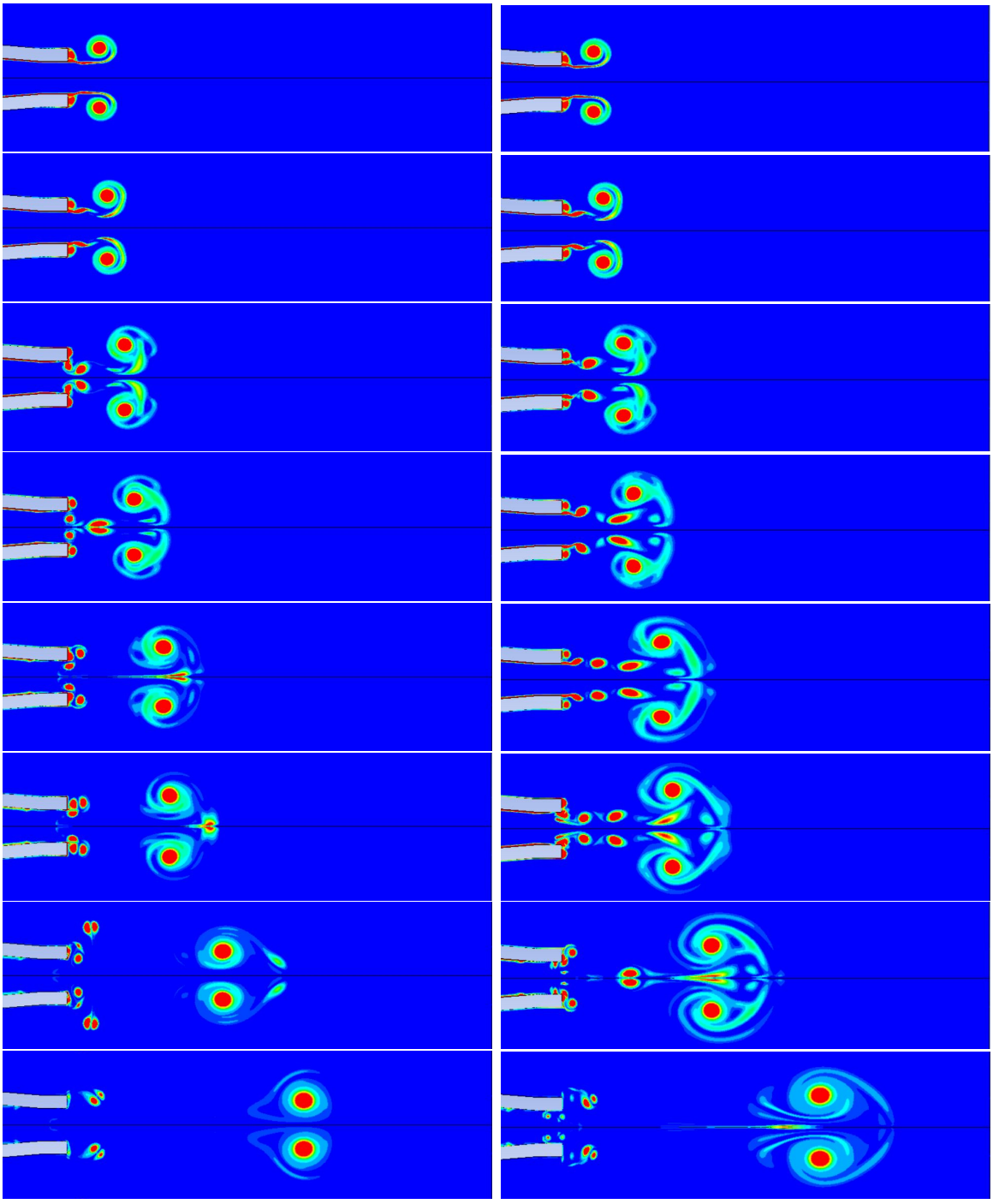

(a) L300 V500, L/D = 8.64 (b) L500 V500, L/D = 14.44

Fig. E.7 Effect of increasing stroke-length beyond L/D = 4 on vortex pair formation. Images used courtesy of ANSYS, Inc.

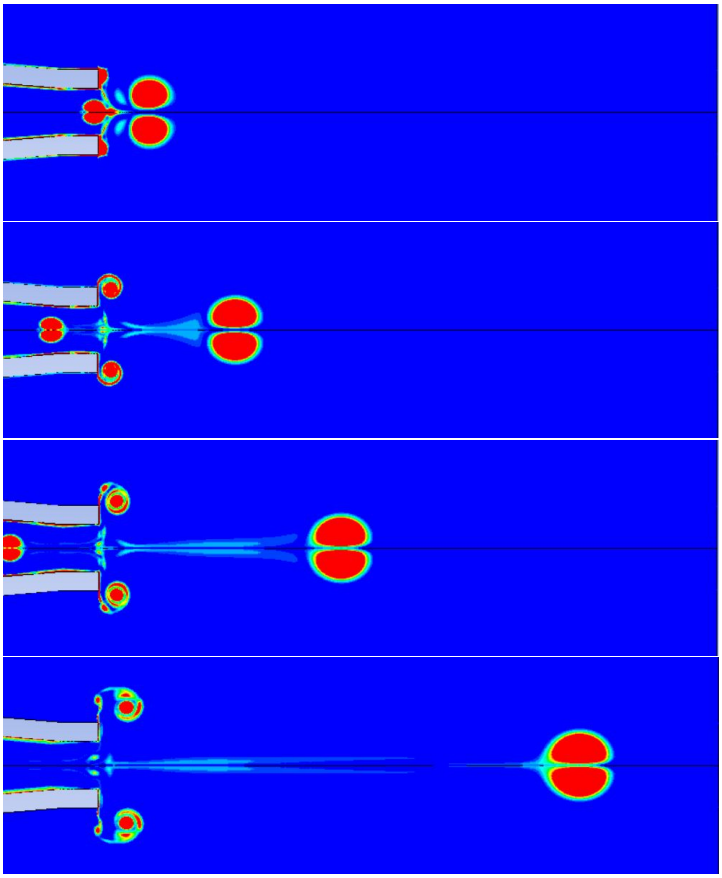

Fig. E.8 Effect of increasing velocity on vortex pair formation. L100 V2000, L/D = 2.88 case. Images used courtesy of ANSYS, Inc.